Electrochemical synthesis and functionalization of graphene materials for energy storage devices

電気化学的手法によるグラフェンの作製と機能化および蓄電デバイスへの適用

September 2020

Benoît Denis Louis Campéon

The Graduate School of Natural Science and Technology

(Doctor Course)

Okayama University

GENERAL INTRODUCTION

Greenhouse gas emissions has already led global warming to 1°C above the pre-industrial level. There is overwhelming evidence that this is resulting in profound consequences for ecosystems and people. To keep global warming to well below 2°C above pre-industrial levels we need unprecedented transitions in all aspect of the society including the energy. At this present-day, fossil fuel represents 85% of world total primary energy consumption making transition toward renewable energy one of the greatest challenges of our century. Most of renewable energies are by nature fluctuating and thus their democratization requires the development of fixed and mobile energy storage systems. Lithium-ion battery (LIBs) is now used in everything from mobile phones to laptops and electric vehicles. This lightweight, rechargeable and powerful system, rewarded in 2019 by the Nobel Prize in Chemistry, holds great hope for tomorrow's ecofriendly society. Yet, current LIBs technology performances and costs are still far from being able to support the energy transition. For these reasons, the research of new electrode materials has become one of the hottest topics of this decade. In 2010, the Nobel Prize in physics rewarded the groundbreaking experiments regarding the two-dimensional material graphene. Graphene, which is an elementary sheet of graphite, consists of a periodic and two-dimensional arrangement of carbon atoms of monoatomic thickness with a honeycomb structure. It is the latest member of the family of carbon allotropes: diamond, graphite, C60 fullerenes and nanotubes. For the first time in 2004, a graphene sheet stable at room temperature was obtained via mechanical exfoliation of graphite by A. Geim and K. Novoselov. This experiment contradicted the theory that a graphene sheet was thermodynamically unstable. As this new material produced by mechanical exfoliation has remarkable and unique properties, they were awarded the Nobel Prize in physics in 2010. Since this discovery, graphene has been the material the most studied by the scientific community for its new and unique physical properties. Indeed, it has a high electric mobility greater than 2.105 $cm^2\ V^{-1}s^{-1}$, an anomalous quantum Hall effect, a modulated forbidden band (for the case of a graphene bilayer) and it is a transparent conductor since, in the optical region, it absorbs only 2.3% of the light. It also has good flexibility and excellent mechanical strength, and its thermal conductivity is ten times higher than that of copper. Due to its fascinating properties, graphene appears to be a very promising material for many technological applications. Its high electrical conductivity could be exploited in the manufacture of future nano-electronic devices such as LIBs. Indeed since 1985, graphite is commonly found in commercial LIBs as anode material. In this context, the application of graphene as electrode material for LIBs holds great promises to change LIBs technology into a reliable solution for the energy transition.

This thesis is divided into two sections, the first one summarizes the common knowledge concerning graphene properties, synthesis routes, and application toward LIBs, the second part details the experimental research conducted.

The first section starts by introducing the various synthesis routes of graphene, from bottom-up to top-down. In parallel, a discussion about the simulated and the experimental graphene research is conducted revealing the room of improvement of current graphene experimental research. Finally, the research progress of graphene application as electrode material for LIBs is detailed.

The second section presents the scientific advances achieved through this Ph.D.; the first part presents the results of electrochemical synthesis of GO, the second part shows the results of graphene synthesis from GO for LIBs application, and the final part presents the application of iron NPs as spacer for GO reduction unlocking superior SIBs performances.

Chapter 1 the general background, aims and objectives are given.

Chapter 2 presents a comprehensive literature review of graphene is given. The various graphene synthesis methods are introduced mechanical exfoliation, chemical vapor deposition, thermal decomposition of SiC, liquid exfoliation, chemical oxidation of graphite, and electro-chemical. Then the functionalization of graphite, graphene, and graphene oxide are detailed and classified between covalent and non-covalent functionalization.
Prior introducing the application of graphene for lithium-ion battery a working principle and historical research background of lithium-ion battery is given to understand in what way graphene is an attractive solution for next generation lithium-ion battery. Then, a list of strategy and research is given and organized between cathode and anode electrodes.

Chapter 3, the non-destructive, uniform, and scalable electrochemical functionalization and exfoliation of graphite is studied. This research investigates an original way to produce high quality graphene oxide. This electrochemical production revealed to be easy, fast eco-friendly, cheap, and scalable. The application of synthesized graphene oxide for water filtration, lithium-ion battery, and oxygen reduction reaction displayed similar to better results as compared with conventional chemical graphene oxide.

Chapter 4, graphene analogs preparation from GO by combine chemical and thermal reduction methods is presented. A list of their properties is given such as oxygen content, size, specific surface area, defect, and conductivity. Then the application of these graphene analogs for high rate performances LIBs is conducted and confronted with their properties. This research allows to draw an efficient graphene synthesis route for graphene-based lithium-ion battery half-cell and full-cell.

Chapter 5 presents the application of Iron nanoparticle templates for constructing 3D graphene frame-work with enhanced performance in sodium-ion batteries. In this research, we synthesis iron NPs on the surface of graphene oxide in order to avoid the restacking of its layers. After removal of iron NPs using acid, as prepared 3D graphene was applied to lithium ion and sodium ion batteries and demonstrated superior performances.

Chapter 6 presents the main conclusions.

Chapters 7 & 8 present the list of publication and the acknowledgement.

Contents

CHAPTER 1

Graphene current progress

Contents

I. SYNTHESIS AND FUNCTIONALIZATION OF GRAPHENE AND ITS DERIVATIVES

I.1. General (Graphite / Graphene)

I.1.1. Graphite

Graphite (Figure 1,2a) is the most stable form of pure carbon at room pressure and temperature, and Desmond J. *et al.* identified its structure in 1924.[1] It is the most commonly found in the form of charcoal. Graphite is a mineral which has a lamellar structure spaced 3.35 Å apart and made up of a hexagonal network of carbon atoms arranged in a honeycomb structure. The bonds within the planes are covalent, while the inter-layer bonds are Van der Waals type (weak bonds), which makes graphite exfoliation relatively easy. Carbon has a tetravalent structure where, in its hexagonal structure, only three electrons are used to covalently bond with the three neighboring carbon atoms. Thus, the fourth valence electron forms weakly localized π bonds with its neighbors of the same plan. The latter electron can, therefore, participate in the electric conduction of graphite but mainly inside a plane. An isolated layer of graphite is called "graphene". Other fillers derived from graphite are marketed as expanded graphite and nano-platelets of graphite.

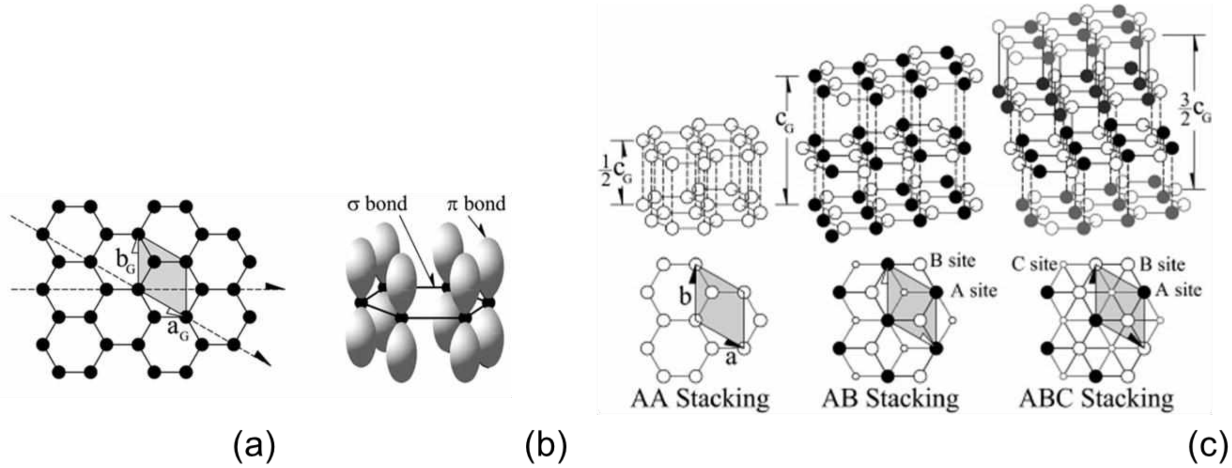

Figure 1: (a) Graphene hexagonal structure of identical carbon atoms. The unit cell (shaded) containing two carbon atoms is shown along with standard unit cell vectors aG and bG. (b) Schematic of the in-plane σ bonds and the π orbitals perpendicular to the plane of the sheets. (c) Three common graphite structures with different graphene stacking arrangements. Reproduced with permission from [2].

Expanded graphite (EG) (Figure 2b) is a filler derived from graphite produced by the expansion of natural graphite. Its structure is always lamellar, but its specific surface is larger (ex: 28.4 m^2 g^{-1}, TIMREX®BNB90) than that of natural graphite (17 m² g^{-1}) and its density apparent is lower (0.15 g cm^{-3} against 2.25 g cm^{-3} for graphite) expanded graphite is parepared from graphite intercalated with alkali metals such as sodium (Na) and potassium (K) or acids such as sulfuric acid (H_2SO_4) and nitric acid (HNO_3) followed by heat treatment (oven or microwave) at a temperature of 1050 °C for 15 secondes.[3,4]

Graphite nanoplatelets (GNP) (Figure 2c) represent a subtler form of natural graphite (~ 10 nm thick). GNP preparation is carried out either by thermal expansion of graphite interspersed with chloride trifluoride,[5] or by microwave irradiation of graphite interspersed with sulfuric acid, followed by ultrasonic sprays or by a ball mill.[6] It is possible to obtain GNP with a diameter between 1 and 15 μm, depending on the time of treatment with ultrasound.[7] The diameter can be further reduced to 1 nm using a vibrating mill.[8] GNP retains some oxygenated functions on the surface of its structure, which makes it slightly polar.

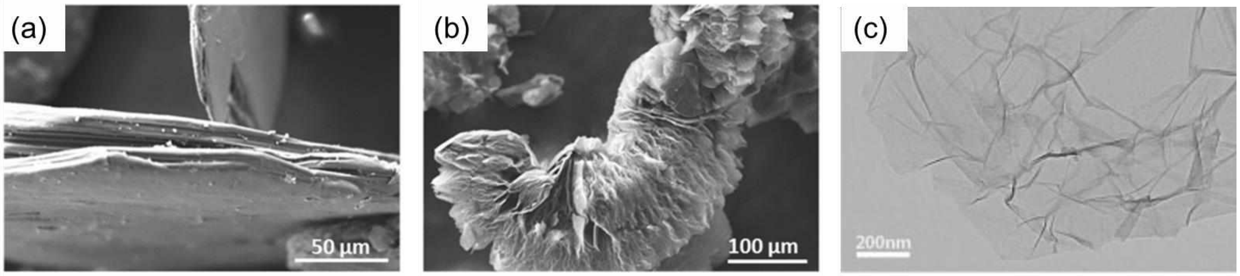

Figure 2: (a) graphite, (b) expanded graphite. Reproduced with permission from [9]. (c) Graphite nanoplatelets. Reproduced with permission from [5].

I.1.2. Graphene

Graphene nanosheets were first isolated in 2004 by Andre Geim and Konstantin Novoselov, who also managed to obtain a single experiment graphene layer from a micromechanical cleavage of graphite (‘’ scotch method tape ").[10]

Graphene is presented as a perfect 2D material and arouses great interest in the scientific world for several years. Its exceptional properties can explain the expectations around this material (Figure 3):

- it is made up of only one atom layer, of hexagonal mesh, whose thickness (on the order of the carbon atom) is 70 picometers, or one-millionth of a hair human.[11]
- it is considered to be the thinnest and lightest material (0.77 mg m^{-2})
- it is among the most resistant materials known to date because it has a Young close to ~ 1000 GPa and a limit at rupture of 130 GPa.[12]
- its modulus of elasticity is high on the order of ~ 0.25 TPa.[13]
- it has a high thermal conductivity ~ 5,000 Wm K^{-1}.[14] For comparison, the thermal conductivity of copper is 400 W.m .K^{-1}.
- its theoretical specific surface is ~ 2,630 m^2 g^{-1}.[15]
- It is impermeable to standard gases, including helium.[16]
- its electrical conductivity is ~ 2,000,000 cm^2 V^{-1}S^{-1} or 200 Sm^2 C^{-1}.[17]
- its melting point is higher than 3000 degrees Celsius.[18]

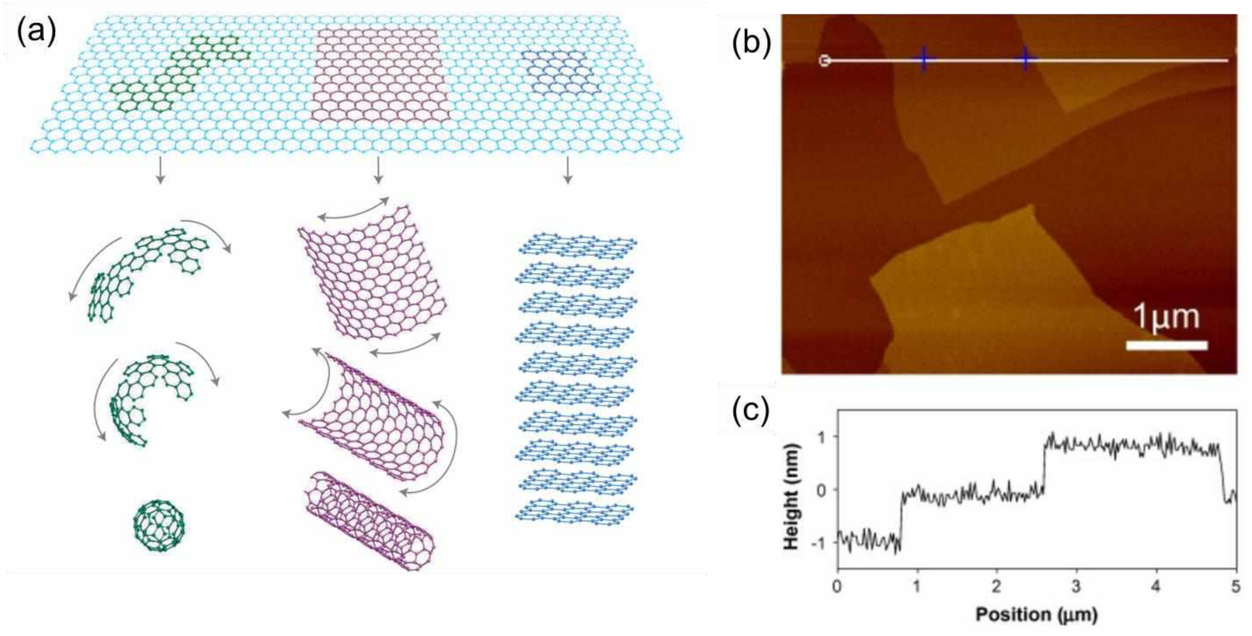

Figure 3: (a) Mother of all graphitic forms. Reproduced with permission from [11]. AFM image of GO sheets on a cleaved mica surface. (b) 2D AFM image and (c) corresponding height profile. Reproduced with permission from **[19]**.

I.2. Synthesis of graphene

Currently, two main methods are used for the production of graphene to the scale of the individual sheet: the "Bottom-up" method (growth of the sheet supported on a substrate) and the "Top-Down" method (formation graphite) (Figure.I.3).[20]

To obtain high-quality graphene three methods can be used. Among the most widely used techniques for obtaining graphene, mechanical exfoliation,[10] chemical vapor deposition (CVD),[21,22] growth of epitaxial on a SiC substrate.[23] All these methods have demonstrated their superiority in terms of quality but still today remain un-scalable. On the other hand, recent progress of the chemical and electrochemical oxidation of graphite or carbon nanotubes and their consecutive reduction into graphene have indicated great hopes toward graphene democratization.[24–26]

In this part, the synthesis of graphene via successive oxidation and reduction of graphite is discussed in detail, and other methods are briefly introduced.

I.2.1. Obtaining graphene by mechanical exfoliation

This method is based on the Top-Down approach, where graphene nanosheets can be produced by direct exfoliation of graphite or oxidized graphite. The so-called method of graphite scotch exfoliation or micromechanical cleavage of graphite constitutes the first experimental method that was used to produce nanosheets of graphene (Figure 4).

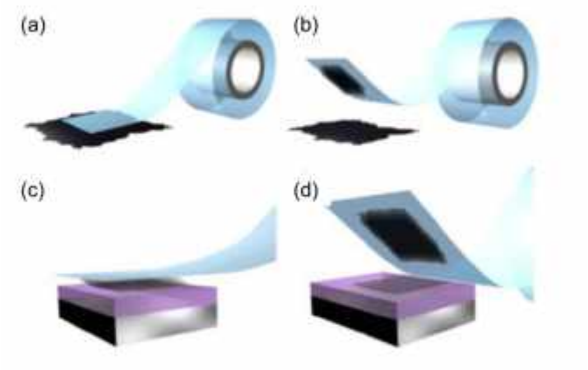

Figure 4: Illustration of mechanical exfoliation of 2D materials using scotch tape. (a) Adhesive tape is pressed against a 2D crystal removing top layers(b). (c) The tape with crystals of layered material is pressed against a surface of choice. (d) Upon peeling few layers are deposited on the substrate surface. Reproduced with permission from **[27]**.

Novoselov *et al.* made this discovery in 2004.[10] This approach is advantageous in obtaining large nanosheets with excellent quality, but its meager yield makes it non suitable for industrial scaling.

I.2.2. Synthesis of graphene by chemical vapor deposition (CVD)

This method (Figure 5) consists in producing the graphene layer by chemical vapor deposition (CVD) on a metal support. Different metals are used for this method, such as Cobalt (Co),[28] Platinum (Pt),[29] Nickel (Ni),[30], and Copper (Cu).[31] The gas sources generally used for this type of deposit are hydrocarbons such as methane, acetylene, or ethylene, which decompose when brought into contact with the surface of metals to form layers of graphene.

The advantage of this method is its low cost and its reproducibility. The specific surface of the graphene synthesized by this method is 2600 m² $g^{-1,}$ according to the literature, this value is higher than that of graphene synthesized by the mechanical exfoliation method. However, this specific surface depends on the size of the metallic film used, the temperature, and the pressure, which are critical elements for graphene growth.[31]

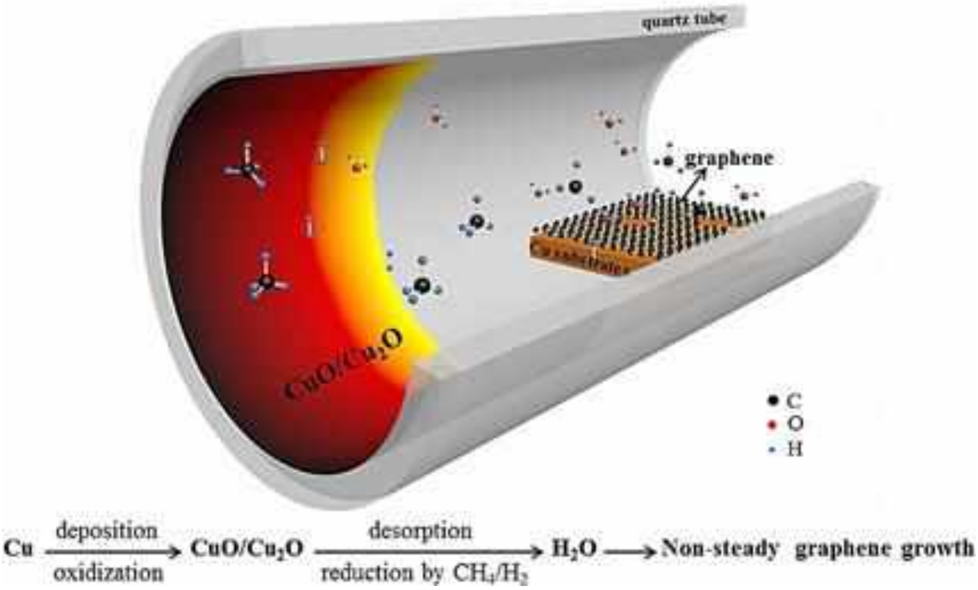

$$Cu \xrightarrow[\text{oxidization}]{\text{deposition}} CuO/Cu_2O \xrightarrow[\text{reduction by } CH_4/H_2]{\text{desorption}} H_2O \longrightarrow \text{Non-steady graphene growth}$$

Figure 5：Chemical Vapor Deposition reactor using methane and H_2O gas environment and copper substrate. Reproduced with permission from**[32]**.

I.2.3. Synthesis of graphene by thermal decomposition of SiC (epitaxial growth)

The third method of graphene synthesis described in the literature consists in heating the surface of a silicon carbide SiC substrate in an ultrahigh-vacuum frame (UHV) up to a temperature close to 1250 ° C to sublimate the silicon (Figure 6).[23,33,34] This method is reproducible, and the Graphene growth can be tuned by adjusting the time and the temperature in the frame. Furthermore, graphene synthesized by this method is more homogeneous than that obtained by the CVD method: the SiC surface is entirely covered by graphene thanks to the multiple surface reconstructions, and the SiC substrate is insulating, so there is no need to transfer the graphene layers to another support.

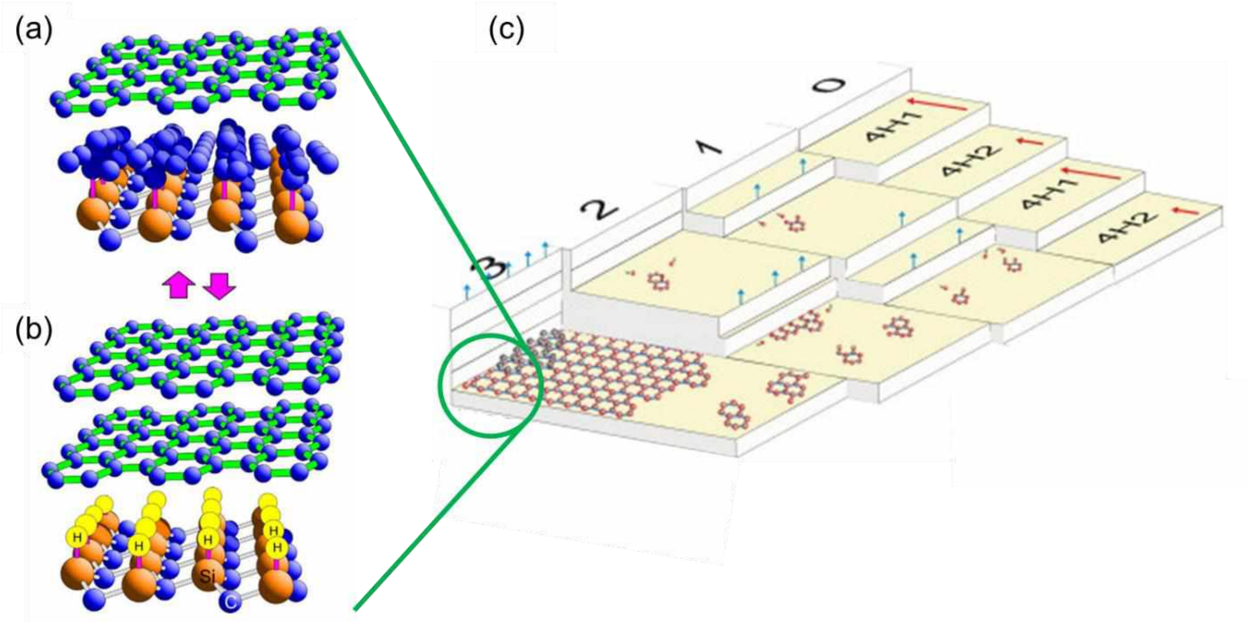

Figure 6: (a) Illustration of single layer graphene on SiC. (b) The structural model suggested for the new phase formed, having a hydrogen intercalated layer and bi-layer graphene after the hydrogenation process. Reproduced with permission from **35** (c) Graphene growth evolution . Reproduced with permission from **36**.

I.2.4. Exfoliation of graphite in solution

However, the most promising route in terms of scalability is the exfoliation of graphite in the liquid phase to give graphene-like materials (Figure 7).[37] This phenomenon relies on using particular solvents, such as N-methyl-pyrrolidone, whose surface energy is so well matched to that of graphene that exfoliation occurs freely. The use of intercalation agents and surfactants generally increases the inter-layer space in graphite. Surfactants play an essential role in the exfoliation and stabilization of graphene in polar solvents such as water.

Recently, Gao H. *et al.* prepared graphene via ultra-sound assisted exfoliation of graphite in supercritical CO_2/H_2O medium.[38] In this system, the high impact force of supercritical fluids and superior penetration power of supercritical CO_2 are combined with exfoliating natural graphite efficiently. Optimized conditions allow the exfoliation of 50 wt.% of stating graphite into a few layers graphene.

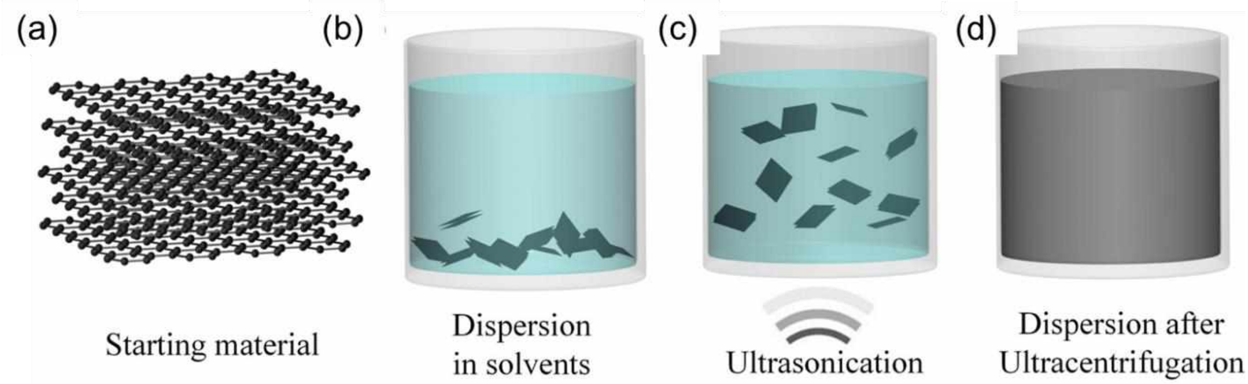

Figure 7: Liquid phase exfoliation of LMs.(a) Graphite, (b) dispersion, (c) ultrasonication and (d) final dispersion after the ultracentrifugation process. Reproduced with permission from **[39]**.

I.2.5. Chemical functionalization of graphite and its derivatives

I.2.5.1. Functionalization of graphite

The high electrical conductivity of graphene is generally due to zero-overlap semimetal with electrons and holes as charge carriers. Also, graphene sheets are insoluble in organic solvents because they re-aggregate by π-π interactions between the sheets. The use of organic or inorganic molecules allowing the chemical functionalization of graphene is, therefore, the most used method for solving these problems.

I.2.5.1.1. Non-covalent functionalization

The principle of non-covalent functionalization of graphite is to maintain graphene π conjugate system. Therefore, it is based on π-π interactions, electrostatic forces and / or hydrophobic interactions between the surface of graphene sheets and a molecule. Molecules (aromatics, surfactants) or polymers can be adsorbed on the graphene surface, which produces electrostatic repulsive forces that keep the sheets separate and prevent their re-aggregation. A good example is a non-covalent functionalization by pyrene. Kim M. *et al.* used Disperse red 1 (DR1), which is a well-known commercially available photochromic molecule containing a pyrene group allowing its non-covalent functionalization on the graphene surface (Figure 8).[40] The authors were able to p-doped graphene and to switch the amount of holes concentration up 18% by changing the illumination from UV light to white light.

Figure 8: Illustration of photoisomerization of DR1P on graphene. Reproduced with permission from **[40]**.

I.2.5.1.2. Covalent functionalization

The chemical modification of the graphene surface is linked to the rehybridization of its sp^2 carbon into sp^3 carbon, which will disturb the electronic conjugation and, therefore, the electrical conductivity. This method is generally applied to enhance graphene solubility, interaction, activity… To prepare covalently functionalized graphene several strategies have already been applied, such as diazonium compounds,[41–44] arynes, nitrenes,[45] carbenes,[46] Diels–Alder cycloaddition reactions,[47] and azomethine ylides,[48]. However, the functionalization through these methods generally results in low degree of functionalization.

I.2.5.2. Synthesis and functionalization of graphene oxide (GO)

I.2.5.2.1. Oxidation of graphite

GO formerly known as graphitic oxide or graphitic acid was prepared for the first time by Brodie et al. in 1859.[49] Then in 1898 and 1958, Staudenmaier and Hummers *et al.* were interested in the oxidation of graphite using strong acids minerals and oxidizing agents such as $KMnO_4$, $KClO_3$, and $NaNO_3$ in the presence sulfuric acid (H_2SO_4) or mixed with nitric acid (HNO_3). [50,51]. Graphite oxide consists of stacks of oxide sheets of graphene with an interlayer spacing between 6 and 10 Å depending on the number of molecules of H_2O, which are present between the graphite planes after the oxidation process.[52] The presence of hydroxyl (-OH), carbonyl (C = O) and epoxide (> O) groups on the surface of sheets and carboxylic acid groups (-COOH) on the edges of the sheets (according to models shown in Figure I.10) allow further chemical functionalization.[53–59] Recently, Gao W. *et al.* studied the structure of GO using the NMR technique ^{13}C, and they showed that the surface of GO contains ketone, lactol and tertiary alcohol in addition to the epoxy functions and hydroxyls (Figure 9).[60]

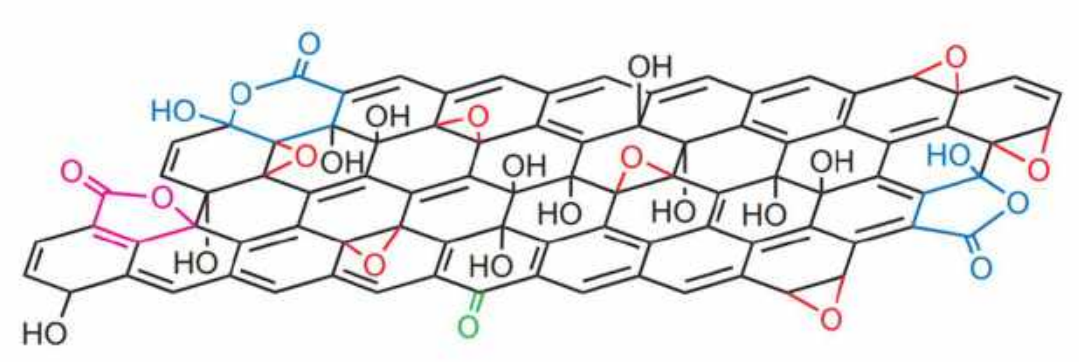

Figure 9: GO structural model, taking into account the five- and six-membered lactol rings (blue), ester of a tertiary alcohol (purple), hydroxyl (black), epoxy (red) and ketone (green) functionalities. The relative ratios are likely to be 115 (hydroxyl and epoxy): 3 (lactol O–C–O): 63 (graphitic sp2 carbon): 10 (lactol þ ester þ acid carbonyl): 9 (ketone carbonyl). Reproduced with permission from **[60]**.

Zeta potential measurements indicated that the suspensions obtained are electrostatically stabilized by negative charges, which can be generated by the carboxylic groups (-COOH) which are present on the edges of each oxidized graphene sheet.[61,62]Also, ultrasound treatment and centrifugation can can be used to fragment the GO sheets, which can lead to a reduction in their lateral dimensions up to a value between 0.1 and 1µm.[63–66] GO is generally dispersed in water solution, but it is also possible to dispersed GO in several organic solutions. Paredes J. I. *et al.* have shown that GO could be dispersed in N,N-dimethylformamide, N-methyl-2-pyrrolidone, tetrahydrofuran, and ethylene glycol.[67] In these solvents' the sonication treatment was enough to produce single-layer GO expressing similar dispersion behavior as in water. The study also points out unsuitable solvents for GO dispersion, such as ethanol, oxylene, acetone, methanol, propanol, and n-hexane (Figure 10).

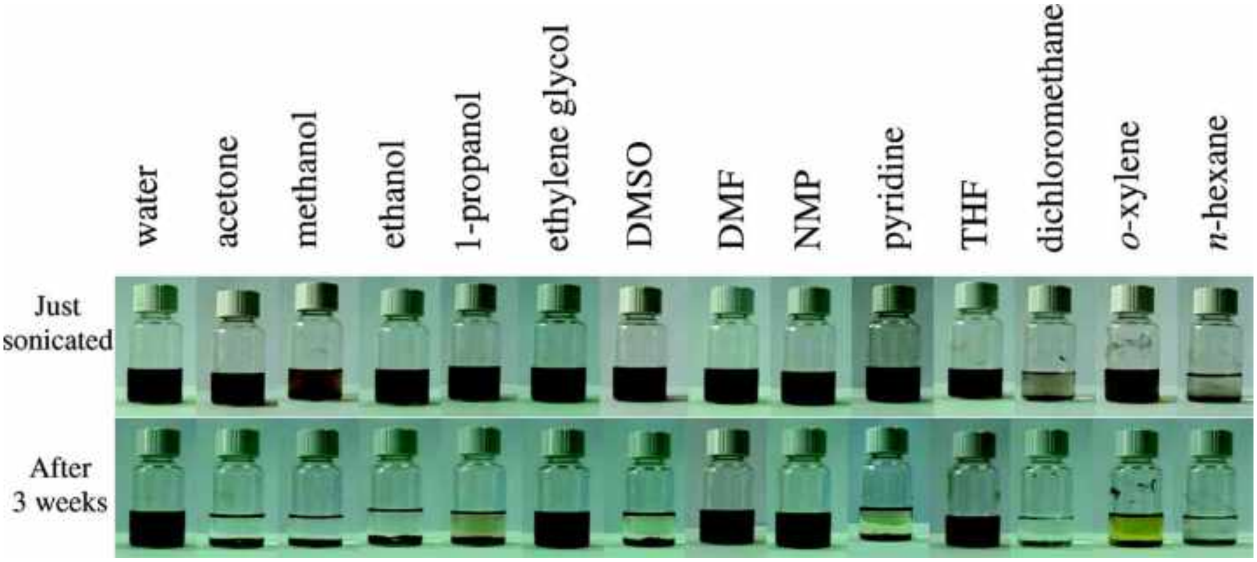

Figure 10: Digital pictures of various GO dispersion. Reproduced with permission from **[67]**.

Besides, GO can be exfoliated in aprotic solvents by reactions with organic compounds such as octadecylamine. Li W. *et al.* prepared graphene functionalized with octadecylamine mixed with polystyrene composite.[68] This material shows superior electrical conductivity compared to pure GO and polystyrene composite due to the improved dispersion and reduction of GO-ODA in comparison with GO.

Mechanical and magnetic agitation are also other methods for exfoliating GO in oxidized graphene nanosheets, but these are lesser effective methods by comparison with the sonication method.

I.2.5.2.2. Covalent functionalization of GO

The chemical functionalization of GO by molecules and / or polymer chains leads to a modification of its properties. The covalent modification of GO can be classified into four categories: nucleophilic substitution, electrophilic additions, condensation reactions, and radical reactions.

I.2.5.2.2.1. Nucleophilic substitution.

The chemical modification of GO by nucleophilic addition is carried out by attacking a doublet of electrons (usually of an amine function) on the epoxide group, which leads to an opening of the cycle and the formation of a secondary amine and a function alcohol.[69–72] Compared with other methods, nucleophilic substitution occurs easily at room temperature and in aqueous medium, making this method attractive for the large-scale production of functionalized graphene.

Bourlinos A.B. *et al.* investigated the modification of GO surface with primary amines, such as $C_nH_{2n+1}NH_2$ (n = 2,3,8,12,18) (Figure 11).[69] As result, the authors' observed that for small primary amine (n = 2, 4, 8, 12), the functionalization could be complete after 20 hours of stirring at room temperature. Differently, longer primary amine (n = 18), the functionalization could only be completed after 90 hours of reflux. This difference of reactivity was ascribed to kinetics reasons. Additionally, XRD measurement showed that the interlayer distance of as functionalized GO increases with the size of the primary. Following this process, Compton O.C. *et al.* has prepared GO functionalized with hexylamine and reduced it under harsh hydrazine condition.[70] This functionalization allows the authors' to stabilize the stacked paper structure during the reduction, maintaining its well-ordered morphology and resulting in uniform conductivity and excellent mechanical properties.

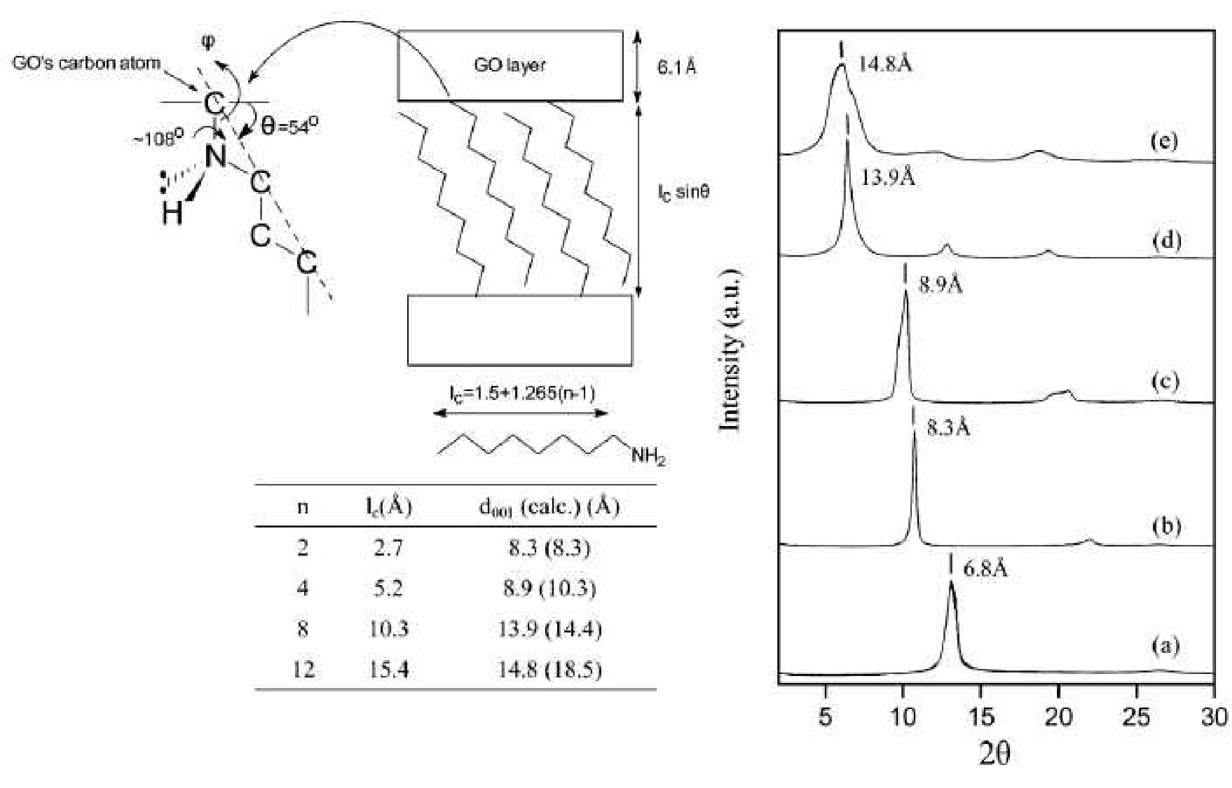

n	l_c(Å)	d_{001} (calc.) (Å)
2	2.7	8.3 (8.3)
4	5.2	8.9 (10.3)
8	10.3	13.9 (14.4)
12	15.4	14.8 (18.5)

Figure 11. XRD of GO after treatment with ethylamine (a), butylamine (b), octylamine (c), and dodecylamine (d). The left part of the figure presents a simple model based on amination of the epoxide groups of GO as the main pathway for the insertion of the amine molecules in the interlayer zone of GO. The table presents the d001 values as a function of number of carbon atoms (n). Reproduced with permission from **[69]**.

In the same way, Wang Z. *et al.* prepared GO functionalized with ethylenediamine (EFG) and sonicated it in $Na_2S_2O_3$ followed by the addition of hydrochloric acid under stirring.[71] Obtained material (EFG-S) was applied as cathode for LIBs and demonstrate superior capacity, capability, and cyclability. A wide variety of amine has now already been applied onto GO, Xu L.Q. *et al.* applied dopamine onto GO (Figure 12).[72] The results show that dopamine can, at the same time, functionalize GO and reduce it into reduced GO (rGO). The application of polydopamine showed the same results while allowing the immobilization of thiol- and amino-terminated poly(ethylene glycol) (PEG) on the surface of rGO in a “grafting-to” process.

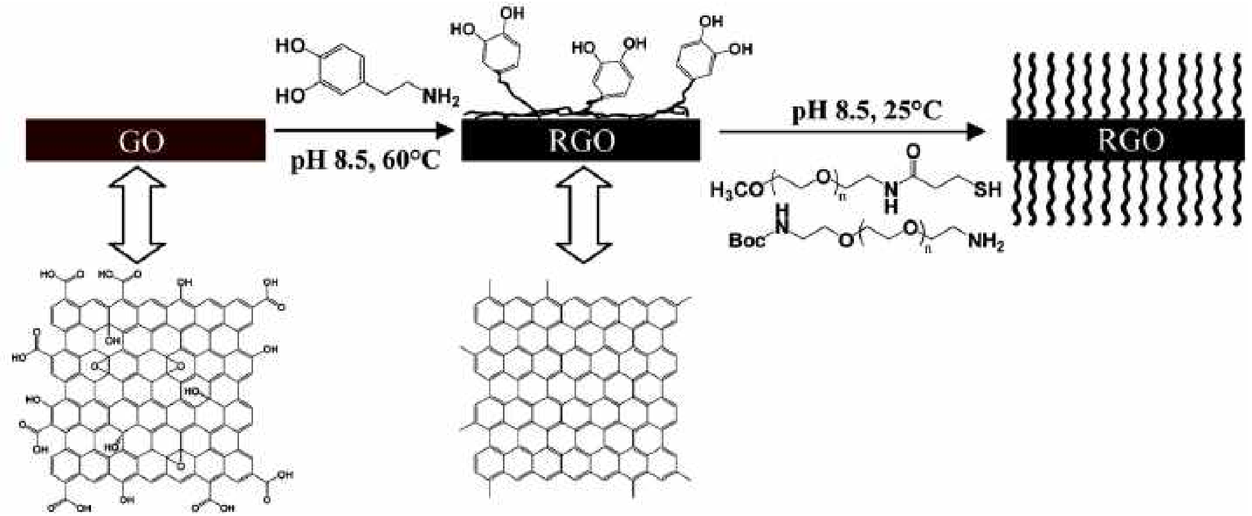

Figure 12: Schematic Illustration of the Preparation of rGO and functionalized rGO. Reproduced with permission from **[72]**.

I.2.5.2.2.2. Electrophilic substitution

The electrophilic substitution with graphene consists of the displacement of a hydrogen atom by an electrophile. The modification of GO by an electrophilic addition reaction often involves the use of diazonium salts.[42,73–76] Paulus G.L.C. *et al.* conduct comparative theoretical and experimental analyses of the diazonium reaction mechanism with graphene.[75] The authors show that the graphene functionalization is mostly governed by kinetics and influenced by electron-hole puddles and ripples. Also, the results show that the degree of reactivity is improved when graphene is mono-layer rather than a few-layers, and when the edge to surface ratio is significant. Lomeda *et al.* functionalized graphene nanosheets using aryl diazonium salt having several functional groups.[42] The authors also showed that the functionalization by aryl diazonium salt leads to GO oxygen content reduction from 32 at.% to 9 at.%. As prepared functionalized GOs were showed to be processable in various organic solvents. Similarly, Sinitskii A. *et al.* used 4-nitrobenzene diazonium tetrafluoroborate to functionalize graphene (Figure 13).[73] This functionalization was shown to form an additional layer onto the graphene surface and to alter graphene electrical properties. Also, the results show that the functionalization process is easy and fast because 5 min of grafting at room temperature was sufficient to reach 60% of the maximum change in the electrical properties.

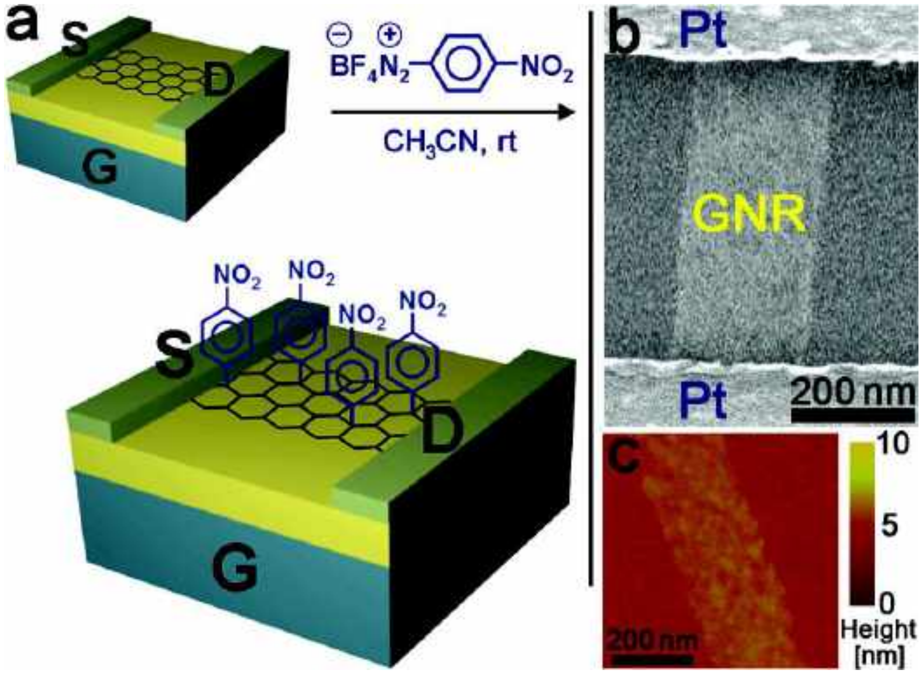

Figure 13: Schematic of the chemical functionalization of GNR devices with 4-nitrophenyl groups. Electronic devices consisted of single graphene layer contacted with Pt source (S) and drain (D) electrodes. The devices were fabricated on a 200-nm-thick thermal SiO_2 over heavily doped p-type Si that was used as a back gate (G). (b) Top-view SEM image of the device. (c) AFM image of a fragment of a typical single graphene layer reduced by annealing at 900 °C in Ar/H_2 on the Si/SiO_2 substrate. Reproduced with permission from **[73]**.

Gao W. *et al* apply diazonium functionalization to prepare a composite for water filtration application.[74] Firstly, sand is coated with GO via simple hydrothermal treatment, then secondly 4-aminothiophenol to functionalized GO surface. As prepared, demonstrate to absorbs 6-fold higher concentration heavy metals and dyes. Fang M. *et al.* combined diazonium addition onto graphene and atom transfer radical polymerization to link polystyrene chains onto graphene (Figure 14).[76] The prepared material is 1 wt.% graphene and 99 wt.% polystyrene and exhibits around 70% and 57% increases in tensile strength and Young's modulus.

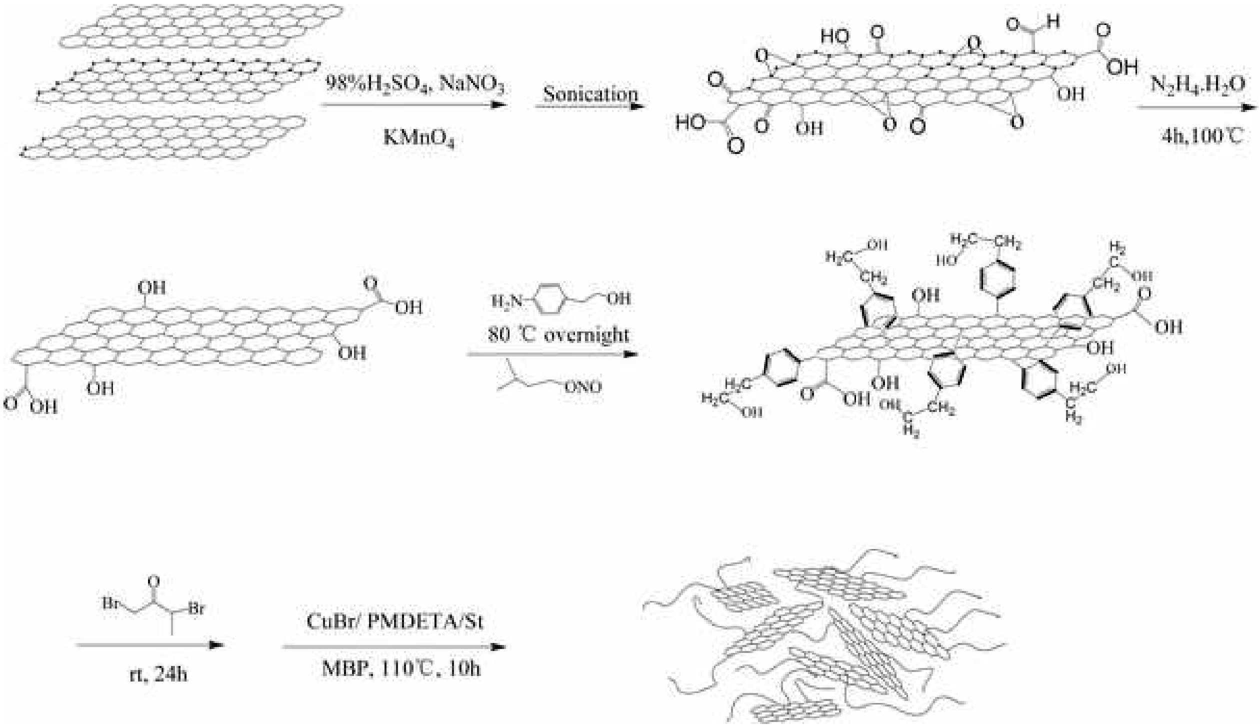

Figure 14. Synthesis route of polystyrene-functionalized graphene-nanosheets. Waiting permission from [76].

I.2.5.2.2.3. Condensation reactions

Condensation reactions are reactions between two functional groups resulting in a final functional group accompanied by the formation of a simple molecule (H_2O, HCl…). The chemical modification of GO can be carried out from the function's hydroxyls and carboxylic acid functions. Jia Z. *et al.* prepared covalently crosslinked graphene oxide (GO) membranes with adjustable inter-layer distance by esterification reactions, using dicarboxylic acids, diols or polyols as the crosslinker and hydrochloric acid as the catalyst.[77] Dicaboxylic acids were employed to crosslink the hydroxyl groups on the basal planes of the GO sheets, the increase of crosslinker length results in the increase of the interlayer distance, the improvement of the elastic moduli by 16-fold and the increase of the permeation fluxes. Diols or polyols were used to crosslink the carboxyl group from the GO edges, the results have shown that (-CH_3) tends to increase the inter sheet distance and that (-OH) tends to increase the penetration of hydrate ions. Salavagione H.J. *et al.* conduct the Polymeric Modification of Graphene through the esterification of carboxylic functional groups of GO and hydroxylic functional groups of poly(vinyl alcohol) (PVA).[78] FTIR and TGA results reveal that the covalent linkages between the graphitic laminates and the PVA are responsible for remarkably altering the crystallinity and thermal stability. Bao H. *et al.* prepared GO coated with chitosan (GO-CS) through an easy amidation process through carboxylic.[57] The authors evaluate and demonstrate that the GO-CS is an excellent nanocarrier for load and delivery of anti-cancer drugs and genes. Stankovitch S. *et al.* prepared several functionalized GO using several organic isocyanates (Figure 15).[79] As synthesized GOs display excellent dispersibility in a polar aprotic solvent. The results suggest that the functionalization proceeds on the carboxyl and hydroxyl groups in GO via the formation of amides and carbamate esters, respectively. The degree of functionalization can be controlled via either the reactivity of the isocyanate or the reaction time.

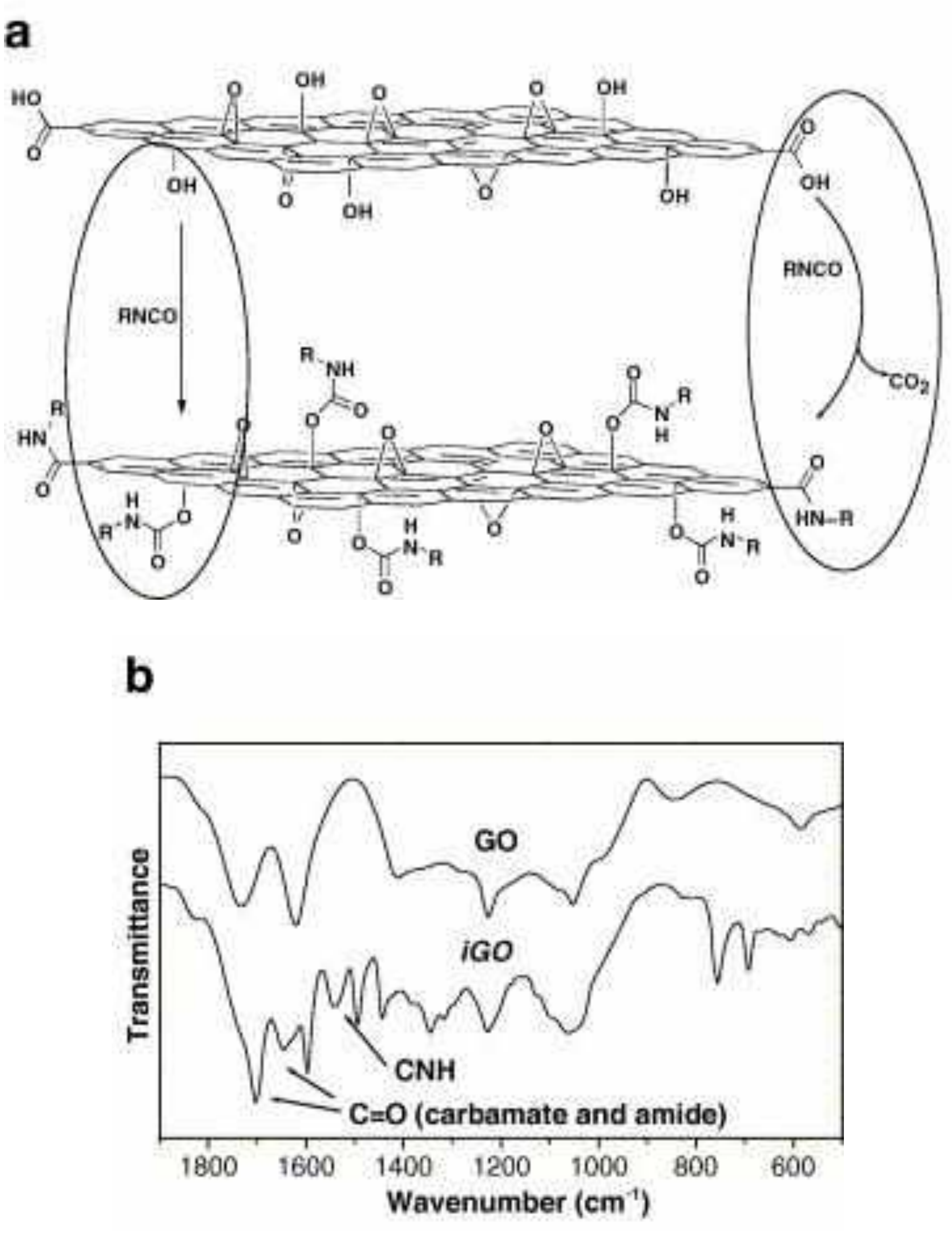

Figure 15: (a) Proposed reactions during the isocyanate treatment of GO where organic isocyanates react with the hydroxyl (left oval) and carboxyl groups (right oval) of graphene oxide sheets to form carbamate and amide functionalities, respectively. (b) FT-IR spectra of GO and phenyl isocyanate-treated GO. Reproduced with permission from[79].

I.2.5.2.2.4. Addition reactions

In organic addition reactions two or more molecules are combined to form a larger molecule.[80–83] He H. *et al.* prepared functionalized GO (f-Gns) using Nitrene chemistry.[80] This attractive but straightforward strategy allows the covalent functionalization of various functional moieties (e.g., hydroxyl, carboxyl, amino, bromine, long alkyl chain...) and polymers (e.g., poly(ethylene glycol), polystryene). The f-GNs morphology is maintained, remaining mainly mono-layers. Also, the analyses show that f-Gns has relatively good conductivity as compared with original GO, 1×10^2 to 1×10^3 S m^{-1}, while its oxygen functional groups exhibit superior thermal stability. Similarly, to this work, Vadukumpully S. *et al.* functionalize graphene using alkylazides and was applied to obtain a uniform distribution of gold nanoparticles.[82] Hsiao M. *et al.* synthesized covalently functionalized graphene using residual oxygen-containing functional groups and POA2000 bearing one MA (abbreviated as MA-POA2000) (Figure 16).[81] Generally, the functionalization of graphene with MA-POA2000 follow the free radical reaction which consists in the breaking the carbon double bonds of graphene surface to generate free reactive sites that bond with amino groups on MA-POA2000. Nevertheless, the residual epoxy functional groups of rGO help to proceed the functionalization through the ring-opening reaction, thus reducing the defect formation from MA-POA2000 functionalization. Georgakilas V *et al.* functionalize graphene through the 1,3 dipolar cycloaddition of azomethine ylide.[83] The results intend to explain that the reaction causes radical changes in the structure of the graphene. As prepared materials were shown to be dispersible in water and organic solvents.

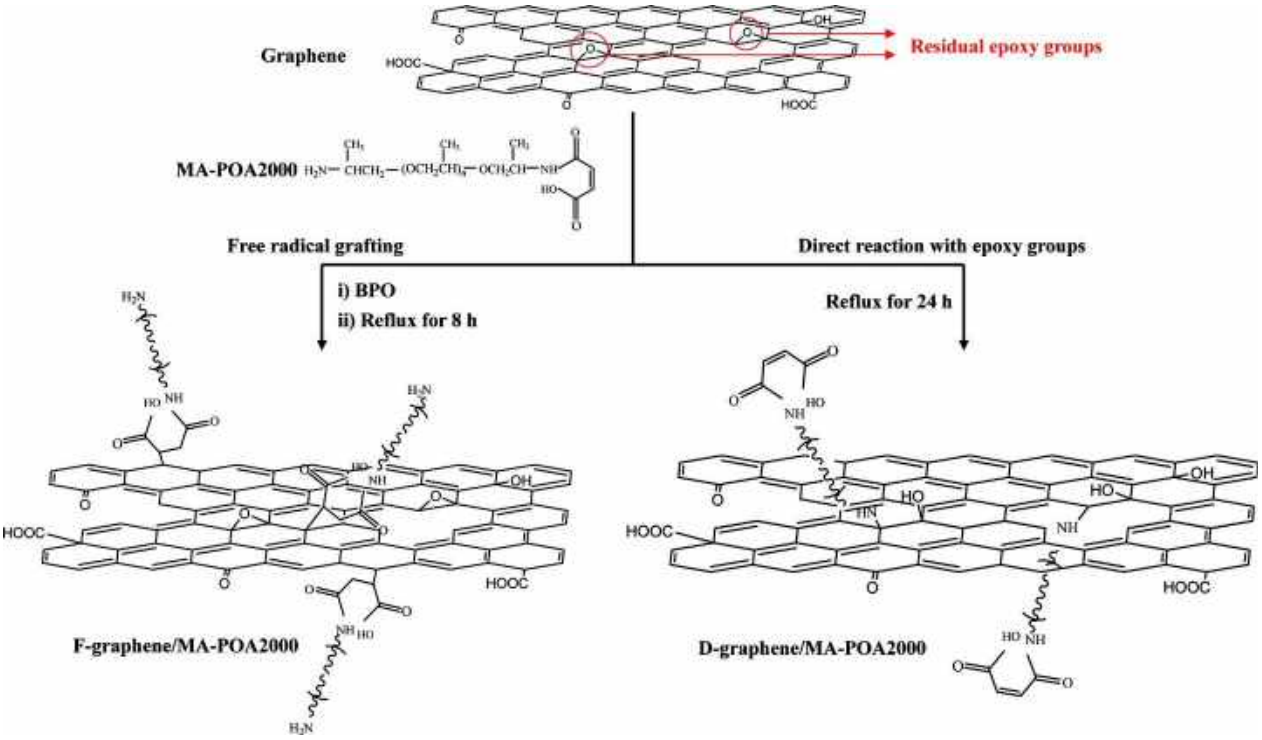

Figure 16: The preparation of F-Graphene/MA-POA2000 and D-Graphene/MA-POA2000. Reproduced with permission from[81].

I.2.5.2.3. Graphene oxide reduction

GO is of great interest not only as an intermediate product to form graphene, but also as a material on its own. GO differs from graphene in containing hydroxyl, epoxy, and carboxyl groups on the surface and more structural defects. The physicochemical properties of GO may vary depending on the degree of oxidation and disorder in the lattice. The oxygen-containing functional groups in GO provide many sites for the anchoring of electroactive materials to form GO-based composites. Reduction is often needed to rebuild the sp^2 structure and achieve the excellent electrical properties since GO is insulating. GO can be reduced using a variety of methods, among which the most used are thermal annealing, microwave reduction, photo-reduction, hydrothermal reduction, electro-chemical, and chemical reduction.

I.2.5.2.3.1. Thermal annealing

The thermal annealing consists in decomposing GO oxygen functional groups by elevating the temperature. In order to control the reduction of GO through thermal annealing temperature, heating time and rate, and atmosphere need to be carefully chosen.[84–93]

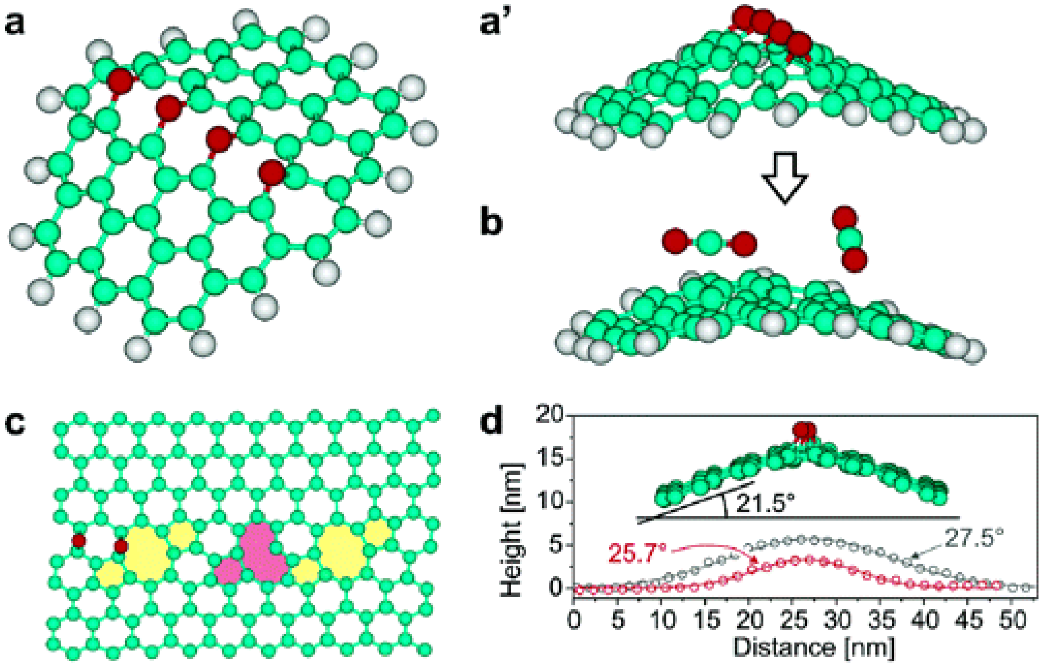

Figure 17: Atomistic model of the graphite oxide to graphene transition. (a, a') In this model linear epoxy cluster are formed. (b) Upon thermal heating epoxy decomposed into carbon dioxide. (c) Top view of the model (d) Expected AFM profile of curved GO. Reproduced with permission from [85].

Initially, the synthesis of graphene nanosheets by the GO reduction method has been studied by Schniepp *et al.*(Figure 17).[85] It is possible to obtain thermally reduced graphene nanosheets by rapid heating

of the GO in an inert environment at high temperatures. Indeed, heating the GO to 1050 ° C for 30 seconds in an inert environment causes exfoliation and reduction of GO. The exfoliation of GO occurs by the pressure generated by the CO_2 gas emitted by the decomposition of carboxylic acid groups (COOH) and epoxides (I> O) located on the GO. This method advantage is that the exfoliation and reduction are done in one step, so this method allows graphene to be obtained without going through a step of prior dispersion of GO in organic solvents.

The temperature is a crucial factor since oxygen functional groups of GO have different thermal stability. Indeed, epoxy, carboxylic, and hydroxy functional groups generally decompose from 200 °C while carbonyl functional groups decompose for temperature above 1000 °C. Schniepp *et al.* found that if the temperature was less than 500 °C, the C/O ratio was no more than 7, while if the temperature reached 750 °C, the C/O ratio could be higher than 13.[85] This intensification of reduction with the temperature can be monitored by XPS measurement (Figure 18).[86–88] As the reduction proceeds, the sp^3 carbon is restored to sp^2 carbon, consequently result in the improvement of the conductivity.[89,90] Wang X. *et al.* have reported that the conductivity improves to 49, 93, 383 to 550 S cm^{-1}, along with the temperature increasing from 550 °C, 700 °C, 900 °C to 1100 °C, respectively.[91]

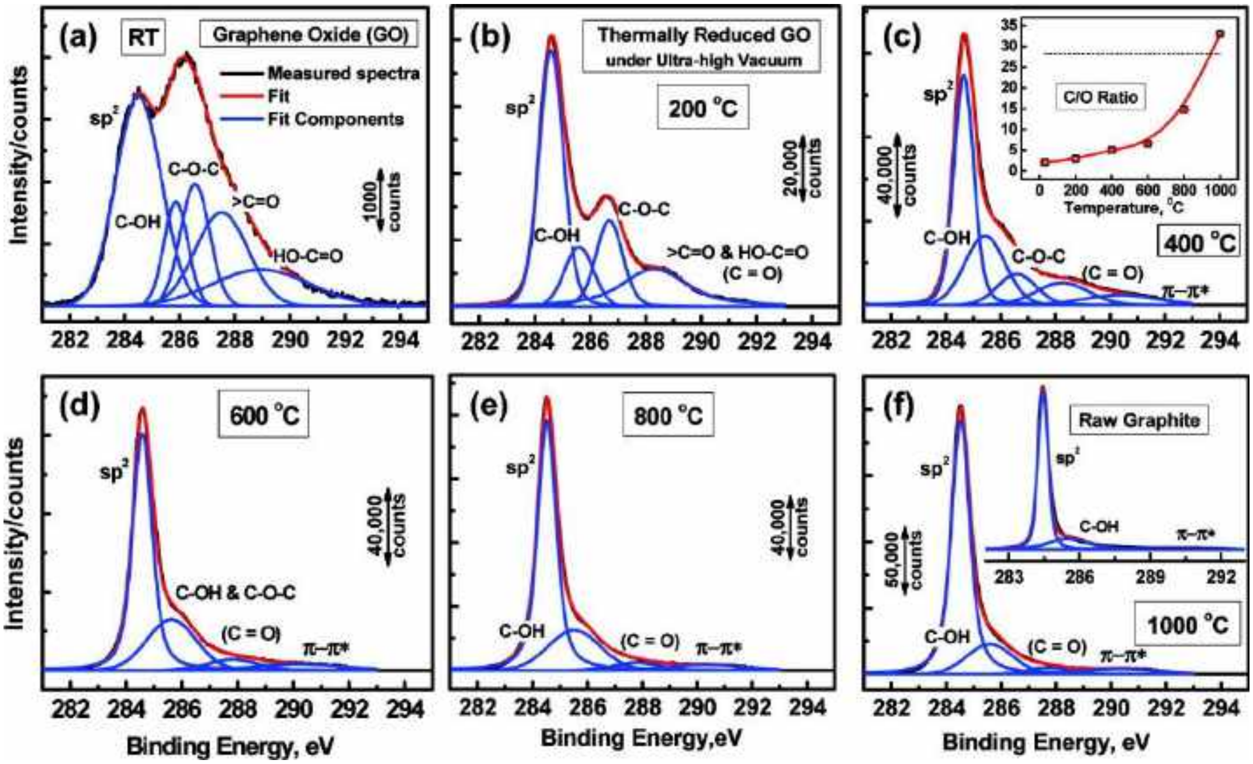

Figure 18: C1s XPS spectra: deconvoluted peaks with increasing reduction temperature. Reproduced with permission from **[88]**.

The annealing atmosphere is an important factor because at elevated temperature the oxygen etching is drastically increased. For these reasons, the thermal reduction of GO is generally conducted in a vacuum, and or inert or reducing agent. Becerril H.A. *et al.* work on the reduction of GO film and shown that he recovery procedure of GO into graphene was optimum when the temperature was elevated to 1100 °C for 3 hours at a pressure of <10^5 Torr.[92] Under lower vacuum, the recovery treatment resulted in the GO film decomposition. Thus, when vacuum and or inert gas atmosphere are at use for GO annealing, such oxygen content needs to be adjusted. Another way to improve the reduction is to use a reducing atmosphere. In this direction, Vallés C. *et al.* prepared conductive paper through the thermal treatments at 700 °C under argon or hydrogen atmosphere at atmospheric pressure.[93] Their results demonstrated that the reduction degree shifted from C/O =

1.2 to C/O = 28.6 for Ar and H_2 atmosphere, respectively. Li X. *et al.* reported that the reduction of GO under ammonia at low temperature, 500°C, generates nitrogen-doped rGO having 10 at.% oxygen and 5 at.% nitrogen.[87]

I.2.5.2.3.2. Microwave reduction

The microwave method consists of sending microwaves through the GO that will agitate free electron, which leads to an increase in temperature and, finally, the decomposition of oxygen functional groups. This heating process is more homogeneous and faster than thermal annealing, which leads to fast oxygen removal and thus exfoliation of GO layers. Zhu Y. *et al.* used a conventional microwave oven to exfoliate and reduce GO (Figure 19).[94] After 1 minute treatment, the material appears crumpled, few-layer thick, and electronically conductive. This martial was applied to the capacitor and displayed specific capacitance values as high as 191 F g^{-1} in KOH electrolyte. Voiry D. *et al.* investigated the effect of microwave on GO.[95] The results show that using a conventional microwave oven, a pulse of only 1 second was sufficient to change a large size GO into pristine graphene expressing holes and electrons mobility >1000 $cm^2\ V^{-1}s^{-1}$ in field-effect transistors.

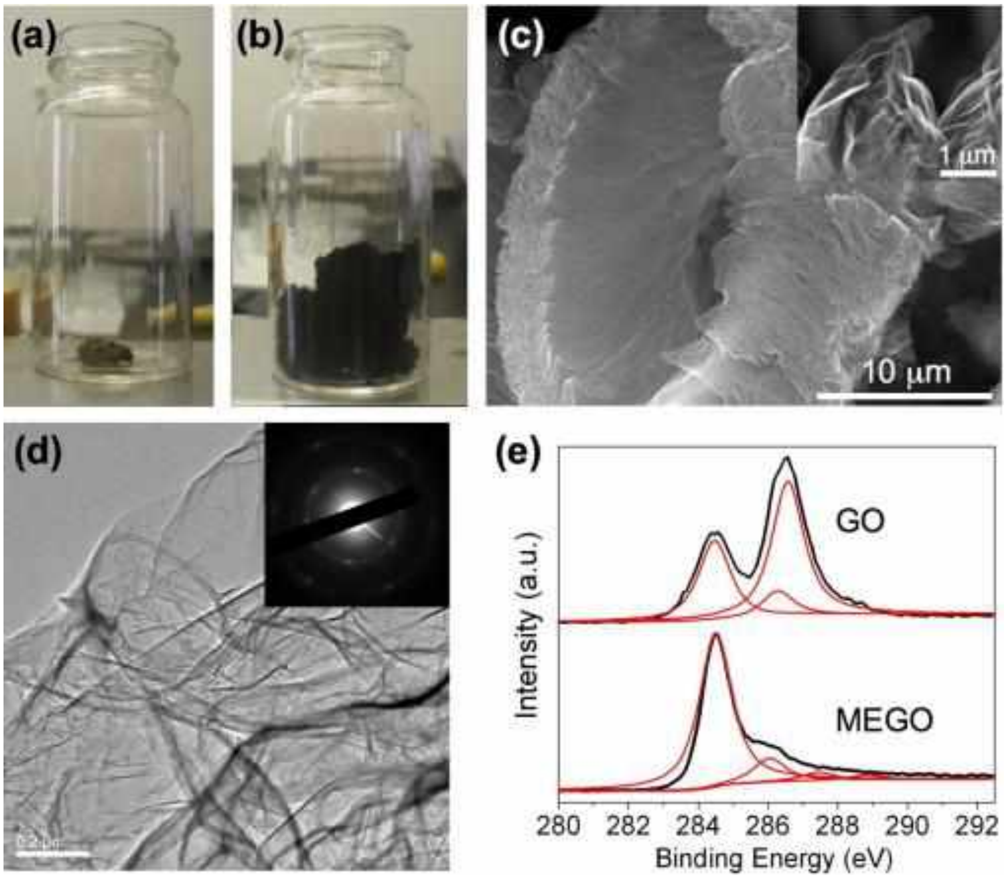

Figure 19: Digital imagesof GO before (a) and after (b) microwave reatment. (c) Corresponding SEM image. (d) Corresponding TEM image and the corresponding electron diffraction pattern. (e) XPS C1s spectra of GO before and after microwave treatment. Reproduced with permission from [94].

I.2.5.2.3.3. Photo-reduction

The photo-reduction consists of using light to send photons on GO. When photons energy is superior or equal to GO band gap, electrons and holes are generated, resulting in the reduction of GO epoxy and hydroxyl functional groups into CO_2 and H_2O respectively.[96–99] Mohnadoss M. *et al.* reduced GO dispersed in water using natural sunlight.[96] Compared with GO reduced via chemical or hydrothermal treatment, sunlight reduced GO show higher oxygen content (C/O = 3.5), but similar electrical conductivity (166 S m^{-1}). Matsumoto Y. *et al.* conducts the reduction of GO using UV irradiation under H_2 or N_2 at room temperature in dry and aqueous conditions. In both dry and aqueous environments, the reduction proceeds and results in high conductivity (Figure 20).[97] Taking advantage of photo-reduction micro size patterned reduction of GO was realized. Hang D. *et al.* applied photo-reduction on GO paper in order to prepare graphene actuators driven by humidity that mimic the cilia of the respiratory tract and tendril climber plant.[99]

Additionally, photo-reduction was also applied to a liquid environment. Gengler R.Y.N*et al.* demonstrate that the photo-reduction of GO in solvent is an ultra-fast indirect process.[98] The study reveals that the ultraviolet light photoionized the solvent creating solvated electrons that transform GO into rGO. The explained mechanism further indicates that the photo reduction process is driven by the chemical potential of solvated electrons and not the heating effect.

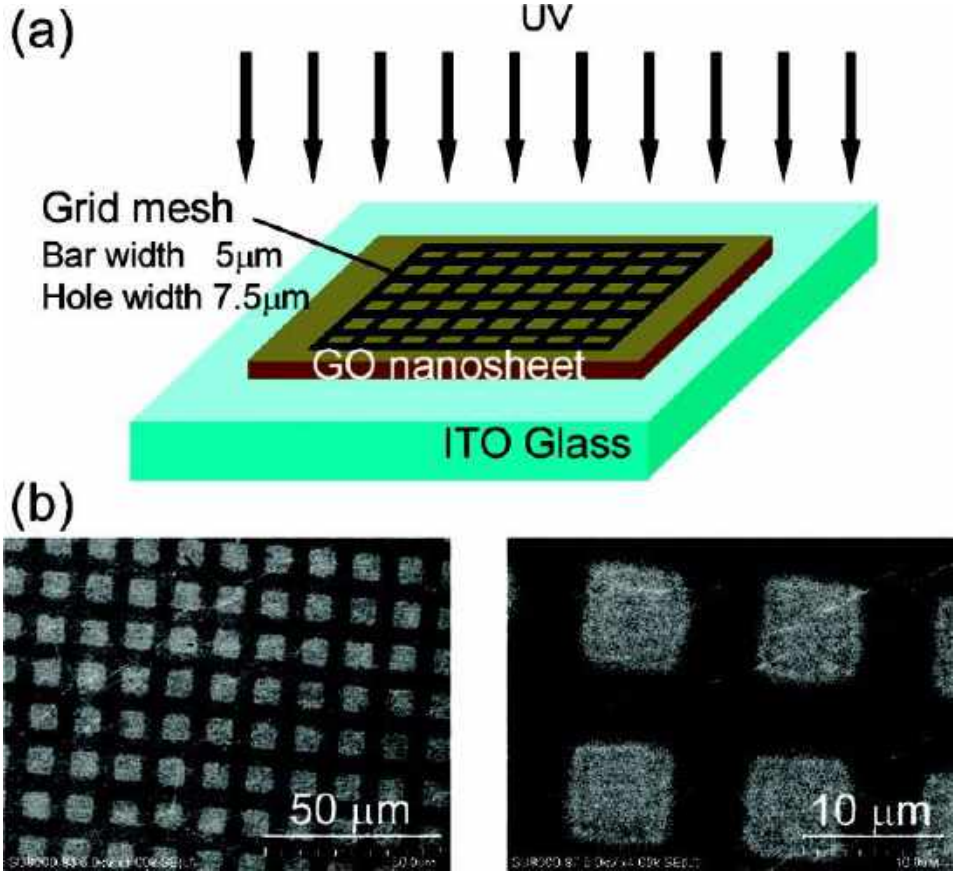

Figure 20: Photopatterning of GO nanosheets. (a) Illustration of the photopatterning and (b) SEM images of sample after photopatterning. Reproduced with permission from **[97]**.

I.2.5.2.3.3. hydrothermal reduction

The hydrothermal reduction method is based on the same reduction mechanism as above thermal annealing but in solution. This method appears to be more eco-friendly, controllable, scalable. Zhou Y. *et al.* prepared graphene through hydrothermal treatment and demonstrate the formation of rGO solution stable in water (Figure 21).[100] Also, the results indicate that this treatment as the ability to recover aromatic structures via repairing the post-reduction defects. Ahmad M.S. *et al.* applied a hydrothermal reduction method to GO in water using guanidine as a nitrogen source.[101]

The as-synthesized material is doped with pyrrolic nitrogen sites, which were demonstrated to catalyze hydrogenation reaction through a radical mechanism.

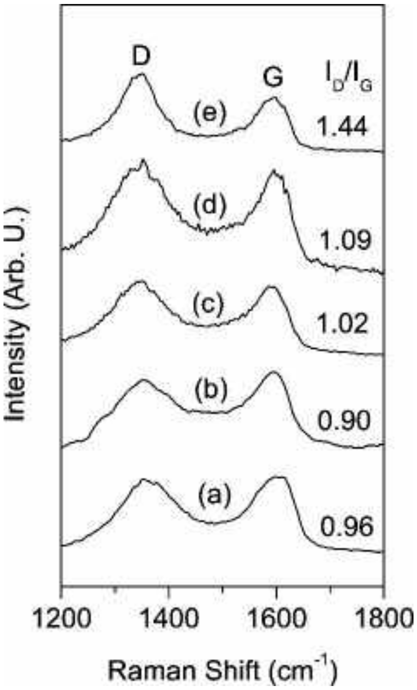

Figure 21: Raman spectra of (a) GO before and after hydrothermal treatment at (b) 180 °C, (c) 150 °C, and (d) 120 °C for 6 h, and (e) hydrazine-reduced GO. Reproduced with permission from [100]

I.2.5.2.3.4. electro-chemical reduction

The electro-chemical reduction of graphene consists in using GO as a cathode, a counter electrode, and an electrolyte. By applying a potential, the oxygen functional groups of graphene are reduced. Most of the literatures draw this method as effective, controllable, green, but lacking in scalability since the current method is limited to film reduction. Shao Y. *et al.* synthesized rGO film via the electrochemical reduction of GO film deposited on glassy carbon electrode (Figure 22).[102] As prepared material was applied for capacitor and showed superior capacitance than carbon nanotubes and chemical rGO. These superior performances were ascribed to remaining oxygen functional groups of electrochemically reduced GO (EGO). An advantage of electrochemical reduction is the possible electro-functionalization of GO as it is reduction proceed. Following this method, Wang Z. *et al.* used N-succinimidyl acrylate as electro-functionalization source to covalently bond glucose oxidase to GO.[103]

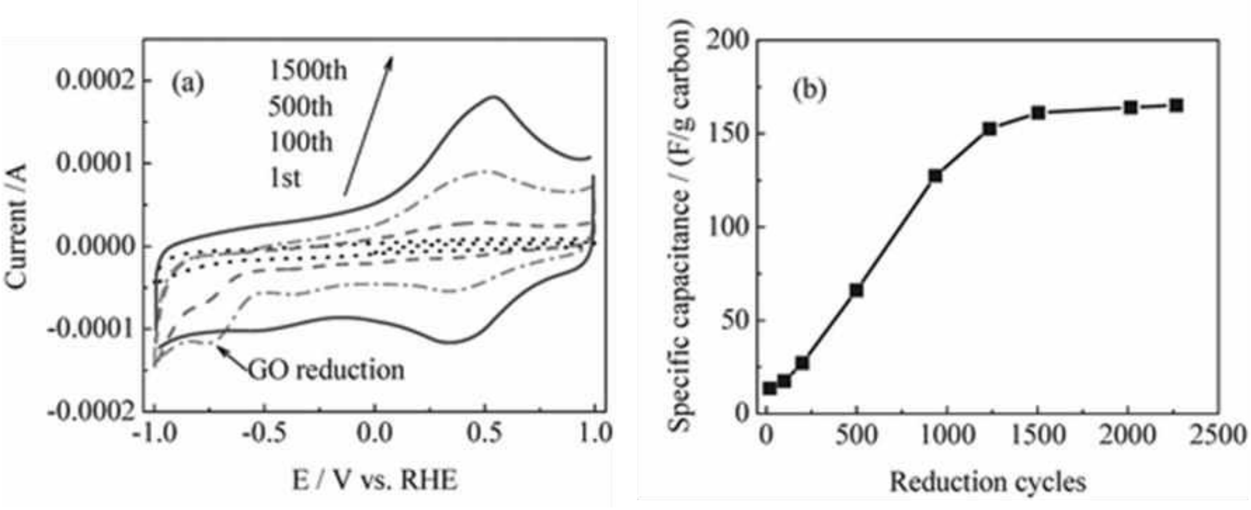

Figure 22: (a) Cyclic voltammograms of the electrochemical reduction of graphene oxide in 0.1 M Na_2SO_4 at 50 mV s^{-1}; (b) the specific capacitance changes with the reduction cycles, measured with cyclic voltammograms (0 to 0.9 V) at 20 mV s^{-1}. Waiting permission from **[102]**.

I.2.5.2.3.5. Chemical reduction

The chemical reduction of GO is carried out from a stable colloidal dispersion of GO or of functionalized GO. The method of chemical reduction of GO described in the literature generally involves the use of hydrazine or its derivatives, such as phenylhydrazine.[104,105] Chemical reduction by hydrazine or its derivatives consists of reducing the oxygen groups present on the surface and on the edges of the GO, which produces general of graphene nanosheets without structural defects. Stankovich *et al.* proposed a mechanism for reducing epoxy functions by hydrazine.[104] Hydrazine or its derivatives are reducing agents known for their effectiveness (Figure 23).[104–106] However, despite its toxicity and its high cost, hydrazine is widely used in the industrial environment. Thus, in the literature, other experimental protocols are proposed to avoid its use. The chemical reduction of GO suspensions can therefore also be performed using different chemical reducing agents such as hydroquinone,[107] sodium borohydride,[108,109] sulfur compounds,[110] Vitamin C,[111,112] Iron,[113] sodium hydroxide,[114,115] amino acids,[112,116] alcohols,[117] sugars,[118] hydroiodic acid,[119] and other powders of metal.[120–122]

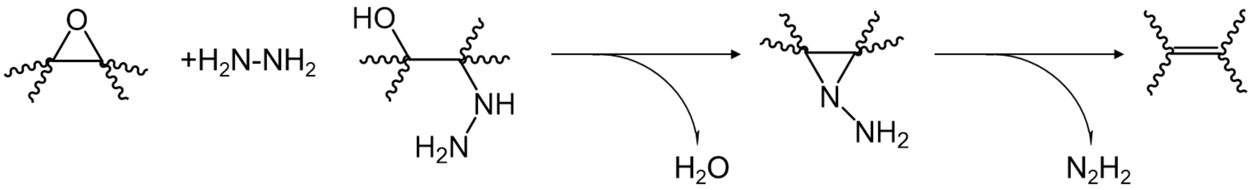

Figure 23: A proposed reaction pathway for epoxide reduction with hydrazine. Reproduced with permission from **[104]**.

I.2.6. Synthesis of graphene and graphene oxide via electro-chemical treatment

In recent years, the need for a cheap, fast, eco-friendly, and scalable graphene synthesis process has arisen because still nowadays, these requirements do not reach market requirements. A potential answer has been drawn within the electro-chemical technology.

The electro-chemical method consists of using graphite as a working electrode, a counter electrode, and an electrolyte. In this method, the electrolyte composition directly determines the properties of obtained graphene; if the electrolyte has a neutral pH it leads to graphite exfoliation into graphene; on the other hand, if the electrolyte has a pH < 2 it leads to graphite exfoliation and oxidation into graphene oxide.

I.2.6.1. Graphene electro-chemical synthesis

The exfoliation of graphite into graphene is based on the intercalation of ionic species between graphite layers. The exfoliation rate can be controlled by the ion composition, size, and decomposition in gases. Liu N. *et al* have synthesized functionalized graphene using aqueous 1-octyl-3-methyl-imidazolium hexafluorophosphate as the electrolyte. In this system, a cation is intercalated between graphene layers and then functionalized onto the graphene layer through the radical formation.[123] A decade later, Parvez K. *et al.* used an aqueous solution of inorganic salts as an electrolyte, such as $(NH_4)_2SO_4$, Na_2SO_4, K_2SO_4 (Figure 24).[124] Compare to the previous system, here; the authors use SO_4^{2-} anion as intercalative species. Once potential is applied, the anion intercalates between graphite layers and decomposes into gas. The interlayer gas formation leads to the exfoliation of graphite into graphene. This method allows the synthesis of a few layers graphene (>85%, ≤3 layers) having a large lateral size (up to 44 μm), a low oxidation degree (C/O = 17.2), and an excellent hole mobility 310 $cm^2\ V^{-1}\ s^{-1}$. Exfoliation in these electrolytes leads to graphene with a high yield large lateral size low oxidation degree, and remarkable hole mobility. Further, highly conductive graphene films (11 $\Omega\ sq^{-1}$) are fabricated on an A4-size paper.

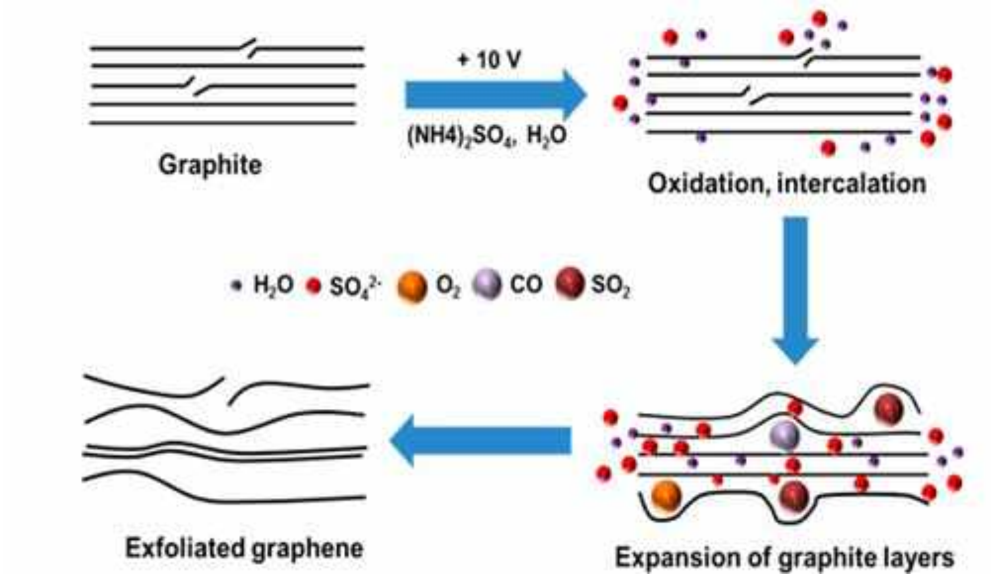

Figure 24: Schematic illustration of the mechanism of electrochemical exfoliation. Reproduced with permission from **[124]**.

I.2.6.2. Graphene oxide electro-chemical synthesis

Electro-chemical graphene oxide (EGO) synthesis is generally conducted using H_2SO_4 as an electrolyte.[24,125] In this system, the application of a potential intercalates wet $HSO4^-$ anion between graphite layers, then as the anodic electrocatalytic oxygen evolution reaction of water proceed, it leads to the formation *O, *OH, *OOH radical which functionalize the graphene's surface. The difficulty of EGO dwells within the ability to maintain graphite connected to the electrode until the oxidation completion. Nevertheless, as the oxidation process gas from H_2O and H_2SO_4 break the graphite framework interrupting the oxidation process. Thus recently Cao J. *et al.* followed by Pei S. *et al.* designed a two-step synthesis process, where the first step consists in the formation of a GIC by maintaining the graphite at about 2 V for 2 hours in high concentration H_2SO_4 electrolyte, then the second step consists in the oxidation and exfoliation of as prepared GIC in lower concentration H_2SO_4 electrolyte (Figure 25).[24,125] Cao J. *et al.* work leads to a GO with a high yield (>70 wt %), good quality (>90%, monolayers), and reasonable oxygen content (17.7 at. %).[24]

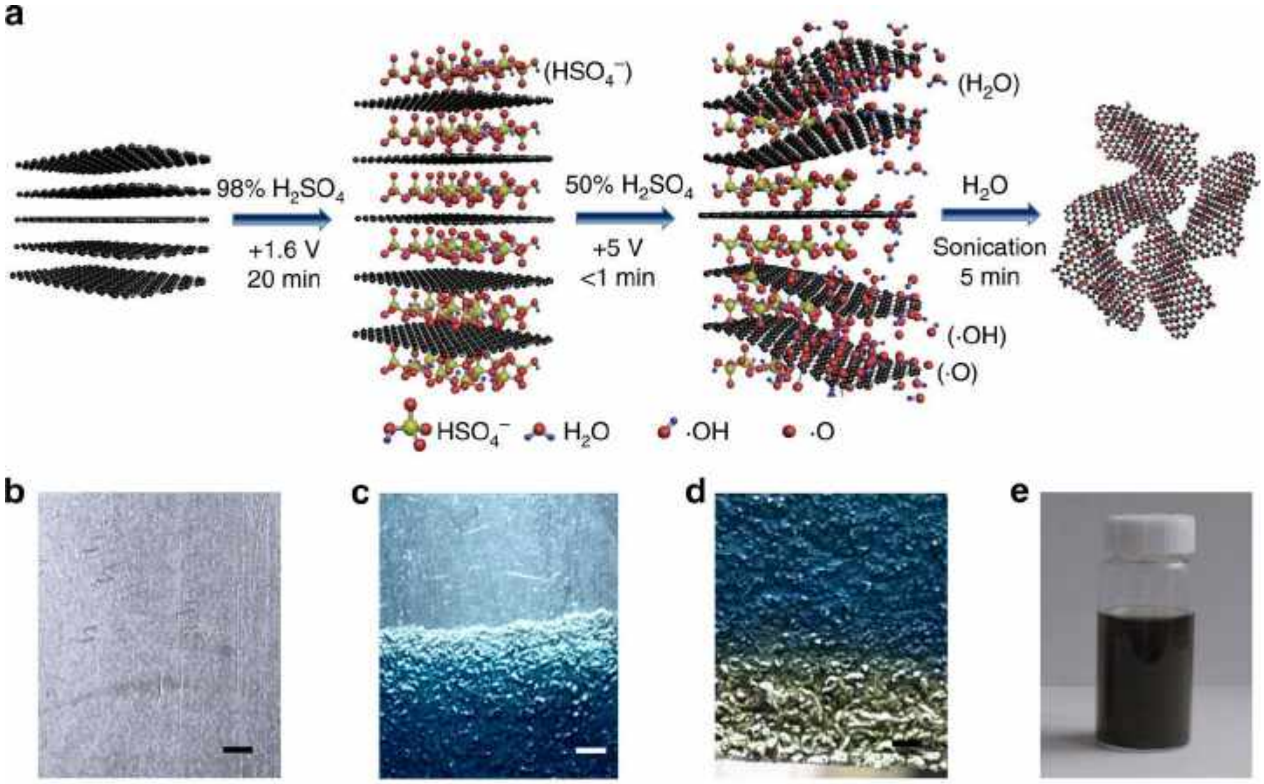

Surface of FGP slice

GICP (blue area)

Graphite oxide (yellow area)

EGO aqueous solution (5 mg·mL^{-1})

Figure 25: Synthesis of EGO by water electrochemical oxidation. (a) Schematic illustration of the synthesis process of EGO by water electrochemical oxidation. (b–d) Digital image of the raw material and the products obtained at each step. Digital image of EGO dispersion in water. Reproduced with permission from **[125]**.

II. GRAPHENE LIBS APPLICATION

II.1. Historical progress

II.1.1. Battery

The operating principle of a battery is relatively simple in its basic configuration (Figure 26). The cell consists of two electrodes, each connected to an electrical circuit and separated by an electrolyte capable of managing the charged species. Often the electrodes are physically separated by barrier materials that prevent the electrodes from making physical contact with each other to avoiding a short circuit in the battery. In discharge mode, when the battery plays a role in controlling the current, an oxidation process occurs at the negative electrode (anode), which initiates the movement of the electrons from the electrodes through the electric circuit. A reciprocal reduction process takes place at the positive electrode (cathode), which is supplied by electrons from the circuit. The cell voltage is highly dependent on the potential difference between the electrodes, and the overall process is spontaneous. For rechargeable (secondary) batteries, the process can be inverted by applying an external current proceeding an opposite redox reaction to the electrodes. This process depends on energy and is not spontaneous.

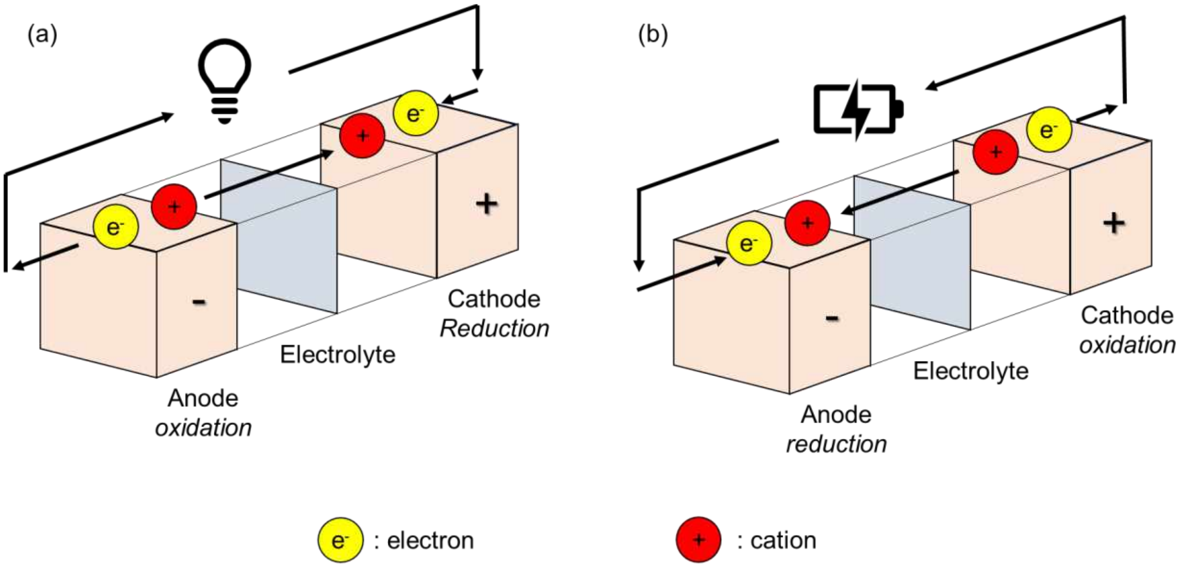

Figure 26: Illustration of battery system. (a) discharging battery, (b) charging battery.

The famous Voltaic pile, named after its inventor Alessandro Volta, consisted of alternating discs of two metals, zinc and copper, separated by a layer of corrugated cardboard or leather soaked in

NaCl aqueous electrolyte (Figure 27).[126] Each pair of zinc and copper constitute a battery, and the pile was composed of about 20 of those batteries stacked together. In this system, the copper is the cathode while the zinc is the anode; thus, the former oxidized, and the second reduced. The as prepared pile was able to generate a potential as high as 1.1 V.[127] Connecting the poles through the device; Volta was able to show how the resulting current produced a spark.

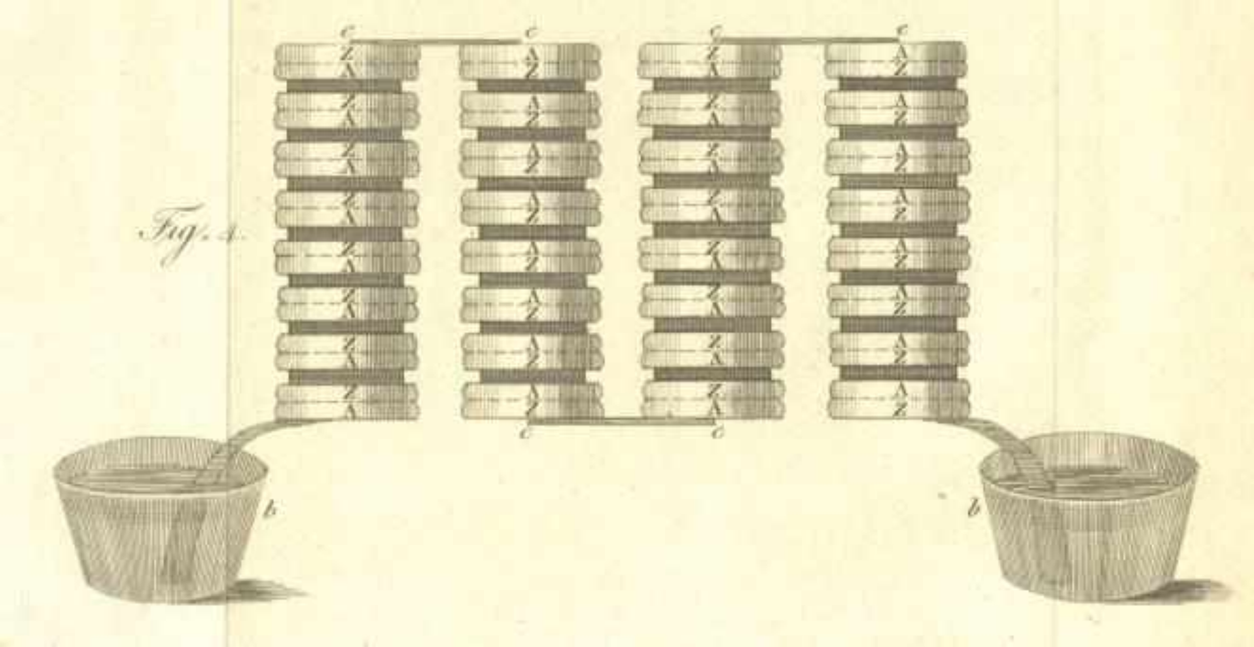

Figure 27: Illustration of Volta experimental setup. Reproduced with permission from [126].

The lead-acid batteries, still used as starter batteries in our cars, were studied in 1854 by Sinsteden W.J. and demonstrated by Plante G. from 1859 to 1860.[128–130] The working principle of this device is the same as the voltaic pile, but it was the first to be rechargeable, named secondary battery. The secondary term comes from an earlier study by Gautherot N., wherein 1801; a secondary current was noticed when wires used in electrochemical experiments were disconnected.[131] Lead-acid batteries are based on two lead electrodes. (PbO_2) separated by an electrolyte containing sulfuric acid. During discharge, the lead electrode (anode) undergoes oxidation to produce electrons, protons, and lead sulfate ($PbSO_4$), but at the cathode, lead oxide reduced to $PbSO_4$. In this case, the cell has a potential of around 2 V, and a typical 12 V car battery consists of six cells connected in series.

Another essential step in battery development occurred in 1899 when Jungner W. described the first nickel-iron (Ni-Fe) and nickel-cadmium (Ni-Cd) batteries. These alkaline batteries were the predecessors of the nickel-metal hydride (Ni-MH) batteries after their marketing in 1989.

II.1.2. Lithium

During the 20th century, the limited energy density of electrical energy devices urges the development of a completely new strategy, selecting lithium as its corner stone. Discovered by Arfwedson J.A. in 1817 and named by him and Berzelius J.J., this metal was considered to have excellent properties for functioning as a battery element (Figure 2).[132,133] Lithium with atomic number 3 is the lightest metal with a density of only 0.53 g cm^{-3}. Besides, the low standard reduction potential (Li^+ / Li vs. -3.05 V vs. SHE) makes it suitable for high-density high-voltage battery cells. However, the major drawback of lithium is that it is a relatively reactive metal that must be protected from water and air. Therefore, the initial research effort dedicated to preparing a dry electrochemical environment suitable for the application of lithium in a battery.

The original electrochemical study on lithium were conducted by Lewis G.N. *et al.* in 1913,[134] but it is only from the 70s that it became a hot topic. Its application necessitates the development of non-aqueous electrolytes, to keep lithium away from water and air. It was not an easy task, and factors such as inertia, melting point, redox stability, the solubility of ions and lithium salts, ion/electron transfer rates, and viscosities had to be taken into account. The study of the non-aqueous electrolyte has initially been conducted by Harris W.S. during his doctoral course, under the supervision of Tobias C.C. in 1958.[135] In this work, propylene carbonate arises as an excellent candidate for electrochemical applications based on alkali metals, including lithium halides. Forward to this work, the scientific community efforts continued to raise our understanding and established the knowledge being the basis of nowadays LIBs. In 1967, Y. Yao *et al.* studied the ionic conductivity in solids and showed that sodium ions could move through solids at the same rate as in molten salts.[136] In 1969, Kummer J.T. *et al.* proposed to use this configuration in batteries.[137] In 1967, Newman J. developed the theory of ion transfer in electrochemical cells.[138]

II.1.3. Intercalation cathodes

The second building bloc of the nowadays used LIBs is the development of reliable material for the cathode electrode since the anode electrode should serve as material for the anode electrode.

Pursuing the work done on ion conductivity in a solid, research efforts were conducted to find a material able to accommodate lithium-ions at a high rate with a high reduction potential. Designing such material is no easy;[139] it requires the material to meet several points:

1. To have an accessible electronic band-structure that allows significant and constant energy changes without intercalation throughout the stoichiometric range.
2. To guest ions in a wide stoichiometric range with minimal structural change.
3. To allow the high diffusion rate of alkaline ions in its structure.
4. To be reversibly intercalated.
5. To show good electronic conductivity.
6. To be insoluble in the electrolyte and avoid the co-insertion of electrolyte components.
7. To near ambient conditions.

The type MX_2 of metal chalcogenide became an attractive solution to meet all the requirements previously cited. In 1965, Rüdorff W. *et al.* showed the ability of TiS_2 to host lithium.[140] In this research, TiS_2 treatment with lithium dispersed in ammonia allows the intercalation of lithium within the layered structure of TiS_2 forming $Li_{0.6}TiS_2$. Following this work, in 1973 Rouxel J. *et al.* and in 1975 Whittingham M.S. *et al.* further study the chemical intercalation of Li_xTiS_2 (with $0 < x \leq 1$).[141,142] Convince by these results, Whittingham M.S. later research focused on the electro-chemical intercalation of MX_2 type metal chalcogenide which leads to him to propose the first cathode electrode for LIBs in 1973, and 3 years later to present the first functional rechargeable LIBs.[143–145]

This LIBs consisted of a $LiTiS_2$ cathode electrode, a lithium metal anode electrode, and a $LiPF_6$ dispersed in propylene carbonate as the electrolyte (Figure 28). The experimental results show a working potential of 2.5 V, an initial current density of 10 mA cm^{-2}, and a reversible intercalation behavior. Additionally, a practical battery was built and evaluated using TiS_2 powder as a cathode electrode, lithium metal as an anode electrode, and $LiClO_4$ dispersed in dimethoxyethane and tetrahydrofuran. The results show excellent cycling performance even after 1100 cycles. In the light of these encouraging results, Exxon company commercialized a battery made of TiS_2 powder as a cathode electrode, lithium metal as an anode electrode, and $C_4H_{12}BLi$ dispersed in dimethoxy-ethane.[146]

Besides, the democratization of this LIBs system was interrupted due to safety risks. Indeed, the highly reactive lithium metal undergoes the progressive formation of lithium dendrite on its surface, which in the end, creates a short-circuit and a potential fire hazard. Since then, an alternative configuration, named rocking chair cells, have been investigated.[147] In this configuration, the lithium-ions exchange between two hosts. In 1938, Rüdorff W. *et al.* showed its principle using two graphite electrodes to move back and forth HSO_4^-.[148] In the rocking chair configuration of LIBs, another electrode replaced lithium metal, thus avoiding safety hazard. At the time it is already well known that lithium-ion can intercalate graphite,[149,150] with a woking potential relatively superior to lithium metal. However, the simultaneous insertion of the lithium-ions and electrolyte lead to the decomposition of the graphite. Therefore, additional scientific efforts had to be conducted.

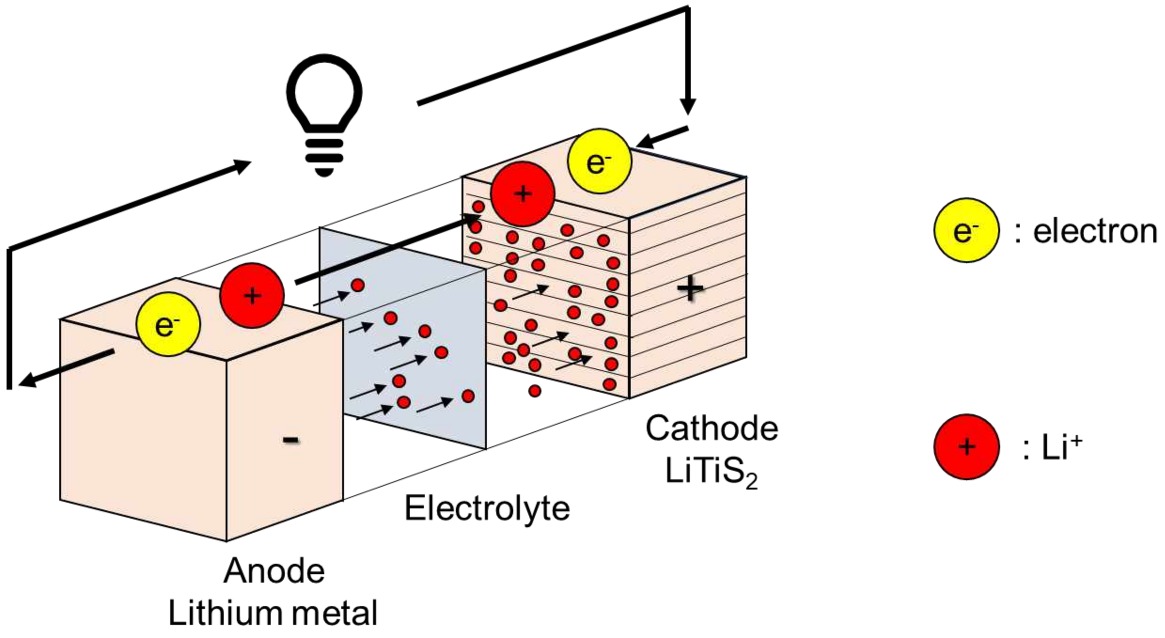

Figure 28: Illustration Lithium-ion battery system made of lithium metal as anode, $LiPF_6$ in propylene carbonate as the electrolyte, and $LiTiS_2$ as cathode.

All the while anode was being developed, the discovery of new cathode materials lead LIBs technology to higher working potential allowing the use of higher working potential material. This improvement eases the application of higher working potential material, compared with lithium metal, as the anode electrode. Indeed, between 1979 and 1980, Goodenough *et al.* discovered that Li_xCoO_2 was an excellent cathode material expressing about 4-5 V vs. Li^+/Li working potential and a reversible intercalation behavior at 1 mA cm^{-2}.[151,152]

II.1.4. Carbon based anodes

The discovery of $LiCoO_2$ cathode material enable the application of higher working potential anode material (vs. Li^+/Li). As mentioned above, the application of graphite as anode was attractive but not possible since this last experience decomposition upon intercalation. Thus, other carbons-based anode electrode materials were investigated. In 1985, after having attempted to apply conducting polymer poly(acetylene) and vapor-phase–grown carbon fibers, Yoshino A. *et al.* finally applied heat-treated petroleum coke as anode electrode material.[153,154] This material, composed of a mixture of graphitic and non-graphitic domains, displays stable reversible intercalation behavior and a working potential of 0.5 V vs. Li^+/Li. This excellent behavior was enabled by the protection of the graphitic domains by the surrounding non-graphitic domains.

Having discover the first suitable anode electrode material for LIBs, Yoshino A. *et al.* built the first full-cell (without lithium metal) LIBs combining their anode electrode material with $LiCoO_2$ cathode electrode material and an electrolyte composed of $LiClO_4$ in propylene carbonate (Figure 29). To demonstrate the safety superiority of their LIBs, a series of experiment was conducted involving the dropping a metal object on the lithium-ion bettery.[155] The results clearly show that the fire hazard is suppressed in by their anode electrode material.

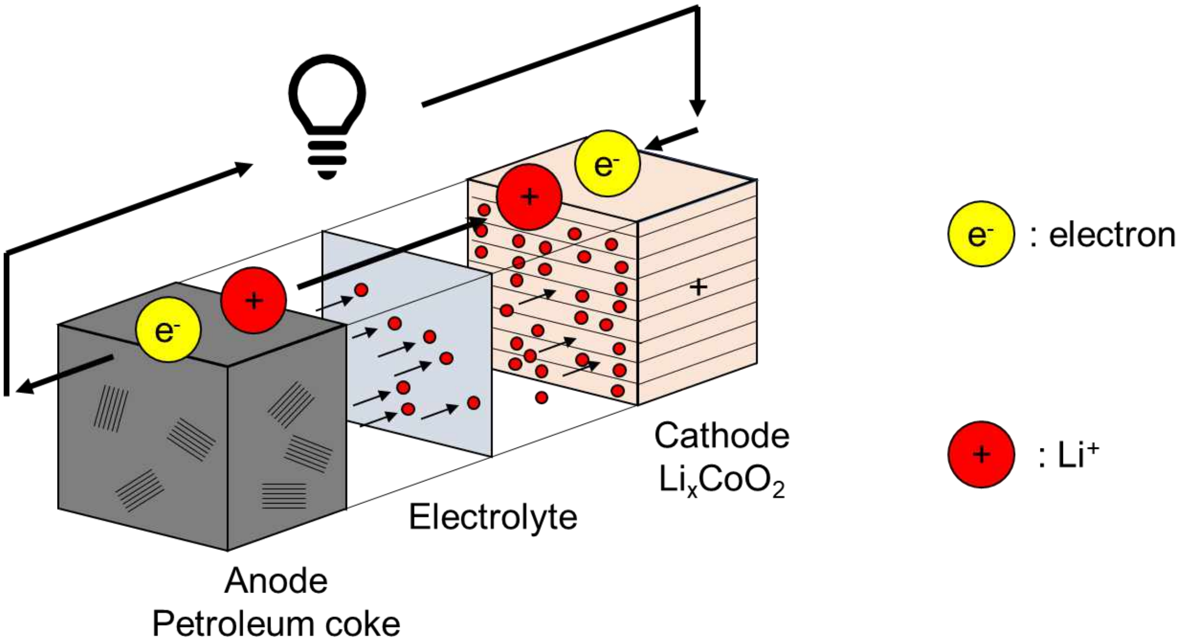

Figure 29: Illustration Lithium-ion battery system made of petroleum coke as anode, $LiClO_4$ in propylene carbonate as the electrolyte, and $LiCoO_2$ as cathode.

This scientific and industrial breakthrough lead to the commercialization of the first full-cell LIBs in 1991.[156] This battery was composed of a $LiCoO_2$ cathode, a heat-treated petroleum coke anode, and a LiPF6 in propylene carbonate electrolyte. This battery has a working potential of 4.1 V and an energy density of about 80 Wh kg^{-1}.

Around the same time, the works of Peled E. *et al.* 1979 and Fong R. *et al.* in 1990 introduce new electrolytes including ethylene carbonate which enable the application of graphite as anode for LIBs.[157,158] This improvement is obtained through the decomposition of the electrolyte on the surface of graphite creating a protective layer, named solid electrolyte interface (SEI), which avoid the electrolyte penetration in the graphite and thus its decomposition. This discovery was quickly accepted and applied by the scientific and industrial communities, leading to the first commercialization of a graphite based full-cell LIBs raising its working potential to 4.2 V and its energy density to 160 Wh kg^{-1}.

II.2. Graphene LIBs application

II.2.1. Introduction

As mentioned previously, the electrical energy storage of LIBs is based on the reversible exchange of lithium-ions between the cathode and the anode host/active materials. As for now, the electrode mechanistic for lithium-ion storage can be categorized as intercalation, where lithium-ion is inserted into and removed from the solid host network, and as alloying, where the lithium lithiation/delithiation is shaped by the redox reaction of the electrode leading to change in the electrode crystalline structure and accompanied by the breaking and recombining chemical bonds. In Figure 30 an overview of the average discharge potentials and specific capacities for all types of electrodes is given. It concludes that the best material in terms of specific capacity is obtained by conversion electrode materials for both anode and cathode. Unfortunately, conversion materials suffer from relatively low electrical conductivity and mostly from high volume expansion caused by considerable mechanical stress, which leads to the disintegration of the active materials and to the SEI cracking through cycling. This drawback makes the cycle life of conversion materials limited.

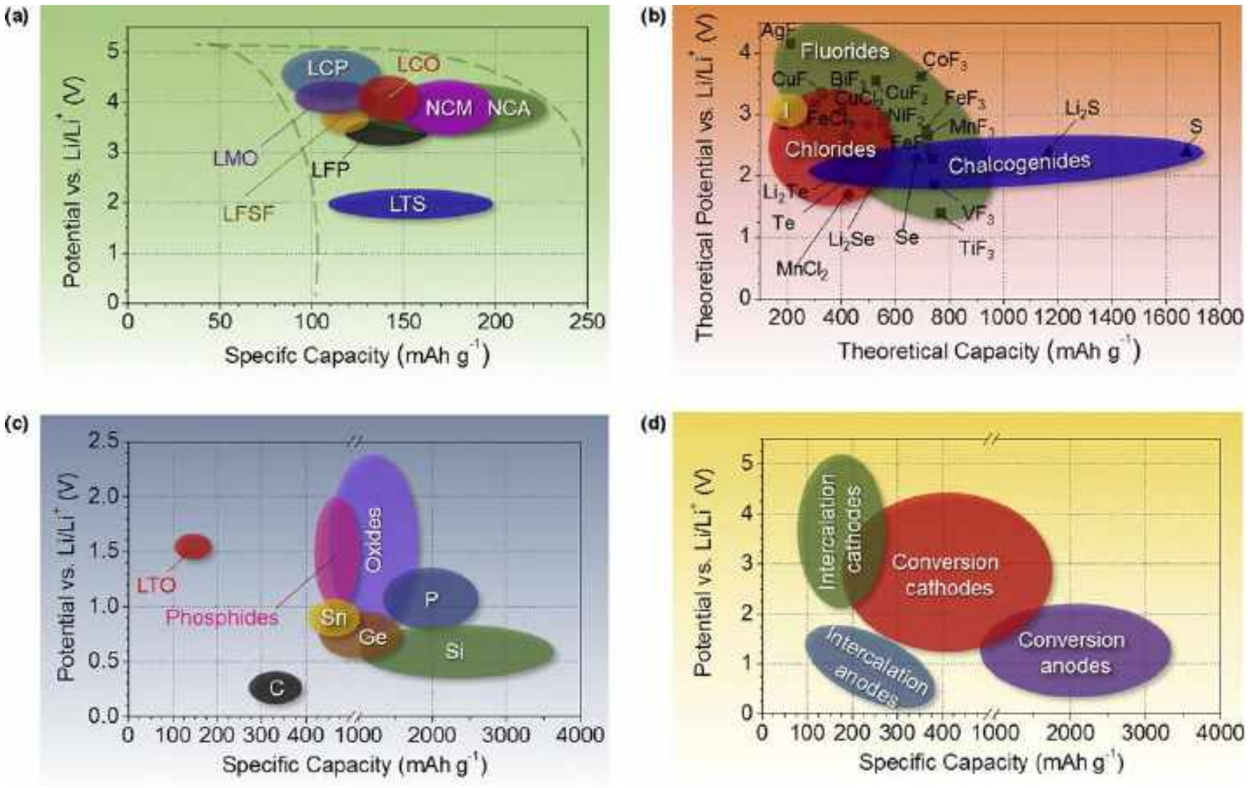

Figure 30: Approximate range of average discharge potentials and specific capacity of some of the most common (a) intercalation-type cathodes (experimental), (b) conversion-type cathodes (theoretical), (c) conversion type anodes (experimental), and (d) an overview of the average discharge potentials and specific capacities for all types of electrodes. Reproduced with permission from [159].

Graphene can be categorized as intercalation material, even if the graphene storage mechanism process through the absorption mechanism, since the graphene crystalline structure remains untouched when intercalation/de-intercalation proceed. Then, we can understand that the specific capacity of graphene would always be lower than other conversion materials, yet due to its carbonaceous nature and its unique morphology (two-dimensional structure, 1 nm thickness, micro to nanometer size) and properties (ultra-high electric conductivity, superior strength, and flexibility, active surface once oxidized), graphene can be directly used as anode or as cathode active material or used to prepare graphene active-composite for anode and cathode. For graphene active-composites, the attached structures can be classified into six different models (Figure 31). In the encapsulation mode, the graphene material encapsulates the particles of electroactive material, while in the mixed model, the graphene material and the active material are mixed mechanically during the electrode preparation process. The particles of electroactive material can also be wrapped in graphene. The anchored model is the most widely reported, where the electroactive nanoparticles are immobilized on the surface of the graphene material. Graphene materials can also be stacked with active materials to form a sandwich-type model or a layered model.

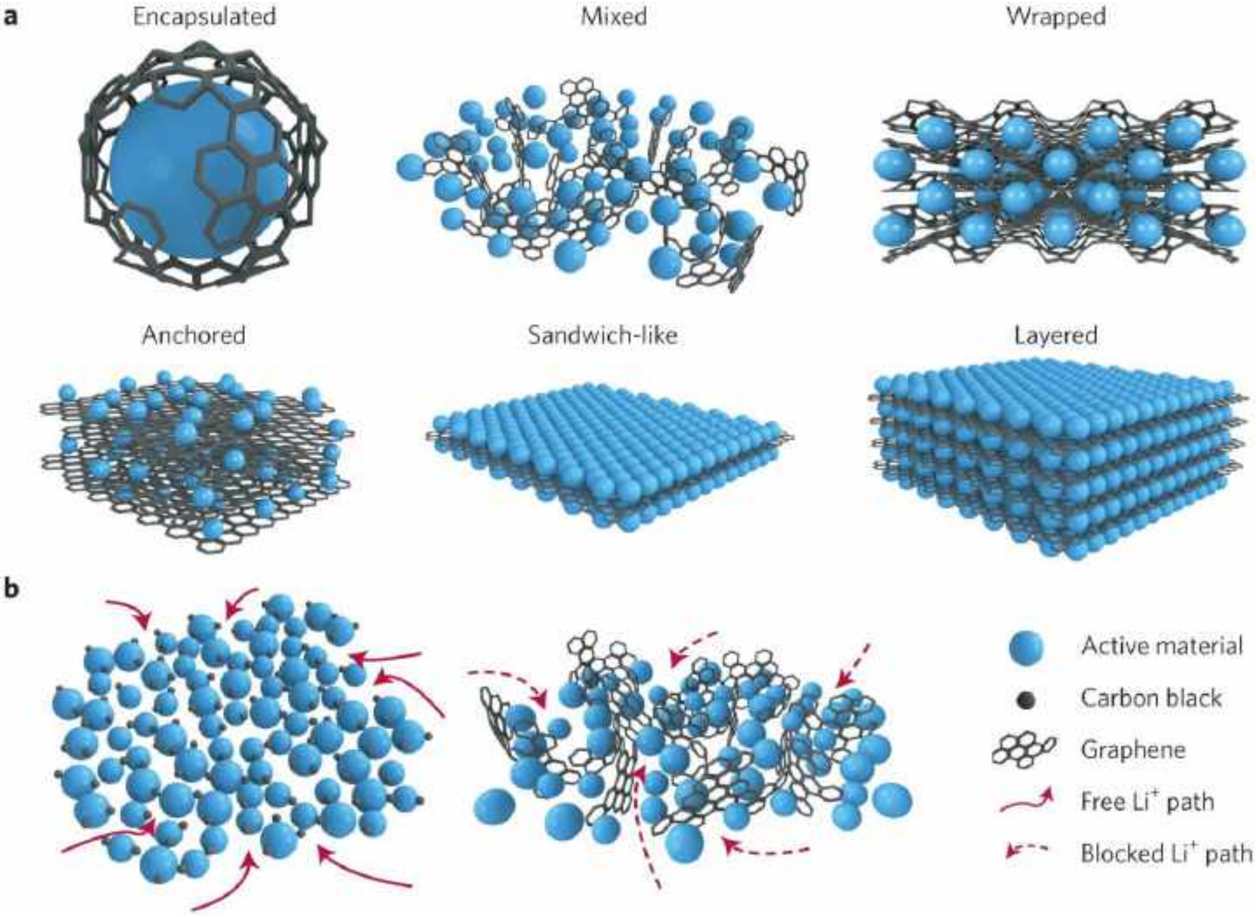

Figure 31: (a) Illustration of the different structures of graphene composite electrode materials. (b) Lithium paths in carbon black- (left) and graphene- (right) based electrodes in the mixed structural model. Reproduced with permission from [160].

II.2.2. Graphene as anode

II.2.2.1. Graphene as active material

Due to its unique properties, graphene has, in the last decade, received considerable attention for its application as active anode material. Indeed, even until now, general LIBs use graphite-based anode limiting the theoretical capacity performance of the anode to 372 mAh g^{-1}. On the other hand, the theoretical capacity performance of graphene is 744 mAh g^{-1} based on the stoichiometry of Li_2C_6, because Li^+ can adhere to both sides of the monolayer graphene sheet.

The most common way to prepare graphene for LIBs is through its oxidation into graphene oxide (GO) and its further reduction into (rGO). In general, the specific capacity for rGO based half-cell anode is between 500 mAh g^{-1} to 800 mAh g^{-1} at 372 mA g^{-1}. [161–163] The performances of rGO can be tuned via modification of its specific surface area, oxygen content, and morphology.

Added to this, can also be considered as graphene anode active material, the hetero-atom doped graphene such as Nitrogen, Boron, sulfur-doped graphene's.[164–166] The doping of heteroatoms into graphene has been found to improve the interaction between Li^+ and the new graphene active site, while leading to superior electrical conductivity, and higher first cycle coulombic efficiency.

II.2.2.2. Graphene composite as active material

II.2.2.2.1 Insertion material graphene composite

Lithium titanium oxide, $Li_4Ti_5O_{12}$ (LTO), is one of the few anode insertion materials commercially available. This material inserts and extracts lithium without a noticeable change in its lattice dimension at a working potential of 1.5 V vs Li/Li^+. Its theoretical capacity is of 175 mAh $g^{-1,}$ making it an excellent candidate for anode LIBs were stability and safety are more critical than energy density. Due to LTO low electronic conductivity ($<10^{-13}$ S cm^{-1}), carbon-based conductive materials are often applied to overcome this limitation, including graphene. Shi Y. *et al.* prepared LTO/rGO composite *via* simple mixing and heat treatment of LTO powder and rGO (Figure 32). [167] The impedance shows a reduced charge transfer resistance from 54 to 36 Ω as the rGO is added. The capability evaluation shows the same trend with a capacity of 122 mAh g^{-1} instead of 92 mAh g^{-1} as rGO is introduced. The cyclability results show excellent behavior with a capacity maintained to 124 mAh g^{-1} after 300 cycles. Similarly, Zhu N. *et al.* demonstrate the same results in preparing LTO/graphene composite *via* the electrospun method.[168] The specific capacity is improved from 47 mAh g^{-1} to 110 mAh g^{-1} and retained a specific capacity of 101 after 1200 cycles.

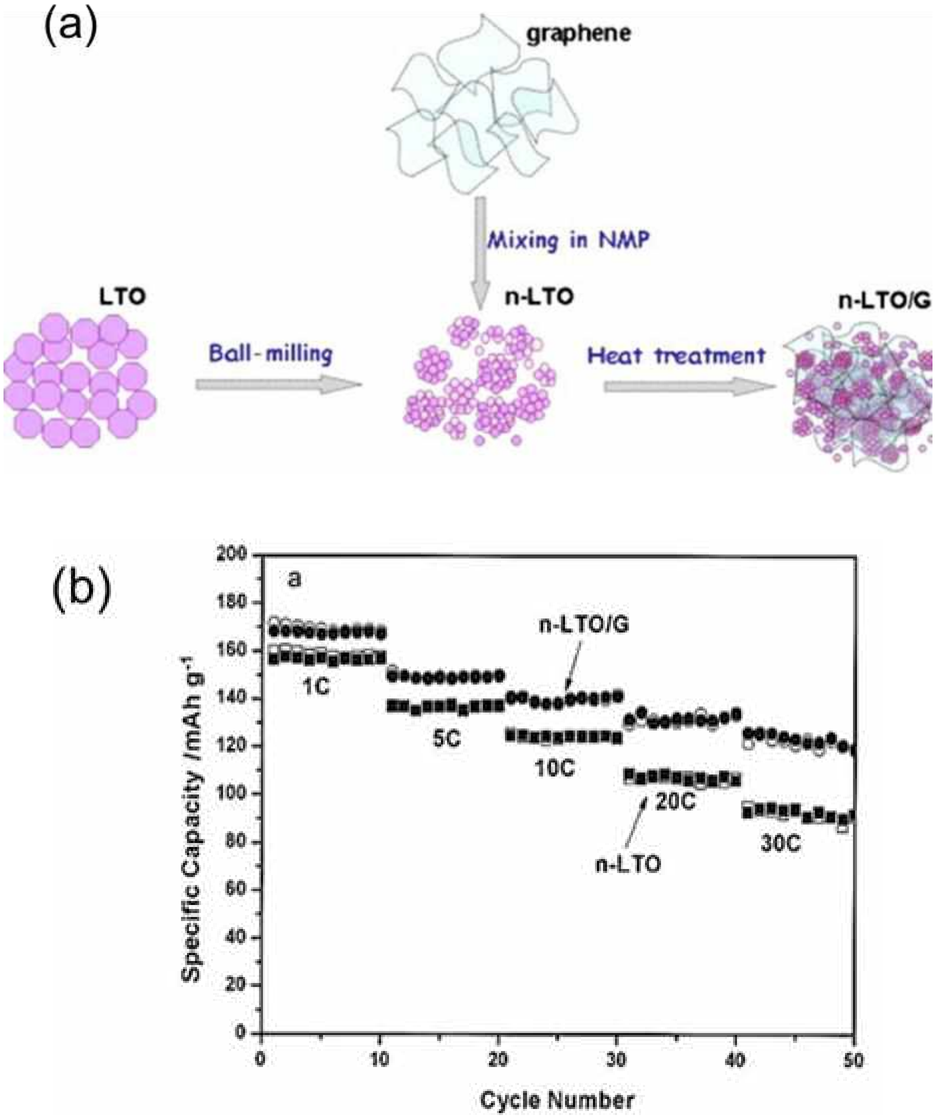

Figure 32: (a) Schematic of the synthesis route of n-LTO and graphene (n-LTO/G) composite , (b) Specific rate capacity of the n-LTO and n-LTO/G. Reproduced with permission from [167].

II.2.2.2.2 Alloying material graphene composite

Having a look at Figure 30 help us to clearly understand that tomorrow LIBs technology will be based on alloying anode materials, such as Si, P, Ge, and Sn. Indeed, those materials hold the highest specific capacity, respectively 3579 mAh g^{-1}, 2596 mAh g^{-1}, 1384 mAh g^{-1}, and 960 mAh g^{-1} after lithium itself. Nevertheless, the application of such materials is limited by their relatively low electric and ionic conductivity, as well as their significant volume expansion upon cycling, reducing their cyclability.

Silicon is among those candidates at the same time the most promising and the most challenging. Indeed, Si has the highest specific capacity and is the most available on earth. However, it has the lowest electrical and ionic conductivity, and the most massive volume expansion after lithiation (300%). To overcome these limitations, graphene has been used to create a conductive framework embedding Si material, able to accommodate its volume expansion. Xiang H. *et al.* prepared graphene/Si composite (Figure 33).[169] First, GO, and silicon nanoparticles were mixed in a 2 to 1 weight ratio, then the freeze-dried mixture was heated 600 °C to obtain the graphene/Si composite. The composite shows a working potential of 0.2 V *vs* Li/Li^+. This composite shows a specific capacity of 1300 mAh g^{-1} at 300 mA g^{-1} and retains a specific capacity of 800 mAh g^{-1} after 30 cycles.

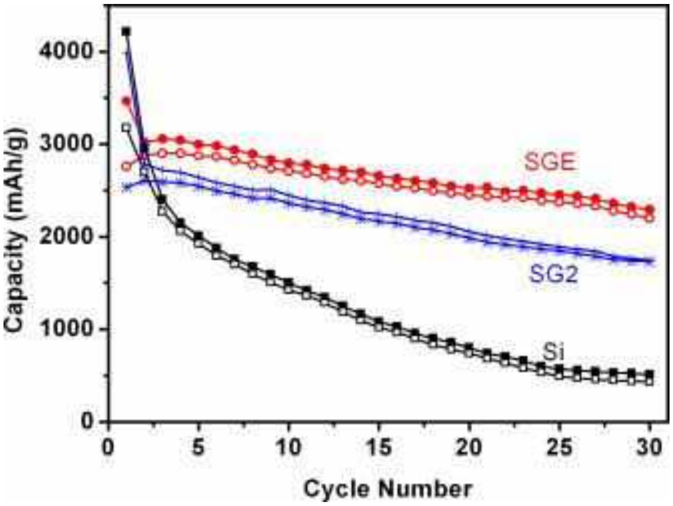

Figure 33: Specific capacity of silicon, SGE (graphene/silicon), SG2 (GO/silicon) at 300 mA g^{-1} based on silicon mass. Reproduced with permission from **[169]**.

II.2.3. Graphene as cathode

II.2.3.1. Graphene as active material

It is well known that oxygen functional groups such as carbonyl, carboxylic, and ester groups as the ability to reversibly store Li^+ and that the large surface area of graphene materials possesses electrical double-layer capacitance (Figure 34).[170,171] Ha *et al.* prepared a free-standing rGO film cathode by reducing GO at 650 °C. The prepared material shows a working potential of 3 V *vs* Li/Li^+ and displays a specific capacity of 115 mAh g^{-1} at 137 mA g^{-1}. Similarly, Wang *et al.* prepared rGO by reducing GO at 100 °C. As prepared rGO displays a specific capacity of 219 mAh g^{-1} at 100 mA g^{-1} and remains as high as 200 mAh g^{-1} after 60 cycles. Another way to think the concept of graphene as the cathode is to consider the application of anion PF_6^- instead of the cation Li^+. Indeed, graphene can reversibly insert and extract PF_6^- from 3 to 4.6 V *vs* Li/Li^+. Aravindan *et al.* prepared rGO *via* thermal reduction of GO at 278 °C.[172] As prepared material shows a working potential of 3.8 V *vs* Li/Li^+ and displays a capacity of 58 mAh g^{-1} at 100 mA g^{-1} which remains as high as 44 mAh g^{-1} after 1000 cycles.

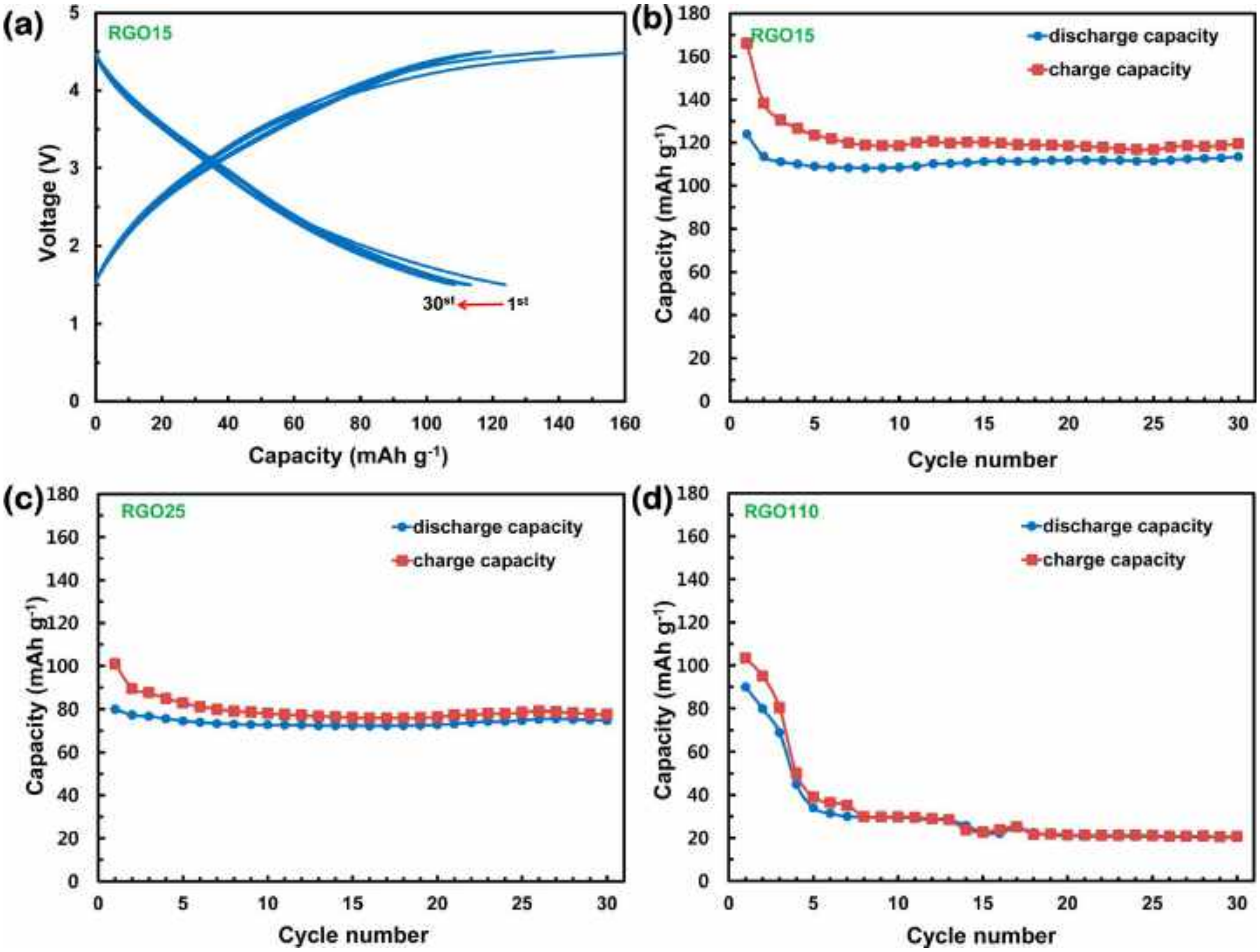

Figure 34: Cathode performances of RGO15, RGO25, and RGO110 films at 0.137 A g^{-1}. (a) Charge–discharge curves of RGO15, cyclability of (b) RGO15, (c) RGO25, and (d) RGO110. RGOX with X = C/O ratio. Reproduced with permission from [170].

II.2.3.2. Graphene composite as active material

II.2.3.2.1 Insertion material graphene composite

Among all cathode insertion material presented in Figure 30, as mentioned in the above sections, $LiCoO_2$ has received intense scientific effort since the early 1980s and lead to the first commercialized LIBs in 1991. This material has proven over the past decades to be a reliable choice of cathode since it shows a relatively high theoretical specific capacity of 274 mAh g^{-1}, a high theoretical volumetric capacity of 1363 mAh cm^{-1}, a low self-discharge, a high discharge voltage 3.8 V *vs* Li/Li^{+}, and an excellent cycling performance. Two of $LiCoO_2$ limitations are its low electronic conductivity and its relatively weak cyclability.

Recently, Tang R. *et al.* prepared $LiCoO_2$/graphene composite by simply mixing $LiCoO_2$ with 2 wt% graphene in NMP (Figure 35).[173] The composite shows similar capacity performance as the original $LiCoO_2$ expressing 158 mAh g^{-1} at 0.1C. On the other hand, the composite shows superior rate capability, 110 mAh g^{-1} at 5C instead of 90 mAh g^{-1}, as well as superior cyclability expressing a specific capacity of 145 mAh g^{-1} after 50 cycles at 1C while original displays a reduced specific capacity of 130 mAh g^{-1}.

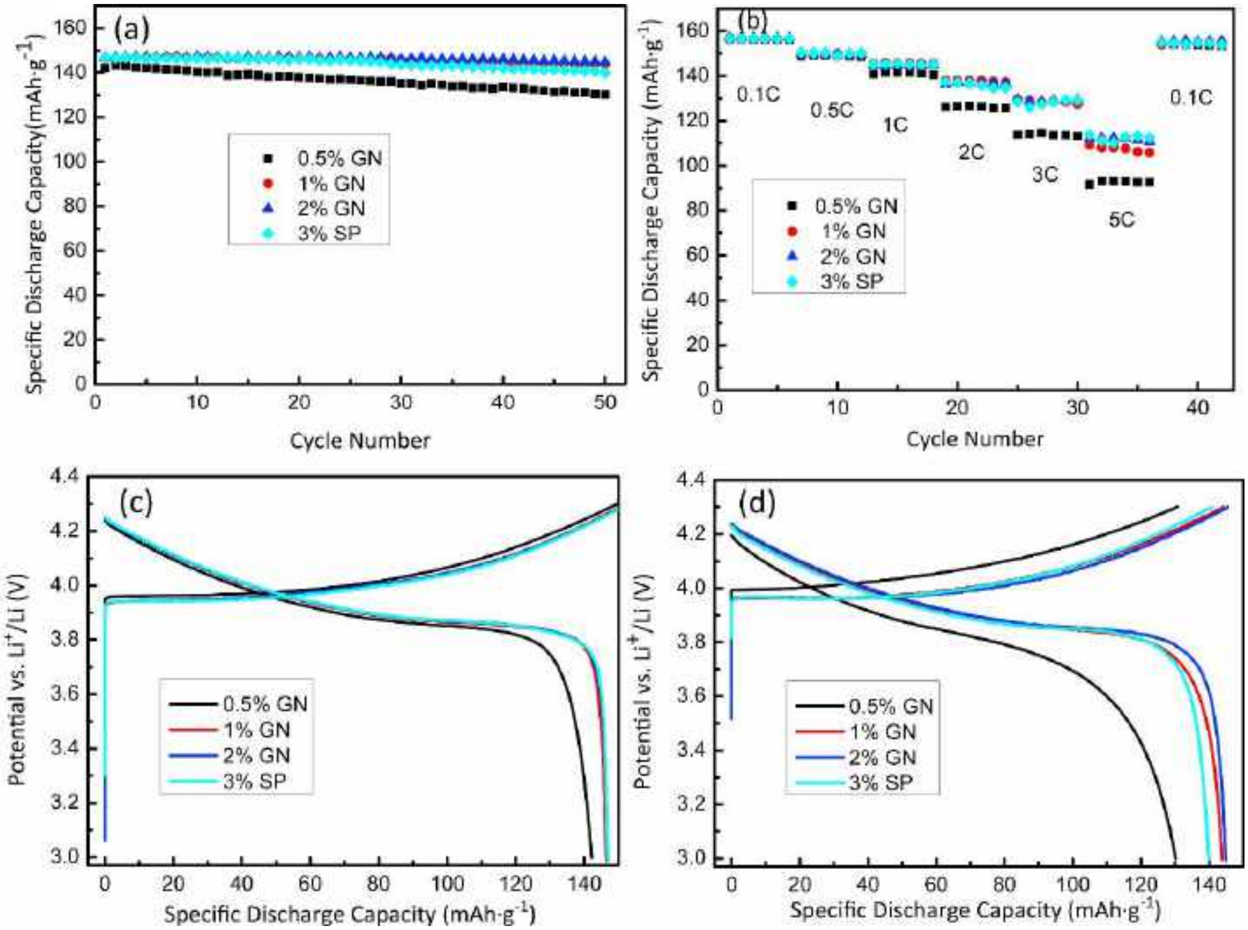

Figure 35: LIBs evaluation of $LiCoO_2$ with different conductive additives (0.5GN, 1GN, 2GN, 3SP). %. (a) Cycling performance at 1C, (b) rate performance, (c) charge/discharge profile at 1C in the 1st cycle; (d) Charge/discharge profile at 1C in the 50th cycle. GN = graphene nano-sheets, SP = Super-P, xGN with x = weight. Reproduced with permission from **[173]**.

II.2.3.2.2 Alloying material graphene composite

S, Se, Te, and I are cathodic alloying materials, as represented in Figure 30. Among these elements, the most intensively studied is S because of its high theoretical specific capacity, 1675 mAh g^{-1}, low cost, and abundance in Earth's crust. However, the application of S as cathode material is limited by its relatively mild working potential 2.4 V *vs* Li/Li^+, low electronic conductivity, dissolution in the electrolyte, low vaporization temperature, and large volume expansion upon lithiation of about 80%.

Wang H. *et al.* recently prepared sulfur particles poly(ethylene glycol) wrapped between carbon black coated GO layers using a simple mixing method in water solution (Figure 36).[174] The LIBs results show that the addition of graphene improves both the capacity and cyclability expressing a specific capacity ~ 520 mAh g^{-1} after 100 cycles at C/5, and excellent capability since the specific capacity remains unchanged at C/2.

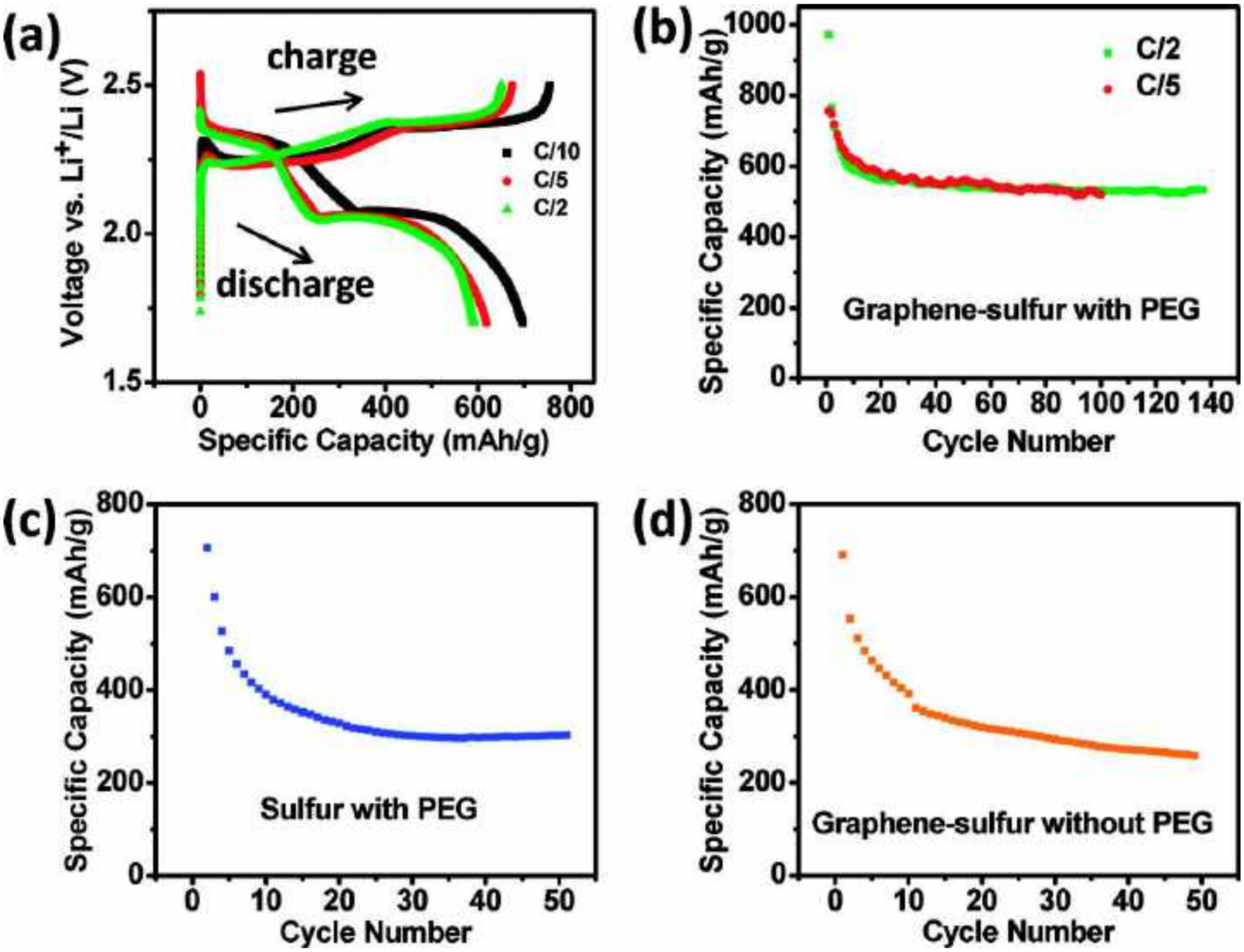

Figure 36: Electrochemical evaluation of graphene–sulfur composites. (a) 10th cycle charge and discharge voltage profiles of the graphene–sulfur composite with PEG coating. (b) Cycling performance of the same composite at rates of ~C/5 and ~C/2. (c) Cycling performance of PEG coated sulfur without graphene coating at the rate of ~C/5. (d) Cycling performance of graphene coated sulfur without any surfactant PEG coating at the rate of ~C/5. PEG = poly(ethylene glycol). Reproduced with permission from [174].

III. CONCLUSION

In order to move toward a more sustainable society the development renewable energy grid and electric car are needed. LIBs technology has already demonstrated its application for mobile devices such as smartphone, laptop, electric car. However, current electrode materials hampered the development for higher energy and power density devices. Therefore, the development of new electrode materials is essential for tomorrow battery technology. The choice of new electrode materials is required to combine higher performances at low cost and with excellent scalability and eco-friendliness.

Graphene, as mentioned above, has showed promising results. However, it still presents several problems hindering its commercial application to batteries. The most promising synthesis method of graphene materials is now conduct through the electro-chemical oxidation of graphite into graphene oxide and graphene. However, at this moment none of the reported synthesis method have been showed to be scalable hindering its production; and the reduction step remain complex as the final product is strongly impacted by the choice of oxidation and reduction methods which create uncertainty for the final LIBs performances (Figure 37).

To address those issues, the research of this thesis is devoted to find new graphene oxide synthesis methods and to clarify what reduction method is the most suitable to LIBs and SIBs.

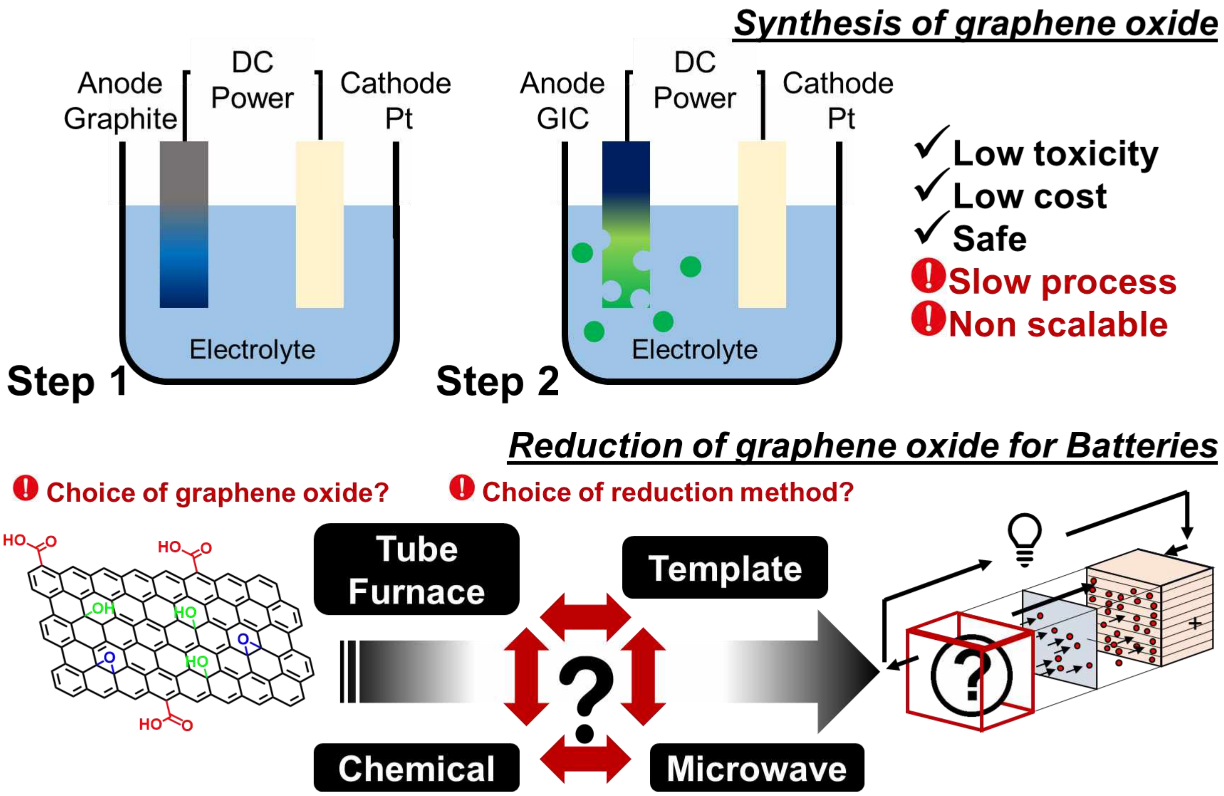

Figure 37: Illustration of promising methods and their limitation for graphene oxide synthesis and its reduction for high performance anode Batteries.

REFERENCES

1. Bernal, J. D. The Structure of Graphite. *Proc. R. Soc. Lond. Ser. Contain. Pap. Math. Phys. Character* **106**, 749–773 (1924).

2. Hass, J., Heer, W. A. de & Conrad, E. H. The growth and morphology of epitaxial multilayer graphene. *J. Phys. Condens. Matter* **20**, 323202 (2008).

3. Viculis, L. M., Mack, J. J., Mayer, O. M., Hahn, H. T. & Kaner, R. B. Intercalation and exfoliation routes to graphite nanoplatelets. *J. Mater. Chem.* **15**, 974–978 (2005).

4. Alam, S. N., Kumar, L. & Sharma, N. Development of Cu-Exfoliated Graphite Nanoplatelets (xGnP) Metal Matrix Composite by Powder Metallurgy Route. *Graphene* **4**, 91–111 (2015).

5. Lee, J. H. *et al.* One-Step Exfoliation Synthesis of Easily Soluble Graphite and Transparent Conducting Graphene Sheets. *Adv. Mater.* **21**, 4383–4387 (2009).

6. Kalaitzidou, K., Fukushima, H. & Drzal, L. T. Multifunctional polypropylene composites produced by incorporation of exfoliated graphite nanoplatelets. *Carbon* **45**, 1446–1452 (2007).

7. Kalaitzidou, K., Fukushima, H., Askeland, P. & Drzal, L. T. The nucleating effect of exfoliated graphite nanoplatelets and their influence on the crystal structure and electrical conductivity of polypropylene nanocomposites. *J. Mater. Sci.* **43**, 2895–2907 (2008).

8. Celzard, A., Marêché, J. F. & Furdin, G. Surface area of compressed expanded graphite. *Carbon* **40**, 2713–2718 (2002).

9. Wang, L. *et al.* The effect of expanded graphite with sodium metasilicate as lubricant at high temperature. *Carbon* **159**, 345–356 (2020).

10. Novoselov, K. S. *et al.* Electric Field Effect in Atomically Thin Carbon Films. *Science* **306**, 666–669 (2004).

11. Geim, A. K. & Novoselov, K. S. The rise of graphene. *Nat. Mater.* **6**, 183–191 (2007).

12. Lee, C., Wei, X., Kysar, J. W. & Hone, J. Measurement of the Elastic Properties and Intrinsic Strength of Monolayer Graphene. *Science* **321**, 385–388 (2008).

13. Gómez-Navarro, C., Burghard, M. & Kern, K. Elastic Properties of Chemically Derived Single Graphene Sheets. *Nano Lett.* **8**, 2045–2049 (2008).

14. Balandin, A. A. *et al.* Superior Thermal Conductivity of Single-Layer Graphene. *Nano Lett.* **8**, 902–907 (2008).

15. Stoller, M. D., Park, S., Zhu, Y., An, J. & Ruoff, R. S. Graphene-Based Ultracapacitors. *Nano Lett.* **8**, 3498–3502 (2008).

16. Bunch, J. S. *et al.* Impermeable Atomic Membranes from Graphene Sheets. *Nano Lett.* **8**, 2458–2462 (2008).

17. Bolotin, K. I. *et al.* Ultrahigh electron mobility in suspended graphene. *Solid State Commun.* **146**, 351–355 (2008).

18. Ganz, E., Ganz, A. B., Yang, L.-M. & Dornfeld, M. The initial stages of melting of graphene between 4000 K and 6000 K. *Phys. Chem. Chem. Phys.* **19**, 3756–3762 (2017).

19. Kinoshita, H., Nishina, Y., Alias, A. A. & Fujii, M. Tribological properties of monolayer graphene oxide sheets as water-based lubricant additives. *Carbon* **66**, 720–723 (2014).

20. Whitener, K. E. & Sheehan, P. E. Graphene synthesis. *Diam. Relat. Mater.* **46**, 25–34 (2014).

21. Reina, A. *et al.* Large Area, Few-Layer Graphene Films on Arbitrary Substrates by Chemical Vapor Deposition. *Nano Lett.* **9**, 30–35 (2009).

22. Wei, D. *et al.* Synthesis of N-Doped Graphene by Chemical Vapor Deposition and Its Electrical Properties. *Nano Lett.* **9**, 1752–1758 (2009).

23. Sutter, P. Epitaxial graphene: How silicon leaves the scene. *Nat. Mater.* **8**, 171–172 (2009).

24. Cao, J. *et al.* Two-Step Electrochemical Intercalation and Oxidation of Graphite for the Mass Production of Graphene Oxide. *J. Am. Chem. Soc.* **139**, 17446–17456 (2017).

25. Morimoto, N., Kubo, T. & Nishina, Y. Tailoring the Oxygen Content of Graphite and Reduced Graphene Oxide for Specific Applications. *Sci. Rep.* **6**, 21715 (2016).

26. Kosynkin, D. V. *et al.* Longitudinal unzipping of carbon nanotubes to form graphene nanoribbons. *Nature* **458**, 872–876 (2009).

27. Novoselov, K. S. & Neto, A. H. C. Two-dimensional crystals-based heterostructures: materials with tailored properties. *Phys. Scr.* **T146**, 014006 (2012).

28. Ramón, M. E. *et al.* CMOS-Compatible Synthesis of Large-Area, High-Mobility Graphene by Chemical Vapor Deposition of Acetylene on Cobalt Thin Films. *ACS Nano* **5**, 7198–7204 (2011).

29. Gao, L. *et al.* Repeated growth and bubbling transfer of graphene with millimetre-size single-crystal grains using platinum. *Nat. Commun.* **3**, 1–7 (2012).

30. Chae, S. J. *et al.* Synthesis of Large-Area Graphene Layers on Poly-Nickel Substrate by Chemical Vapor Deposition: Wrinkle Formation. *Adv. Mater.* **21**, 2328–2333 (2009).

31. Li, X. *et al.* Large-Area Graphene Single Crystals Grown by Low-Pressure Chemical Vapor Deposition of Methane on Copper. *J. Am. Chem. Soc.* **133**, 2816–2819 (2011).

32. Shen, C. *et al.* Effects of Cu contamination on system reliability for graphene synthesis by chemical vapor deposition method. *Carbon* **127**, 676–680 (2018).

33. Emtsev, K. V., Speck, F., Seyller, Th., Ley, L. & Riley, J. D. Interaction, growth, and ordering of epitaxial graphene on SiC{0001} surfaces: A comparative photoelectron spectroscopy study. *Phys. Rev. B* **77**, 155303 (2008).

34. Riedl, C., Coletti, C. & Starke, U. Structural and electronic properties of epitaxial graphene on SiC(0\hspace0.167em0\hspace0.167em0\hspace0.167em1): a review of growth, characterization, transfer doping and hydrogen intercalation. *J. Phys. Appl. Phys.* **43**, 374009 (2010).

35. Virojanadara, C., Zakharov, A. A., Yakimova, R. & Johansson, L. I. Buffer layer free large area bi-layer graphene on SiC(0001). *Surf. Sci.* **604**, L4–L7 (2010).

36. Yazdi, G. R. *et al.* Growth of large area monolayer graphene on 3C-SiC and a comparison with other SiC polytypes. *Carbon* **57**, 477–484 (2013).

37. Hernandez, Y. *et al.* High-yield production of graphene by liquid-phase exfoliation of graphite. *Nat. Nanotechnol.* **3**, 563–568 (2008).

38. Gao, H., Zhu, K., Hu, G. & Xue, C. Large-scale graphene production by ultrasound-assisted exfoliation of natural graphite in supercritical CO2/H2O medium. *Chem. Eng. J.* **308**, 872–879 (2017).

39. Bonaccorso, F. & Sun, Z. Solution processing of graphene, topological insulators and other 2d crystals for ultrafast photonics. *Opt. Mater. Express* **4**, 63–78 (2014).

40. Kim, M., Safron, N. S., Huang, C., Arnold, M. S. & Gopalan, P. Light-Driven Reversible Modulation of Doping in Graphene. *Nano Lett.* **12**, 182–187 (2012).

41. Jin, Z. *et al.* Click Chemistry on Solution-Dispersed Graphene and Monolayer CVD Graphene. *Chem. Mater.* **23**, 3362–3370 (2011).

42. Lomeda, J. R., Doyle, C. D., Kosynkin, D. V., Hwang, W.-F. & Tour, J. M. Diazonium Functionalization of Surfactant-Wrapped Chemically Converted Graphene Sheets. *J. Am. Chem. Soc.* **130**, 16201–16206 (2008).

43. Delamar, M., Hitmi, R., Pinson, J. & Saveant, J. M. Covalent modification of carbon surfaces by grafting of functionalized aryl radicals produced from electrochemical reduction of diazonium salts. *J. Am. Chem. Soc.* **114**, 5883–5884 (1992).

44. Xia, Z. *et al.* Electrochemical Functionalization of Graphene at the Nanoscale with Self-Assembling Diazonium Salts. *ACS Nano* **10**, 7125–7134 (2016).

45. Liu, L.-H., Lerner, M. M. & Yan, M. Derivitization of Pristine Graphene with Well-Defined Chemical Functionalities. *Nano Lett.* **10**, 3754–3756 (2010).

46. Chua, C. K., Ambrosi, A. & Pumera, M. Introducing dichlorocarbene in graphene. *Chem. Commun.* **48**, 5376–5378 (2012).

47. Sarkar, S., Bekyarova, E., Niyogi, S. & Haddon, R. C. Diels−Alder Chemistry of Graphite and Graphene: Graphene as Diene and Dienophile. *J. Am. Chem. Soc.* **133**, 3324–3327 (2011).

48. Quintana, M. *et al.* Functionalization of Graphene via 1,3-Dipolar Cycloaddition. *ACS Nano* **4**, 3527–3533 (2010).

49. Brodie, B. C. XIII. On the atomic weight of graphite. *Philos. Trans. R. Soc. Lond.* **149**, 249–259 (1859).

50. Staudenmaier, L. Verfahren zur Darstellung der Graphitsäure. *Berichte Dtsch. Chem. Ges.* **31**, 1481–1487 (1898).

51. Hummers, W. S. & Offeman, R. E. Preparation of Graphitic Oxide. *J. Am. Chem. Soc.* **80**, 1339–1339 (1958).

52. Zheng, S., Tu, Q., Urban, J. J., Li, S. & Mi, B. Swelling of Graphene Oxide Membranes in Aqueous Solution: Characterization of Interlayer Spacing and Insight into Water Transport Mechanisms. *ACS Nano* **11**, 6440–6450 (2017).

53. Guo, S., Nishina, Y., Bianco, A. & Ménard-Moyon, C. A Flexible Method for Covalent Double Functionalization of Graphene Oxide. *Angew. Chem.* **n/a**,.

54. Bravo, I. *et al.* One-step reduced/quinone functionalized graphene oxide as reagentless lactate biosensing platform. *Sens. Actuators B Chem.* **267**, 533–541 (2018).

55. Yang, H. *et al.* Covalent functionalization of polydisperse chemically-converted graphene sheets with amine - terminated ionic liquid. *Chem. Commun.* **0**, 3880–3882 (2009).

56. Oh, J. *et al.* Graphene oxide porous paper from amine-functionalized poly(glycidyl methacrylate)/ graphene oxide core-shell microspheres. *J. Mater. Chem.* **20**, 9200–9204 (2010).

57. Bao, H. *et al.* Chitosan-Functionalized Graphene Oxide as a Nanocarrier for Drug and Gene Delivery. *Small* **7**, 1569–1578 (2011).

58. Yang, X. *et al.* Multi-functionalized graphene oxide based anticancer drug -carrier with dual-targeting function and pH-sensitivity. *J. Mater. Chem.* **21**, 3448–3454 (2011).

59. Luo, X. *et al.* Graphene Oxide-Polymer Composite Langmuir Films Constructed by Interfacial Thiol-Ene Photopolymerization. *Nanoscale Res. Lett.* **12**, 99 (2017).

60. Gao, W., Alemany, L. B., Ci, L. & Ajayan, P. M. New insights into the structure and reduction of graphite oxide. *Nat. Chem.* **1**, 403–408 (2009).

61. Kazi, S. N. *et al.* Investigation on the use of graphene oxide as novel surfactant to stabilize weakly charged graphene nanoplatelets. *Nanoscale Res. Lett.* **10**, 212 (2015).

62. Lu, J., Do, I., Fukushima, H., Lee, I. & Drzal, L. T. Stable Aqueous Suspension and Self-Assembly of Graphite Nanoplatelets Coated with Various Polyelectrolytes. *Journal of Nanomaterials* https://www.hindawi.com/journals/jnm/2010/186486/ (2010) doi:10.1155/2010/186486.

63. Zhang, L. *et al.* Size-controlled synthesis of graphene oxide sheets on a large scale using chemical exfoliation. *Carbon* **47**, 3365–3368 (2009).

64. Pan, S. & Aksay, I. A. Factors Controlling the Size of Graphene Oxide Sheets Produced via the Graphite Oxide Route. *ACS Nano* **5**, 4073–4083 (2011).

65. Gonçalves, G. *et al.* Breakdown into nanoscale of graphene oxide: Confined hot spot atomic reduction and fragmentation. *Sci. Rep.* **4**, 1–8 (2014).

66. Chen, J. *et al.* Size distribution-controlled preparation of graphene oxide nanosheets with different C/O ratios. *Mater. Chem. Phys.* **139**, 8–11 (2013).

67. Paredes, J. I., Villar-Rodil, S., Martínez-Alonso, A. & Tascón, J. M. D. Graphene oxide dispersions in organic solvents. *Langmuir ACS J. Surf. Colloids* **24**, 10560–10564 (2008).

68. Li, W. *et al.* Simultaneous surface functionalization and reduction of graphene oxide with octadecylamine for electrically conductive polystyrene composites. *Carbon* **49**, 4724–4730 (2011).

69. Bourlinos, A. B. *et al.* Graphite Oxide: Chemical Reduction to Graphite and Surface Modification with Primary Aliphatic Amines and Amino Acids. *Langmuir* **19**, 6050–6055 (2003).

70. Compton, O. C., Dikin, D. A., Putz, K. W., Brinson, L. C. & Nguyen, S. T. Electrically Conductive “Alkylated” Graphene Paper via Chemical Reduction of Amine-Functionalized Graphene Oxide Paper. *Adv. Mater.* **22**, 892–896 (2010).

71. Wang, Z. *et al.* Enhancing lithium–sulphur battery performance by strongly binding the discharge products on amino-functionalized reduced graphene oxide. *Nat. Commun.* **5**, 1–8 (2014).

72. Xu, L. Q., Yang, W. J., Neoh, K.-G., Kang, E.-T. & Fu, G. D. Dopamine-Induced Reduction and Functionalization of Graphene Oxide Nanosheets. *Macromolecules* **43**, 8336–8339 (2010).

73. Sinitskii, A. *et al.* Kinetics of Diazonium Functionalization of Chemically Converted Graphene Nanoribbons. *ACS Nano* **4**, 1949–1954 (2010).

74. Gao, W. *et al.* Engineered Graphite Oxide Materials for Application in Water Purification. *ACS Appl. Mater. Interfaces* **3**, 1821–1826 (2011).

75. Paulus, G. L. C., Wang, Q. H. & Strano, M. S. Covalent Electron Transfer Chemistry of Graphene with Diazonium Salts. *Acc. Chem. Res.* **46**, 160–170 (2013).

76. Fang, M., Wang, K., Lu, H., Yang, Y. & Nutt, S. Covalent polymer functionalization of graphene nanosheets and mechanical properties of composites. *J. Mater. Chem.* **19**, 7098–7105 (2009).

77. Jia, Z. & Wang, Y. Covalently crosslinked graphene oxide membranes by esterification reactions for ions separation. *J. Mater. Chem. A* **3**, 4405–4412 (2015).

78. Salavagione, H. J., Gómez, M. A. & Martínez, G. Polymeric Modification of Graphene through Esterification of Graphite Oxide and Poly(vinyl alcohol). *Macromolecules* **42**, 6331–6334 (2009).

79. Stankovich, S., Piner, R. D., Nguyen, S. T. & Ruoff, R. S. Synthesis and exfoliation of isocyanate-treated graphene oxide nanoplatelets. *Carbon* **44**, 3342–3347 (2006).

80. He, H. & Gao, C. General Approach to Individually Dispersed, Highly Soluble, and Conductive Graphene Nanosheets Functionalized by Nitrene Chemistry. *Chem. Mater.* **22**, 5054–5064 (2010).

81. Hsiao, M.-C. *et al.* Preparation of Covalently Functionalized Graphene Using Residual Oxygen-Containing Functional Groups. *ACS Appl. Mater. Interfaces* **2**, 3092–3099 (2010).

82. Vadukumpully, S., Gupta, J., Zhang, Y., Qin Xu, G. & Valiyaveettil, S. Functionalization of surfactant wrapped graphene nanosheets with alkylazides for enhanced dispersibility. *Nanoscale* **3**, 303–308 (2011).

83. Georgakilas, V. *et al.* Organic functionalisation of graphenes. *Chem. Commun.* **46**, 1766–1768 (2010).

84. Álvarez, P. *et al.* Tuning graphene properties by a multi-step thermal reduction process. *Carbon* **90**, 160–163 (2015).

85. Schniepp, H. C. *et al.* Functionalized Single Graphene Sheets Derived from Splitting Graphite Oxide. *J. Phys. Chem. B* **110**, 8535–8539 (2006).

86. Jo, J. *et al.* Facile synthesis of reduced graphene oxide by modified Hummer's method as anode material for Li-, Na- and K-ion secondary batteries. *R. Soc. Open Sci.* **6**, 181978.

87. Li, X. *et al.* Simultaneous Nitrogen Doping and Reduction of Graphene Oxide. *J. Am. Chem. Soc.* **131**, 15939–15944 (2009).

88. Ganguly, A., Sharma, S., Papakonstantinou, P. & Hamilton, J. Probing the Thermal Deoxygenation of Graphene Oxide Using High-Resolution In Situ X-ray-Based Spectroscopies. *J. Phys. Chem. C* **115**, 17009–17019 (2011).

89. Wang, Y. *et al.* Reduced graphene oxide film with record-high conductivity and mobility. *Mater. Today* **21**, 186–192 (2018).

90. Chen, C.-M. *et al.* Annealing a graphene oxide film to produce a free standing high conductive graphene film. *Carbon* **50**, 659–667 (2012).

91. Wang, X., Zhi, L. & Müllen, K. Transparent, Conductive Graphene Electrodes for Dye-Sensitized Solar Cells. *Nano Lett.* **8**, 323–327 (2008).

92. Becerril, H. A. *et al.* Evaluation of Solution-Processed Reduced Graphene Oxide Films as Transparent Conductors. *ACS Nano* **2**, 463–470 (2008).

93. Vallés, C., David Núñez, J., Benito, A. M. & Maser, W. K. Flexible conductive graphene paper obtained by direct and gentle annealing of graphene oxide paper. *Carbon* **50**, 835–844 (2012).

94. Zhu, Y. *et al.* Microwave assisted exfoliation and reduction of graphite oxide for ultracapacitors. *Carbon* **48**, 2118–2122 (2010).

95. Voiry, D. *et al.* High-quality graphene via microwave reduction of solution-exfoliated graphene oxide. *Science* **353**, 1413–1416 (2016).

96. Mohandoss, M., Gupta, S. S., Nelleri, A., Pradeep, T. & Maliyekkal, S. M. Solar mediated reduction of graphene oxide. *RSC Adv.* **7**, 957–963 (2017).

97. Matsumoto, Y. *et al.* Simple Photoreduction of Graphene Oxide Nanosheet under Mild Conditions. *ACS Appl. Mater. Interfaces* **2**, 3461–3466 (2010).

98. Gengler, R. Y. N. *et al.* Revealing the ultrafast process behind the photoreduction of graphene oxide. *Nat. Commun.* **4**, 1–5 (2013).

99. Han, D.-D. *et al.* Bioinspired Graphene Actuators Prepared by Unilateral UV Irradiation of Graphene Oxide Papers. *Adv. Funct. Mater.* **25**, 4548–4557 (2015).

100. Zhou, Y., Bao, Q., Tang, L. A. L., Zhong, Y. & Loh, K. P. Hydrothermal Dehydration for the "Green" Reduction of Exfoliated Graphene Oxide to Graphene and Demonstration of Tunable Optical Limiting Properties. *Chem. Mater.* **21**, 2950–2956 (2009).

101. Ahmad, M. S., He, H. & Nishina, Y. Selective Hydrogenation by Carbocatalyst: The Role of Radicals. *Org. Lett.* **21**, 8164–8168 (2019).

102. Shao, Y., Wang, J., Engelhard, M., Wang, C. & Lin, Y. Facile and controllable electrochemical reduction of graphene oxide and its applications. *J. Mater. Chem.* **20**, 743–748 (2010).

103. Wang, Z., Zhou, X., Zhang, J., Boey, F. & Zhang, H. Direct Electrochemical Reduction of Single-Layer Graphene Oxide and Subsequent Functionalization with Glucose Oxidase. *J. Phys. Chem. C* **113**, 14071–14075 (2009).

104. Stankovich, S. *et al.* Synthesis of graphene-based nanosheets via chemical reduction of exfoliated graphite oxide. *Carbon* **45**, 1558–1565 (2007).

105. Pham, V. H. *et al.* One-step synthesis of superior dispersion of chemically converted graphene in organic solvents. *Chem. Commun.* **46**, 4375–4377 (2010).

106. Wang, H., Robinson, J. T., Li, X. & Dai, H. Solvothermal Reduction of Chemically Exfoliated Graphene Sheets. *J. Am. Chem. Soc.* **131**, 9910–9911 (2009).

107. Wang, G. *et al.* Facile Synthesis and Characterization of Graphene Nanosheets. *J. Phys. Chem. C* **112**, 8192–8195 (2008).

108. Yang, Z., Zheng, Q., Qiu, H., Li, J. & Yang, J. A simple method for the reduction of graphene oxide by sodium borohydride with CaCl2 as a catalyst. *New Carbon Mater.* **30**, 41–47 (2015).

109. Chua, C. K. & Pumera, M. Reduction of graphene oxide with substituted borohydrides. *J. Mater. Chem. A* **1**, 1892–1898 (2013).

110. Chen, W., Yan, L. & Bangal, P. R. Chemical Reduction of Graphene Oxide to Graphene by Sulfur-Containing Compounds. *J. Phys. Chem. C* **114**, 19885–19890 (2010).

111. Fernández-Merino, M. J. *et al.* Vitamin C Is an Ideal Substitute for Hydrazine in the Reduction of Graphene Oxide Suspensions. *J. Phys. Chem. C* **114**, 6426–6432 (2010).

112. Gao, J. *et al.* Environment-Friendly Method To Produce Graphene That Employs Vitamin C and Amino Acid. *Chem. Mater.* **22**, 2213–2218 (2010).

113. Zhang, L. *et al.* Facile synthesis of iron oxides/reduced graphene oxide composites: application for electromagnetic wave absorption at high temperature. *Sci. Rep.* **5**, 1–9 (2015).

114. Zhou, T. *et al.* A simple and efficient method to prepare graphene by reduction of graphite oxide with sodium hydrosulfite. *Nanotechnology* **22**, 045704 (2010).

115. Chen, C., Kong, W., Duan, H.-M. & Zhang, J. Theoretical simulation of reduction mechanism of graphene oxide in sodium hydroxide solution. *Phys. Chem. Chem. Phys.* **16**, 12858–12864 (2014).

116. Chen, D., Li, L. & Guo, L. An environment-friendly preparation of reduced graphene oxide nanosheets via amino acid. *Nanotechnology* **22**, 325601 (2011).

117. Dreyer, D. R., Murali, S., Zhu, Y., Ruoff, R. S. & Bielawski, C. W. Reduction of graphite oxide using alcohols. *J. Mater. Chem.* **21**, 3443–3447 (2011).

118. Akhavan, O., Ghaderi, E., Aghayee, S., Fereydooni, Y. & Talebi, A. The use of a glucose-reduced graphene oxide suspension for photothermal cancer therapy. *J. Mater. Chem.* **22**, 13773–13781 (2012).

119. Moon, I. K., Lee, J., Ruoff, R. S. & Lee, H. Reduced graphene oxide by chemical graphitization. *Nat. Commun.* **1**, 1–6 (2010).

120. Chen, M. *et al.* Sn Powder as Reducing Agents and SnO2 Precursors for the Synthesis of SnO2-Reduced Graphene Oxide Hybrid Nanoparticles. *ACS Appl. Mater. Interfaces* **5**, 13333–13339 (2013).

121. Liu, P., Huang, Y. & Wang, L. A facile synthesis of reduced graphene oxide with Zn powder under acidic condition. *Mater. Lett.* **91**, 125–128 (2013).

122. Fan, Z. *et al.* An environmentally friendly and efficient route for the reduction of graphene oxide by aluminum powder. *Carbon* **48**, 1686–1689 (2010).

123. Liu, N. *et al.* One-Step Ionic-Liquid-Assisted Electrochemical Synthesis of Ionic-Liquid-Functionalized Graphene Sheets Directly from Graphite. *Adv. Funct. Mater.* **18**, 1518–1525 (2018).

124. Parvez, K. *et al.* Exfoliation of Graphite into Graphene in Aqueous Solutions of Inorganic Salts. *J. Am. Chem. Soc.* **136**, 6083–6091 (2014).

125. Pei, S., Wei, Q., Huang, K., Cheng, H.-M. & Ren, W. Green synthesis of graphene oxide by seconds timescale water electrolytic oxidation. *Nat. Commun.* **9**, 145 (2018).

126. *Philosophical Transactions of the Royal Society of London*. (W. Bowyer and J. Nichols for Lockyer Davis, printer to the Royal Society, 1800).

127. Placke, T., Kloepsch, R., Dühnen, S. & Winter, M. Lithium ion, lithium metal, and alternative rechargeable battery technologies: the odyssey for high energy density. *J. Solid State Electrochem.* **21**, 1939–1964 (2017).

128. Planté, G. *The storage of electrical energy, and researches in the effects created by currents combining quantity with high tension*. (London, Whittaker, 1887).

129. Planté, G. Nouvelle Pile Secondaire d'une Grande Puissance. *Comptes Rendus Acad Sci* (1860).

130. Sinsteden, W. J. Versuche über den Grad der Continuität und die Stärke des Stroms eines grössern magneto-elektrischen Rotations. *Ann Phys Chem* **92**, 1–21 (1854).

131. Gautherot, N. Sur le galvanisme. *Ann Chim* **39**, 203–210 (1801).

132. Arfwedson, J. A. Untersuchung einiger bei der Eisen-Grube von Utö vorkommenden Fossilien und von einem darin gefundenen neuen feuerfesten Alkali. *J Chem Phys* **22**, 93–117 (1818).

133. Berzelius, J. J. Ein neues mineralisches Alkali und ein neues Metall. *J Chem Phys* **21**, 44–48 (1817).

134. Lewis, G. N. & Keyes, F. G. THE POTENTIAL OF THE LITHIUM ELECTRODE. *J. Am. Chem. Soc.* **35**, 340–344 (1913).

135. Harris, W. S. Electrochemical Studies in Cyclic Esters. *PhD Thesis Univ. Calif. Berkeley* (1958).

136. Yung-Fang Yu Yao & Kummer, J. T. Ion exchange properties of and rates of ionic diffusion in beta-alumina. *J. Inorg. Nucl. Chem.* **29**, 2453–2475 (1967).

137. Kummer, J. T. & Neill, W. Thermo-Electric Generator. *US Pat. No* 3,458,356 (1969).

138. Newman, J. Transport in Electrolytic Solutions. *Adv Electrochem Electrochem Eng* **5**, 87–135 (1967).

139. Whittingham, M. S. Chemistry of intercalation compounds: Metal guests in chalcogenide hosts. *Prog. Solid State Chem.* **12**, 41–99 (1978).

140. Rüdorff, W. *Chimia* **19**, 489 (1965).

141. Bichon, J., Danot, M. & Rouxel, J. Systematique Structurale Pour Les Series d'intercalaires Mxtis2 (M= Li, Na, K, Rb, Cs). *Comptes Rendus Acad Sci Ser C Sci Chim* **276**, 1283– 1286 (1973).

142. Whittingham, M. S. & Gamble, F. R. The lithium intercalates of the transition metal dichalcogenides. *Mater. Res. Bull.* **10**, 363–371 (1975).

143. Whittingham, M. S. Electrointercalation in transition-metal disulphides. *J. Chem. Soc. Chem. Commun.* 328–329 (1974) doi:10.1039/C39740000328.

144. Whittingham, M. S. Electrical Energy Storage and Intercalation Chemistry. *Science* **192**, 1126–1127 (1976).

145. Whittingham, M. S. Batterie à Base de Chalcogénures. *Belg. Pat. No* 819672 (1975).

146. Whittingham, M. S. History, Evolution, and Future Status of Energy Storage. *Proc. IEEE* **100**, 1518–1534 (2012).

147. Armand, M. & Touzain, P. Graphite Intercalation Compounds as Cathode Materials. *Mater Sci Eng* **31**, 319–329 (1977).

148. Rüdorff, W. & Hofmann, U. Über Graphitsalze. *Z Anorg Allg Chem* **238**, 1–50 (1938).

149. Schafhaeutl, C. Über die Verbindungen des Kohlenstoffes mit Silicium, Eisen und anderen Metallen, welche die verschiedenen Gallungen von Roheisen, Stahl und Schmiedeeisen bilden. *J Prakt Chem* **3**, 129 (1840).

150. Fredenhagen, K. & Cadenbach, G. Die Bindung von Kalium durch Kohlenstoff. *Z Anorg Allg Chem* **158**, 249 (1926).

151. Goodenough, J. B. & Mizushima, K. Fast Ion Conductors. *US Pat. No* 4,357,215 (1982).

152. Mizushima, K., Jones, P. C., Wiseman, P. J. & Goodenough, J. B. LixCoO2 (0. *Mater. Res. Bull.* **15**, 783–789 (1980).

153. Yoshino, A., Snechida, K. & Nakajima, T. Secondary Battery. *US Pat. No* 4,668,595 (1987).

154. Yoshino, A., Snechida, K. & Nakajima, T. *Jpn. Pat. No* 1989293 (1985).

155. Yoshino, A. The Birth of the Lithium-Ion Battery. *Angew Chem Int Ed* **51**, 5798– 5800 (2012).

156. Nishi, Y. The Development of Lithium Ion Secondary Batteries. *Chem Rec* **1**, 406– 413 (2001).

157. Peled, E. The Electrochemical Behavior of Alkali and Alkaline Earth Metals in Nonaqueous Battery SystemsThe Solid Electrolyte Interphase Model. *J Electrochem Soc* **126**, 2047–2051 (1979).

158. Fong, R., Sacken, U. & Dahn, J. R. Studies of Lithium Intercalation into Carbons Using Nonaqueous Electrochemical Cells. *J Electrochem Soc* **137**, 2009–2013 (1990).

159. Nitta, N., Wu, F., Lee, J. T. & Yushin, G. Li-ion battery materials: present and future. *Mater. Today* **18**, 252–264 (2015).

160. Raccichini, R., Varzi, A., Passerini, S. & Scrosati, B. The role of graphene for electrochemical energy storage. *Nat. Mater.* **14**, 271–279 (2015).

161. Wang, G., Shen, X., Yao, J. & Park, J. Graphene nanosheets for enhanced lithium storage in lithium ion batteries. *Carbon* **47**, 2049–2053 (2009).

162. Cheng, Q. *et al.* Graphene-Like-Graphite as Fast-Chargeable and High-Capacity Anode Materials for Lithium Ion Batteries. *Sci. Rep.* **7**, 1–14 (2017).

163. Zhan, Y. *et al.* Iodine doped graphene as anode material for lithium ion battery. *Carbon* **94**, 1–8 (2015).

164. Yun, Y. S. *et al.* Effects of sulfur doping on graphene-based nanosheets for use as anode materials in lithium-ion batteries. *J. Power Sources* **262**, 79–85 (2014).

165. Wu, F. *et al.* Facile Synthesis of Boron-Doped rGO as Cathode Material for High Energy Li–O2 Batteries. *ACS Appl. Mater. Interfaces* **8**, 23635–23645 (2016).

166. Du, M. *et al.* Synthesis of nitrogen-doped reduced graphene oxide directly from nitrogen-doped graphene oxide as a high-performance lithium ion battery anode. *RSC Adv.* **4**, 42412–42417 (2014).

167. Shi, Y., Wen, L., Li, F. & Cheng, H.-M. Nanosized Li4Ti5O12/graphene hybrid materials with low polarization for high rate lithium ion batteries. *J. Power Sources* **196**, 8610–8617 (2011).

168. Zhu, N. *et al.* Graphene as a conductive additive to enhance the high-rate capabilities of electrospun Li4Ti5O12 for lithium-ion batteries. *Electrochimica Acta* **55**, 5813–5818 (2010).

169. Xiang, H. *et al.* Graphene/nanosized silicon composites for lithium battery anodes with improved cycling stability. *Carbon* **49**, 1787–1796 (2011).

170. Ha, S. H., Jeong, Y. S. & Lee, Y. J. Free Standing Reduced Graphene Oxide Film Cathodes for Lithium Ion Batteries. *ACS Appl. Mater. Interfaces* **5**, 12295–12303 (2013).

171. Li, Y., Sheng, K., Yuan, W. & Shi, G. A high-performance flexible fibre-shaped electrochemical capacitor based on electrochemically reduced graphene oxide. *Chem. Commun.* **49**, 291–293 (2013).

172. Aravindan, V., Mhamane, D., Ling, W. C., Ogale, S. & Madhavi, S. Nonaqueous Lithium-Ion Capacitors with High Energy Densities using Trigol-Reduced Graphene Oxide Nanosheets as Cathode-Active Material. *ChemSusChem* **6**, 2240–2244 (2013).

173. Tang, R. *et al.* How a very trace amount of graphene additive works for constructing an efficient conductive network in LiCoO2-based lithium-ion batteries. *Carbon* **103**, 356–362 (2016).

174. Wang, H. *et al.* Graphene-Wrapped Sulfur Particles as a Rechargeable Lithium–Sulfur Battery Cathode Material with High Capacity and Cycling Stability. *Nano Lett.* **11**, 2644–2647 (2011).

CHAPTER 2

Non-destructive, Uniform, and Scalable Electrochemical Functionalization and Exfoliation of Graphite

ABSTRACT: Exfoliation of graphite through functionalization is a promising technique to produce two-dimensional (2D) nanocarbons on a large scale. Due to the high stability of graphite, a conventional functionalization of graphite has been performed in harsh conditions, such as in concentrated sulfuric acid. Therefore, environmental and safety have been problems for scaling up the operation. In contrast, the electrochemical functionalization of a graphite electrode has recently attracted considerable attention because it does not require oxidants or sulfuric acid. However, 2D carbons produced through the existing electrochemical method are generally lacking in quality, due to the non-uniform destruction of the intermediately functionalized graphite. This paper reports a method for the non-destructive functionalization of graphite using HBF_4 diluted by water or methanol as an electrolyte. It is confirmed that the choice of solvents and electrochemical conditions enabled fine control over the functionalization degree and the type of functional groups on 2D carbons. Compared to chemically generated 2D carbons, the electrochemically generated 2D carbon exhibits similar or better physical and chemical properties when used in lithium-ion battery electrodes and water purification membranes. This electrochemical method is also applicable to a continuous flow system, thus promising the mass production of 2D carbons for future industrialization.

I. INTRODUCTION

With their excellent properties, sustainability, and economic benefits, nanocarbon materials have gained wide attention. Among nanocarbons, graphene, a two-dimensional (2D) honeycomb lattice of sp^2 carbon with single-atom thickness, became one of the most exciting research topics since its isolation and characterization by Geim and Novoselov in 2004.[1] The unique properties of graphene include excellent electrical conductivity, [2–4] high flexibility,[5] and large surface area.[6] To exploit such properties in specific applications, however, it is necessary to improve the production methods of graphene (top-down approach[1,7,8-12] and bottom-up approach[13–15]) and the modulation of its structure (atom doping,[8,16,17] covalent functionalization,[18,19] and non-covalent functionalization[20,21]). Current methods to prepare graphene all present several disadvantages in terms of e.g. scalability, cost, homogeneity, and structural controllability. These drawbacks have restricted the mass production and practical uses of graphene.

In the last few years, the electrochemical method has become attractive for producing and functionalizing graphene as an easy, fast, safe, scalable, and green procedure.[22–29] Two synthesis pathways have been considered: electrochemical intercalation-exfoliation[22] and electrochemical intercalation-functionalization.[30] The former one is based on gas generation between graphite layers through the intercalation and decomposition of the intercalant molecules. While less defective graphene is generated through this method, the production of single-layer graphene is difficult due to the uncontrollable gas generation and the destruction of graphite framework. The latter approach also uses intercalation to expand the interlayer distance, and afterwards the intercalant directly reacts with the graphite layers. The main characteristic of this method is that the sp^2 honeycomb structure of graphene is converted into sp^3 carbons before re-aggregation occurs. Also, the mode and degree of functionalization can be finely controlled by tuning the electrochemical conditions. Therefore, we focused on the electrochemical intercalation-functionalization technique in this research to obtain homogeneous functionalized graphene (defective) while avoiding the destruction of the graphite framework.

Generally, there is a competition between the intercalation and the decomposition of intercalant into gas, which destroys the graphite framework before its complete functionalization. Aryldiazonium salts are well-known electrochemically active reagents generating aryl radicals and N_2 gas.[31–34] They have been applied to the electrochemical intercalation-functionalization method, but the inhomogeneous destruction of graphite still occurs to generate a multi-layered product.[30] To solve this problem, two-step electrochemical oxidations of graphite was investigated using H_2SO_4 electrolyte.[27,28] The initial step consists of forming a homogeneous graphite intercalated compound (GIC) in highly concentrated H_2SO_4 electrolyte, and the second step consists of oxidation of GIC in low-concentration H_2SO_4 by active oxygen species generated from water. The material obtained through this method shows improved homogeneity, morphology, and oxidation degree. However, such a two-step reaction cannot be applied in a continuous system or on an industrial scale (which requires one-step and simple procedures). Inspired by this two-step method, we tried to find an optimum system that can separate the intercalation step and functionalization step in a one-pot procedure while suppressing gas generation that destroys the graphite framework.

Herein, the one-pot electrochemical intercalation-functionalization of graphite was achieved using HBF_4 diluted by water or methanol as an electrolyte. This results in the formation of electrochemical graphene oxide (EGO) with a yield >99% due to the limited gas generation, avoiding the destruction of the graphite framework, thus enabling uniform functionalization. More interestingly, our system showed two reaction modes: conventional electrolysis in the electrolyte (within the first 5 min of reaction) and reaction outside the electrolyte by capillary effect (after 5 to 60 min depending on the length of the graphite electrode). After the electrochemical treatment, only simple washing, mixing, and sonication steps were necessary to purify and exfoliate the product to single-layer EGO. The EGOs prepared in water (EGO^W) and methanol (EGO^M) have 49.0 wt% and 43.9 wt% oxygen, respectively, as determined by CHN elemental analysis. These values are similar to chemical graphene oxide prepared by improved Hummers' method (CGO; 50.2 wt% O),[35] but larger than that prepared in a conventional aqueous H_2SO_4 system (EGO^S; 28.5 wt% O),[28] suggesting uniform and complete oxidation in the HBF_4 system. Despite the relatively high oxygen contents of EGO^W and EGO^M, their oxidation properties were weaker than those of CGO, with the respective conversion of benzyl alcohol to benzaldehyde being 41%, 25%, and 60%. Since the EGOs can be completely exfoliated to a single layer, we prepared them into a thin membrane for use in water purification, where up to 90% of methyl orange was removed. Thermally reduced graphene oxides (tEGOs and tCGO, respectively) were also shown to have high electrical conductivity of ~40000 S/m. Thus, the tEGOs were evaluated in the anode of lithium-ion batteries (LIBs) with a capacity of 195 mAh g^{-1} at 20C, which represents an improvement of 572% compared to that of the original graphite.

II. RESULTS AND DISCUSSION

I.1. EGO synthesis mechanistic study

EGO synthesis was conducted using a graphite foil of 5 cm × 4 cm × 20 μm. A two-electrode system was employed using platinum wire as a cathode, graphite foil as an anode, and a solution of HBF_4/water or HBF_4/methanol as an electrolyte (Figure 1a). The electrochemical intercalation-functionalization was conducted at a constant current density (180 mA cm^{-2}) for 6 min with a cut-off voltage of 14 V. During this process, the graphite foil became 400 times thicker (from 20 μm to 8 mm) without destruction (Figure 1b), which is different from previously reported EGOs. In the aqueous H_2SO_4 electrolyte system, however, destruction of graphite occurred.[27,28] Afterward, the expanded EGO was collected by filtration and easily washed until the pH became 7. The neutralized product was then dispersed in water by sonication for 30 min to generate single-layer EGO. A spongy EGO was obtained by freeze-drying for 48 h. As prepared EGO contained a small

Table 1. XPS atomic quantification.

Sample	**GO**			**Hydrazine reduced**			**Thermally reduced**		
	CGO	**EGOW-42%**	**EGOM-20%**	**hyCGO**	**hyEGOW**	**hyEGOM**	**tCGO**	**tEGOW**	**tEGOM**
C (at.%)	63.4	69.6	68.1	84.4	89.6	79.9	90.7	90.9	91.6
O (at.%)	34.8	28.4	29.4	15.6	10.4	20.1	9.3	9.1	8.4
S (at.%)	1.8	-	-	-	-	-	-	-	-
F (at.%)	-	2.0	2.5	-	-	-	-	-	-

amount of fluorine atoms which were derived from BF_4^- decomposition and can be removed by general reduction procedure of GO, such as heating (Table 1).

We next investigated the different phenomena during the electrochemical treatments in various electrolyte systems. The electrical potential drives the action of ionic species in the electrolyte, and therefore linear sweep voltammetry (LSV) was performed under the same conditions used for EGO^W synthesis (electrolyte: 20% HBF_4 and 80% water) and EGO^M synthesis (electrolyte: 20% HBF_4, 30% water, and 50% methanol), using a graphite foil as working electrode, a platinum wire as a counter electrode, and saturated calomel electrode (SCE) as reference electrode. For comparison, a conventional aqueous H_2SO_4 system (20% H_2SO_4 and 80% water) was also investigated by LSV in order to understand the difference between BF_4^- and HSO_4^- intercalant (Figure 2aiii). The measured LSV curve for EGO^W (Figure 2ai) indicated four consecutive reaction steps: the electrolyte polarization from 0.3 to 1.6 V, the intercalation of hydrated BF_4^- at 1.7 V, the functionalization by active oxygen species generated from water electrolysis inside the graphite from 2.2 to 2.7 V, and the gas generation from 2.7 V. For EGO^M (Figure 2aii), the polarization and intercalation potentials were the same as with EGO^W, yet the functionalization potential range was widened to 2.0–3.0 V, suppressing the gas generation reaction till 3.0 V. In contrast, in the case of H_2SO_4 (Figure 2aiii), the LSV measurement showed only 3 consecutive reactions: the electrolyte polarization from 0.5 to 1.5 V, the intercalation of hydrated HSO_4^- at 1.6 V, and the gas generation from 2.0 V. The absence of a clear signal for functionalization reaction reflects the fact that the decomposition of HSO_4^- into SO_x gas competes with its intercalation, which leads to the destruction of graphite framework before its complete oxidation. The different LSV results also correspond to the visible behavior. The graphite expanded in the HBF_4 electrolyte system, while the H_2SO_4 electrolyte system resulted in the exfoliation and destruction of the graphite framework (Figure 1b, video S1 and S2).

To gain deeper insights into the electrochemical process, EGO formation was observed under an optical microscope using highly oriented pyrolytic graphite (HOPG) as an anode, platinum wire as a cathode, and an aqueous HBF_4 solution as the electrolyte. As the intercalation proceeded, a rainbow-colored band moved successively, suggesting the progress of intercalation (Figure 2b, video S3 and S4), while the same experiment in aqueous H_2SO_4 resulted in a destructive reaction process.

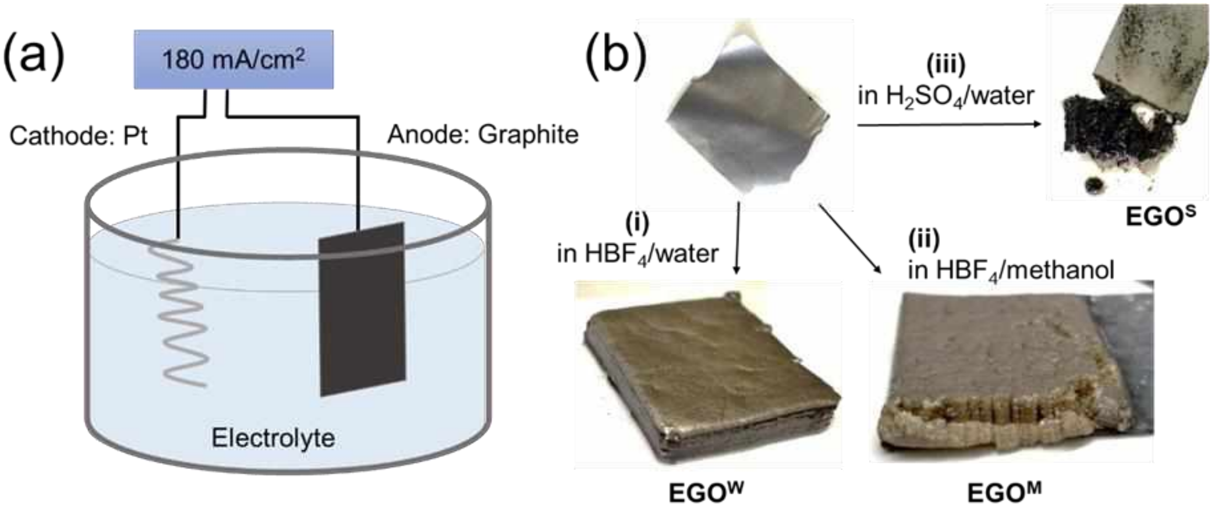

Figure 1. Electrochemical synthesis of graphene oxide. (a) Schematic illustration of the EGO synthesis system, (b) visual change of graphite into (i) EGO^{W} by HBF$_4$/water, (ii) EGO^{M} by HBF$_4$/methanol, and (iii) EGO^{S} by H$_2$SO$_4$/water.

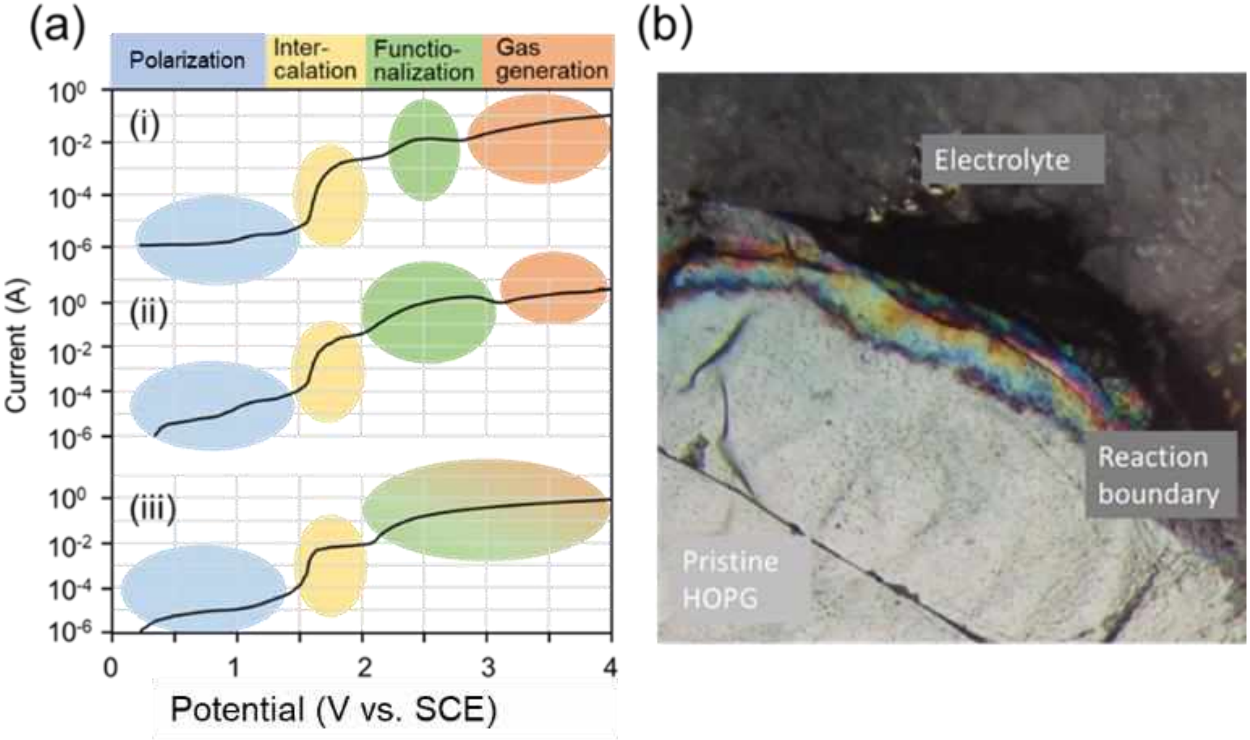

Figure 2. (a) LSV analysis under the synthesis conditions of (i) EGO^{W}, (ii) EGO^{M}, and (iii) EGO^{S}. (b) Optical microscope observation during the electrochemical treatment of HOPG.

The intercalation process was confirmed by the X-ray diffraction (XRD) analysis of graphite foil electrochemically treated with aqueous HBF_4 electrolyte, showing typical patterns of GIC (Figure 3).[25] In contrast, such GIC patterns were not observed when the H2SO4/water electrolyte was used. The HBF_4 system allows EGO synthesis via non-destructive intercalation, which led to the unexpected phenomenon of graphite foil oxidation outside the electrolyte. Initially, intercalation and functionalization occurred from 0 to 5 min. The graphite in the electrolyte was quickly intercalated and consequently expanded (Figure 4, video S5). Finally, the expansion progressed to the top of the graphite foil that was outside the electrolyte. This phenomenon was derived from the capillary absorption of electrolyte by the graphite layers upon their intercalation and functionalization, and it was not observed in the H_2SO_4 electrolyte system.

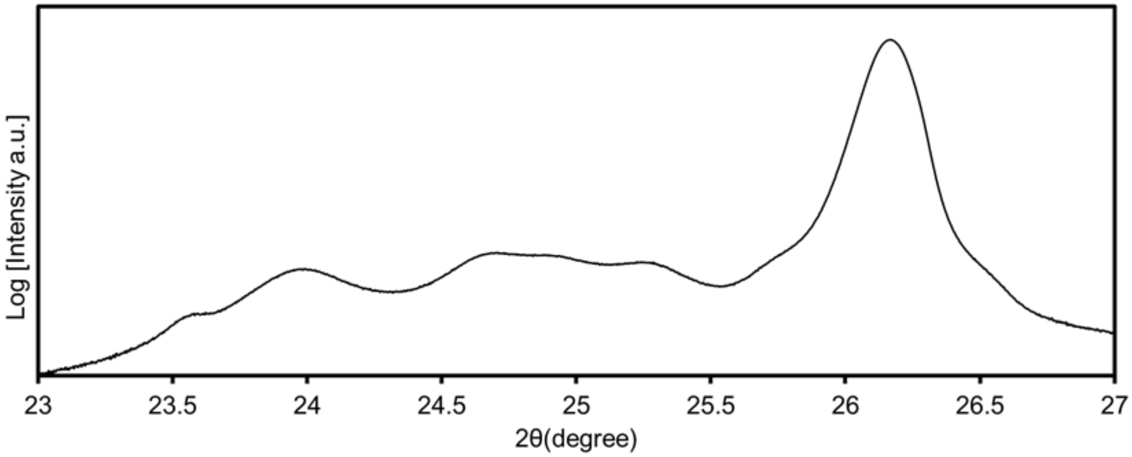

Figure 3. Graphite intercalated by HBF_4 after 3 min at 0.7 A.

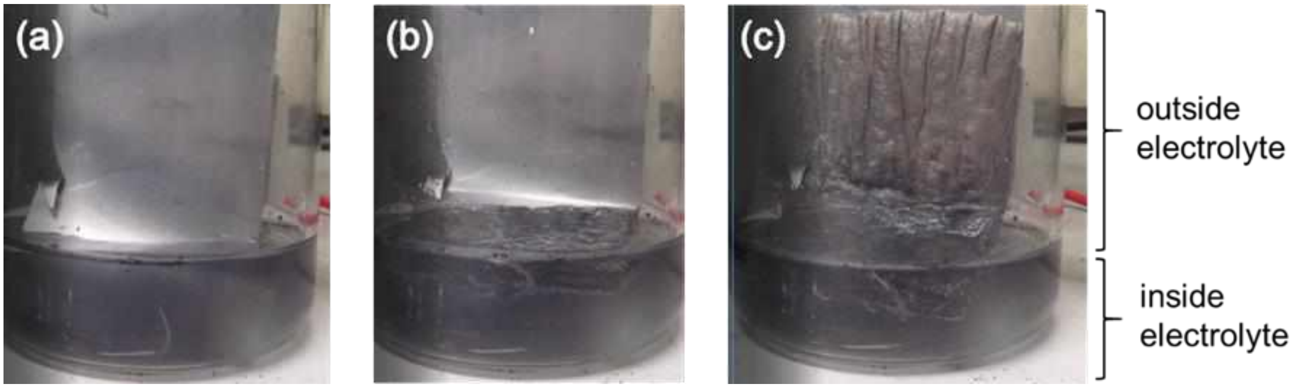

Figure 4. Electrochemical synthesis of EGO^W: (a) pristine graphite foil before electrochemical treatment; (b) within 5 min of electrochemical treatment, only the part of graphite inside the electrolyte expanded and; (c) after 5 min, the part of graphite foil outside the electrolyte also expanded by capillary effect.

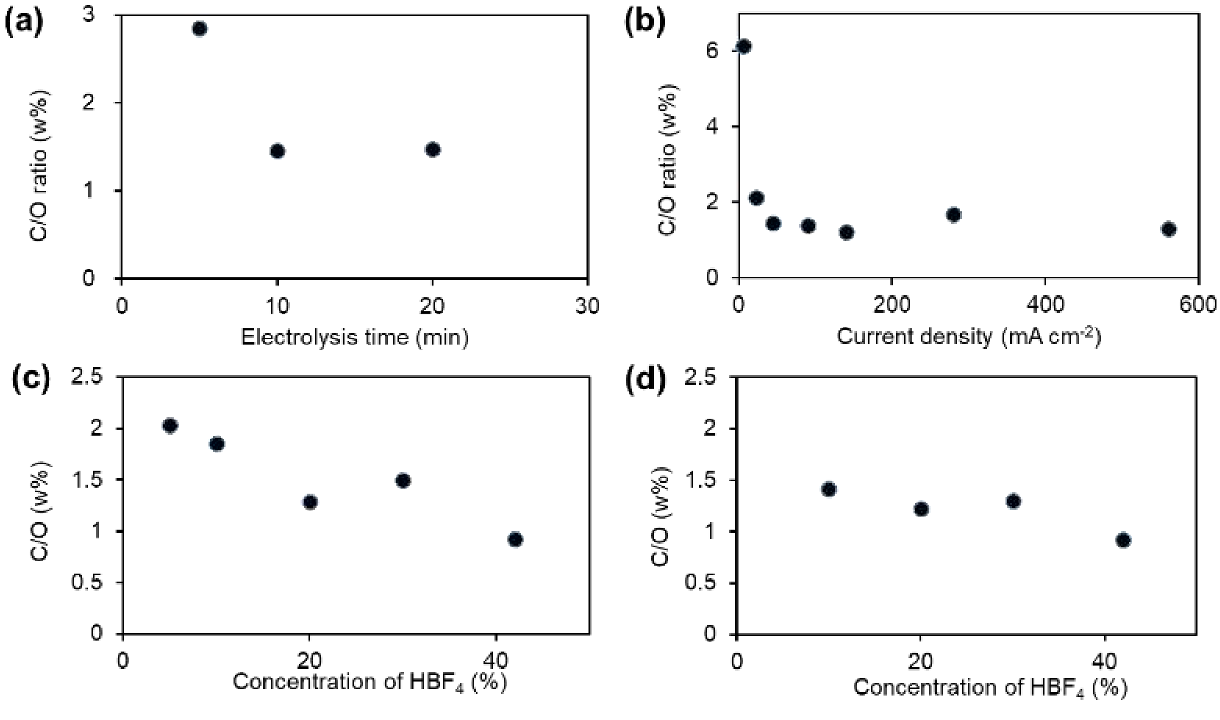

Figure 5. Optimization of the synthesis condition in terms of (a) reaction time, (b) current density, and (c) electrolyte concentration for EGO^W. (d) Concentration dependence for EGO^M.

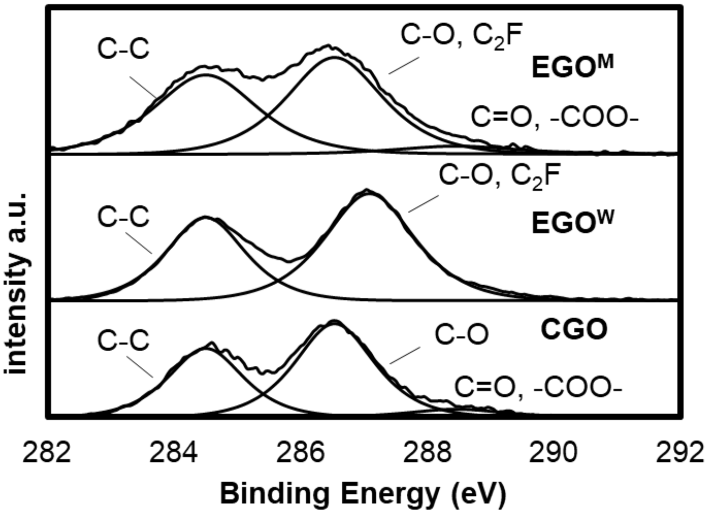

Figure 6. XPS C1s analysis of chemical graphene oxide (CGO), Electrochemical graphene oxide in water (EGO^W), Electrochemical graphene oxide in methanol (EGO^M).

All these results demonstrate the superiority of BF_4^- over HSO_4^- as an intercalatant owing to its superior stability allowing the graphite framework to be intercalated, functionalized without destruction.

II.2. EGO synthesis optimization

After understanding the plausible pathways of EGO synthesis, we next tried to optimize the electrochemical conditions to finely tune the EGO structure and properties. As clarified by the LSV analysis (Figure 5a), electrochemical reactions such as intercalation, functionalization, and gas generation can be controlled by the voltage and the amount of charge passed. To evaluate the functionalization degree of EGOs prepared under different electrochemical conditions, CHN elemental analysis was conducted for each sample to calculate the carbon/oxygen (C/O) mass ratios. For EGO^W synthesis at constant current, the C/O mass ratio decreased from 2.85 to 1.46 from 5 to 10 min, while extending the electrochemical treatment did not induce any further oxidation (Figure 5a). During the electrochemical reaction at constant current, the potential increased due to the loss of conductivity when the conductive sp^2 was converted to the insulating sp^3 carbon structure. After 10 min, the voltage increased drastically from 12 to 16 V to indicate completion of the functionalization, which is in good agreement with the C/O mass ratio. Therefore, a cutoff voltage of 14 V can be used as an indicator of the functionalization degree. Next, the effect of current density was investigated. From 6 to 90 mA cm^{-2}, the C/O mass ratio decreased from 6.14 to 1.38. At a higher current density of > 180 mA cm^{-2}, no clear improvement was observed while much heat was generated (Figure 5b), indicating that the graphite foil could not accommodate current densities higher than 180 mA cm^{-2}. In order to speed up the production rate of EGO^{W} with high efficiency, a current density of ca. 180 mA cm^{-2} is recommended. Considering the influence of HBF_4 concentration, the best result was obtained for 42% HBF_4 with a C/O mass ratio of 0.99 (Figure 5c), which is almost the same as that of CGO (0.88). As the water content in the electrolyte increased, the C/O mass ratio also increased. This phenomenon can be explained by the lower amount of intercalated BF4^{-} and more gas generation by water decomposition. A similar tendency was observed for EGO^{M} (Figure 5d), in which the C/O mass ratio decreased as the concentration of HBF_4 was increased. However, at 10% HBF_4, the C/O mass ratio of EGO^{W} was 1.82 while that of EGO^{M} reached only 1.42, suggesting that methanol prevented the gas generation and the destruction of graphite foil to enable uniform and complete functionalization.

The samples discussed in the following sections were prepared using the optimized conditions. For EGO^{W}, 42% HBF_4 and 58% water was the best electrolyte (the sample was labeled as EGO^{W}-42%), and for EGO^{M} it was 20% HBF_4, 30% water, and 50% methanol (the sample was labeled as EGO^{M}-20%). Additionally, X-ray photoelectron spectroscopy (XPS) was used to clarify the atomic composition of the as-prepared sample surface (5 nm depth). The survey analysis revealed the C-1s and O-1s peaks in all samples. In addition, a slight F-1s peak was observed for EGOs (Figure 6 and Table 1). The oxygen contents of EGO^{W}-42% and EGO^{M}-20% were 34.2 wt% and 35.2 wt%, respectively, which are slightly lower than that of CGO (40.5 wt%); and the C/O mass ratios were of 1.8 and 1.7. These values are quite smaller than those of previously reported EGOs (C/O mass ratio = 3.5–5.7),[27,36] indicating that our EGOs were deeply oxidized.

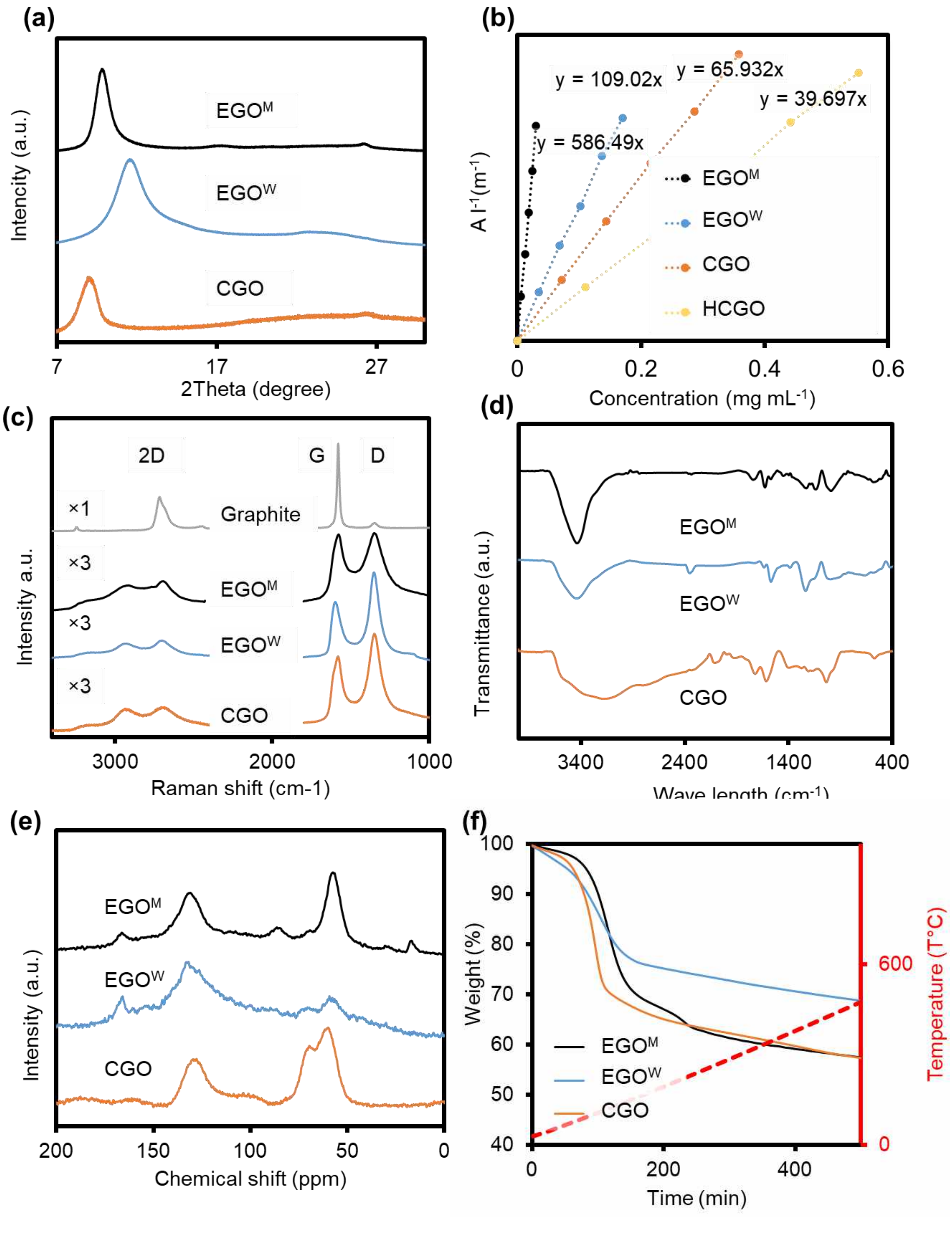

Figure7. Characterization of as-synthesized CGO, highly oxidized CGO (HCGO), EGO^W, and EGO^M using (a) XRD, (b) Lambert-Beer coefficient, (c) Raman, (d) FT-IR, (e) solid state ^{13}C NMR, and (f) TGA techniques: temperature ramp (red dashed line).

II.3 EGOs characterization

The XRD patterns of EGO^{W}-42% and EGO^{M}-20% (Figure 7a) were compared with that of CGO. We found a shift of the GO (002) diffraction peak depending on the prepara tion conditions. While CGO and EGO^{M} showed similar patterns, this peak in EGO^{W} appeared at a higher angle. These XRD results indicate that the sheet distance of EGO^{W} is smaller than those of EGOM and CGO, in good agreement with the nature and degree of its functionalization (to be described later). The UV-Vis spectra of EGO^{W}-42%, EGO^{M}-20%, and CGO (Figure 8) have an absorption band centered at 232 nm corresponding to the π-π* transitions of aromatic C=C bonds, as well as a shoulder at 298 nm corresponding to the n–π* transitions of C=O bonds.[37,38] In addition, a clear improvement in the absorbance was observed over the whole spectra for all EGOs, suggesting that these samples have a less disrupted conjugated electronic structure (CES).[27] To further investigate the CES in our materials, the Lambert-Beer coefficient at 660 nm was estimated by monitoring the absorbance as a function of GO concentration.[27,39] The absorbance divided by the cell length was plotted (Figure 7b). All samples followed the Lambert-Beer Law, with extinction coefficients of 109.0, 586.5, 65.9,

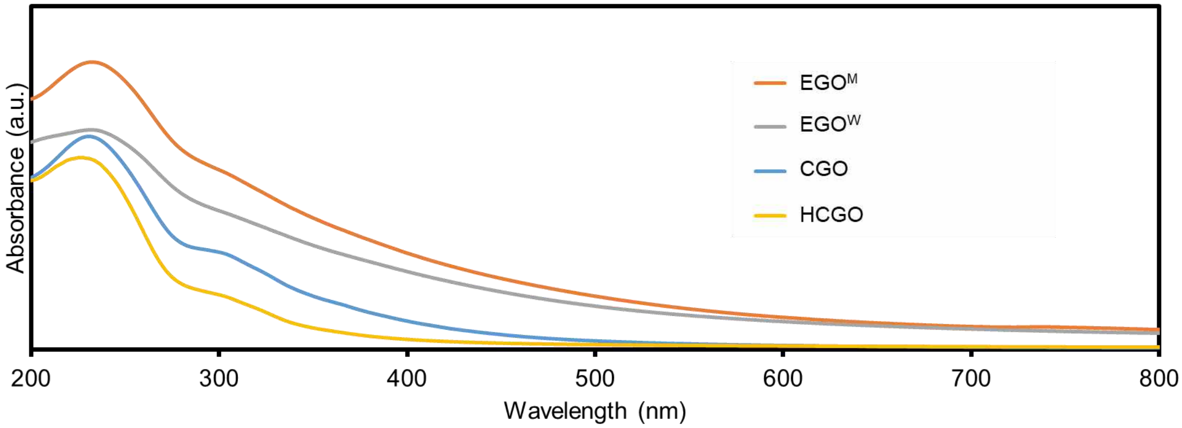

Figure 8. UV-Vis of GOs dispersion in water

and 39.7 L g^{-1} m^{-1} for EGO^{W}-42%, EGO^{M}-20%, CGO, and highly oxidized CGO (HCGO), respectively.[15] These results indicate that the CES is less disrupted in the EGOs than in CGOs, and EGO^{M}-20% has a more continuous CES than EGO^{W}-42%. Yet, the extinction coefficients of our samples remained beneath the standard values of pristine graphene structure (from ~2000 to ~6600 L g^{-1} m^{-1}).[39] The formation of few-layers and defects was confirmed by Raman spectroscopy (Figure 7c). The starting graphite foil showed two intense peaks at 1578 and 2714 cm^{-1} that correspond to the G band and the 2D band, respectively.[40] After electrochemical treatment, a new peak appeared at 1360 cm^{-1} and was attributed to the D band, suggesting that the sp^2 honeycomb structure of graphite was transformed to sp^3 carbons by covalent functionalization and the formation of defects and disorders. An additional effect of the electrochemical treatment is the change in the 2D band to a low intensity and symmetric peak shape, indicating the formation of a few-layered graphene-like material.[41] The intensity ratio between the D and G bands (I_D/I_G) was similar for EGOs and CGO at 1.1, indicating a similar level of defects despite their different oxidation methods.

Next, we compared the functional groups formed on the graphene structures of EGO^W-42%, EGO^M-20%, and CGO. According to the Fourier-transform infrared spectroscopy (FT-IR) analysis (Figure 7d), EGOs and CGO showed similar spectral patterns, i.e., O-H stretching vibrations (3420 cm^{-1}), C=O stretching vibration (1720–1740 cm^{-1}), C=C stretching vibration (1590–1620 cm^{-1}), and C-O vibrations (1250–1000 cm^{-1}).[42] In addition, EGO^M-20% contained characteristic bands of the methoxy group (2976, 1467, and 1056 cm^{-1}).[43] To support the FT-IR analysis and to understand the distribution of functional groups on the EGOs, XPS analysis was performed. As mentioned above, this analysis indicates the presence of C-1s, O-1s, and also F-1s. Deconvolution analysis of narrow-scan XPS data for the C-1s peak of EGOs confirms the presence of C-O (286.5 eV) and C=O and –COO- (289 eV) while suggesting the presence of C2F (288.5 eV). Additionally, the C-1s region did not present any π to π* component (290.5 eV), indicating that only a limited conjugated structure existed in the EGOs after the uniform oxidation. Finally, the EGOs were analyzed by solid state 13C NMR (Figure 7e), which confirmed the presence of epoxy (60 ppm), hydroxyl (72 ppm), and carboxyl (168 ppm) functional groups. EGO^M-20% also presented methyl (16 ppm), fluoride (85 ppm), and methoxy (60 ppm) groups.[44,45] The chemical structure of EGOs determined by FT-IR and XPS is consistent with that by 13C NMR.

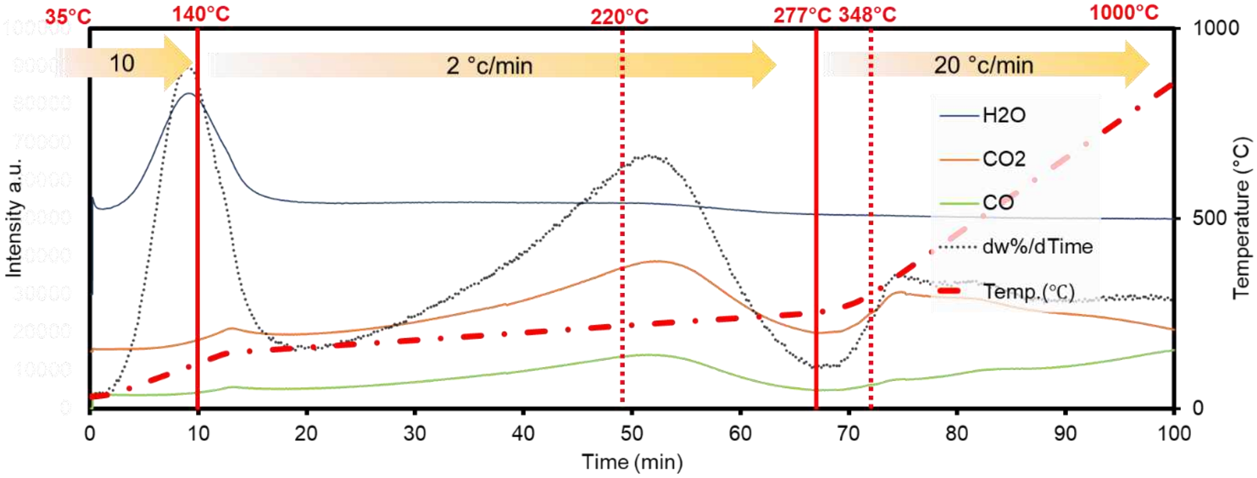

Figure 9. TGA-MS results. Gaseous species mainly formed from EGO^W

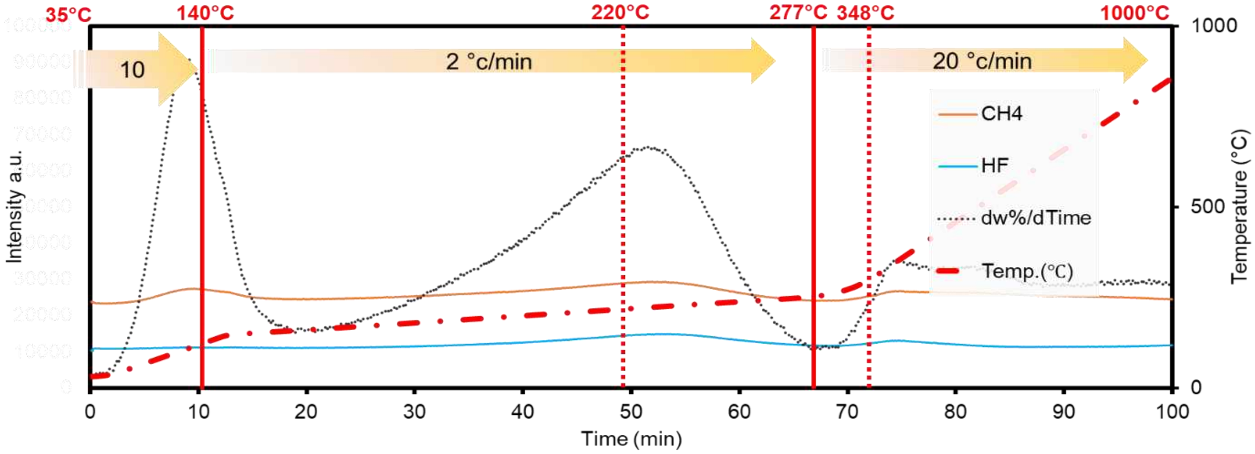

Figure 10. TGA-MS results. Gaseous species moderately formed from EGO^W

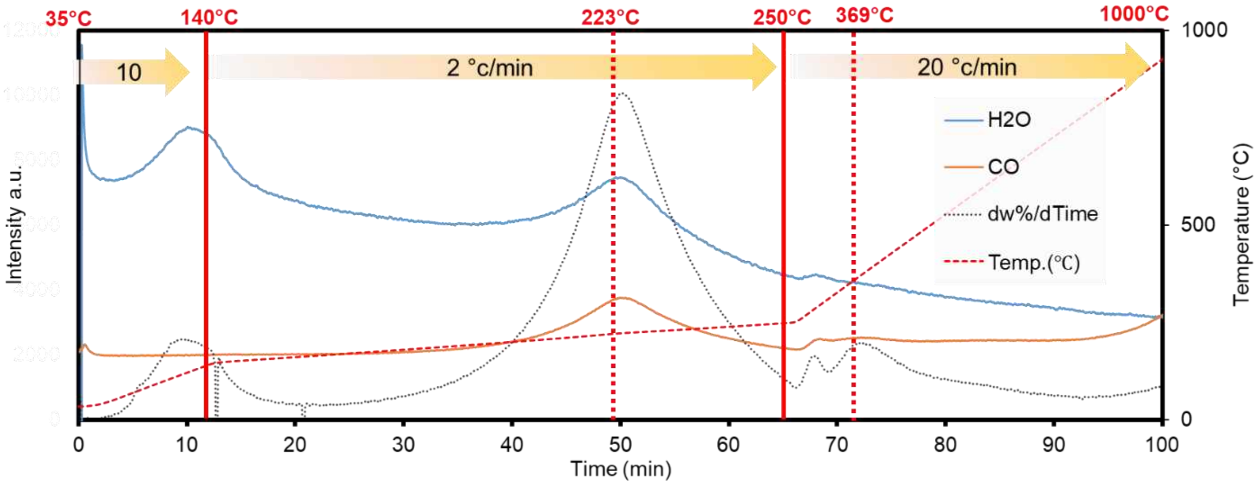

Figure 11. TGA-MS results. Gaseous species mainly formed from EGO^M

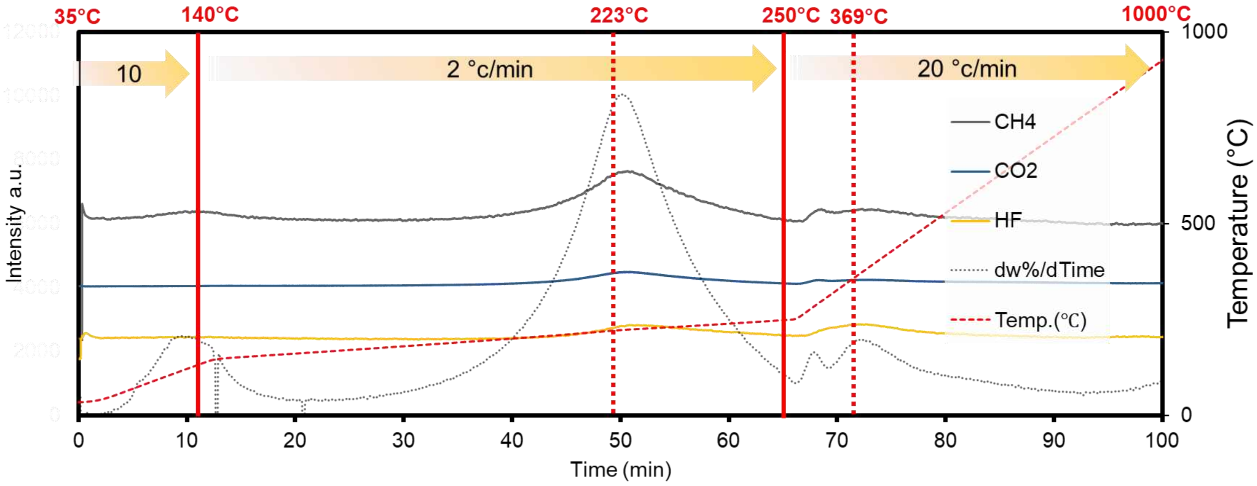

Figure12. TGA-MS results. Gaseous species moderately formed from EGO^M

The functional groups on GO can be removed via thermal treatment (Figure 7f).[46] CGO generally discharges CO, CO_2, and water at 130–200 °C, while the EGOs are expected to discharge other species derived from the HBF_4 and methanol. From the thermogravimetric analysis-mass spectroscopy (TGA-MS) results, EGO^W-42% discharged HF at 200 °C and 320 °C (Figure 9 and 10) and EGO^M-20% discharged HF and methane at 200 °C and 320 °C (Figure 11 and 12). These results support the introduction of fluorine into EGO^W-42% and that of fluorine and methoxy groups into EGO^M-20%.

II.4. Morphological study

To confirm the formation of single-layer structure in the EGOs, scanning electron microscopy (SEM) and atomic force microscopy (AFM) analyses were performed. For SEM measurement, the EGOs were deposited on a SiO_2/Si substrate. The lateral size distribution obtained from more than 100 EGO sheets was 0.45 ± 0.03 μm (0.04–1.78 μm) and 0.12 ± 0.01 μm (0.031–0.363 μm) for EGO^W-42% and EGO^M-20%, respectively (Figure 13a,b, Figure 14 and 15). For AFM analysis, EGO sheets were deposited on mica by spin-coating. The analysis of more than 100 EGO flakes gave a mean thickness of 1.36 and 1.27 nm, respectively, for EGO^W-42% and EGO^M-20%, confirming their monolayer nature (Figure 13c,d).[47] The AFM analysis of EGO^W-42% and EGO^M-20% also revealed that over 62% and 88% of the sheets were mono layers (<1.5 nm) and more than 95% and 97% were monolayers to bilayers (~2 nm), respectively (Figure 16 and 17). In sum, the morphological analysis of EGOs by SEM and AFM revealed that the electrochemical methods using HBF_4 produced highly homogeneous and few-layered GOs.

The dispersibility of the as-prepared EGOs was evaluated and compared with that of CGO. Freeze-dried GOs were dispersed in water or methanol at a concentration of 0.33 mg ml^{-1}. All GOs showed good dispersibility in water, and nematic liquid crystal behavior was maintained for at least two months (Figure 13e-g, Figure 18).[48] In contrast, interestingly, only EGO^M-20% remained dispersed in methanol after as long as one week, whereas EGO^W-42% and CGO aggregated (Figure 13h-j). This phenomenon might be induced by the high affinity between EGO^M-20% and methanol.

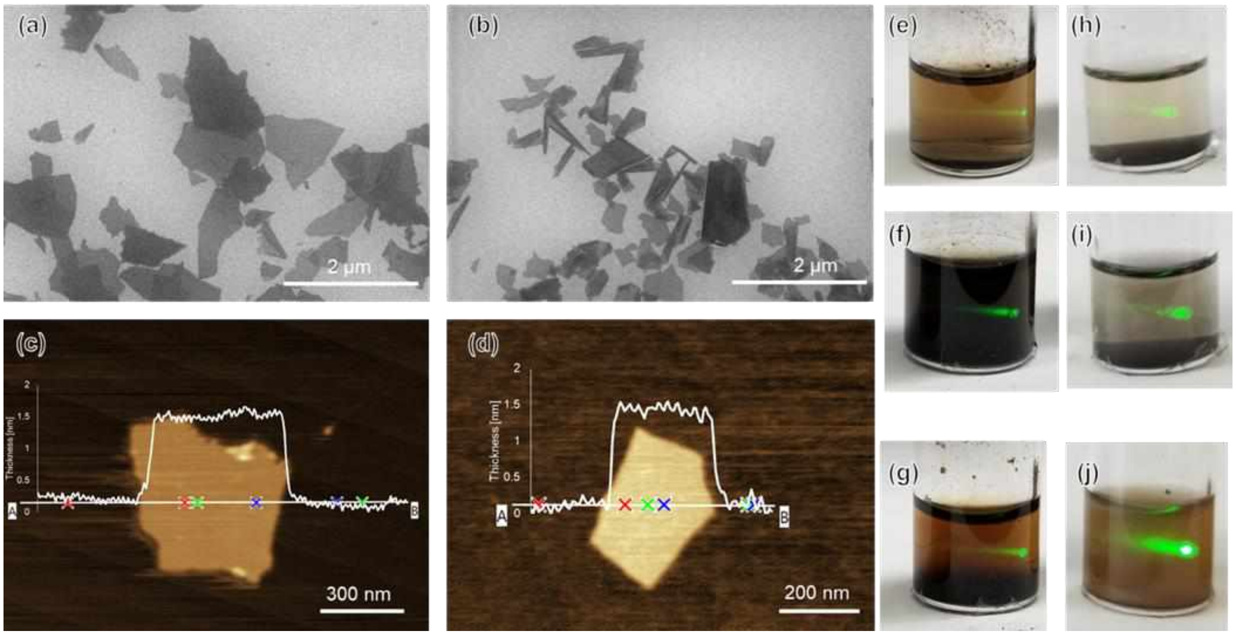

Figure 13. SEM images of (a) EGO^W and (b) EGO^M, (c) AFM images of EGO^W and (d) EGO^M. Photographs of (e) CGO, (f) EGO^W, and (g) EGO^M dispersed in water after two months; and those of (h) CGO, (i) EGO^W, and (j) EGO^M dispersed in methanol after one week.

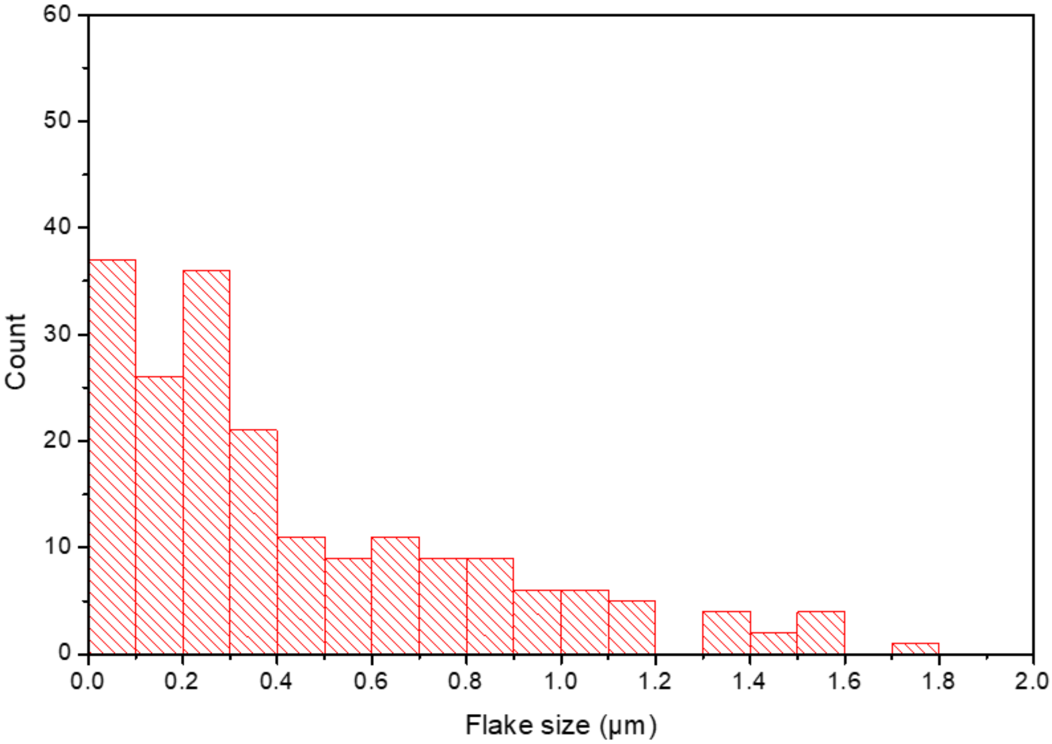

Figure 14. Flake size histogram of more than 100 EGO^W flakes

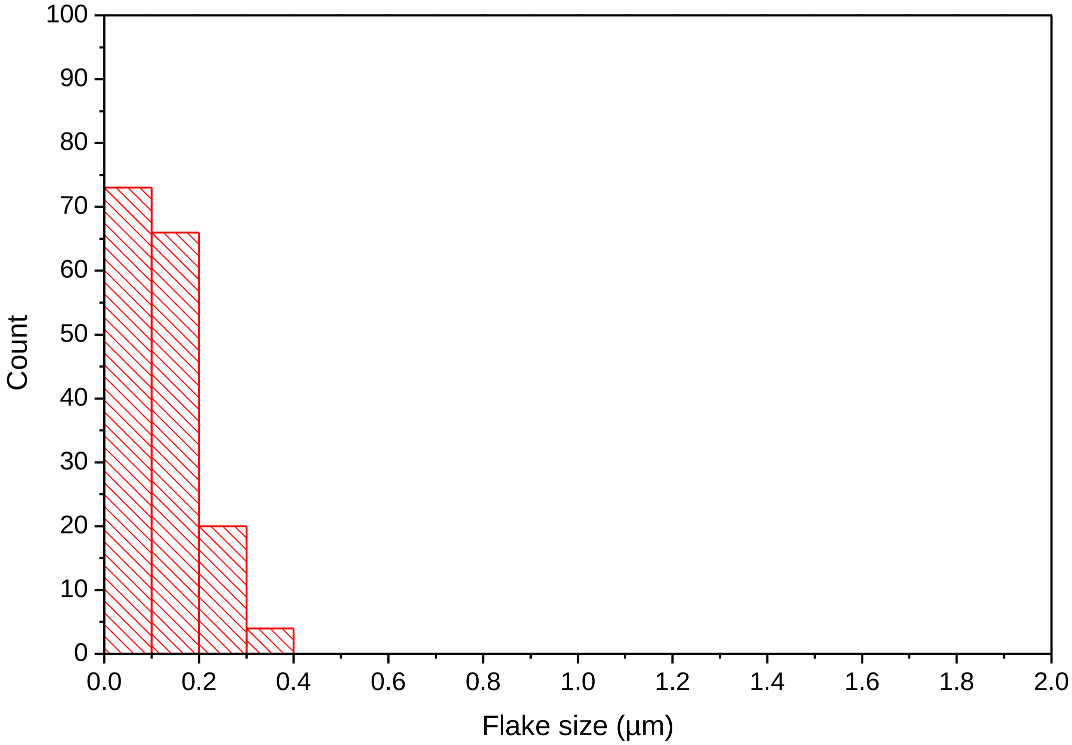

Figure 15. Flake size histogram of more than 100 EGO^{M} flakes

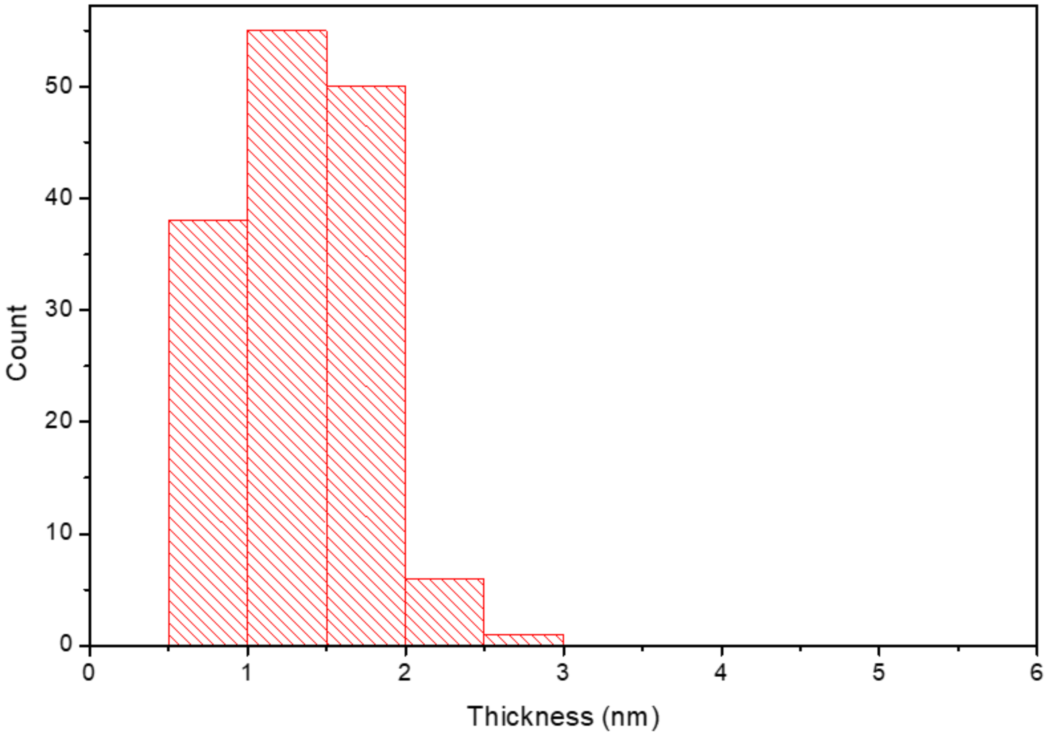

Figure 16. Flake thickness histogram of more than 100 EGO^{W} flakes

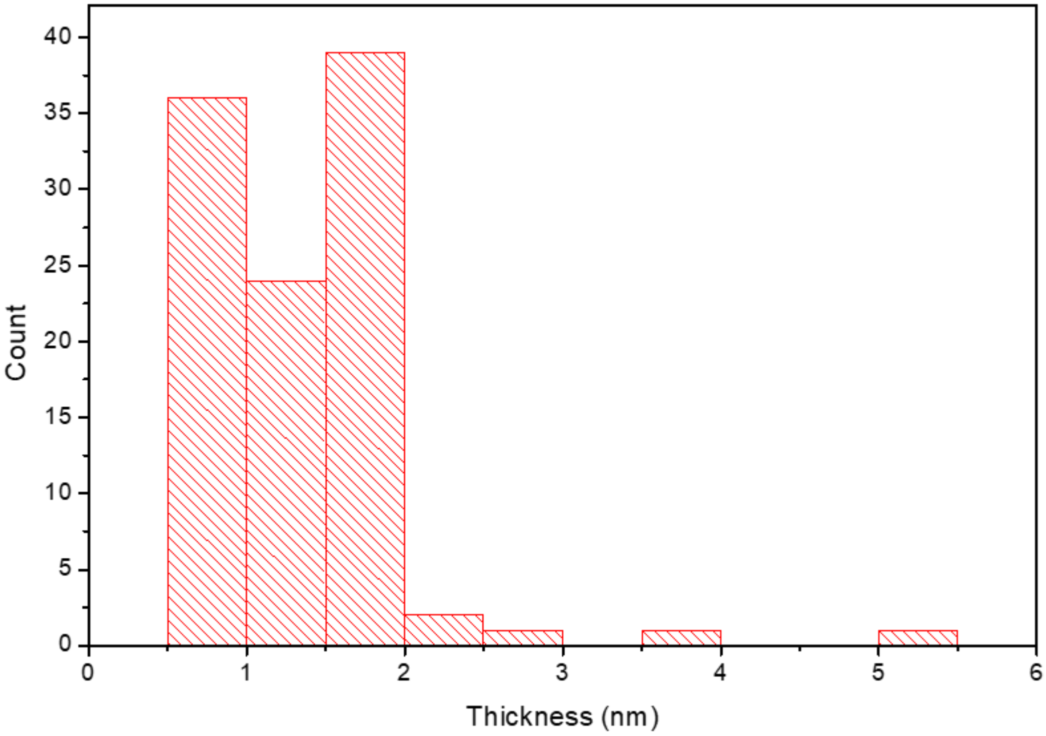

Figure 17. Flake thickness histogram of more than 100 EGO^M flakes

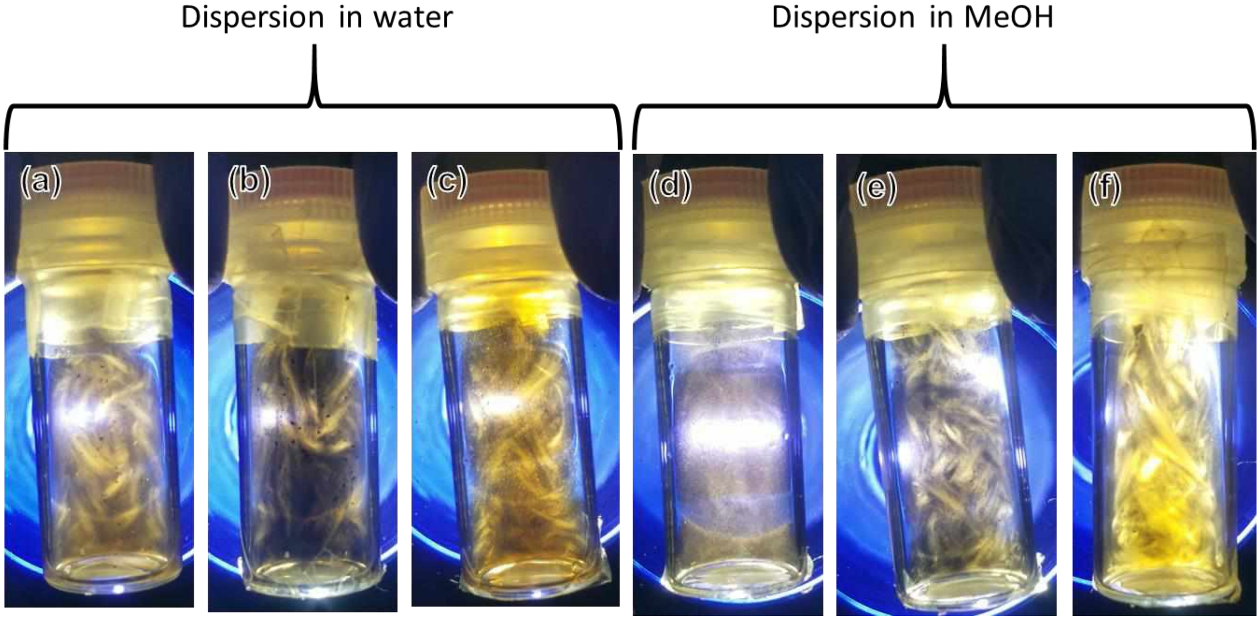

Figure 18. The pictures were taken using simple flash light, 2 light poralizer filter, and a digital camera. The pictures were taken 10 second after the sample agitation. 0.33 mg ml-1 dispersion in water of (a) CGO, (b) EGOW, (c) EGOM, and in MeOH of (d) CGO, (e) EGOW, (f) EGOM.

The above characterization results revealed that the produced EGOs have similar morphology but different types of functional groups compared with those of CGO. CGO has been widely investigated for practical applications, and therefore we tested our EGOs for use in energy storage devices and membranes. In addition, the oxidative property of EGOs derived from their oxygenated functional groups was evaluated.

II.5. Reduction of EGOs

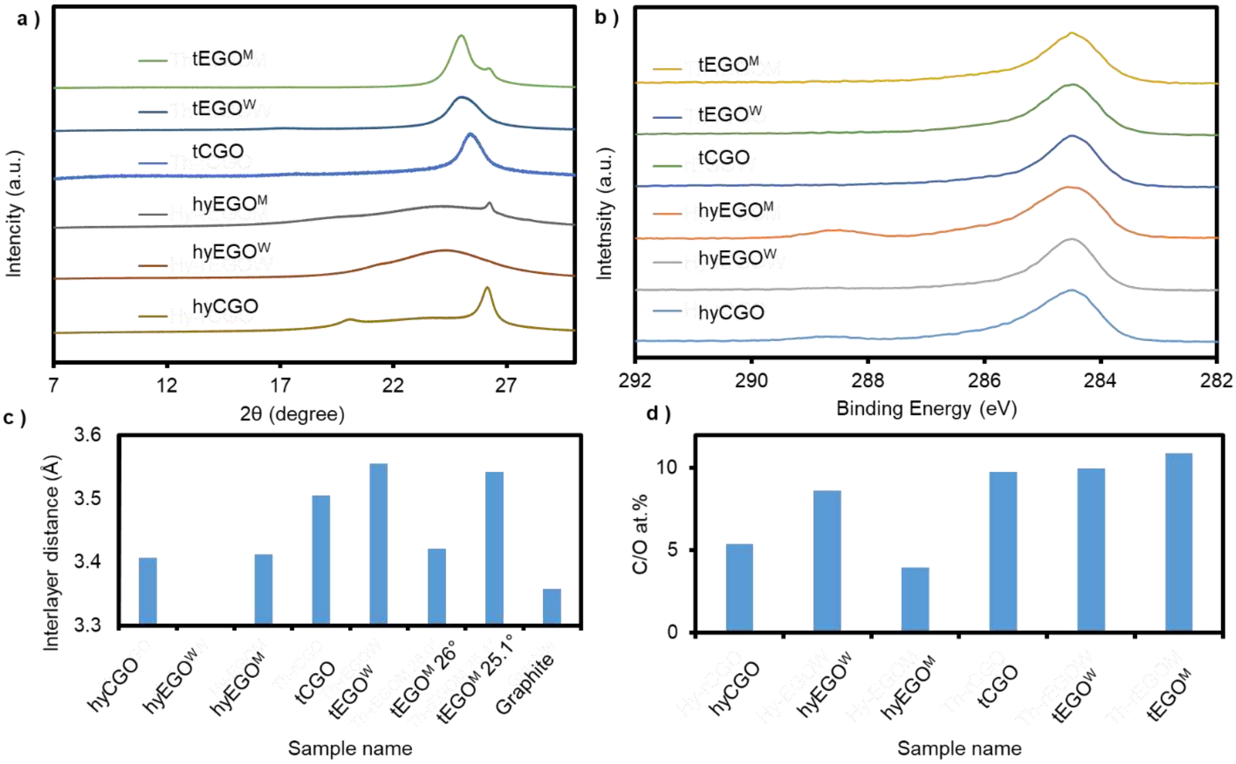

Figure 19. Analysis after reduction process: a) XRD, b) XPS C1s, c) interlayer distance, d) XPS atomic quantification

Two reduction methods were used chemical reduction and thermal reduction. The former one was performed by dispersing the as prepared GOs into water, adding 0.4 mL g^{-1} of hydrazine, and heating the solution for 2 h at 90 °C. The latter was performed in tube oven by keeping the temperature at 220 °C for 2 h followed by 600 °C for 1 h. Both materials were further dispersed in water, filtrated through membrane paper and finally pressed to form a palette. In Figure 19a,c, the

XRD spectra of reduced GOs by hydrazine (hyGO) and by thermal reduction (tGO) show a shift to higher diffraction angle. This phenomenon due to the removal of functional groups on the surface of graphene is confirmed in Figure 19b,d by XPS analysis. Thus a correlation between the restacking and the reduction degree was observed.

II.6. Electrical conductivity of the reduced EGOs

The conductivity measurement was performed on thermally and chemically reduced EGOs palettes using a 4-probes measurement system. The results (Figure 20) shows the efficiency of the thermal reduction method over chemical reduction and its critical effect in the case of EGO^M. Original conductivity of hyCGO and $hyEGO^W$ was relatively high 18900 S m^{-1} and 19200 S m^{-1}, respectively. On the other hand, $hyEGO^M$ was only of 2800 S m^{-1}. This significant difference is due to the original functional groups of EGO^M and their strength over chemical reduction via hydrazine. The thermal reduction based on the TGA survey allows the decomposition of most functional groups present on CGO and EGOs samples. The results indicate the optimization and homogenization of the conductivity as high as 53600 S m^{-1}, 55000 S m^{-1}, and 31400 S m^{-1} for tCGO, $tEGO^W$, and $tEGO^M$ respectively. These results confirm the strength of thermal reduction method and its advantage for electrical application.

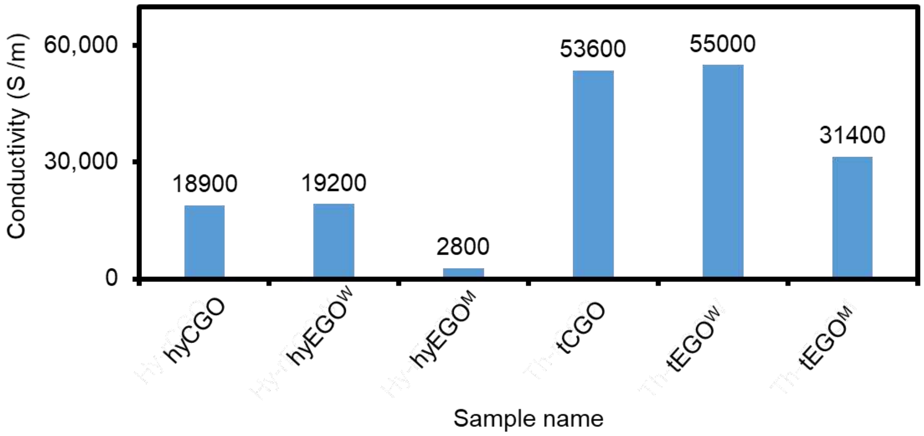

Figure 20. Conductivity measurement of GOs after hydrazine and thermal reduction

II.7. Evaluation and scalability of EGO

II.7.1. Lithium ion battery evaluation

For energy storage, the GO samples were engineered into electrodes and used as anode in LIBs. Based on their thermal behavior (Figure 7f), the EGOs and CGO were heated under N_2 atmosphere at 650 °C to convert them to conductive graphene-like materials, and the thermally treated EGO^W, EGO^M, and CGO are termed $tEGO^W$, EGO^M, and tCGO, respectively (Figure 19 and 20). After assembling the coin cells, the LIB performance was evaluated in terms of capacity as a function of charging rate. In the results (Figure 21), $tEGO^W$, $tEGO^M$, and tCGO all showed similar performance exceeding that of graphite. At a charging rate of 372 mA g^{-1} (1C) the capacities were 495, 554, and 513 mAh g^{-1}; and these values were 163, 195, and 176 mAh g^{-1} at a charging rate of 7440 mA g^{-1} (20C), respectively. Compared with graphite, $tEGO^M$ showed a capacity increase of 72% at 1C and 572% at 20C. These results are good agreement with previously reported reduced GO used as active material for half-cell lithium ion battery (Table 2).

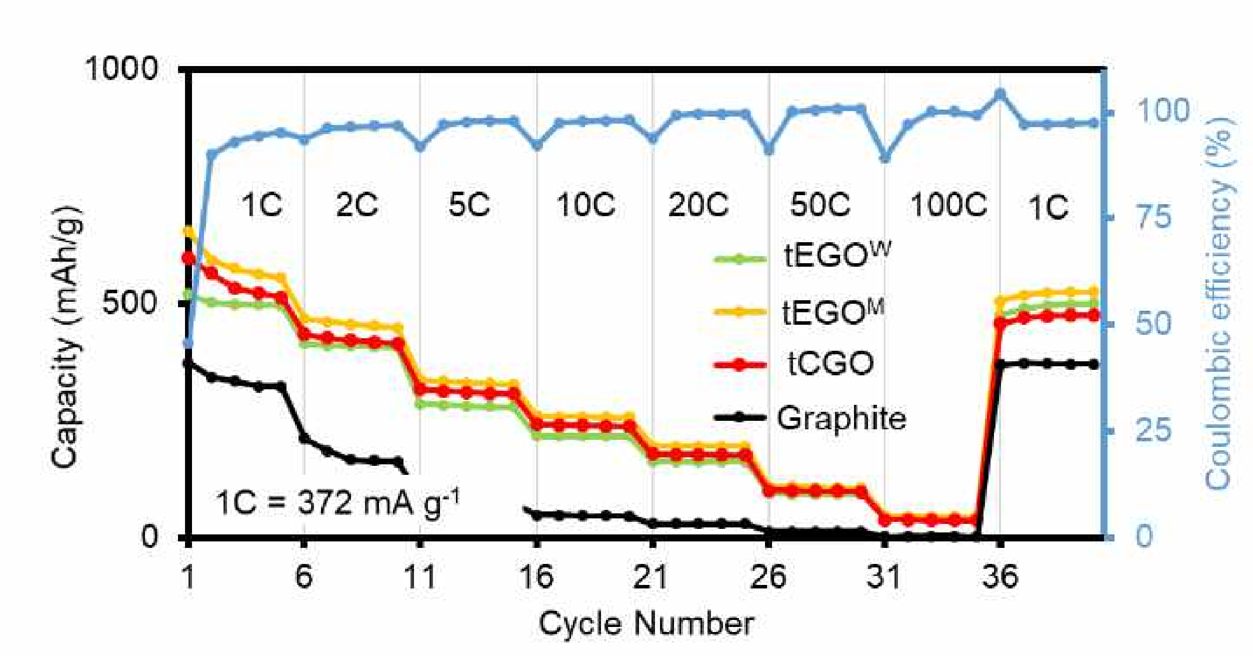

Figure 21. LIBs capacity performance at different current rate (1C = 372 mAh g^{-1}): Graphite (Black), tCGO (red), $tEGO^W$(green), $tEGO^M$(orange). Coulombic efficiency of $tEGO^W$ (blue).

Table 2. Reduced graphene oxide as active material for half-cell lithium ion battery

Name	Current density (mA g^{-1})	Capacity (mAh g^{-1})	Ref.
Graphene nanosheets (hydrazine reduced GO)	372	570	49
S-Doped graphene	374	870	50
Graphene-Like-Graphite	1C	225	51
Bare graphene	500	400	52
Iodine graphene	500	536	52
tEGO^{M}	372	554	This work

II.7.2. Water membrane filtration evaluation

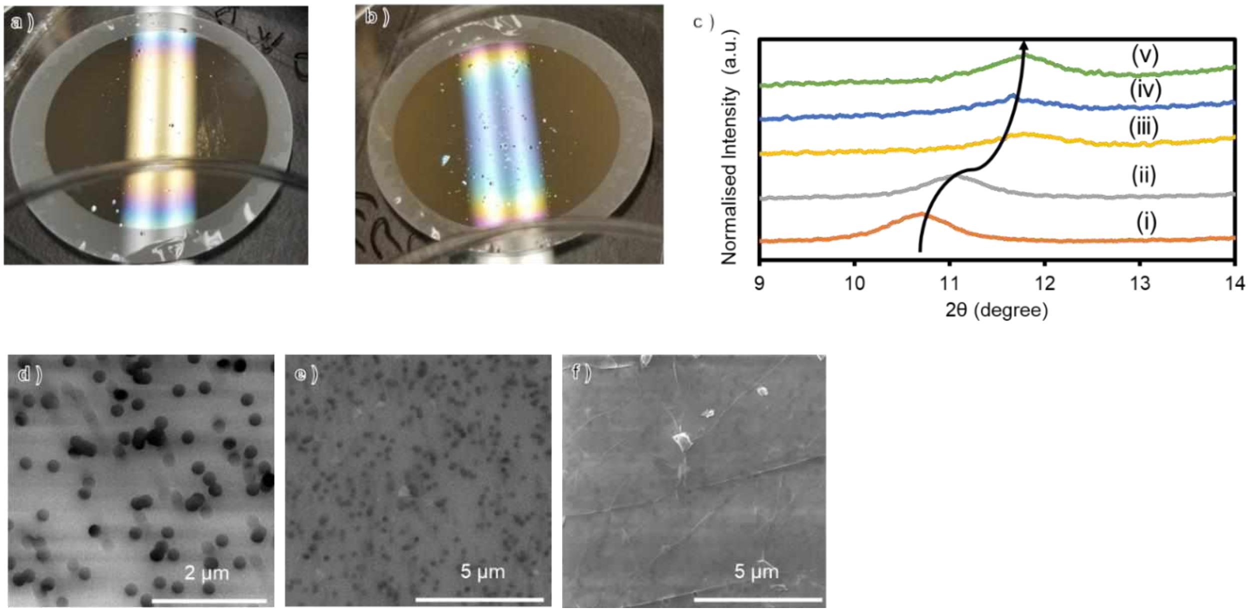

Figure 22. The appearance of prepared membrane a) EGO^W, b) EGO^M. c) XRD of EGO^M membrane heated at 150°C for (i) 1 min, (ii) 5 min, (iii) 10 min, (iv) 15 min, (v) 30 min. SEM image of EGO^M membrane d) before heating treatment, e) 5 min heating treatment, and f) 10 min heating treatment.

Next, to efficiently utilize the two-dimensional morphology of EGOs, they were prepared into thin membranes (Figure 22) and tested for excluding dye molecules (10 µg ml^{-1} of methyl orange under 0.1 ml min^{-1} flow at 35 Kgf cm^{-2}). The membranes were prepared by few simple steps: first we dispersed the GOs powder into 0.1 mg ml^{-1} deionized water, followed by two centrifugations at 6000 rpm for 5 min to remove the possible deposit (few layers' graphene oxide), then filtration of 6 ml of the as-prepared GO solution through polycarbonate membrane (PC), and finally drying for 1 day at room temperature. The obtained membranes showed the mirror-like shape and once exposed to white light diffraction was observed indicating the good alignment of EGO layers, Figure 22a and 22b. Before evaluation, the membranes were heated at 150°C to ensure good stability in water environment. The property of the GO membranes was characterized by combining SEM and XRD. Figure 22c indicates that the reduction results in mild restacking of the EGOM membranes which saturate from 10 min. Figure 22d-f shows that from 10 min heating at 150°C, fractures are formed on the surface of EGOM membrane. In order to ensure good water stability and avoid cracks, the heating time was fixed at 5 min.

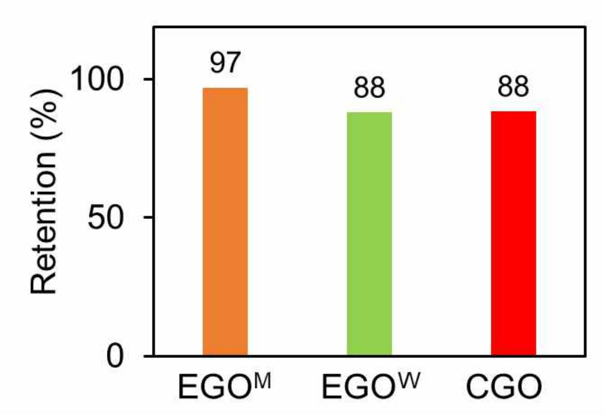

Figure 23. Evaluation of EGO in water filtration membrane: red (CGO), green (EGO^{W}), orange (EGO^{M}).

Membranes prepared with EGO^{W}-42% and EGO^{M}-20% excluded 88% and 97% of the methyl orange molecules, respectively, which is comparable to the performance of the membrane based on CGO (Figure 23).

II.7.3. Chemical reactivity of graphene oxide

To measure the chemical reactivity derived from the functional groups, the oxidation properties of EGOs were investigated using the oxidation of benzyl alcohol to benzaldehyde as model reaction.[15]

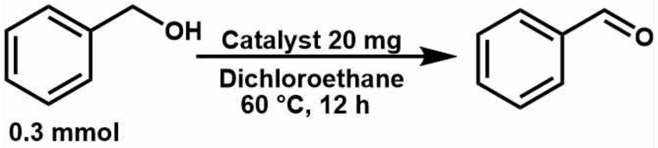

Entry	GO	Yield %
1	CGO	60
2	$\mathrm{EGO}_{\mathrm{W}}$	41
3	$\mathrm{EGO}_{\mathrm{M}}$	25

Figure 24. Oxidative property of different GOs.

$\mathrm{EGO}^{\mathrm{W}}$-42% and $\mathrm{EGO}^{\mathrm{M}}$-20% promoted the reaction to achieve 41% and 25% yields, respectively, while CGO showed a yield of 60% (Figure 24), suggesting that the EGOs are less oxidative. The oxidative property of GO would be derived from the endoperoxide functional group, which was only detected in CGO and HCGO by solid state ^{13}C NMR at 110 ppm (Figure 25). Considering the potential harm to humans, the less oxidative EGOs are preferred over CGO.

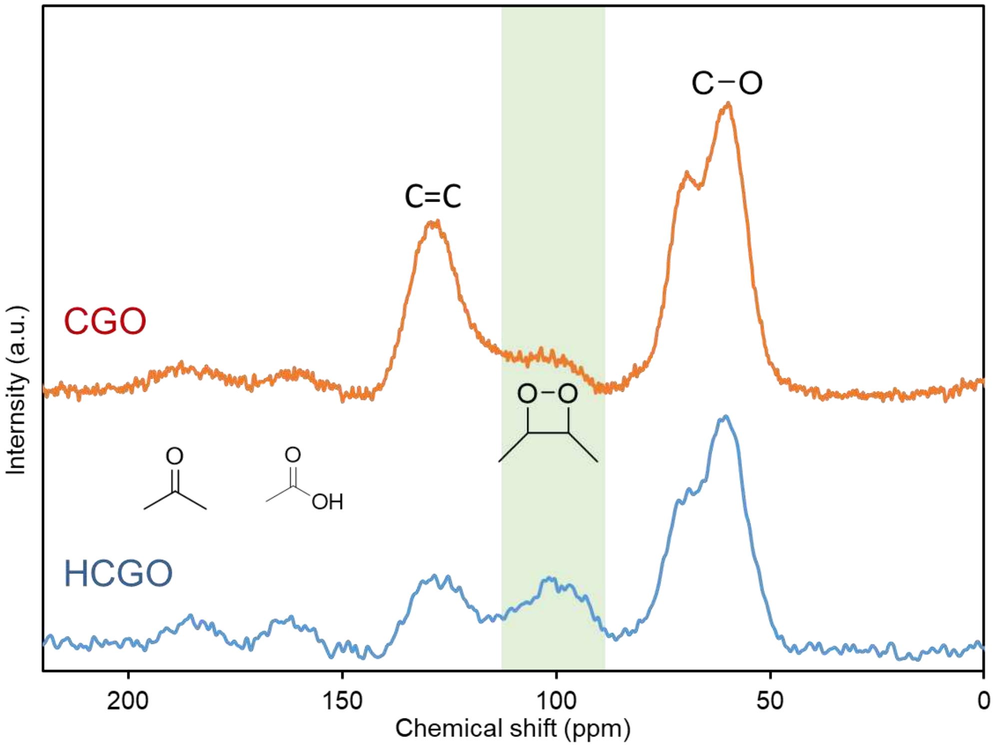

Figure 25. Solid-state ^{13}C NMR of CGO and HCGO

II.7.4. Scalability evaluation of EGO

Motivated by such advantages, we further developed the mass synthesis of EGO by a continuous flow system (Figure 26). On the left side of Figure 26, a graphite foil roll of 25 m length and 4 cm width is placed. The graphite foil is carried by a metallic roll which is used to connect the graphite to the anode. The graphite progress from left to right going inside the electrolyte (HBF_4). In the electrolyte, a cathode is soaked allowing to realize the electrochemical oxidation of the graphite foil. The oxidized graphite foil continues to progress to the right and is dragged out from the electrolyte. Within one day, this prototype system was able to produce 32 g of EGO^W-42%.

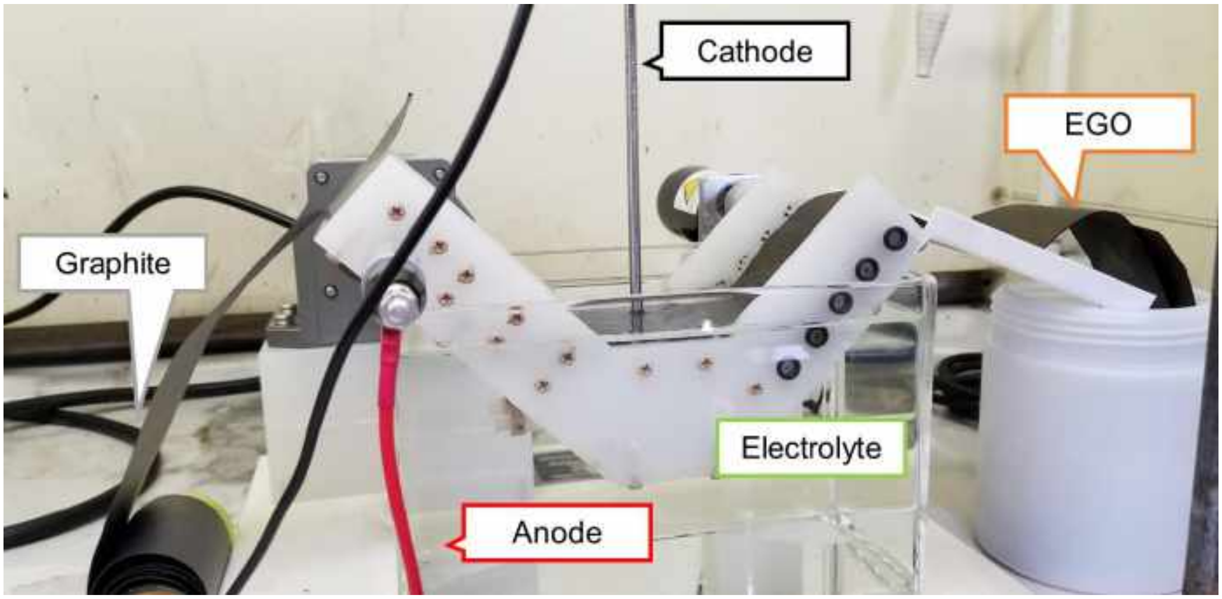

Figure 26. Continuous flow electrochemical treatment system developed using graphite sheet (left) to produce EGO (right).

III. CONCLUSION

In summary, the electrochemical functionalization of graphite to GO was developed by using HBF_4 as an electrolyte. The non-destructive nature of the intercalated species (BF_4^-) results in the expansion of graphite while preventing the exfoliation and formation of un-oxidized graphite domain before functionalization, thus achieving a high 2D carbon formation ratio of >99%. Saturated HBF_4 aqueous electrolyte and that diluted by methanol produced materials with similar morphology (66% and 88% monolayers) and oxygen content (28.4 at% and 29.4 at%, respectively).

Introduction of the methoxy functional group allowed the EGO^M to be dispersed in organic solvents, thus extending its processability. Additionally, promising results were obtained in using the EGOs for energy storage and water filtration, thus guaranteeing their wide scope of application. Finally, this process was adapted to a flow system to enable continuous production using a simple home-made reactor. This research will contribute to enabling the fine-tuning the functional groups, functionalization degree, and large-scale production of 2D carbons in the future.

EXPERIMENTAL SECTION

1. Materials

HBF_4, methanol, $KMnO_4$, H_2SO_4, 30% aq. H_2O_2, hydrazine hydrate, were purchased from Wako Pure Chemical Industries, Ltd. Graphite foil was provided from KANEKA. All the chemicals were used directly without further purification.

2. Characterization instrumentation

Elemental analyses were performed by PERKINELMER 2400II. Freeze-dried of GO was performed by ADVANTEC DRZ350WC. XPS was measured by JPS-9030 with a pass energy of 20 eV. The crystalline structure of samples was characterized by X-ray diffraction (XRD) using a PANalytical Co. X' part PRO using Cu Kα radiation (λ= 1,541 Å) in the 2θ range of 5–75°. The operating tube current and voltage were 30 mA and 40 kV, respectively. The data was collected at the step size of 0.017° and the type of scan was continuous. The UV-Vis measurements were conducted on a JASCO V-670 spectrophotometer. The morphology was measured by transmission electron microscopy (TEM) JEOL JEM-2100F and atomic force microscopy (AFM) SHIMADZU SPM-9700HT, while the functional groups on the surface of prepared catalyst were recorded by Fourier transform infrared spectrometer (FT-IR SHIMADZU IR Tracer 100), the sample for FT-IR were dried and mixed with KBr, and then pressed up to 1.3 mm-diameter pellets. The products were quantified by gas chromatography GC (Shimadzu GC-2014 equipped with flame ionized detector FID detector). Electrical conductivities were measured by using MITSUBISHI CHEMICAL ANALYTECH MCP-T610. The cyclic voltammograms of the second cycle were collected on Solartron 1287 electrochemical instrument at the scan rate 50 mV s^{-1}. Raman spectra were measured by Horiba Jobin Yvon Inc. T-64000. The thermogravimetry analysis (TGA) was conducted on a RIGAKU TG 8121.

Solid-state ^{13}C NMR spectra were recorded using an NMR system (11.7 T magnet, DD2 spectrometer; Agilent technology Inc.) at a magic angle spinning (MAS) speed of 10 kHz. A single pulse sequence with a 3.2 μs pulse and repetition time (10 s) was applied. The signal of TMS was applied to a reference at 0 ppm. Because a broad background ^{13}C signal which stems from a spacer, a top cover and a bottom drive tip in a MAS sample rotor was not negligible, we measured ^{13}C spectra of not only the samples in sample rotors but also of blank (the sample rotors only). The net signal spectra were obtained by subtracting the blank spectra from the former spectra including sample and background signal. Each spectrum was obtained by accumulation over 5000 scans.

3. Preparation of CGO

Natural flake graphite (3.0 g) was stirred in 95% H_2SO_4 (75 mL). $KMnO_4$ (9.0 g) was gradually added to the solution keeping the temperature <10 °C. The mixture was then stirred at 35 °C for 2 h. The resulting mixture was diluted by water (75 mL) under vigorous stirring and cooling so that temperature does not exceed 50 °C. The suspension was further treated by 30% aq. H_2O_2 (7.5 mL). The resulting graphite oxide suspension was purified by centrifugation with water until neutralization, and freeze-dried.

Highly oxidized chemical graphene oxide (HCGO) was produced by applying the same procedure as above replacing graphite by CGO.

4. Preparation of GO samples for elemental analysis

GO is hydrophilic, and adsorb ca. 10 wt% of water by exposing air. We dried GO under vacuum at 50 °C for three days, of which method is following a previous report.[15,35]

5. Li-ion battery anode sheets preparation

The working electrodes were made of active material (graphite and rGO), conductive material (acetylene black), and binder (Polyvinylidene fluoride) in a weight ratio of 7:2:1 by using N-Methyl-2-pyrrolidone as a solvent and a copper foil as the current collector. In order to obtain the homogeneous active and conductive material powder, both materials were mixed in a distilled water-ethanol solution (v/v, 1/1). After mixing, the solution was filtered using Merck Millipore JAWP04700 filter. The powder was freeze and then freeze-dry under vacuum at 30 °C for 24 h. The dry powder was set into ball-milling for 30 min at 300 RPM to reduce the particle size. Then the powder was at first mixed with NMP to obtain a homogeneous slurry and then with the binder.

The slurry (active material, conductive material, binder) was spread on a copper foil using a Doctor blade (100 µm thickness). The sheet was dried under vacuum at room temperature for 24 h and in air at 120 °C for 20 min. Finally, sheets with a diameter of 15.95 mm were punched and pressed.

6. Coin cells assembling

The CR2032 coin cells were assembled in an argon-filled glove box using metallic lithium as the counter electrode with a Whatman 1823-257 as a separator and 70 µL electrolyte. The electrolyte was 1 M L^{-1} $LiPF_6$ dissolved in a mixture of ethylene carbonate (EC), diethyl carbonate (DEC) (v/v, 3/7).

7. Battery cycling

The charge and discharge cycling tests were performed using a multi-channel battery tester (580 8 channel Battery Cycler Scribner Associates Incorporated) with a voltage window of 0.01 V and 3 V. Each cells were subject to discharge charge cycles at different current rates: 1C, 2C, 5C, 10C, 20C, 50C, 100C, and 1C for stability. All currents have been calculated using 372 mAh g^{-1} as a theoretical specific capacity.

8. Oxidation of benzyl alcohol

Typically, 0.3 mmol of benzyl alcohol, 20 mg of GO, and 0.5 mL of dichloroethane were added to 30 mL round bottom flask, and the mixture was heated at 60 °C under air. After 12 hours, the reaction mixture was cooled and analyzed by gas chromatography using decane as an internal standard.

REFERENCES

1. Novoselov KS, Geim AK, Morozov SV, Jiang D, Zhang Y, Dubonos SV, Grigorieva IV, Firsov A A. Electric Field Effect in Atomically Thin Carbon Films. Science 2004;306:666-669.

2. Li D, Müller MB, Gilje S, Kaner RB, Wallace GG. Processable aqueous dispersions of graphene nanosheets. Nat. Nanotechnol. 2008;3(2):101-105.

3. Stankovich S, Dikin DA, Piner RD, Kohlhaas KA, Kleinhammes A, Jia Y, Wu Y, Nguyen SBT, Ruoff R. S. Synthesis of graphene-based nanosheets via chemical reduction of exfoliated graphite oxide. Carbon 2007;45(7):1558-1565.

4. Xu Y. ; Shi G. Assembly of chemically modified graphene: methods and applications. J. Mater. Chem. 2011;21:3311-3323.

5. Lee C, Wei X, Kysar JW, Hone J. Measurement of the elastic properties and intrinsic strength of monolayer graphene. Science 2008;321(5887):385-388.

6. Stankovich S, Dikin DA, Dommett GHB, Kohlhaas KM, Zimney EJ, Stach EA, Piner RD, Nguyen ST, Ruoff RS. Graphene-based composite materials. Nature 2006;442: 282–286.

7. Buzaglo M, Ruse E, Levy I, Nadiv R, Reuveni G, Shtein M, Regev O. Top-Down, Scalable Graphene Sheets Production: It Is All about the Precipitate. Chem. Mater. 2017;29:9998-10006.

8. Wei D, Liu Y, Wang Y, Zhang H, Huang L, Yu G. Synthesis of N-doped graphene by chemical vapor deposition and its electrical properties. Nano Lett. 2009 ;9(5):1752-1758.

9. Li C, Shi Y, Chen X, He D, Shen L, Bao N. Controlled synthesis of graphite oxide: Formation process, oxidation kinetics, and optimized conditions. Chem. Eng. Sci. 2018;176:319-328.

10. Lim JY, Mubarak NM, Abdullah EC, Nizamuddin S, Khalid M, Inamuddin. Recent trends in the synthesis of graphene and graphene oxide based nanomaterials for removal of heavy metals — A review. J. Ind. Eng. Chem. 2018 ;66:29-44.

11. Rowley-Neale SJ, Randviir EP, Abo-Dena AS, Banks CE. An overview of recent applications of reduced graphene oxide as a basis of electroanalytical sensing platforms. Appl. Mater. Today. 2018 ;10:218-226.

12. Yoo MJ, Park HB. Effect of hydrogen peroxide on properties of graphene oxide in Hummers method. Carbon. 2019 ;141:515-522.

13. Hummers WS, Offeman RE. Preparation of Graphitic Oxide. J. Am. Chem. Soc. 1958;80:1339.

14. Jiao L, Zhang L, Wang X, Diankov G, Dai H. Narrow graphene nanoribbons from carbon nanotubes. Nature 2009;458(7240):877-880.

15. Morimoto N, Kubo T, Nishina Y. Tailoring the Oxygen Content of Graphite and Reduced Graphene Oxide for Specific Applications. Sci. Rep. 2016;6:21715.

16. Li X, Wang H, Robinson JT, Sanchez H, Diankov G, Dai H. Simultaneous nitrogen doping and reduction of graphene oxide. J. Am. Chem. Soc. 2009;131(43):15939-44.

17. Sheng Z.-H, Shao L, Chen JJ, Bao WJ, Wang FB, Xia XH. Catalyst-free synthesis of nitrogen-doped graphene via thermal annealing graphite oxide with melamine and its excellent electrocatalysis. ACS Nano 2011;5(6):4350-8.

18. Fang M, Wang K, Lu H, Yang Y, Nutt, S. Covalent polymer functionalization of graphene nanosheets and mechanical properties of composites. J. Mater. Chem. 2009;19:7098-7105.

19. Kuila T, Bose S, Mishr, AK, Khanra P, Kim NH, Lee JH. Chemical functionalization of graphene and its applications. Prog. Mater. Sci. 2012;57(7):1061-1105.

20. Bai H, Xu Y, Zhao L, Li C, Shi G. Non-covalent functionalization of graphene sheets by sulfonated polyaniline, Chem. Commun. 2009; 13: 1667-1669.

21. Teng CC, Ma CCM, Lu CH, Yang SY, Lee SH, Hsiao MC, Yen MY, Chiou KC, Lee TM. Thermal conductivity and structure of non-covalent functionalized graphene/epoxy composites. Carbon 2011; 49(15): 5107-5116.

22. Parvez K, Wu ZS, Li R, Liu X, Graf R, Feng X, Müllen K. Exfoliation of graphite into graphene in aqueous solutions of inorganic salts. J. Am. Chem. Soc. 2014 ;136(16):6083-6091.

23. Zhong YL, Swager TM. Enhanced Electrochemical Expansion of Graphite for in Situ Electrochemical Functionalization. J. Am. Chem. Soc. 2012;134:17896-17899.

24. Najafabadi AT, Gyenge E. Synergistic production of graphene microsheets by simultaneous anodic and cathodic electro-exfoliation of graphitic electrodes in aprotic ionic liquids. Carbon 2015;84: 449-459.

25. Cooper AJ, Wilson NR, Kinloch IA, Dryfe RAW. Single stage electrochemical exfoliation method for the production of few-layer graphene via intercalation of tetraalkylammonium cations. Carbon 2014; 66:340-350.

26. Allagui A, Abdelkareem MA, Alawadhi H, Elwakil AS, Reduced Graphene Oxide Thin Film on Conductive Substrates by Bipolar Electrochemistry. Sci. Rep. 2016;6:21282.

27. Cao J, He P, Mohammed MA, Zhao X, Young RJ, Derby B, Kinloch IA, Dryfe RAW. Two-Step Electrochemical Intercalation and Oxidation of Graphite for the Mass Production of Graphene Oxide. J. Am. Chem. Soc. 2017;139(48):17446-17456.

28. Pei S, Wei Q, Huang K, Cheng HM, Ren W. Green synthesis of graphene oxide by seconds timescale water electrolytic oxidation. Nat. Commun. 2018;9(1):145.

29. Najafabadi AT; Gyenge E. High-yield graphene production by electrochemical exfoliation of graphite: Novel ionic liquid (IL)–acetonitrile electrolyte with low IL content. Carbon 2014;71:58-69.

30. Ejigu A, Kinloch IA, Dryfe RAW. Single Stage Simultaneous Electrochemical Exfoliation and Functionalization of Graphene. ACS Appl. Mater. Interfaces 2017;9:710-721.

31. Eissa S, Tlili C, L'Hocine L, Zourob M. Electrochemical immunosensor for the milk allergen β-lactoglobulin based on electrografting of organic film on graphene modified screen-printed carbon electrodes. Biosens. Bioelectron. 2012;38(1):308-13.

32. Mooste M, Kibena E, Kozlova J, Marandi M, Matisen L, Niilisk A, Sammelselg V, Tammeveski K. Electrochemical properties of gold and glassy carbon electrodes electrografted with an anthraquinone diazonium compound using the rotating disc electrode method RCS Adv. 2016;6: 40982-40990.

33. Fortgang P, Tite T, Barnier V, Zehani N, Maddi C, Lagarde F, Loir AS, Jaffrezic-Renault N, Donnet C, Garrelie F, Chaix C. Robust Electrografting on Self-Organized 3D Graphene Electrodes. ACS Appl. Mater. Interfaces 2016;8(2):1424-1433

34. Azevedo J, Fillaud L, Bourdillon C, Noël JM, Kanoufi F, Jousselme B, Derycke V, Campidelli S, Cornut R. Localized Reduction of Graphene Oxide by Electrogenerated Naphthalene Radical Anions and Subsequent Diazonium Electrografting. J. Am. Chem. Soc. 2014;136: 4833-4836.

35. Morimoto N; Suzuki H, Takeuchi Y, Kawaguchi S, Kunisu M, Bielawski CW, Nishina Y. Real-Time, in Situ Monitoring of the Oxidation of Graphite: Lessons Learned. Chem. Mater. 2017;29: 2150-2156.

36. Abdelkader AM, Kinloch IA, Dryfe RAW. High-yield electro-oxidative preparation of graphene oxide. Chem. Commun. 2014;50: 8402-8404.

37. Xu Y, Liu Z, Zhang X, Wang Y, Tian J, Huang Y, Ma Y, Zhang X, Chen Y. A Graphene Hybrid Material Covalently Functionalized with Porphyrin: Synthesis and Optical Limiting Property. Adv. Mater. 2009;21:1275-1279.

38. Lei Z, Lu L, Zhao XS. The electrocapacitive properties of graphene oxide reduced by urea. Energy Environ. Sci. 2012;5:6391-6399.

39. Hernandez Y, Nicolosi V, Lotya M, Blighe FM, Sun Z, De S, McGovern IT, Holland B, Byrne M, Gun'Ko YK, Boland JJ, Niraj P, Duesberg G, Krishnamurthy S, Goodhue R, Hutchison J, Scardaci V, Ferrari AC, Coleman JN. High-yield production of graphene by liquid-phase exfoliation of graphite. Nat. Nanotechnol. 2008;3(9):563-568.

40. Ferrari AC, Basko DM. Raman spectroscopy as a versatile tool for studying the properties of graphene. Nat. Nanotechnol. 2013;8(4):235-46.

41. Yoon D, Moon H, Cheong H, Choi JS, Choi JA, Park BH. Variations in the Raman Spectrum as a Function of the Number of Graphene Layers. J. Korean Phys. Soc. 2009;55:1299-1303.

42. Marcano DC, Kosynkin DV, Berlin JM, Sinitskii A, Sun Z, Slesarev A, Alemany LB, Lu W, Tour JM. Improved synthesis of graphene oxide. ACS Nano 2010;4(8):4806-4814.

43. Plyler EK. Infrared Spectra of Methanol, Ethanol, and n-Propanol, National Bureau of Standards, 1952.

44. Giraudet J, Dubois M, Hamwi A, Stone WEE, Pirotte P, Masin F. Solid-State NMR (^{19}F and ^{13}C) Study of Graphite Monofluoride $(CF)_n$: ^{19}F Spin−Lattice Magnetic Relaxation and ^{19}F/^{13}C Distance Determination by Hartmann−Hahn Cross Polarization. J. Phys. Chem. B 2005;109:175-181.

45. Thomas HR, Day SP, Woodruff WE, Vallés C, Young RJ, Kinloch IA, Morley GW, Hanna JV, Wilson NR, Rourke JP. Deoxygenation of Graphene Oxide: Reduction or Cleaning? Chem. Mater. 2013;25:3580-3588.

46. Diby Ossonon B, Bélanger D. Synthesis and characterization of sulfophenyl-functionalized reduced graphene oxide sheets. RSC Adv. 2017;7:27224-27234.

47. Yamamoto S, Kinoshita H, Hashimoto H, Nishina Y. Facile preparation of Pd nanoparticles supported on single-layer graphene oxide and application for the Suzuki–Miyaura cross-coupling reaction. Nanoscale 2014;6:6501-6505.

48. Shen TZ, Hong SH, Song JK. Electro-optical switching of graphene oxide liquid crystals with an extremely large Kerr coefficient. Nat. Mater. 2014;13(4):394-9

49. Wang G, Shen X, Yao J, Park J. Carbon 2009;47:2049 —2053.

50. Yun YS, Le VD, Kim H, Chang SJ, Baek SJ, Park S, Kim BH, Kim YH, Kang K, Jin HJ. J. Power Sources 2014;262:79 —85.

51. Cheng Q, Okamoto Y, Tamura N, Tsuji M, Maruyama S, Matsuo Y. Sci. Rep. 2017;7:14782.

52. Zhan Y, Zhang B, Cao L, Wu X, Lin Z, Yu X, Zhang X, Zeng D, Xie F, Zhang W, Chen J, Meng H. Carbon 2015;94:1-8.

CHAPTER 3

Sophisticated rGO synthesis and pre-lithiation unlocking full-cell lithium-ion battery high-rate performances

ABSTRACT: For the application to portable devices and storage of renewable energies, high-performance lithium-ion batteries are in great demand. To this end, the development of high-performance electrode materials has been actively investigated. However, even if new materials exhibit high performance in a simple evaluation, namely half-cell tests, it is often impossible to obtain satisfactory performance with an actual battery (full cell). In this study, the structure of graphene analogs is modified in various ways to change crystallinity, disorder, oxygen content, electrical conductivity, and specific surface area. These graphene analogs are evaluated as negative electrodes for lithium-ion batteries, and we found reduced graphene oxide prepared by combination of chemical reduction and thermal treatment was the optimum. In addition, a full cell is fabricated by combining it with $LiCoO_2$ modified with $BaTiO_3$ which is applicable to high-speed charge-discharge cathode material developed in our previous research. In general, pre-lithiation is performed for the anode when assembling full cells. In this study, we developed a "direct pre-lithiation" method in which the electrode and lithium foil were in direct contact before assembling a full cell, and created a lithium-ion battery with an output of 293 Wh kg^{-1} at 8,658 W kg^{-1}.

I. INTRODUCTION

In the past few decades, tremendous efforts have been made to develop high-performance electrode materials. Materials with low working potentials, such as Si, Ge, and Sn, have been investigated as anode materials due to their high capacity.[1–3] However, all of them lack in rate capability and stability induced by significant volume expansion.[4] Carbon-based materials, such as graphite and hard carbon, present even lower working potentials.[5] Carbon-based materials show excellent stability due to their relatively limited volume expansion;[6,7] however, compared to Si, Ge, and Sn, they have a lower capacity. The carbon-based materials also suffer from slow rate capability due to the slow intercalation process. In the recent years, graphene-based materials have emerged as a solution to improve both the capacity and capability performances of anode materials.[8] Amidst the high working potential materials, $LiCoO_2$ became by far the most popular layered transition metal oxide for the cathode. It has a high theoretical capacity of 274 mAh g^{-1} and limited self-discharge; in contrast, $LiCoO_2$ typically has limited cyclability and poor high rate capability.[9,10] To solve these problems, the deposition of Al_2O_3 layer *via* atomic layer deposition technic on $LiCoO_2$ was generally applied improving both the cyclability and rate performances.[11–13] We previously reported the stable and high rate capability cathode material composed of $BaTiO_3$ decorated $LiCoO_2$ (BTO-LCO) prepared by a simple sol-gel route.[14,15] We experimentally proved the incorporated artificial dielectric layer promotes the Li migration at the triple-phase, namely BTO-LCO-electrolyte, interface.

In the past research, anode and cathode were often separately evaluated by assembling half-cell using Li foil as a counter electrode. But, the technological transfer from half-cell to full-cell is limited in performances due to maladjusted choice of anode that lacks in stability, cyclability, and rate capability. Combined with our specially designed high rate performance cathode (BTO-LCO), graphene has the potential to solve those problems due to its flexibility limiting cracking during cycling, high capacity, excellent cyclability, and high rate capability;[16–18] however, a clear guideline for the optimization of graphene structure for LIBs has not been provided.

Herein, we design various graphene analogs as anode for LIBs by reducing graphene oxide (GO) using chemical, thermal, and microwave reduction methods. The graphene analogs are evaluated by half-cell using Li foil as a counter electrode, then by full-cell using BTO-LCO cathode and graphene anode. The results demonstrate the successful technology transfer from high-performance cathode half-cells toward higher full-cell performance.

II. RESULTS AND DISCUSSION

II.1. Synthesis and characterization of anode materials

The anode materials, graphene analogs, were synthesized from graphite, through its consecutive oxidation, exfoliation, and reduction. Oxidation and exfoliation of graphite were performed by our modified Hummers' method to obtain 0.83 wt% graphene oxide (GO) dispersion in water.[19] Then, the as-prepared materials were firstly chemically reduced using hydrazine (62.5 μL g^{-1} and 1 mL g^{-1}), hydrazine scavenges oxygen functional groups and breakdown into N_2H_2 and H_2O to produce reduced graphene oxide (rGO) with the oxygen content of 39 wt.% and 14 wt.%, termed as $HrGO_{39}$ and $HrGO_{14}$, respectively.[19–23] Next, both HrGOs were further reduced by heating in a tube furnace or microwave reactor. In these thermal treatments, oxygen functional groups and graphene decomposes into CO and CO_2 gases.[24–26] In the tube furnace, the samples were heated under N_2 from 0 to 300 °C in 3 hours, 300 to 1,000 °C in 35 minutes, and kept at 1,000 °C for 3 hours; samples were named $HrGO_{XT}$ (X= 39 or 14). For microwave treatment, the samples were exposed to 750 W microwave under N_2 for 5 seconds, reaching 1,000 °C within 2 seconds; samples were named $HrGO_{XMW}$ (X= 39 or 14). In the case of $HrGO_{39MW}$, microwave treatment results in fast and large CO and CO_2 generation inducing an enormous pressure between graphene layers resulting in their exfoliation and in the increase of their pore size diameter (Table 1).

Next, the structural analyses of graphene analogs were performed. X-ray diffraction (XRD) patterns (Figure 1a and 2) showed the homogeneous expansion of interlayer distance of graphite from 0.34 nm to 0.88 nm by oxidation (Figure 1ai and 2). A mild chemical reduction slightly narrowed the interlayer distance of $HrGO_{39}$ to 0.79 nm (Figure 1aii), while substantial chemical reduction caused amorphization of $HrGO_{14}$ (Figure 1av). The thermal reduction at 1,000 °C for 3 hours provided similar amorphous material (Figure 1aiii and 1avi). After microwave treatment, peaks at 26 ° became sharper, suggesting partial graphitization (Figure 1aiv and 1avii), while the intensity of HrGO$_{XMW}$ remains 60 times lower than the original graphite (Figure 2).

Table 1: Effect of thermally induced CO and CO$_2$, SSA, and conductivity of rGOs.

Reducing method	**Hydrazine** 62.5 µL g^{-1}			**Hydrazine** 1 mL g^{-1}		
		Tube furnace	**Microwave**		**Tube furnace**	**Microwave**
Sample name	**HrGO$_{39}$**	**HrGO$_{39T}$**	**HrGO$_{39MW}$**	**HrGO$_{14}$**	**HrGO$_{14T}$**	**HrGO$_{14MW}$**
Effect of thermally induced CO and CO$_2$	-	rGO decomposition	rGO exfoliation	-	Low	Low
Oxygen wt%	39.07	2.87	4.77	14.42	5.49	6.52
SSA (m^2 g^{-1})	88	93	532	217	422	333
Pore diameter (nm)	3.5	5.2	26.5	6.8	6.7	7.4
Pore Volume (cm^3 g^{-1})	5.7 10^{-2}	0.111	3.512	0.354	0.662	0.592
Conductivity (S m^{-1})	7.7 10^{-2}	5.6 10^3	4.0 10^2	2.1 10^3	4.4 10^3	1.7 10^3

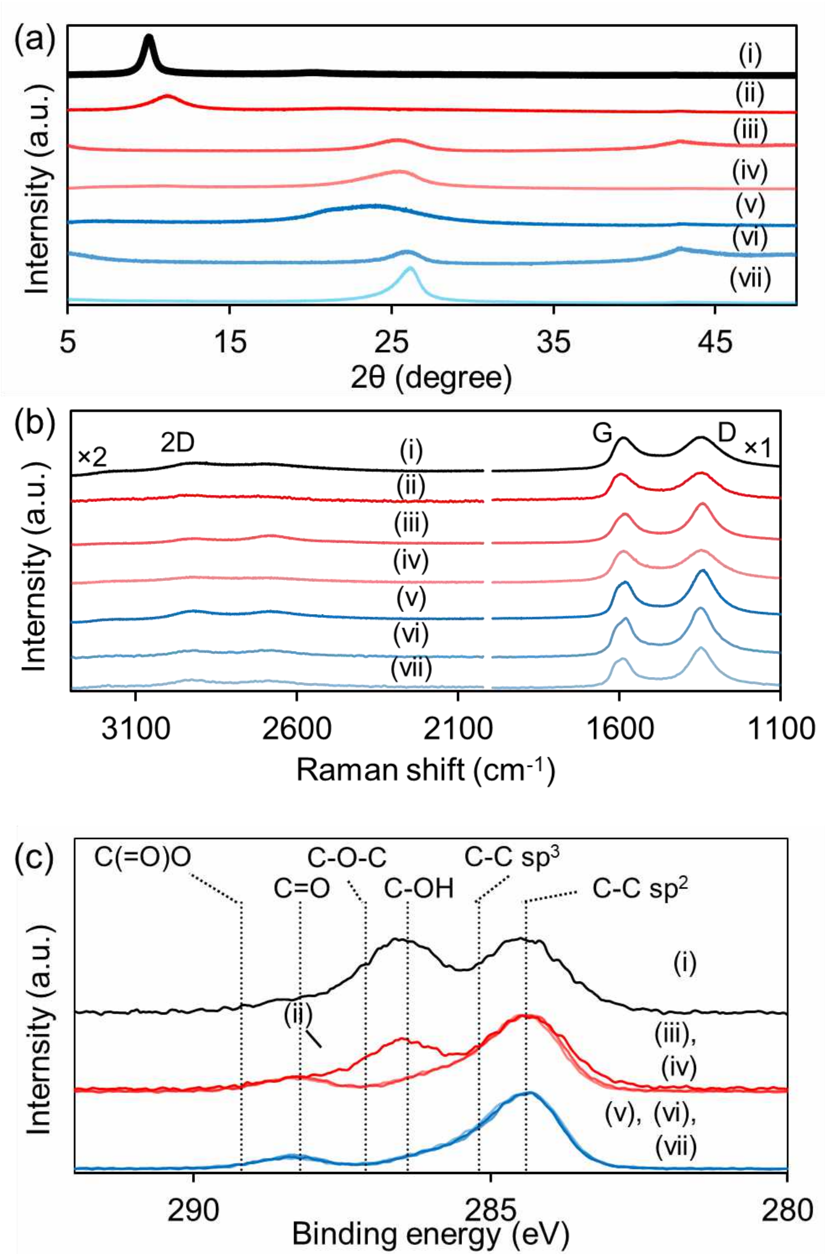

Figure 1: Characterization of (i) GO, (ii) HrGO$_{39}$, (iii) HrGO$_{39T}$, (iv) HrGO$_{39MW}$, (v) HrGO$_{14}$, (vi) HrGO$_{14T}$, (vii) HrGO$_{14MW}$. (a) XRD, (b) RAMAN spectroscopy, (c) XPS C1s narrow scan.

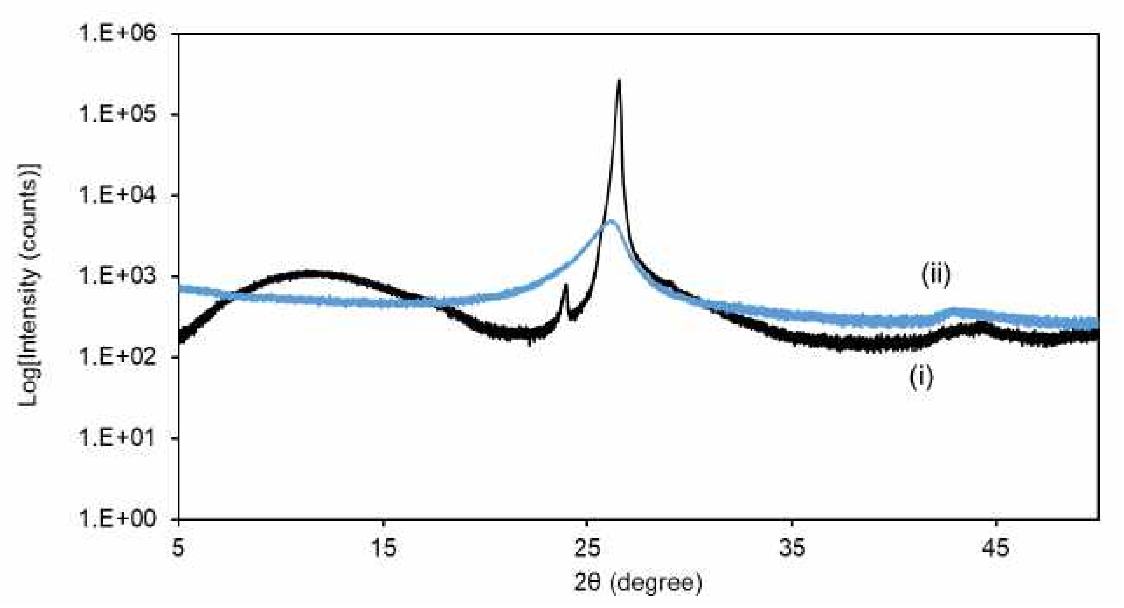

Figure 2: XRD spectra of (i) graphite and (ii) $HrGO_{14MW}$.

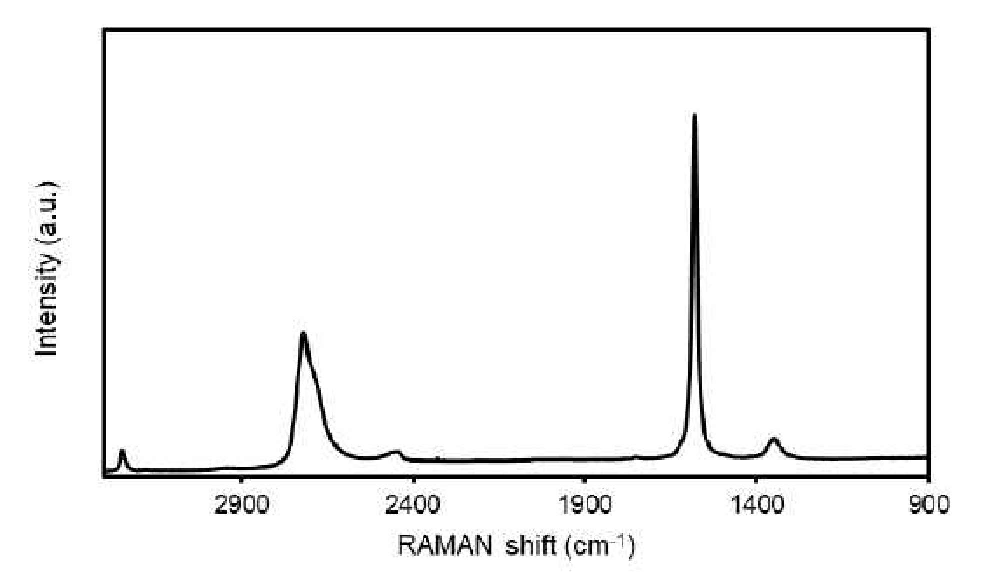

Figure 3: RAMAN spectra of graphite.

Raman spectra (Figure 1b and 3) were measured to confirm the degree of the defect (intensity ratio of D band and G band; I_D/I_G) and the formation of few-layer (shape of 2D band).[27] Through the graphite oxidation into GO, the I_D/I_G changes from 0.1 to 1.1, and its 2D band became symmetrical, indicating the formation of defects and few-layer material respectively. After reduction by hydrazine, the I_D/I_G values of $HrGO_{39}$ and $HrGO_{14}$ were 1.1 and 1.4, respectively, indicating the presence of large amounts of defect and disorder.[19,27] After further reduction in tube furnace, both $HrGO_{39T}$ and $HrGO_{14T}$ showed an I_D/I_G value of 1.4. The microwave treatment of HrGOs did not affect to the I_D/I_G values of $HrGO_{39MW}$ and $HrGO_{14MW}$. These results indicate the limited defect healing effects of these treatments.

Morphological observation of rGOs was performed by SEM and TEM analyses (Figure 4 and 5). Both analyses confirm the few-layer structures of all rGOs. Furthermore, in good agreement with our previous work,[19] the formation of a wrinkled 2D structure was confirmed for $HrGO_{39MW}$, $HrGO_{14}$, $HrGO_{14T}$, $HrGO_{14MW}$, while $HrGO_{39}$ preserved the flat 2D structure of GO.

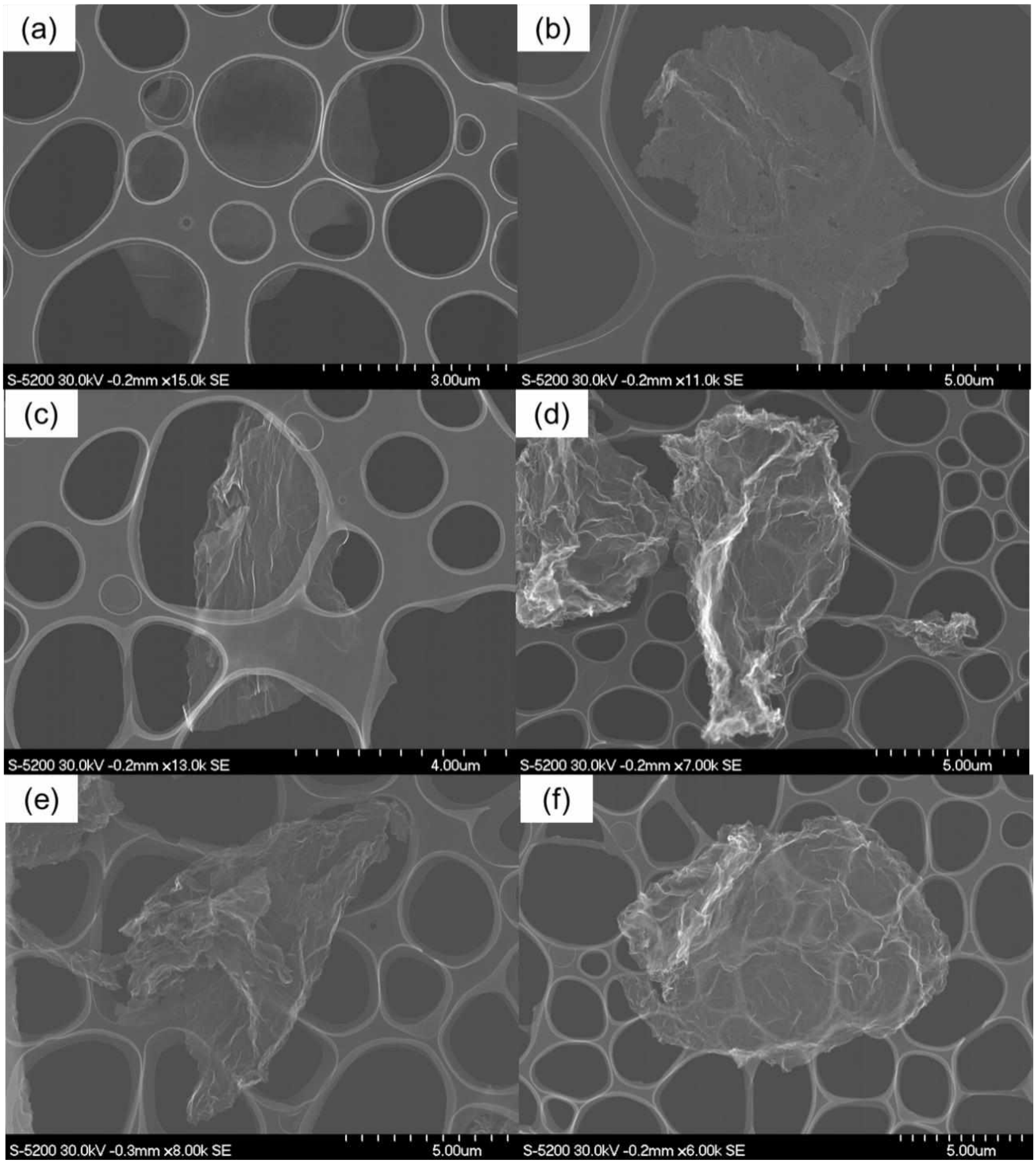

Figure 4: SEM image of (a) $HrGO_{39}$, (b) $HrGO_{39T}$, (c) $HrGO_{39MW}$, (d) $HrGO_{14}$, (e) $HrGO_{14T}$, (f) $HrGO_{14MW}$.

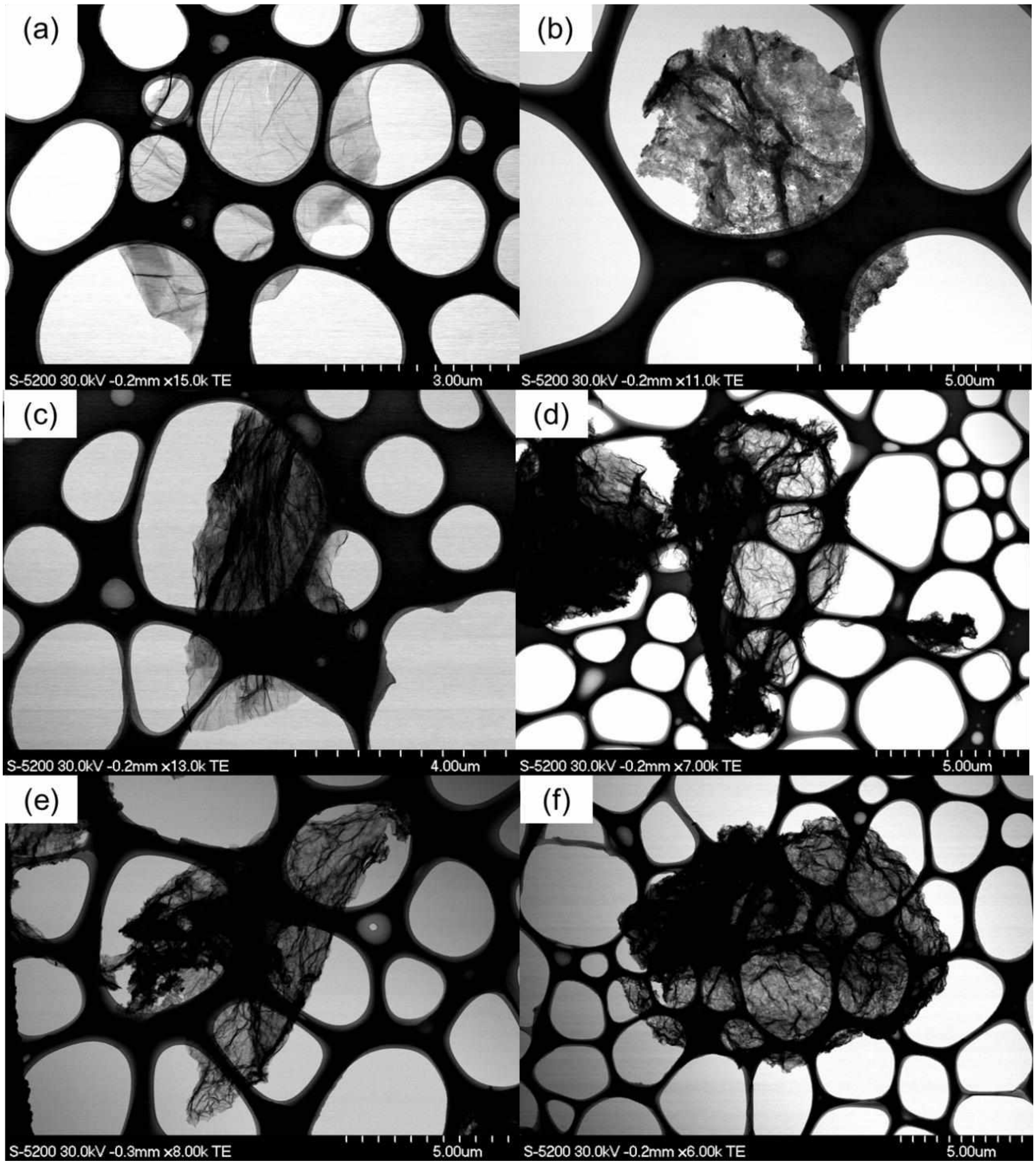

Figure 5: TEM image of (a) $HrGO_{39}$, (b) $HrGO_{39T}$, (c) $HrGO_{39MW}$, (d) $HrGO_{14}$, (e) $HrGO_{14T}$, (f) $HrGO_{14MW}$.

Table 2: Elemental analysis of GO and rGOs. XPS analysis of graphite. The symbol "–" indicates no signal detected, "()" indicates signal within error.

Element (wt%)	C	O	H	N	S
Graphite (XPS)	98.14	1.86	-	-	-
GO	45.41	47.6	2.93	0.73	3.33
$HrGO_{39}$	57.20	39.07	2.07	0.66	(1.00)
$HrGO_{39T}$	96.228	2.87	(0.39)	0.51	-
$HrGO_{39MW}$	93.86	4.77	(0.58)	0.57	(0.22)
$HrGO_{14}$	80.85	14.42	(1.06)	3.17	(0.50)
$HrGO_{14T}$	91.88	5.49	(0.61)	1.89	(0.13)
$HrGO_{14MW}$	91.02	6.52	(0.53)	1.76	(0.17)

Elemental analysis of as-prepared samples (Table 1 and 2) shows the formation of oxygen functional groups through oxidation; the oxygen content increased from 1.9 wt.% to 47.6 wt.%.[19] After chemical reduction, the oxygen content decrease reaching 39.1 wt.% and 14.4 wt.% for $HrGO_{39}$ and $HrGO_{14}$, respectively. The microwave treatment resulted in 4.8 wt.% and 6.5 wt.% for $HrGO_{39MW}$ and $HrGO_{14MW}$, respectively, while the tube furnace treatment resulted in 2.9 wt.% and 5.5 wt.% for $HrGO_{39T}$ and $HrGO_{14T}$ respectively. The higher oxygen content HrGO was more efficiently reduced. We believe that the reduction was accelerated by CO originated from oxygen functional groups.[24]

X-ray photoelectron spectroscopy (XPS) was conducted to identify oxygen functional groups (Figure 1ei and 6). The narrow C 1s spectra of GO showed the presence of C-OH (286.5 eV), C-O-C (287.1 eV), C=O (288.2 eV), and C(=O)O (289.2 eV) upon oxidation, and the removal of C-OH and C-O-C was observed upon reduction steps. As C=O groups remained nearly the same amount after reduction, its superior stability toward reduction methods was recognized.[28]

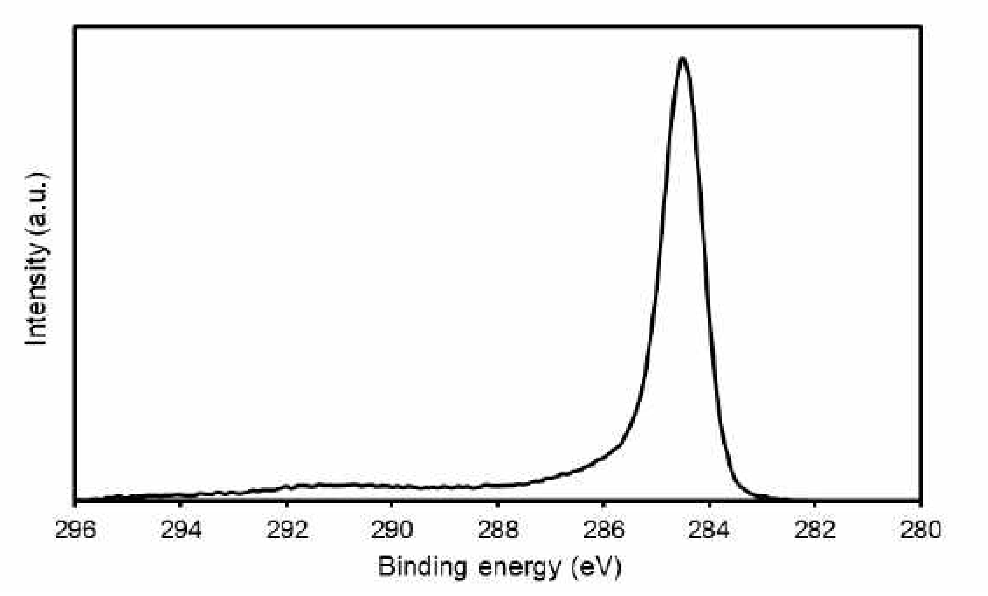

Figure 6: XPS C1s of graphite.

The electroconductivity was measured by a four-point probe method (Table 1). GO was not sufficiently conductive to be measured, but after mild and strong chemical reductions, the conductivity increased to 7.7×10^{-2} and 2.1×10^{3} S m-1, respectively. After tube furnace treatment, the conductivity increased up to 5.6×10^{3} and 4.4×10^{3} S m-1 for $HrGO_{39T}$ and $HrGO_{14T}$, respectively. These results denote the correlation between the increase of the conductivity and the decrease of oxygen functional group of graphene. The microwave treatment also modified the conductivity to 4.0×10^{2} and 1.7×10^{3} S m-1 for $HrGO_{39MW}$ and $HrGO_{14MW}$, respectively, yet the values were lower than expected. This is caused by the morphology of $HrGO_{XMW}$; the $HrGO_{XMW}$ are tough and sponge-like structure, making it difficult to form pellets for electroconductivity measurement. Therefore, electron conductivity may be underestimated for $HrGO_{XMW}$.

Finally, the porous structure and the specific surface areas (SSA) of all samples were investigated by nitrogen isothermal absorption. The results are summarised in Table 1. The adsorption-desorption isotherm (Figure 7a,b) of all samples shows a type IV nitrogen adsorption with a capillary condensation step and a hysteresis loop between the adsorption and desorption, which correspond to a mesoporous material. The SSA was evaluated by Brunauer–Emmett–Teller (BET) method for all rGOs (Table 1). Chemically reduced rGOs displayed higher SSA as the hydrazine amount was increased, reaching 88 m^2 g^{-1} and 217 m^2 g^{-1} for $HrGO_{39}$ and $HrGO_{14}$, respectively. These results suggest the presence of oxygen functional groups limits N_2 to access interlayer spaces.[29,30] Initially,

$HrGO_{14}$ has an wrinkled 2D structure (Figure 4d and 5d), and mild oxygen content, expressing a mild SSA of 217 m^2 g^{-1}. The tube furnace treatment slowly removes the oxygen functional groups preserving the wrinkled 2D structure of $HrGO_{14}$ (Figure 4e and 5e) resulting in mild SSA improvement up to 422 m^2 g^{-1}. The microwave treatment removes, quickly and on a short period, the oxygen functional groups preserving the wrinkled 2D structure of $HrGO_{14}$ (Figure 4f and 5fd) resulting in smaller SSA improvement compared with tube furnace method, reaching only 333 m^2 g^{-1}.

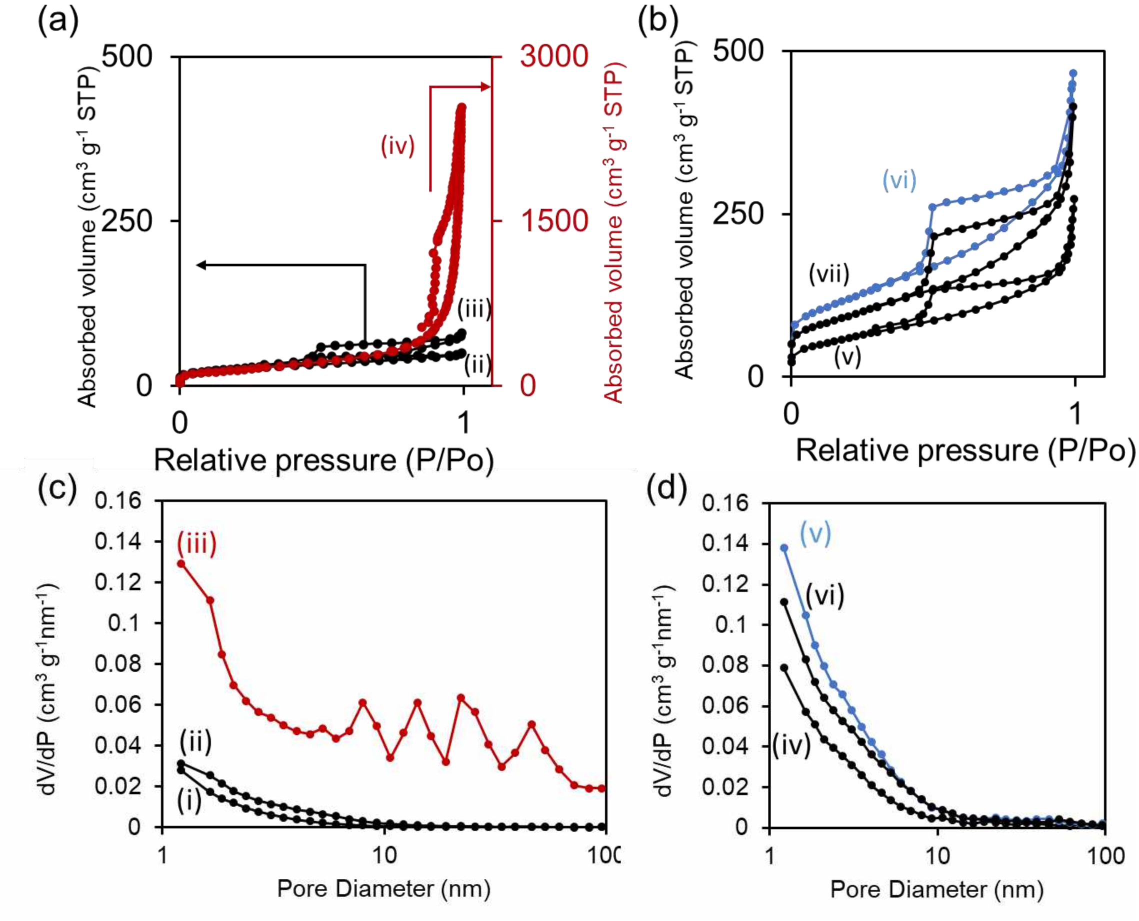

Figure 7: Isothermal N2 absorption-desorption of (a) HrGO39s and (b) HrGO14s. Pore volume distribution of (c) HrGO39s and (d) HrGO14s. (i) HrGO39, (ii) HrGO39T, (iii) HrGO39MW, (iv) HrGO14, (v) HrGO14T, (vi) HrGO14MW.

Initially, $HrGO_{39}$ has a flat 2D structure (Figure 4a and 5b), and large oxygen content, expressing a small SSA of 88 m^2 g^{-1}. The tube furnace treatment slowly removes the oxygen functional groups preserving the flat 2D structure of $HrGO_{39}$ (Figure 4b and 5b) resulting in small SSA improvement up to 93 m^2 g^{-1}. The microwave treatment explosively removes the large amount of oxygen functional groups of $HrGO_{39}$ resulting in exfoliated wrinkled 2D structure (Figure 4c and 5c), and large SSA improvement up to 532 m^2 g^{-1}. This last result indicates that in order to obtain a large SSA rGO needs to have both low oxygen content and a wrinkled 2D structure. The pore size distribution was evaluated by Barrett-Joyner-Halenda (BJH) method for all rGOs (Figure 7 and Table 1). The results indicate that the chemical reduction can generate mesopores, reaching a pore volume of 0.057 and 0.354 cm^3 g^{-1} for $HrGO_{39}$ and $HrGO_{14}$, respectively. The results for thermal reduction of those samples indicate the accentuation of the mesopore amount. For $HrGO_{14}$, the reduction by furnace method is more effective than the microwave method, reaching 0.662 and 0.592 cm^3 g^{-1} for $HrGO_{14MW}$ and $HrGO_{14MW}$, respectively. For $HrGO_{39}$, the reduction by microwave method is more effective than the furnace method, reaching a pore volume of 3.512 and 0.111 for $HrGO_{39MW}$ and $HrGO_{39T}$, respectively. The drastic increase of pore volume for $HrGO_{39MW}$ is correlated with the formation of macropores resulting from the explosive gas formation during the reduction reaction. This change in the pore volumes leads to a pore size diameter of $HrGO_{39MW}$ to 26.5 nm, where pore sizes of all other samples remained between 3 to 8 nm. These results indicate that the oxygen content of GO, the heating time, and heating speed should be chosen accordingly to optimize the pore volume distribution and the SSA by thermal treatment. Specifically, when oxygen content is low (14.4 wt.%), the heating time has more influence than heating speed, in contrast, when the oxygen content is high (39.1 wt%), the heating speed has more influence than heating time.

Taken together, precise control over rGO properties can be possible by simply designing the reduction routes. In other words, performing the same reduction on rGOs lead to different results when different oxygen content rGOs are used.

II.2. LITHIUM-ION

II.2.1. Half-cell study

The characteristics and performances of anode materials were assessed by a constant charge-discharge test in half cell vs. Li^+/Li. Based on the graphite's theoretical capacity, the current rate was fixed as 1C = 372 mA g^{-1}, and the voltage window was fixed between 0.01 V and 3.0 V to realize complete discharge and charge of lithium into the carbon host.

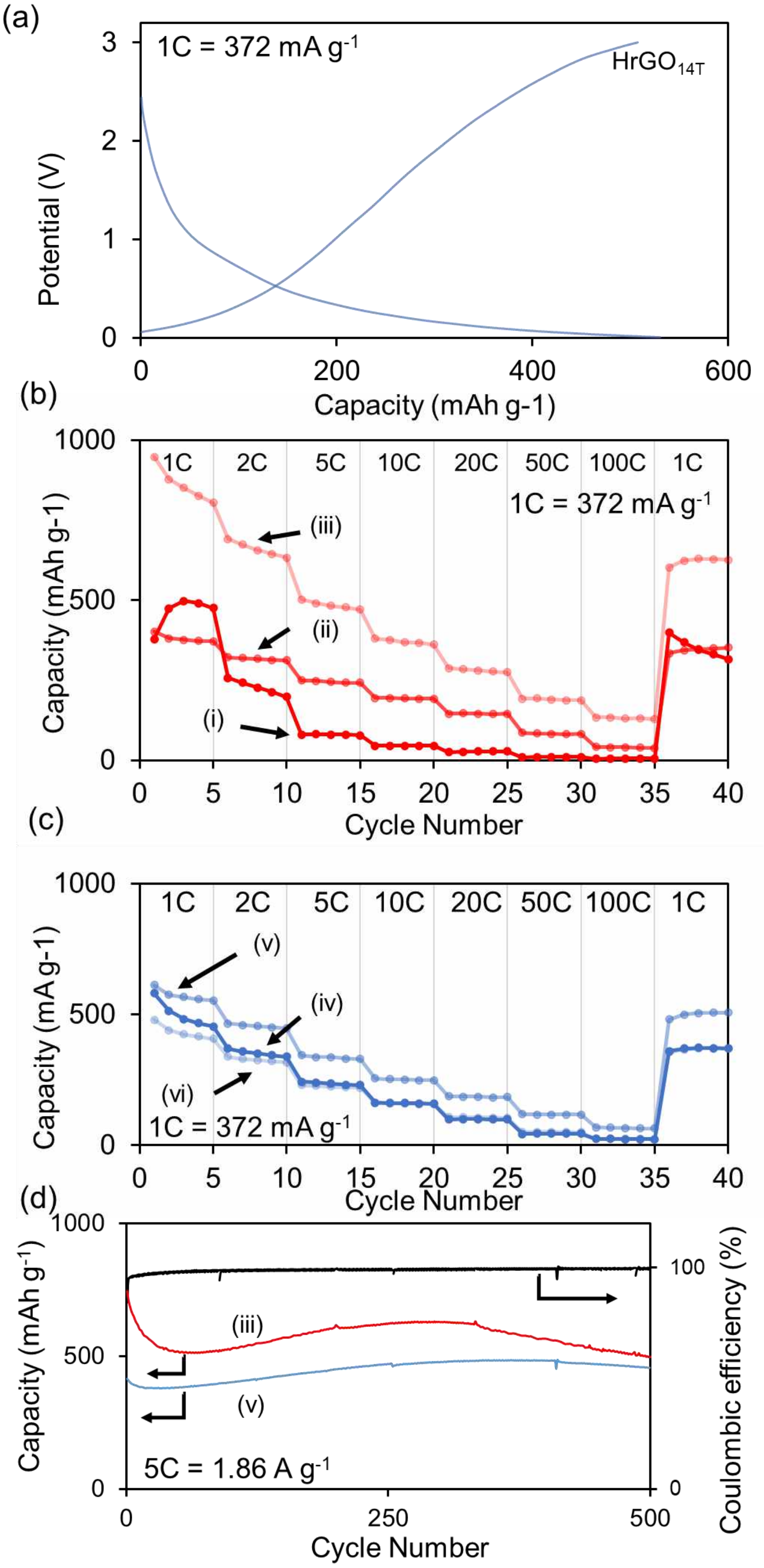

Figure 8: Half-cell lithium ion battery results of (i) $HrGO_{39}$, (ii) $HrGO_{39T}$, (iii) $HrGO_{39MW}$, (iv) $HrGO_{14}$, (v) $HrGO_{14T}$, (vi) $HrGO_{14MW}$. (a) galvanostatic charge discharge behavior, (b) and (c) rate capacity performances, (d) cycling performances and coulombic efficiency.

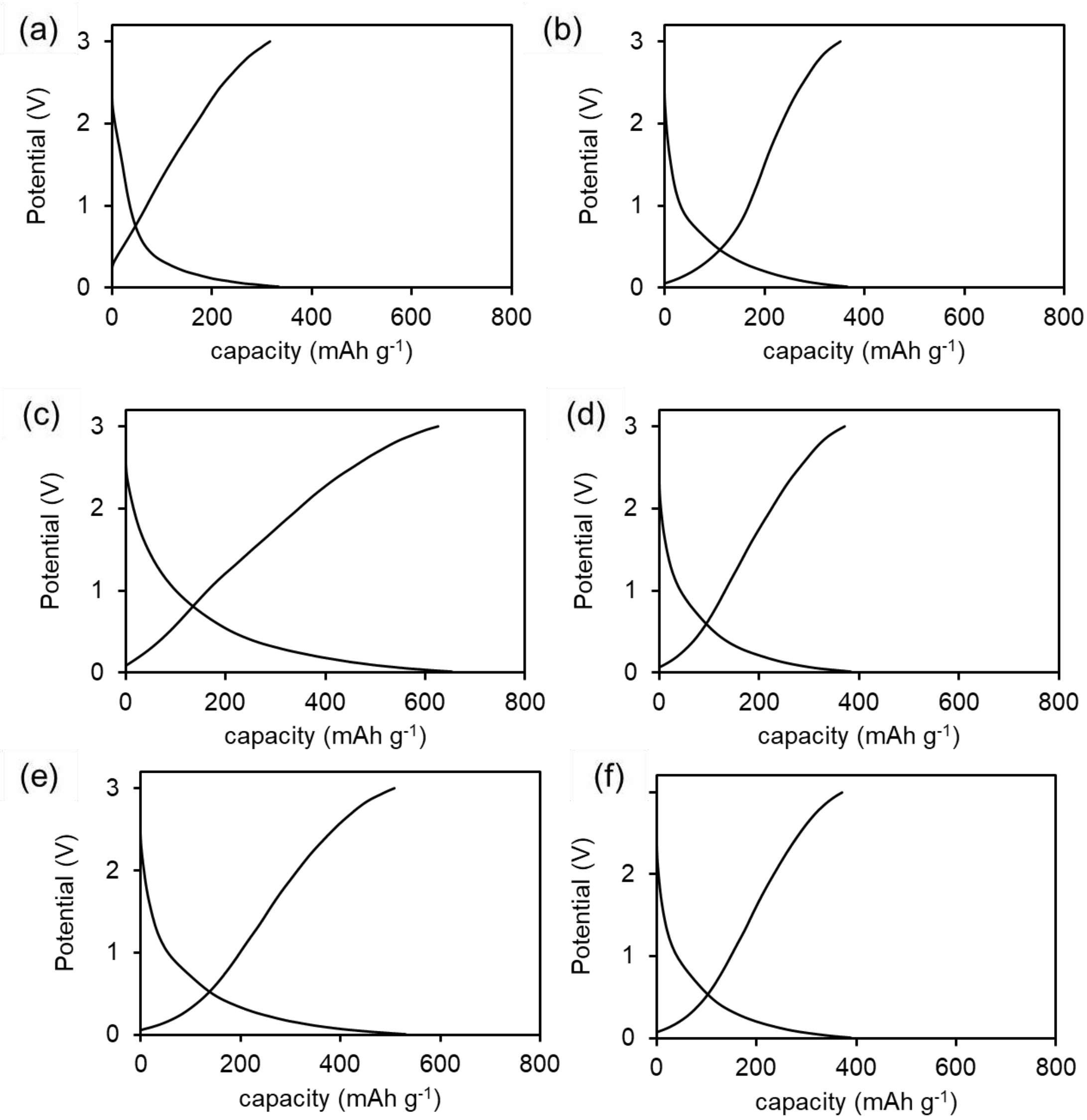

Figure 9: Charge discharge behavior of (a) $HrGO_{39}$, (b) $HrGO_{39T}$, (c) $HrGO_{39MW}$, (d) $HrGO_{14}$, (e) $HrGO_{14T}$, (f) $HrGO_{14MW}$.

In Figure 8a, the charge-discharge behavior of $HrGO_{14T}$ is displayed. $HrGO_{14T}$ and other rGOs (Figure 9) show adsorption behavior. The difference in behavior transcribes the change from battery to capacitor behavior from graphite to rGOs through the oxidation-reduction processes. The rate performance (Figure 8b and 8c) present the consecutive charge response for 5 cycles from 1C to 100C. It demonstrates that all samples, except $HrGO_{39}$, have improved capacity compared to original graphite. This first difference highlights the improvement of capacity from graphite to rGOs as a result of lithium storage on both sides of graphene layers and internal spaces. Thus, the results for rGOs present an improved capacity as the SSA increase, reaching the capacity of 507 and 629 mAh g^{-1} at 1C for $HrGO_{14T}$ and $HrGO_{39MW}$, respectively. At 20C, their capacity decreased to 186 and 281 mAh g^{-1} for $HrGO_{14T}$ and $HrGO_{39MW}$. These results indicate the higher capacity and the superior rate capability of $HrGO_{14T}$ and $HrGO_{39MW}$. The cyclability of $HrGO_{14T}$ and $HrGO_{39MW}$ were evaluated over 500 cycles at 5C (Figure 8d and Figure 10), expressing superior stability and excellent coulombic efficiency among all. The charge-discharge cycling of as-prepared carbon materials showed three phases; at first, the capacity decreased until the 20 and 70 cycles, then increased until the 420th and 399th cycles, and finally decreased for $HrGO_{14T}$ and $HrGO_{39MW}$ respectively.

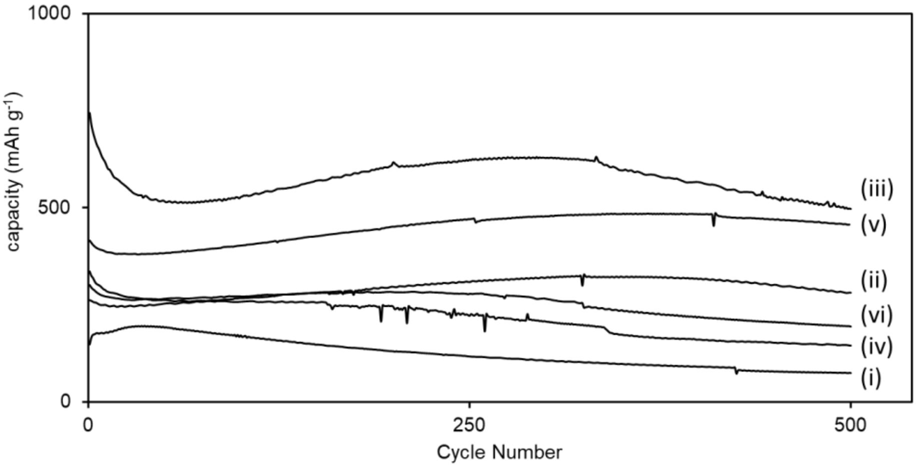

Figure 10: Cyclability of half-cell LIBs of: (i) $HrGO_{39}$, (ii) $HrGO_{39T}$, (iii) $HrGO_{39MW}$, (iv) $HrGO_{14}$, (v) $HrGO_{14T}$, (vi) $HrGO_{14MW}$.

Next, the potential was plotted against the differential capacity (Figure 11). The storage mechanism of lithium by graphene analogs can be divided from 0.01 V to 0.7 V and from 0.7 V to 3.0 V between the lithium intercalation/deintercalation occurring in graphene inter-layer and the lithium adsorption/desorption and redox reactions occurring on the graphene surface, respectively. In Figure 12, the capacity evolution above and below 0.7 V is presented. Bellow 0.7 V, all graphene samples expressed an increase and decrease in their deintercalation behavior, originating from graphene interlayer wetting with the electrolyte and the formation of the solid electrolyte interface (SEI) formation, respectively. The SEI is formed by the decomposition of the solvent and lithium salt into a protective layer between the active material and the electrolyte.[31] The SEI hiders the

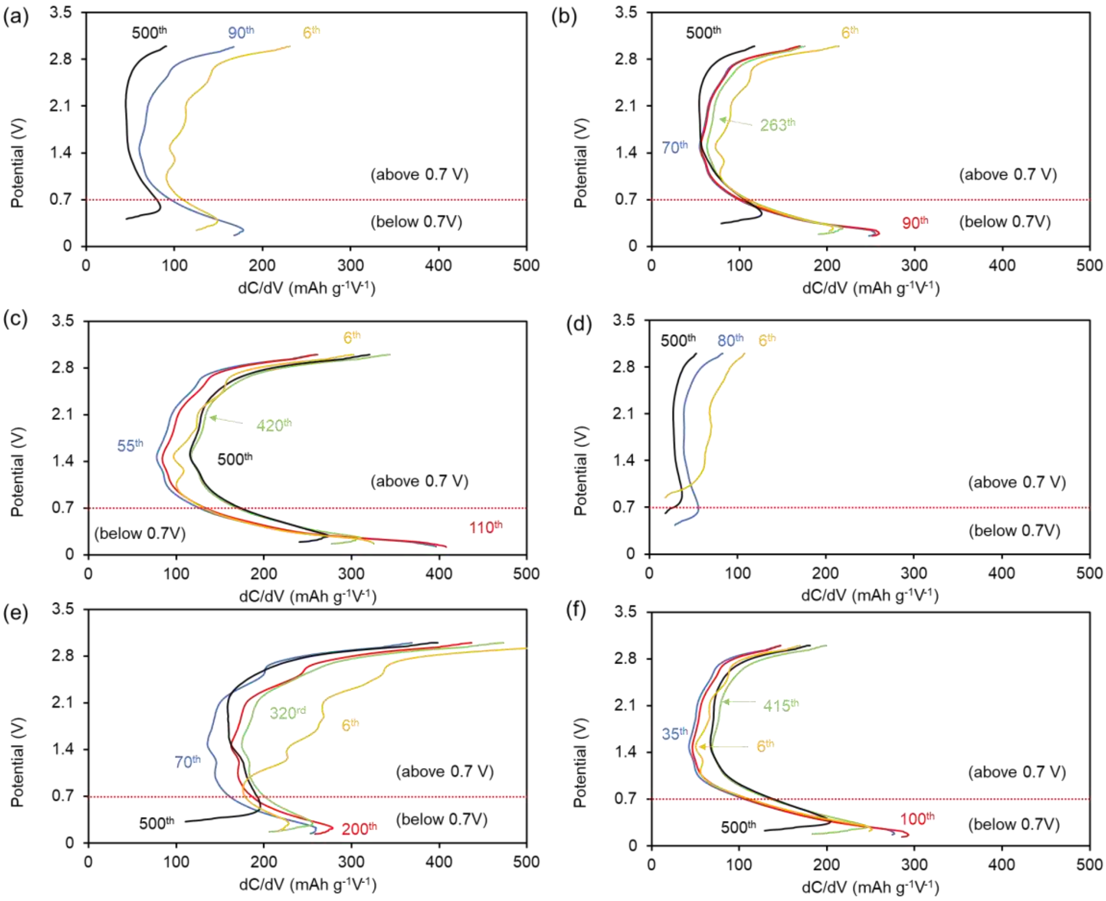

Figure 11: Differential capacity plot of half-cell LIBs of: (a) $HrGO_{14}$, (b) $HrGO_{14MW}$, (c) $HrGO_{14T}$, (d) $HrGO_{39}$, (e) $HrGO_{39MW}$, (f) $HrGO_{39T}$.

diffusion of Li^+ and isolates graphene from the electrode and the electrolyte leading to reduced performance. The SEI is mostly generated from the initial discharge process and is sensitive to graphene size, edge to basal plan ratio, pore size, and surface composition. Wetting electrode materials also leads to form SEI, and graphene volume change induces stress leading to the SEI crack and reformation.[32] Above 0.7 V, all graphene samples showed three successive phases: 1) a decrease corresponding to the fading of oxygen redox reactions at 1.2 V, 1.8 V, and 2.5 V related to graphene carbonyl oxygen functional groups; 2) an increase corresponding to the wetting of graphene by the electrolyte resulting in an increased active surface; 3) a decrease originating from the continuous SEI formation isolating graphene from the electrode and the electrolyte. The maximum desorption capacity performances of graphene analogs are observed to correlate with their SSA (Figure 13). The HrGOs results indicate that chemical reduction improves both the deintercalation and desorption behaviors by removing oxygen functional groups from its interlayer and surface (Figure 11a,d,12a,d). Furthermore, compared with thermally reduced samples, chemically reduced HrGOs did not present

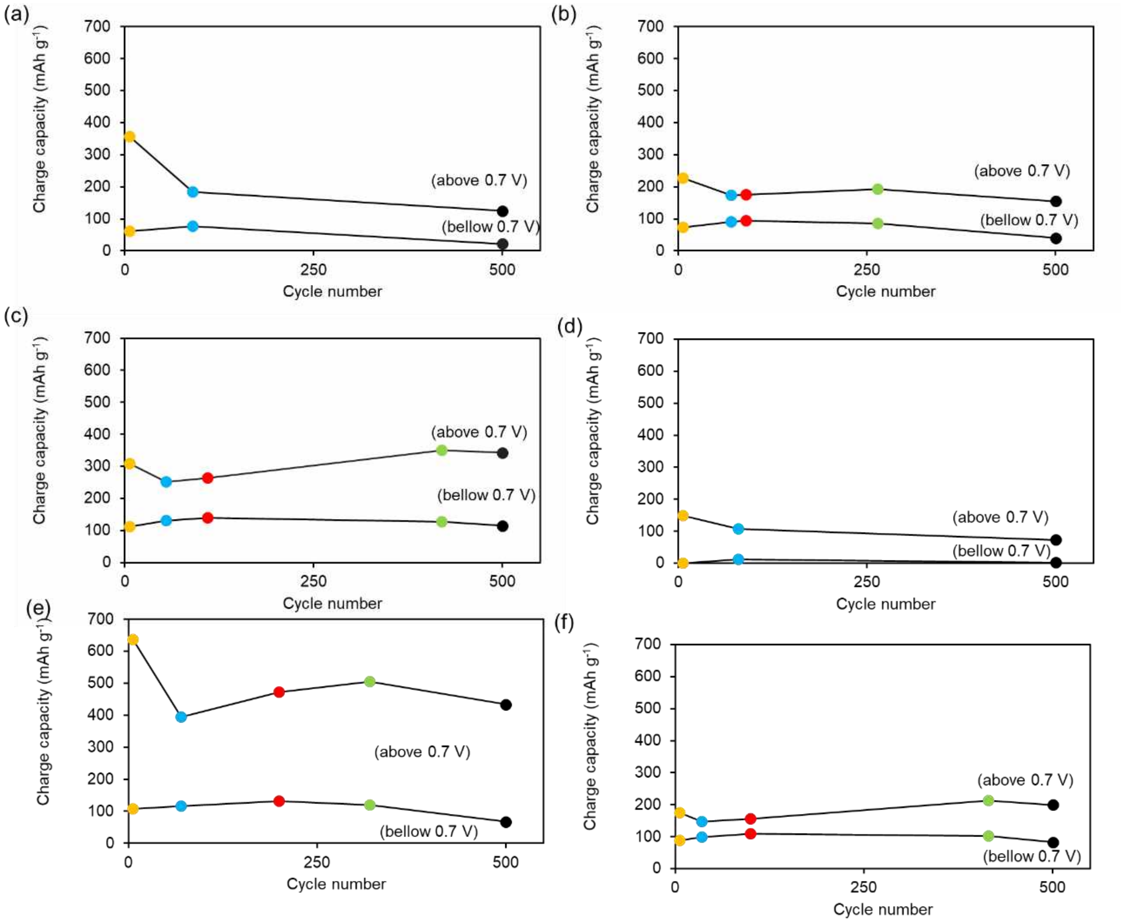

Figure 12: Capacity evolution above and below 0.7 V of half-cell LIBs of: (a) HrGO$_{14}$, (b) HrGO$_{14MW}$, (c) HrGO$_{14T,}$ (d) HrGO$_{39}$, (e) HrGO$_{39MW}$, (f) HrGO$_{39T}$.

any increase of capacity related to the Li$^+$ desorption denoting the fasten of SEI formation from excess oxygen functional groups. For HrGO$_{14}$, the tube furnace reduction method improved the intercalation and adsorption behavior, while the microwave method improved the intercalation behavior partially and only stabilized the adsorption behavior (Figure 11,12). Compared with HrGO$_{14}$, HrGO$_{14MW}$ has similar wrinkled 2D structure (Figure 5d,e), superior SSA, from 217 mm^2 g^{-1} to 333 m^2 g^{-1}, and lower oxygen content, from 14 wt.% to 6.5 wt.%. This difference results in mild capacity increase and clear stability improvement, demonstrating that the capacity is related with the SSA and that large amount of oxygen tends to reduce graphene LIBs stability. Compared with HrGO$_{14MW}$, HrGO$_{14T}$ has identical wrinkled 2D structure (Figure 5f), similar oxygen content, 5.5 wt.%, and larger SSA, 422 m^2 g^{-1}. This difference confirms that the capacity is correlating with the SSA and that small oxygen content difference has limited effect on graphene LIBs stability.

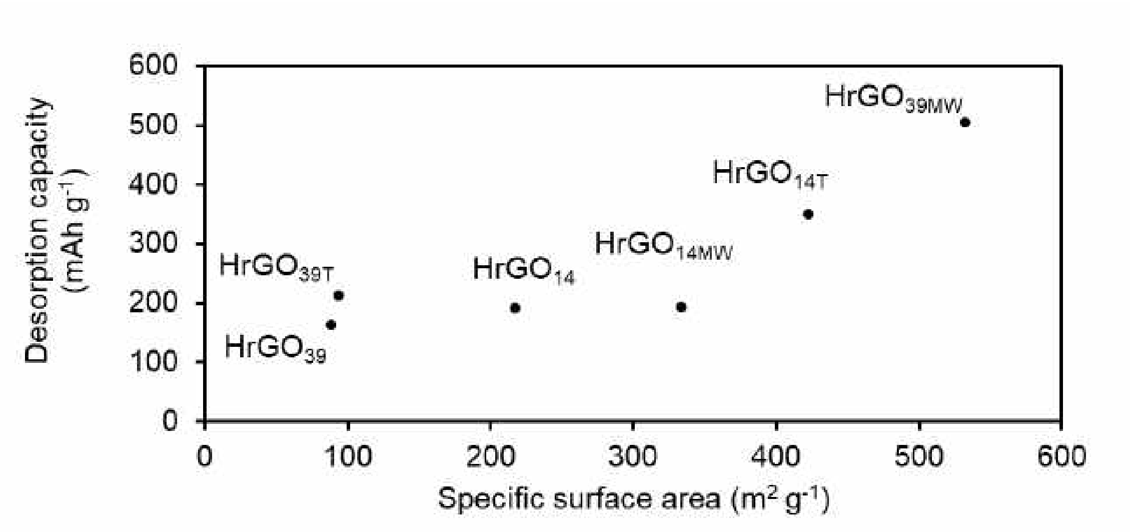

Figure 13: Maximum desorption capacity versus SSA of graphene analogs.

Above chemical and morphological analysis of HrGO$_{14x}$ revealed the decrease of the oxygen content and the increase of SSA and micropore amount, which are responsible for the superior capacity performance of HrGO$_{14T}$ over HrGO$_{14MW}$. For HrGO$_{39}$, the tube furnace heating reduction method improved the intercalation and the adsorption behavior, while the microwave method improved the intercalation behavior and more drastically the adsorption behavior (Figure 11,12). Compared with HrGO$_{39}$, HrGO$_{39T}$ has similar flat 2D structure (Figure 5a,b) and SSA, from 88 mm^2 g^{-1} to 93 m^2 g^{-1}, and lower oxygen content, from 39 wt.% to 2.9 wt.%. This difference results in slight capacity performance and clear stability improvement, highlighting that large amount of oxygen tends to reduce graphene LIBs stability. Compared with HrGO$_{39T}$, HrGO$_{39MW}$ has similar oxygen content, 4.8 wt.%, an original wrinkled 2D structure (Figure 5c), and a larger SSA, 532 m^2 g^{-1}. This difference indicates that the capacity is drastically improve by the formation of a wrinkled 2D structure as it leads to superior SSA, and that small oxygen content difference has limited effect on graphene LIBs stability. According to the chemical and morphological analyses, superior performance of HrGO$_{39MW}$ is due to its low oxygen content, which reduce SEI formation, superior SSA, which increase intercalation and adsorption behaviors, and original macropores corresponding to 6 times more pore volume compared with HrGO$_{14T}$, which is correlated with the drastic increase of the absorption capacity. Furthermore, among all samples, HrGO$_{39MW}$ expressed significant fluctuation in its capacity through cycling despite that it showed the highest capacity; this phenomenon would be related to the large pore volume and diameter of HrGO$_{39MW}$, which accelerates its wetting rate and SEI formation, leading to faster active surface increase and graphene isolation from the electrode and the electrolyte, respectively.

These results indicate that in order to produce the best rGO for LIBs in terms of capacity, rate capability, and cyclability; rGO should be synthesized from GO at its highest oxygen level, the reduction steps should start with a fast temperature increase, to exfoliate graphene layers taking advantage of oxygen functional groups decomposition, and maintain this high temperature to remove residual oxygen functional groups. As obtained rGO will displayed high SSA, high conductivity, and low oxygen content, which respectively mainly influence rGO capacity, capability, and stability.

II.2.2. Full-cell study

Convinced by the above results, we decided to assemble a full-cell combining $HrGO_{39MW}$, and our previously reported BTO-LCO as a cathode (Figure 14). We expected that both of these high rate capability materials hold great promises for high rate capability full-cell LIBs system. In order to build a full-cell system, irreversible consumption of lithium upon cycling must be considered since the lithium amount is limited in the full-cell; in the case of a half-cell, excess lithium can be supplied from the counter Li electrode.[32] The lithium consumption can be caused by (1) the SEI formation and (2) the additional SEI formation at the cracks upon charge/discharge cycle. As for cathode, BTO-LCO suppresses the formation of native SEI at a triple-phase junction, where the redox reaction actively occurs.[14,15] However, carbon-based electrodes suffer from large irreversible lithium consumption upon the first lithiation process (Table 3).

To overcome this problem, we investigated several pre-lithiation methods; chemical pre-lithiation, electrochemical pre-lithiation, and direct contact pre-lithiation (DCPL).[33–35] Compared with chemical and electrochemical pre-lithiation DCPL is fast, easy, and scalable. For these reasons, DCPL was applied to our rGOs (Figure 15a). The DCPL was performed by pressing the anode and lithium foil in the presence of 1 M L^{-1} $LiPF_6$ dissolved in a mixture of ethylene carbonate (EC) and diethyl carbonate (DEC) (v/v, 3/7).

By using the $LIPF_6$ electrolyte, we consider a flow of electron is created due to the difference of potential between the active anode material and the lithium foil.[33–35] In order to control and optimize the DCPL, a time study was conducted (Figure 16). The results showed that as the DCPL time increases, more lithium is absorbed into the carbon electrode, decreasing its half-cell initial potential. The DCPL was continued until potential values were stabilized (state of charge (SOC) of 50%).

Sample name	$HrGO_{39}$	$HrGO_{39T}$	$HrGO_{39MW}$	$HrGO_{14}$	$HrGO_{14T}$	$HrGO_{14MW}$
First discharge (mAh g^{-1})	1472	1163	2191	1529	1791	1428
First charge (mAh g^{-1})	379	402	947	581	612	480
Capacity loss (mAh g^{-1})	1093	761	1244	948	1179	948

Table 3: Charge discharge capacity of rGOs for the first cycle.

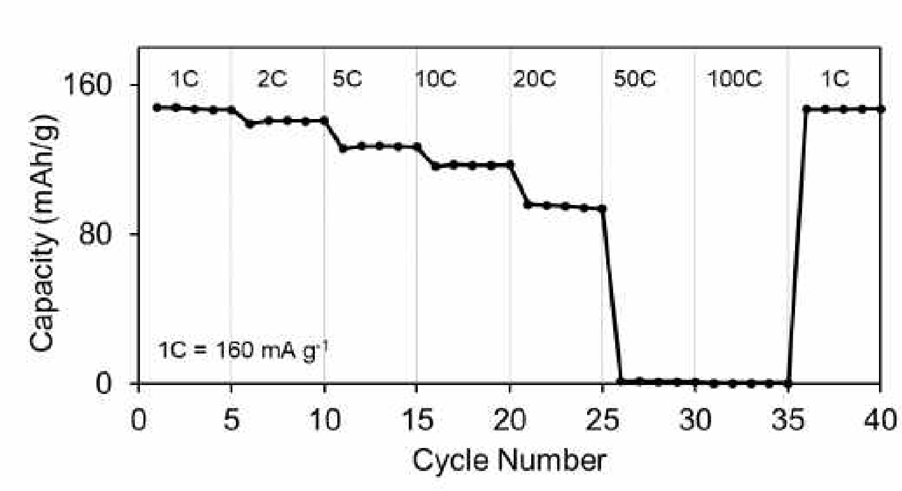

Figure 14: Half-cell capacity response of $BaTiO_3$ modified $LiCoO_2$ lithium ion battery.

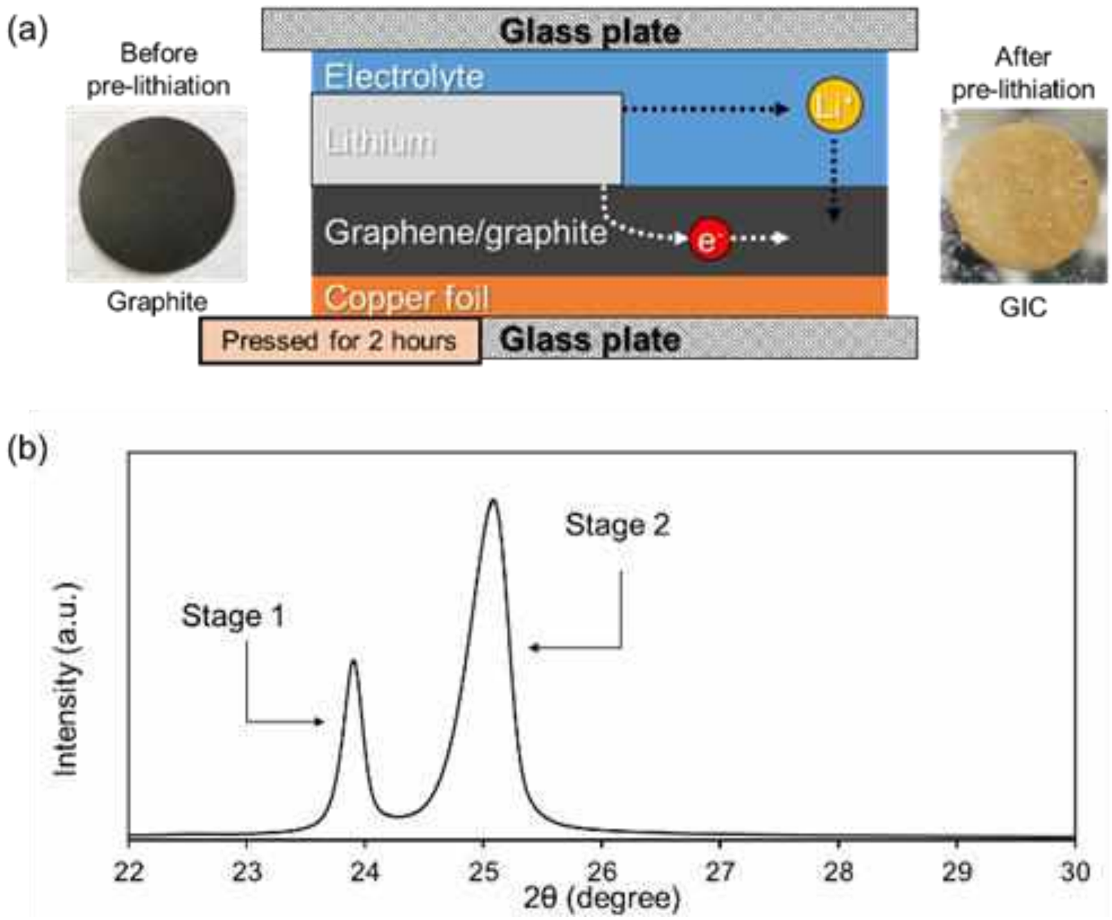

Figure 15: (a) illustration and digital images of DCPL treatment, (b) Ex-situ XRD of pre-lithiated graphite electrode.

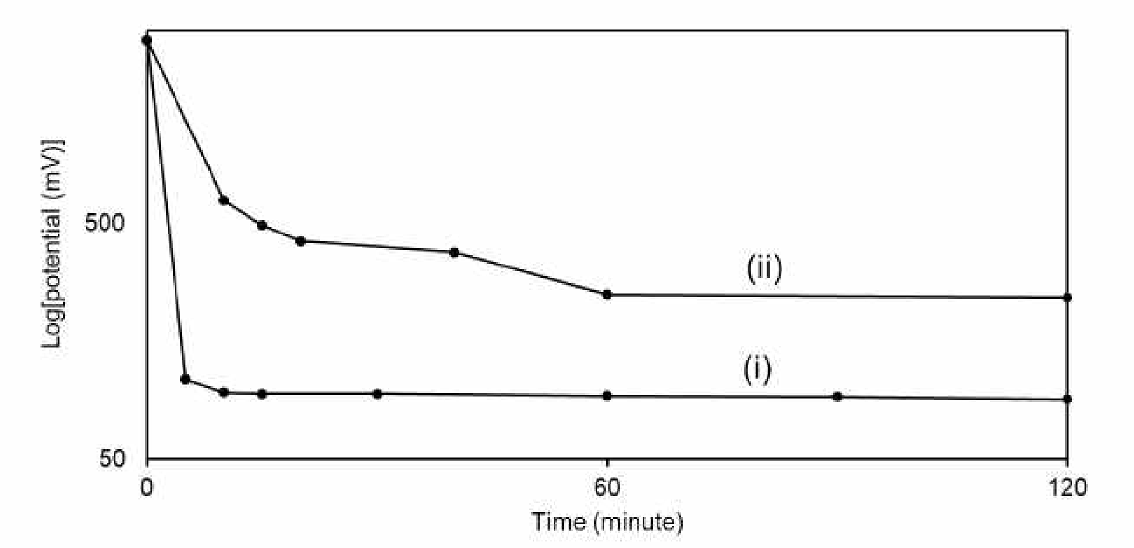

Figure 16: Initial open circuit voltage of (i) graphite and (i) $HrGO_{14T}$ half-cell as pre-lithiation time increase.

Table 4: Effects of pre-lithiation of HrGO14T charge discharge capacity during the first cycle.

	$HrGO_{39MW}$	
	No treatment	Pre-lithiation
First discharge (mAh g^{-1})	1872	234
First charge (mAh g^{-1})	624	661

In the case of graphite after only 15 min of DCPL, the potential stabilized at 100 mV, indicating complete pre-lithiation, while for $HrGO_{39MW}$, the pre-lithiation required 2 hours to reach a stable value of 250 mV. The lithiation of the graphite electrode was visually recognizable; changing color from black to yellow was observed (Figure15a). The progress of lithiation was also confirmed by XRD; its original structure showed a peak at 26.3° while after DPCL it displayed a mixture of graphite interacted compound stage 1 at 23.9° and stage 2 at 25.1° (Figure 15b). The effect of DCPL on graphite or $HrGO_{14T}$ anode half-cells was evaluated, as a result, the initial irreversible capacity decreased (Table 4), and the SEI formation within 1.4 V to 1.0 V disappeared (Figure 17), indicating the successful SEI formation by our DCPL treatment.

In light of these positive results, full-cell was prepared by applying DCPL on anode material prior assembly. Two full-cells were assembled composed of a BTO-LCO cathode and a $HrGO_{39MW}$ anode using a capacity ratio of anode to cathode (N/P ratio) of 1.1 and 2.3, respectively named $LC\text{-}rGO_{1.1}$ and $LC\text{-}rGO_{2.3}$. The full-cells were evaluated at constant current at various current rate from 1C (1C = 160 mA g^{-1}) to 100C.

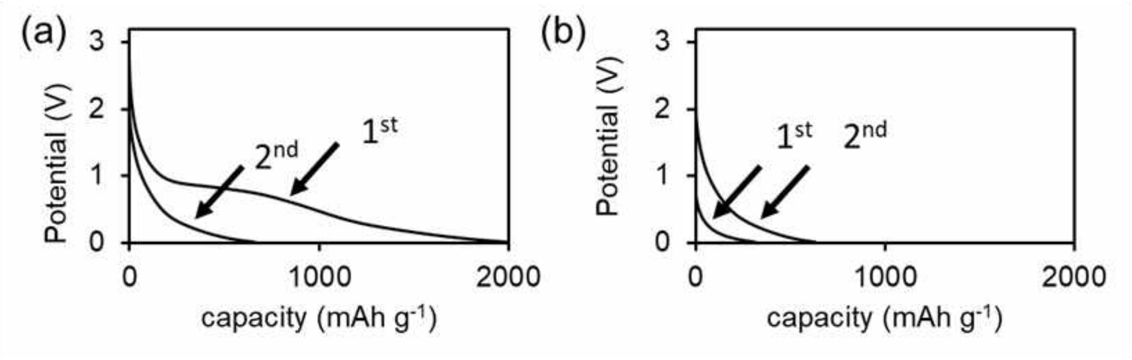

Figure 17: Half-cell lithium ion battery discharge behavior of 1st and 2nd cycle of: $HrGO_{14MW}$ (a) no treatment, (b) pre-lithiation.

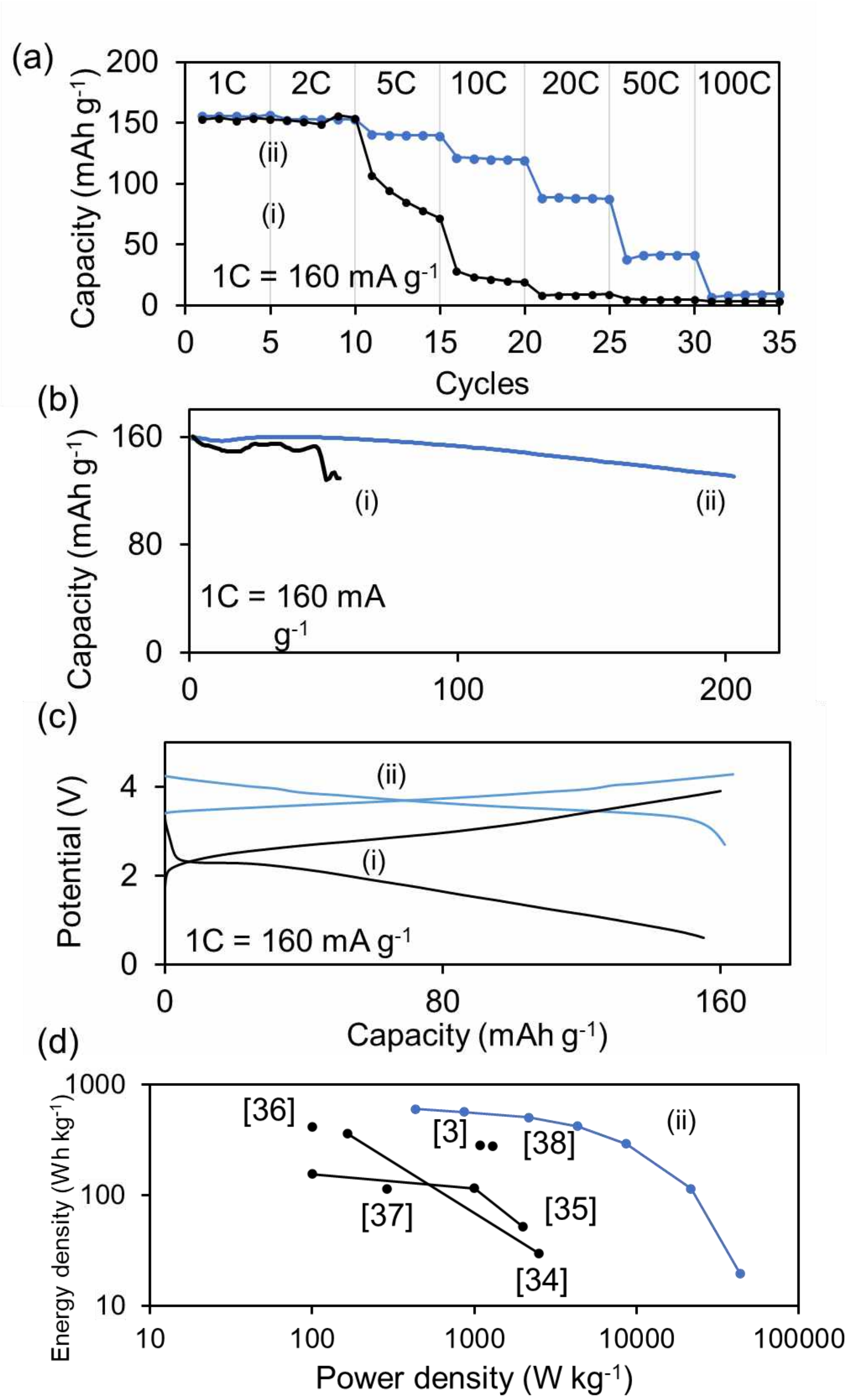

Figure 18: Full-cell lithium ion battery results of LC-rGO with N/P equal to (i) 1.1, (ii) 2.3. (a) Full-cell rate performances, (c) Full-cell cyclability at 1C, (c) full-cell galvanostatic charge discharge behavior, (d) Ragone plots of lithium metal oxide full-cell.

The results (Figure 18a) show that both designs have similar capacity performances at 1C and 2C showing a capacity of 154 mAh g^{-1}. At higher current density LC-rGO$_{2.3}$ showed superior rate capability performance compared with LC-rGO$_{1.1}$, at 20C LC-rGO$_{2.3}$ showed 88 mAh g^{-1} while LC-rGO$_{1.1}$ showed 10 mAh g^{-1}, corresponding to 56%

and 6% capacity retention once compared with the maximum capacity at 1C. Furthermore, stability study indicated that LC-rGO$_{1.1}$ start fading after only 50 cycles (Figure 18bi), while LC-rGO$_{2.3}$ remained stable even after 180 cycles (Figure 18bii). All these results demonstrate the higher capacity, rate capability, and stability of LC-rGO$_{2.3}$ over LC-rGO$_{1.1}$. The poor stability and capability of lower N/P ratio LC-rGO might be due to the irreversible capacity consumption of rGO electrode from the LC electrode, as in this configuration rGO volume deformation upon lithium absorption and desorption lead to higer mechanical stress and SEI cracking. Moreover, the charge-discharge behavior of LC-rGO$_{2.3}$ full-cell showed excellent battery behavior similar to BTO-LCO half-cell, displaying a flat charge-discharge plateau at 3.7 V (Figure 18cii). Furthermore, LC-rGO$_{2.3}$ showed similar to better capacity performances compared with BTO-LCO cathode half-cell; at 50C, the full-cell shows 42 mAh g^{-1} while the half-cell shows close to 0 mAh g^{-1} (Figure 14). These results demonstrate the superiority of our pre-lithiated rGO over lithium foil, opening the door for high rate performance LIBs. Compared with other recently reported LIBs full-cells (Figure 18d), our LC-rGO full-cell showed superior power and energy densities;[36–41] LC-rGO2.3 delivered 604 Wh kg-1 at 432 W kg-1 and maintained 293 Wh kg-1 at 8,658 W kg-1 and 20 Wh kg-1 at 43,333 W kg-1.

III. CONCLUSION

In summary, the combination of chemical and thermal reduction process allows excellent control over rGO crystallinity, disorder, oxygen content, conductivity, and surface area. These differences are ascribed to the amount and speed of oxygen functional group decomposition. The application of as-prepared rGOs toward half-cell LIBs technology reveals that the control of such reduction methods and thus control over rGO properties is a key to unlock high capacity, high rate capability, high stability anode materials. Furthermore, optimized rGO applied toward full-cell LIBs using our original DCPL method allows perfect technology transfer from our previous high rate BTO-LCO cathode half-cell toward higher energy density and power density full-cell.

EXPERIMENTAL SECTION

1. Materials

HBF$_4$, methanol, KMnO$_4$, H$_2$SO$_4$, 30% aq. H$_2$O$_2$, hydrazine hydrate, were purchased from Wako Pure Chemical Industries, Ltd. Graphite foil was provided from KANEKA. All the chemicals were used directly without further purification.

2. Characterization instrumentation

Elemental analyses were performed by PERKINELMER 2400II. Freeze-dried of GO was performed by ADVANTEC DRZ350WC. XPS was measured by JPS-9030 with a pass energy of 20 eV. The crystalline structure of samples was characterized by X-ray diffraction (XRD) using a PANalytical Co. X' part PRO using Cu Kα radiation (= 1.541 Å) in the 2θ range of 5–75°. The operating tube current and voltage were 30 mA and 40 kV, respectively. The data was collected at the step size of 0.017° and the type of scan was continuous. The UV-Vis measurements were conducted on a JASCO V-670 spectrophotometer. The morphology was measured by transmission electron microscopy (TEM) JEOL JEM-2100F and atomic force microscopy (AFM) SHIMADZU SPM-9700HT, while the functional groups on the surface of prepared catalyst were recorded by Fourier transform infrared spectrometer (FT-IR SHIMADZU IR Tracer 100), the sample for FT-IR were dried and mixed with KBr, and then pressed up to 1.3 mm-diameter pellets. The products were quantified by gas chromatography GC (Shimadzu GC-2014 equipped with flame ionized detector FID detector). Electrical conductivities were measured by using MITSUBISHI CHEMICAL ANALYTECH MCP-T610. The cyclic voltammograms of the second cycle were collected on Solartron 1287 electrochemical instrument at the scan rate 50 mV s^{-1}. Raman spectra were measured by Horiba Jobin Yvon Inc. T-64000. The thermogravimetry analysis (TGA) was conducted on a RIGAKU TG 8121.

Solid-state ^{13}C NMR spectra were recorded using an NMR system (11.7 T magnet, DD2 spectrometer; Agilent technology Inc.) at a magic angle spinning (MAS) speed of 10 kHz. A single pulse sequence with a 3.2 μs pulse and repetition time (10 s) was applied. The signal of TMS was applied to a reference at 0 ppm. Because a broad background ^{13}C signal which stems from a spacer, a top cover and a bottom drive tip in a MAS sample rotor was not negligible, we measured ^{13}C spectra of not only the samples in sample rotors but also of blank (the sample rotors only). The net signal spectra were obtained by subtracting the blank spectra from the former spectra including sample and background signal. Each spectrum was obtained by accumulation over 5000 scans.

3. Preparation of CGO

Natural flake graphite (3.0 g) was stirred in 95% H_2SO_4 (75 mL). $KMnO_4$ (9.0 g) was gradually added to the solution keeping the temperature <10 °C. The mixture was then stirred at 35 °C for 2 h. The resulting mixture was diluted by water (75 mL) under vigorous stirring and cooling so that temperature does not exceed 50 °C. The suspension was further treated by 30% aq. H_2O_2 (7.5 mL). The resulting graphite oxide suspension was purified by centrifugation with water until neutralization, and freeze-dried.

Highly oxidized chemical graphene oxide (HCGO) was produced by applying the same procedure as above replacing graphite by CGO.

4. Preparation of GO samples for elemental analysis

GO is hydrophilic and adsorb ca. 10 wt% of water by exposing air. We dried GO under vacuum at 50 °C for three days, of which method is following a previous report.[19,42]

5. Li-ion battery anode sheets preparation

The working electrodes were made of active material (graphite and rGO), conductive material (acetylene black), and binder (Polyvinylidene fluoride) in a weight ratio of 7:2:1 by using N-Methyl-2-pyrrolidone as a solvent and a copper foil as the current collector. In order to obtain the homogeneous active and conductive material powder, both materials were mixed in a distilled water-ethanol solution (v/v, 1/1). After mixing, the solution was filtered using Merck Millipore JAWP04700 filter. The powder was freeze and then freeze-dry under vacuum at 30 °C for 24 h. The dry powder was set into ball-milling for 30 min at 300 RPM to reduce the particle size. Then the powder was at first mixed with NMP to obtain a homogeneous slurry and then with the binder. The slurry (active material, conductive material, binder) was spread on a copper foil using a Doctor blade (100 µm thickness). The sheet was dried under vacuum at room temperature for 24 h and in air at 120 °C for 20 min. Finally, sheets with a diameter of 15.95 mm were punched and pressed.

6. Coin cells assembling

The CR2032 coin cells were assembled in an argon-filled glove box using metallic lithium as the counter electrode with a Whatman 1823-257 as a separator and 70 µL electrolyte. The electrolyte was 1 M L^{-1} $LiPF_6$ dissolved in a mixture of ethylene carbonate (EC), diethyl carbonate (DEC) (v/v, 3/7).

7. Battery cycling

The charge and discharge cycling tests were performed using a multi-channel battery tester (580 8 channel Battery Cycler Scribner Associates Incorporated) with a voltage window of 0.01 V and 3 V. Each cells were subject to discharge charge cycles at different current rates: 1C, 2C, 5C, 10C, 20C, 50C, 100C, and 1C for stability. All currents have been calculated using 372 mAh g^{-1} as a theoretical specific capacity.

8. Oxidation of benzyl alcohol

Typically, 0.3 mmol of benzyl alcohol, 20 mg of GO, and 0.5 mL of dichloroethane were added to 30 mL round bottom flask, and the mixture was heated at 60 °C under air. After 12 hours, the reaction mixture was cooled and analyzed by gas chromatography using decane as an internal standard.

REFERENCES

1. Gao, X., Wang, F., Gollon, S. & Yuan, C. Micro Silicon–Graphene–Carbon Nanotube Anode for Full Cell Lithium-ion Battery. *J. Electrochem. En. Conv. Stor.* **16**, 011009-011009–6 (2018).
2. Xu, H. *et al.* Roll-to-roll prelithiation of Sn foil anode suppresses gassing and enables stable full-cell cycling of lithium ion batteries. *Energy Environ. Sci.* (2019) doi:10.1039/C9EE01404G.
3. Lee, S. W., Ryu, I., Nix, W. D. & Cui, Y. Fracture of crystalline germanium during electrochemical lithium insertion. *Extreme Mechanics Letters* **2**, 15–19 (2015).
4. Zhang, Q. *et al.* Harnessing the concurrent reaction dynamics in active Si and Ge to achieve high performance lithium-ion batteries. *Energy Environ. Sci.* **11**, 669–681 (2018).
5. Fujimoto, H., Tokumitsu, K., Mabuchi, A., Chinnasamy, N. & Kasuh, T. The anode performance of the hard carbon for the lithium ion battery derived from the oxygen-containing aromatic precursors. *Journal of Power Sources* **195**, 7452–7456 (2010).
6. Tian, H., Xin, F., Wang, X., He, W. & Han, W. High capacity group-IV elements (Si, Ge, Sn) based anodes for lithium-ion batteries. *Journal of Materiomics* **1**, 153–169 (2015).
7. Liu, X. H. *et al.* Size-Dependent Fracture of Silicon Nanoparticles During Lithiation. *ACS Nano* **6**, 1522–1531 (2012).
8. Yoo, E. *et al.* Large Reversible Li Storage of Graphene Nanosheet Families for Use in Rechargeable Lithium Ion Batteries. *Nano Lett.* **8**, 2277–2282 (2008).
9. Cho, J., Kim, Y. J. & Park, B. Novel LiCoO2 Cathode Material with Al2O3 Coating for a Li Ion Cell. *Chem. Mater.* **12**, 3788–3791 (2000).

10. Cho, J., Kim, Y. J. & Park, B. LiCoO2 Cathode Material That Does Not Show a Phase Transition from Hexagonal to Monoclinic Phase. *J. Electrochem. Soc.* **148**, A1110–A1115 (2001).
11. Scott, I. D. *et al.* Ultrathin Coatings on Nano-LiCoO2 for Li-Ion Vehicular Applications. *Nano Lett.* **11**, 414–418 (2011).
12. Jung, Y. S. *et al.* Enhanced Stability of LiCoO2 Cathodes in Lithium-Ion Batteries Using Surface Modification by Atomic Layer Deposition. *J. Electrochem. Soc.* **157**, A75–A81 (2010).
13. Teranishi, T. *et al.* Aluminum Interdiffusion into LiCoO2 Using Atomic Layer Deposition for High Rate Lithium Ion Batteries. *ACS Appl. Energy Mater.* **1**, 3277–3282 (2018).
14. Teranishi, T. *et al.* High-rate performance of ferroelectric BaTiO3-coated LiCoO2 for Li-ion batteries. *Appl. Phys. Lett.* **105**, 143904 (2014).
15. Teranishi, T. *et al.* Low-Temperature High-Rate Capabilities of Lithium Batteries via Polarization-Assisted Ion Pathways. *Advanced Electronic Materials* **4**, 1700413 (2018).
16. Cai, X., Lai, L., Shen, Z. & Lin, J. Graphene and graphene-based composites as Li-ion battery electrode materials and their application in full cells. *J. Mater. Chem. A* **5**, 15423–15446 (2017).
17. Ripeng Luo, W. L. & Ripeng Luo, W. L. Overview of Graphene as Anode in Lithium-ion Batteries. *Journal of Electronic Science and Technology* 1–12 doi:10.11989/JEST.1674-862X.6032519.
18. Zhu, X., Zhu, Y., Murali, S., Stoller, M. D. & Ruoff, R. S. Nanostructured Reduced Graphene Oxide/Fe2O3 Composite As a High-Performance Anode Material for Lithium Ion Batteries. *ACS Nano* **5**, 3333–3338 (2011).

19. Morimoto, N., Kubo, T. & Nishina, Y. Tailoring the Oxygen Content of Graphite and Reduced Graphene Oxide for Specific Applications. *Scientific Reports* **6**, 21715 (2016).
20. Stankovich, S. *et al.* Synthesis of graphene-based nanosheets via chemical reduction of exfoliated graphite oxide. *Carbon* **45**, 1558–1565 (2007).
21. Kim, M. C., Hwang, G. S. & Ruoff, R. S. Epoxide reduction with hydrazine on graphene: A first principles study. *J. Chem. Phys.* **131**, 064704 (2009).
22. Park, S. *et al.* Chemical structures of hydrazine-treated graphene oxide and generation of aromatic nitrogen doping. *Nat Commun* **3**, 1–8 (2012).
23. Chua, C. K. & Pumera, M. Chemical reduction of graphene oxide: a synthetic chemistry viewpoint. *Chem. Soc. Rev.* **43**, 291–312 (2013).
24. Schniepp, H. C. *et al.* Functionalized Single Graphene Sheets Derived from Splitting Graphite Oxide. *J. Phys. Chem. B* **110**, 8535–8539 (2006).
25. Wu, Z.-S. *et al.* Synthesis of Graphene Sheets with High Electrical Conductivity and Good Thermal Stability by Hydrogen Arc Discharge Exfoliation. *ACS Nano* **3**, 411–417 (2009).
26. McAllister, M. J. *et al.* Single Sheet Functionalized Graphene by Oxidation and Thermal Expansion of Graphite. *Chem. Mater.* **19**, 4396–4404 (2007).
27. Ferrari, A. C. & Basko, D. M. Raman spectroscopy as a versatile tool for studying the properties of graphene. *Nature Nanotechnology* **8**, 235–246 (2013).
28. Pei, S. & Cheng, H.-M. The reduction of graphene oxide. *Carbon* **50**, 3210–3228 (2012).
29. Gadipelli, S. & Guo, Z. X. Graphene-based materials: Synthesis and gas sorption, storage and separation. *Progress in Materials Science* **69**, 1–60 (2015).

30. Diby Ossonon, B. & Bélanger, D. Synthesis and characterization of sulfophenyl-functionalized reduced graphene oxide sheets. *RSC Advances* **7**, 27224–27234 (2017).
31. Mukherjee, R., Thomas, A. V., Krishnamurthy, A. & Koratkar, N. Photothermally Reduced Graphene as High-Power Anodes for Lithium-Ion Batteries. *ACS Nano* **6**, 7867–7878 (2012).
32. An, S. J. *et al.* The state of understanding of the lithium-ion-battery graphite solid electrolyte interphase (SEI) and its relationship to formation cycling. *Carbon* **105**, 52–76 (2016).
33. Park, H. *et al.* In situ synchrotron wide-angle X-ray scattering study on rapid lithiation of graphite anode via direct contact method for Li-ion capacitors. *Journal of Power Sources* **283**, 68–73 (2015).
34. Holtstiege, F., Bärmann, P., Nölle, R., Winter, M. & Placke, T. Pre-Lithiation Strategies for Rechargeable Energy Storage Technologies: Concepts, Promises and Challenges. *Batteries* **4**, 4 (2018).
35. Shellikeri, A. *et al.* Pre-Lithiation of Carbon Anodes Using Different Lithium - Sources. *ECS Trans.* **77**, 293–303 (2017).
36. Wang, C. *et al.* Fabrication and Shell Optimization of Synergistic TiO2-MoO3 Core–Shell Nanowire Array Anode for High Energy and Power Density Lithium-Ion Batteries. *Advanced Functional Materials* **25**, 3524–3533 (2015).
37. Yu, Y. *et al.* Achieving High-Energy Full-Cell Lithium-Storage Performance by Coupling High-Capacity V2O3 with Low-Potential Ni2P Anode. *ACS Appl. Mater. Interfaces* **11**, 19–25 (2019).
38. Fang, Z. *et al.* Preparation and Optimization of New High-Power Nanoscale Li4Ti5O12 Full-Cell System. (2018) doi:info:doi/10.1166/jnn.2018.16385.

39. Ming, H. *et al.* High dispersion of TiO2 nanocrystals within porous carbon improves lithium storage capacity and can be applied batteries to LiNi0.5Mn1.5O4. *J. Mater. Chem. A* **2**, 18938–18945 (2014).

40. Sun, H. *et al.* Hard carbon/lithium composite anode materials for Li-ion batteries. *Electrochimica Acta* **52**, 4312–4316 (2007).

41. Sun, Z. *et al.* A Practical Li-Ion Full Cell with a High-Capacity Cathode and Electrochemically Exfoliated Graphene Anode: Superior Electrochemical and Low-Temperature Performance. *ACS Appl. Energy Mater.* **2**, 486–492 (2019).

42. Morimoto, N. *et al.* Real-Time, in Situ Monitoring of the Oxidation of Graphite: Lessons Learned. *Chem. Mater.* **29**, 2150–2156 (2017).

CHAPTER 4

Iron nanoparticle templates for constructing 3D graphene frame-work with enhanced performance in sodium-ion batteries

ABSTRACT: This study examines the synthesis and electrochemical performance of three-dimensional graphene for use as Li-ion batteries and Na-ion batteries. The in-situ formation of iron hydroxide nanoparticles (Fe(OH)x NPs) of various weights on the surface of graphene oxide, followed by thermal treatment at elevated temperature and washing using hydro-chloric acid, furnished 3D graphene. The characterization confirmed the prevention of stacking graphene layers by over 90% more than thermal treatment without Fe(OH)x. The electrochemical performance of the 3D graphene was evaluated as a counter electrode for lithium metal and sodium metal in a half-cell configuration. This material showed good cycling ability with a charging capacity of 507 mAh g-1 at 372 mA g-1 in Li-ion battery and 252 mAh g-1 at 100 mA g-1 in Na-ion battery, which is 1.4 and 1.9 times higher, respectively, than the graphene prepared without Fe(OH)x tem-plates.

I. INTRODUCTION

Among all rechargeable batteries, Li-ion batteries (LIBs) certainly improved our lives with their high energy density, tiny memory effect, and low self-discharge. Since the commercialization of LIBs in 1990, graphite electrode has been used as an anode material despite its small theoretical capacity of 372 mAh g^{-1}.[1] The small interlayer distance of graphite induces a limited storage space, as well as a narrow diffusion pathway for the Li ions, leading to its small electric capacity and low rate capability. Furthermore, the small distance between graphite layers hampers the utilization of Na ions, which are more abundant in resources than Li ions.[2–6] Therefore, the aim of research in the area of rechargeable batteries is the development of high capacity electrodes with adequate space between graphene layers.

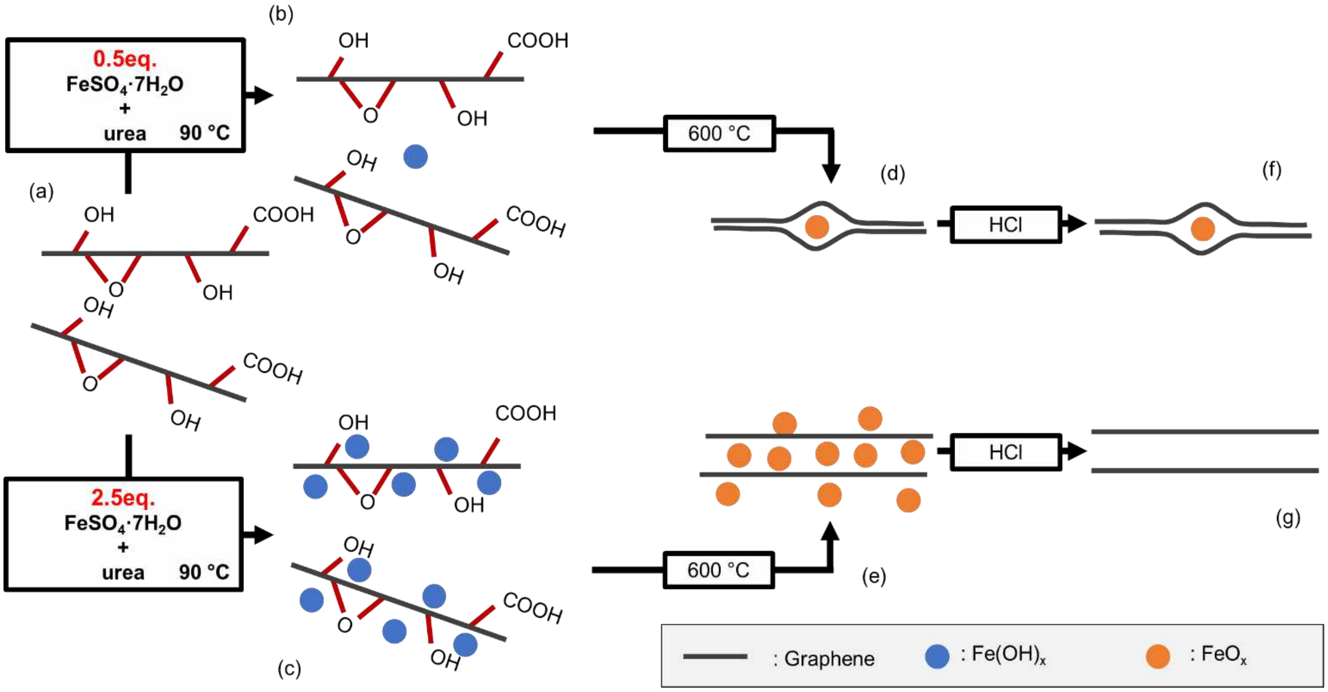

Figure 1. rGO synthesis: (a) GO, (b) GO-$Fe(OH)_{0.5}$, (c) GO-$Fe(OH)_{2.5}$, (d) rGO-$FeO_{0.5}$, (e) rGO-$FeO_{2.5}$, (f) $G_{0.5}$, (g) $G_{2.5}$.

To address these issues, graphene emerged as a candidate material to provide higher energy and power density LIBs and Na-ion batteries (SIBs). Indeed, it is considered that graphene can adsorb ions on both sides and defect sites.[1,7] However, the aggregation and re-stacking lead to a much smaller specific surface area than the theoretical value. As a result, the space and pathway for ion storage and mobility are reduced, leading to a small capacity and low rate capability. In the present work, we report a cost-effective and scalable approach to produce 3D graphene architectures, which are unstacked forms of reduced graphene oxide (rGO) with the aid of iron oxide nanoparticles (FeO_x NPs) between graphene layers. Initially, GO, urea, and $FeSO_4 \cdot 7H_2O$ were mixed in water to form GO-$Fe(OH)_x$. Then it was dried and thermally treated under N_2 to form rGO-FeO_x. Finally, iron was etched with aq. HCl to form 3D graphene. This research demonstrates that adjusting the ratio of $FeSO_4 \cdot 7H_2O$ and GO (Fe/GO), and the heating temperature enables the formation of excellent materials for LIBs, displaying 745 mAh g^{-1} at 372 mA g^{-1} instead of 525 mAh g^{-1}, as well as for SIBs, expressing 362 mAh g^{-1} at 100 mA g^{-1} instead of 173 mAh g^{-1}. This synthesis approach presents a promising route for the large-scale production of rGO as electrode materials for SIBs.

II. RESULTS AND DISCUSSION

The 3D graphene was prepared in four steps, as illustrated in Figure 1. For the first step, highly dispersible GO was prepared from graphite by our modified Hummers' method (Figure 1a).[8,9] In the second step, iron hydroxide nanoparticles ($Fe(OH)_x$ NPs) were formed on the surface of the GO layer by heating the GO, $FeSO_4 \cdot 7H_2O$, and urea in water at 90 °C for 2 hours (Figure 1b,c).[10] The formed GO-$Fe(OH)_x$ composite was collected by centrifugation, and then freeze dried. The obtained materials were termed GO-$Fe(OH)_x$ (x= 0.5, 1.0, 1.5, 2.5). In the third step, GO-$Fe(OH)_x$ was thermally treated under N_2 atmosphere to form unstacked rGO and FeO_x composite (rGO-FeO_x), where the GO reduction and FeO_x NPs formation occurred simultaneously (Figure 1 d,e). The FeO_x NPs worked as spacers to prevent the re-stacking of graphene sheets. The samples were prepared by introducing various iron amounts: 0 eq., 0.5 eq., 1 eq., 1.5 eq., and 2.5 eq. of the weight of GO, respectively. These were termed rGO and rGO-FeO_x (x= 0.5, 1.0, 1.5, 2.5). The temperature of thermal treatment was investigated from 90 to 600 °C. In the last step, 3D graphene was obtained by washing FeO_x NPs out with concentrated hydrochloric acid (Figure 1f, g). Obtained samples were termed G_x (x= 0.5, 1.0, 1.5, 2.5).

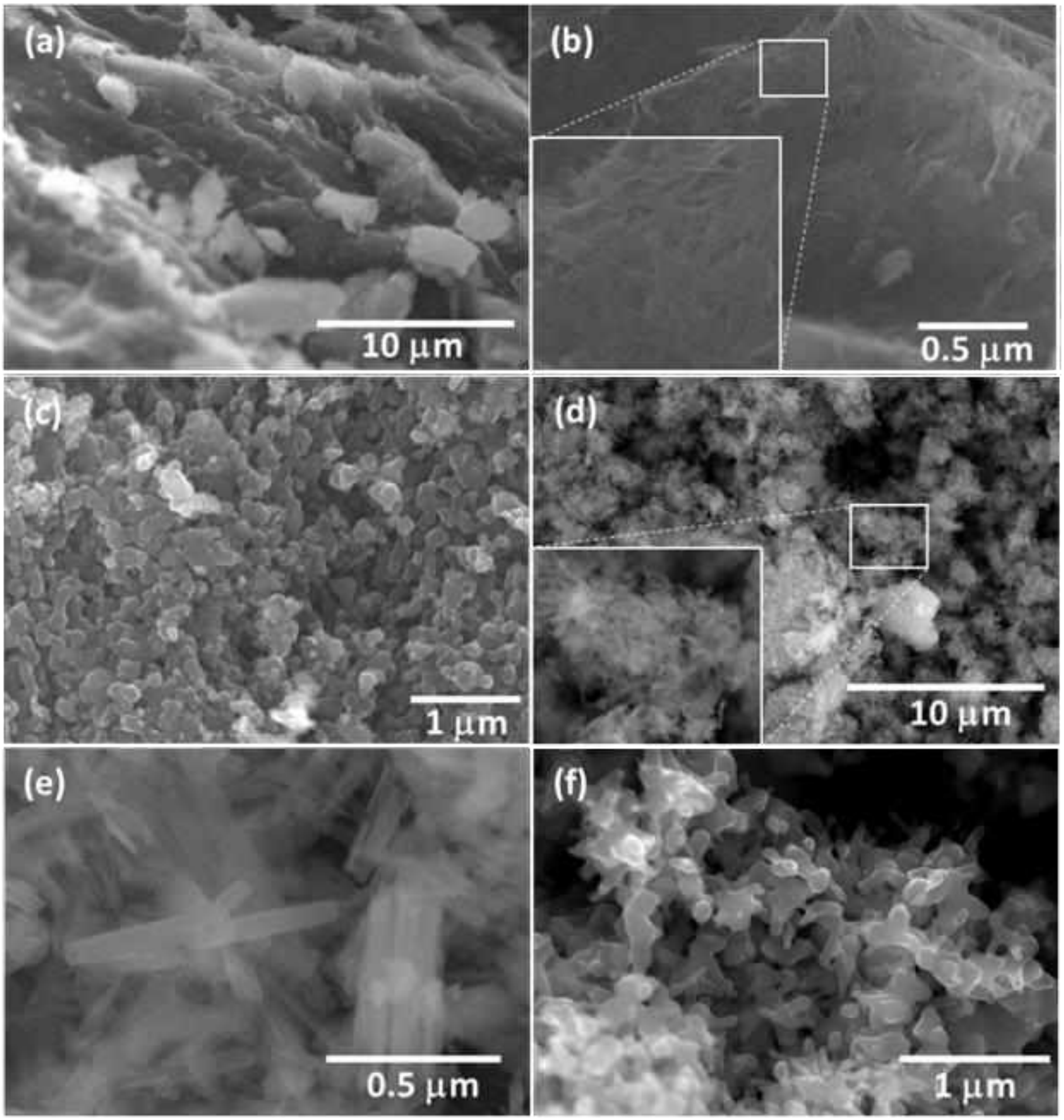

Figure 2. SEM images: (a) aggregated Fe(OH)$_x$ produced by NH$_3$, (b) corresponding magnified image, (c) FeO$_x$ obtained by NH$_3$ method, (d) needle like Fe(OH)$_x$ produced by urea, (e) corresponding magnified image, (f) FeO$_x$ obtained by urea method.

Iron NPs synthesis. As the role of iron NPs is the cornerstone of this strategy, its synthesis was initially optimized. The formation of Fe(OH)$_x$ NPs was investigated using NH$_3$ or urea.[10] In both approaches, Fe(OH)$_x$ was obtained by the reaction of iron ions with hydroxyl ions. In the former situation, dense $Fe(OH)_x$ particles were obtained (Figure 2a, b). In contrast, urea produced a fluffy $Fe(OH)_x$ composed of needle-like particles that were expected to widen the distance between graphene interlayers (Figure 2d, e). In the case of urea treatment, we noticed that the walls of the reactors were uniformly coated with the orange color of $Fe(OH)_x$, suggesting the slow formation of $Fe(OH)_x$ translating the uniform formation of GO-Fe(OH). In contrast, in the case of NH_3, nothing was formed on the walls. Therefore, we concluded that the $Fe(OH)_x$ was slowly formed, and uniform production of GO-$Fe(OH)_x$ was achieved when urea was used. X-ray diffraction (XRD) for the iron hydroxide compounds prepared by urea or NH_3 showed completely different patterns: NH_3 provided amorphous $Fe(OH)_x$, while urea provided crystalline $Fe(OH)_x$ (Figure 3iii, iv), supporting the slow and uniform formation of $Fe(OH)_x$ by urea.

After 600 °C thermal treatment under N_2, $Fe(OH)_x$ prepared with both NH_3 and urea turned into similar FeO_x particles (Figure 2c, f). XRD analysis revealed Fe_3O_4 was mainly formed (Figure 3i, ii).[11] A stronger intensity and sharper peak were observed on the sample prepared by the urea method, indicating its higher crystallinity.

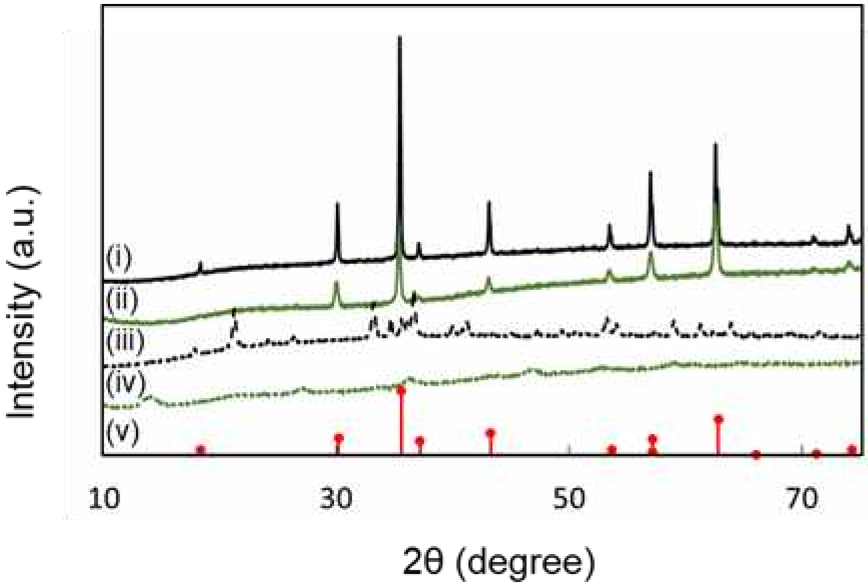

Figure 3. XRD patterns of (i) FeO_x from Urea, (ii) FeO_x from NH_3, (iii) $Fe(OH)_x$, (iv) $Fe(OH)_x$, (v) simulation of Fe_3O_4.

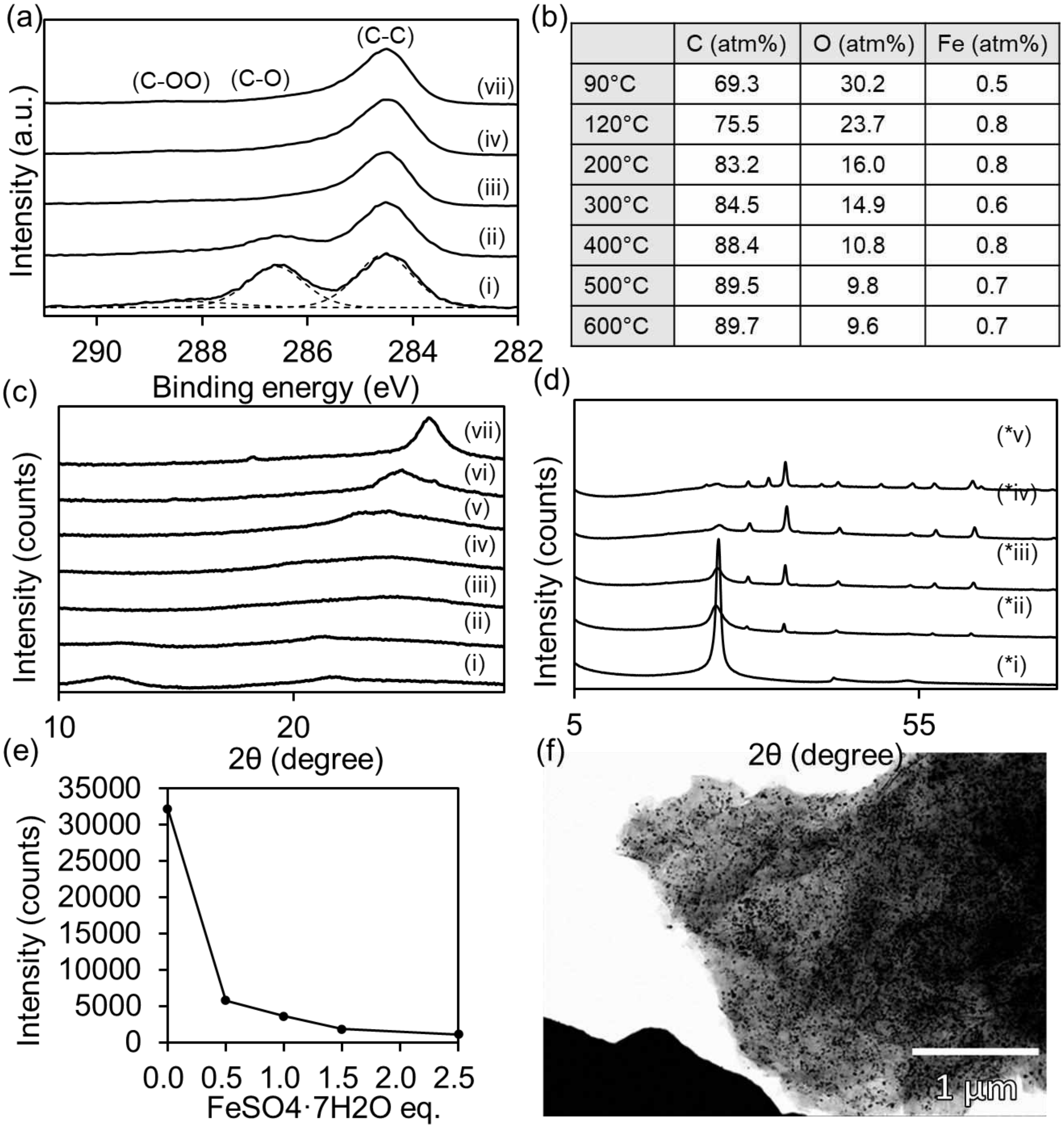

	C (atm%)	O (atm%)	Fe (atm%)
90°C	69.3	30.2	0.5
120°C	75.5	23.7	0.8
200°C	83.2	16.0	0.8
300°C	84.5	14.9	0.6
400°C	88.4	10.8	0.8
500°C	89.5	9.8	0.7
600°C	89.7	9.6	0.7

Figure 4. (a) C 1s XPS of rGO-FeO1.0 composites prepared at various temperatures. (b) Atomic concentration ratio of rGO-Fe1.0 surface prepared by XPS. (c) XRD patterns of rGO-FeO1.0 composites prepared at various temperatures: (i) before heating, (ii) 120 °C, (iii) 200 °C, (iv) 300 °C, (v) 400 °C, (vi) 500 °C, (vii) 600 °C. (d) XRD patterns of rGO-FeOX composites prepared in various FeSO4·7H2O amounts: (*i) 0 eq., (*ii) 0.5 eq., (*iii) 1 eq.%, (*iv) 1.5 eq., (*v) 2.5 eq. (e) XRD patterns of effect of prevention of rGO re-stacking by various FeSO4·7H2O amounts, (f) TEM image of rGO-FeO1.5.

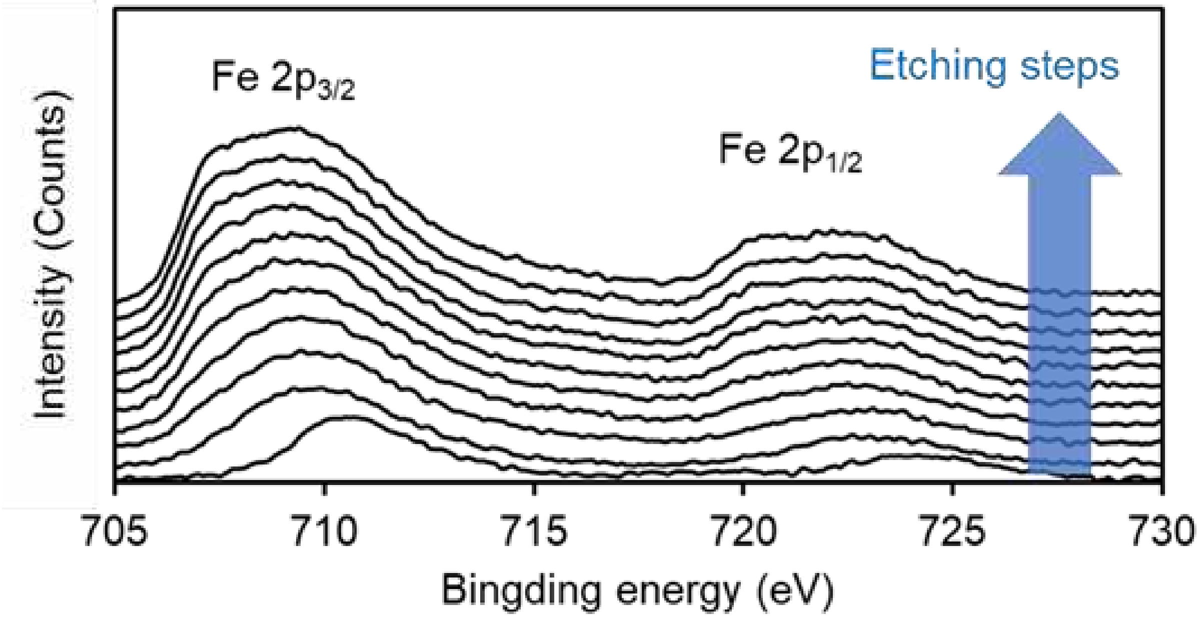

Figure 5. Iron sandwiched between GO layers was confirmed by XPS, with etching of surface layer by layer by Argon ion beam.

Based on the above investigations, we decided to use the urea method to synthesize GO-Fe(O)H_x composites for the following studies.

Synthesis and characterization of rGO-FeOx. We investigated the structural change by thermal treatment from 90 to 600 °C for GO-Fe$(OH)_{1.0}$. The chemical state and elemental composition were observed by X-ray photoelectron spectroscopy (XPS) (Figure 4a). The C 1s region of GO-Fe$(OH)_{10}$ could be separated into three waveforms, 284.5 eV, 286.6 eV, and 288.3 eV, which were considered C-C, C-O, and C=O, respectively.[8,12,13] As the temperature increased, the intensity of C-O and C=O decreased.[14] The oxygen, carbon, and iron atomic ratios were obtained by peak area quantification of XPS data (Figure 4b). Heating at higher than 500 °C produced an oxygen concentration below 10%. Far lower Fe contents than expected were obtained in the XPS measurement for all the samples (Figure 4b) due to the features of XPS measurement (i.e., XPS can only provide surface information). This result suggests that iron particles are present inside the GO layers. To confirm this hypothesis, we used an argon ion beam to etch the surface systematically, and measured XPS accordingly (Figure 5). All the samples showed two peaks attributed to Fe 2p3/2 and Fe 2p1/2, respectively, which were split by spin-orbit interaction. The iron peaks were very weak in the spectrum for the measurement of the composite surface prior to etching, because surface iron species were washed off during the purification treatment. After etching, the peaks of Fe 2p3/2 and

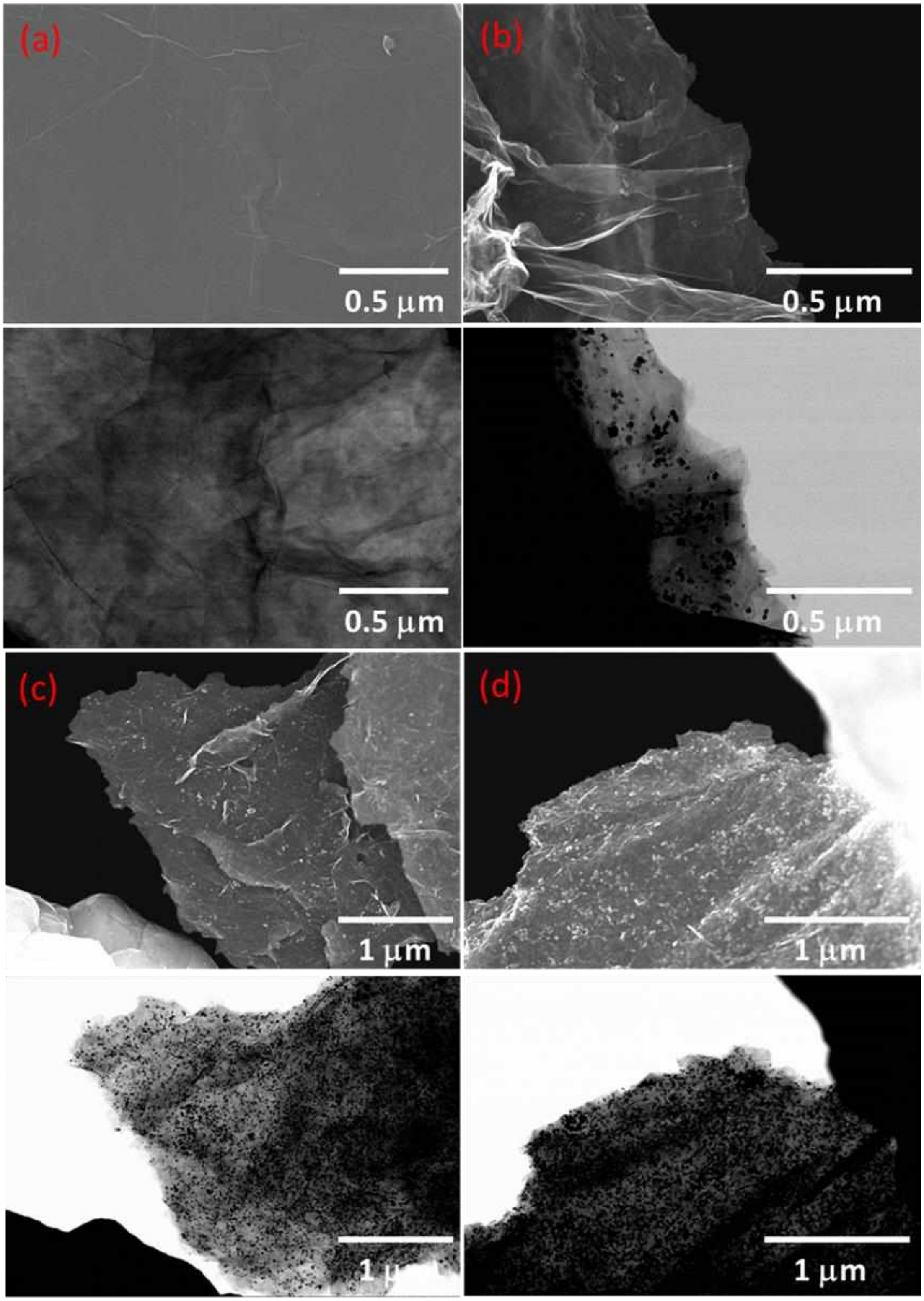

Figure 6. SEM (upper) and TEM (lower) images of rGO and iron oxide nano-particles with various amount of iron prepared in 600◦C. (a) rGO-$FeO_{0.5}$, (b) rGO-$Fe_{1.0}$, (c) rGO-$Fe_{1.5}$, (d) rGO-$Fe_{2.5}$.

Fe 2p1/2 suddenly became stronger, indicating that iron was located inside the layers of rGO. Furthermore, even after several etchings, the intensity of peaks became constant, demonstrating that the amount of iron particles contained inside the rGO interlayer was uniform.

The structural change of rGO and the formation of FeO_x were investigated at different temperatures by XRD (Figure 4c). It has been reported that GO shows a clear (002) diffraction peak at around 2θ = 12°, and it shifts at around 26° by reduction.[13,15,16] As shown in Figure 4c, all the (002) peaks of rGO-$FeO_{1.0}$ were weak and broad, suggesting the iron particles were well anchored between GO sheets. Treatment of GO-$Fe(OH)_{1.0}$ at 90 °C (Figure 4ci) showed a small GO-like (002) diffraction at 2θ= 12°, meaning that the reduction of GO was not completed. Increasing the temperature to 120 °C was enough to reduce the GO (002) peak (Figure 4cii). By a further temperature increase, the peak of graphite appeared and became sharper and closer to 26°, suggesting the partial graphitization in rGO-$FeO_{1.0}$ (Figure 4ciii-viii). In the following section, rGO-FeO_x were prepared at 600 °C.

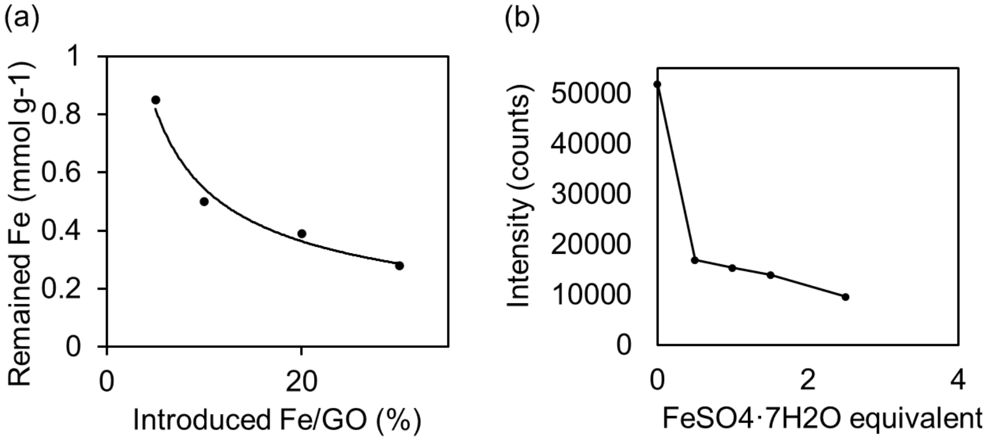

Figure 7. (a) Atomic absorption of Fe from burned ashes of rGO with various iron amounts, (b) XRD patterns of G_X prepared at various iron amounts: (i) 0 eq., (ii) 0.5 eq., (iii) 1 eq., (iv) 1.5 eq., (v) 2.5 eq.

To prevent the graphitization, the amount of iron was investigated. The degree of rGO stacking was investigated by XRD for rGO-FeO_x with various iron contents treated at 600 °C (Figure 4d).

By introducing only 0.5 eq. iron to the weight of GO, the (002) peak of rGO-$FeO_{0.5}$ became smaller, about 18% of rGO without iron (Figure 4e). As the amount of iron was increased, the (002) peak weakened and almost disappeared with 2.5 eq. iron to the weight of GO, reaching only 3% of rGO without iron. These results support the hypothesis that the in-situ formation of $Fe(OH)_x$ NPs between GO sheets lowers the stacking of rGO sheets during thermal reduction.

The morphology of rGO-FeO_x was observed by scanning electron microscopy (SEM) and transmission electron microscopy (TEM) (Figure 6 and 4f). SEM and TEM both confirmed the formation of FeO_x NPs. More interestingly, larger numbers of particles were observed for TEM than SEM, suggesting that FeO_x NPs were present inside the rGO layers since SEM can only detect the NPs on the surface.

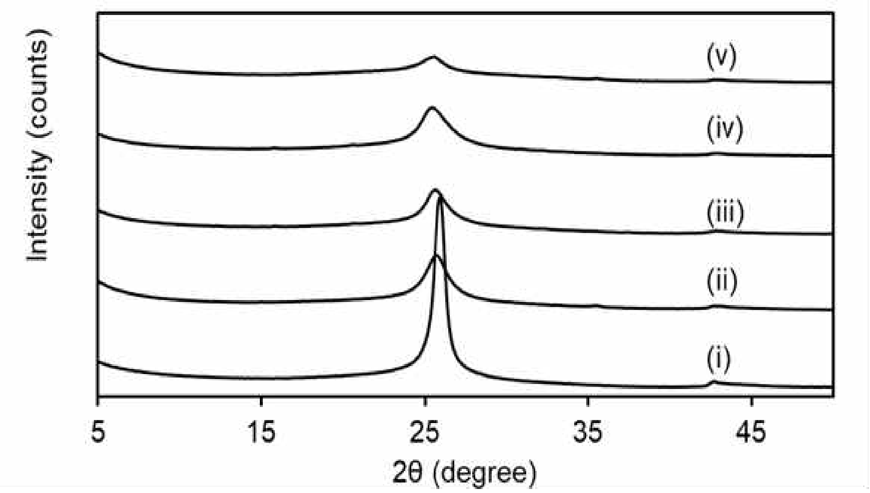

Figure 8. XRD of (i) rGO, (ii) $G_{0.5}$, (iii) $G_{1.0}$, (iv) $G_{1.5}$, (v) $G_{2.5}$.

Removal of FeO_x NPs from rGO-FeO_x. G_x was synthesized by washing out FeO_x from rGO-FeO_x using concentrated hydrochloric acid. After treatment, G_x could not be affected by a magnet. To confirm the remaining iron species, G_x was analyzed by atomic absorption spectroscopy (Figure 7a). The result indicated that the amount of iron in $G_{2.5}$ was below 0.3 mmol g^{-1}. Interestingly, we observed that the amount of remaining iron decreased with the amount of iron originally present, indicating that it is more difficult to remove iron species from rGO-FeO_x prepared from a smaller iron amount. We believe that low iron loading on GO led to the formation of iron species wrapped by graphene, which were inaccessible to hydrochloric acid, while graphene could not wrap iron species when its amount was high, enabling the access to hydrochloric acid. The stacking degree of G_x was evaluated by XRD; the graphite (002) peak was reduced as the amount of iron increased (Figure 7b and Figure 8). With only 0.5 eq. $FeSO_4 \cdot 7H_2O$, the stacking was lowered by 68%, and with 2.5 eq. the stacking was lowered by 92%, demonstrating that G_x preserved the unstacked nature of rGO-FeO_x after the removal of FeO_x NPs.

LIBs and SIBs evaluation. The Li-ion and Na-ion storage capabilities of G_x were evaluated in a half-cell configuration using 2032-type coin cells. The electrodes were prepared using G_x as active materials and polyvinylidene fluoride as a binder without adding any conductive materials. A comparative study was conducted using rGO and G_x prepared with various iron contents by charge–discharge cycle tests at a current rate ranging from 0.186 to 37.2 A g^{-1} and from 20 to 400 mA g^{-1} for LIBs and SIBs, respectively.

For LIBs at 186 mA g^{-1}, rGO expressed a specific capacity of 600 mAh g^{-1}, while $G_{0.5}$ had a specific capacity of 453 mAh g^{-1} (Figure 9a,b). The inferior performance of $G_{0.5}$ reflects the formation of non-accessible space for Li ions. The specific capacity gradually increased with the increase of iron loading, reaching a maximum specific capacity of 750 mAh g^{-1} for $G_{2.5}$. At 3.72 A g^{-1}, the specific capacity of rGO decreased by 67%, reaching 200 mAh g^{-1} while the specific capacity of $G_{2.5}$ decreased by 53% to 350 mAh g^{-1}, denoting the superior capability of $G_{2.5}$ for high-rate LIB. After 45 cycles, at 372 mA g^{-1}, the capacity stabilized, and the charging capacity was 362 mAh g^{-1} for rGO and 507 mAh g^{-1} for $G_{2.5}$. The increase of the specific capacity was correlated with the increased charge-discharge potential between 0.8 V and 2.8 V (Figure 9b).

For the SIBs evaluation at 20 mA g^{-1}, rGO, $G_{0.5}$, and $G_{1.0}$ expressed similar specific capacities of around 150 mAh g^{-1} (Figure 9b,c). The low amount of Fe NPs did not improve the active surface of G_x for large ions (Na^+); therefore, there was no visible impact on the performance. In contrast, $G_{1.5}$ and $G_{2.5}$ showed increases of the specific capacity to 230 mAh g^{-1} and 297 mAh g^{-1}, respectively. At 400 mA g^{-1}, the specific capacity of rGO decreased by 55%, reaching 68 mAh g^{-1}, while the specific capacity of $G_{2.5}$ decreased by 52% to 143 mAh g^{-1} denoting the superior capability of $G_{2.5}$ for Na-ion batteries. After 30 cycles, the capacity stabilized, reaching a stable charge capacity performance at 100 mA g^{-1} of 130 mAh g^{-1} for rGO, while $G_{2.5}$ reached 252 mAh g^{-1}. The increase of charge specific capacity was correlated with the increased capacity between 0.3 V and 2.2 V (Figure 9b), translating the improvement of Na^+ absorption in unstacked graphene layers.

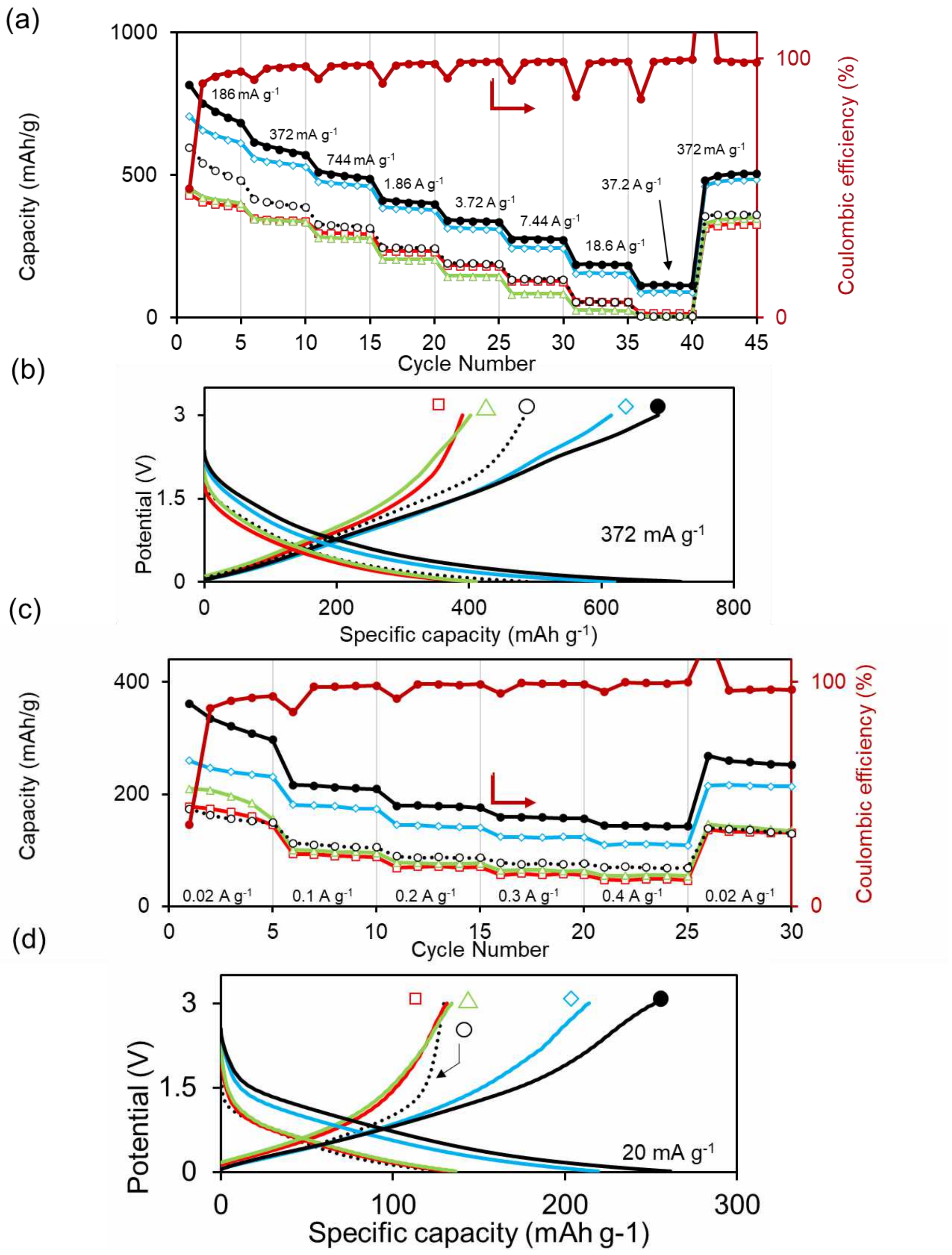

Figure 9. LIBs evaluation of G_x prepared with different iron content: (a) specific charge capacity at different current rate and coulombic efficiency, (b) 5th cycle charge behaviour at 372 mA g^{-1}. SIBs evaluation of G_x prepared with different iron content: (c) specific charge capacity at different current rate and coulombic efficiency, (d) 5th cycle charge behaviour at 20 mA g^{-1}. Samples: rGO (black circle), G0.5 (blue square), G1.0 (green triangle), G1.5 (blue diamond), G2.5 (black round).

These results demonstrate that the un-stacking of graphene layers and formation of the graphene 3D structure improve the overall capacitor behavior, enabling more linear charge behavior. Unlocking the full capacitor behavior of graphene leads to superior capacity performance.

III. CONCLUSION

In summary, we have designed a simple, cost-effective, and scalable method for the synthesis of 3D graphene applying FeO_x NPs as inter-layer spacers. The synthesis of iron NPs was investigated using $FeSO_4 \cdot 7H_2O$ as the iron source and urea or NH_3 as the base. The results revealed that directly using NH_3 formed aggregated and lower crystallinity NPs, while urea slowly decomposed into NH_3 led to the formation of iron NPs with a needle-like structure and superior crystallinity. Given these convincing results, the urea method was applied to GO aqueous dispersion, resulting in the formation of GO-$Fe(OH)_x$. The reduction of GO at high temperature in N_2 atmosphere led to the formation of rGO-FeO_x, while lowering the staking level of graphene layers by FeO_x NPs. Then, iron NPs were removed using HCl to obtain 3D graphene, which preserved the unstacked nature of the original rGO-FeO_x. In light of the positive result, the 3D graphene was applied to LIBs and SIBs, providing superior capacity and capability performances. The best results were obtained for $G_{2.5}$ which displayed 590 mAh g^{-1} at 372 mA g^{-1} for LIBs and 297 mAh g^{-1} at 20 mA g^{-1} for SIBs.

IV. EXPERIMENTAL SECTION

Materials. $KMnO_4$, H_2SO_4, 30% aq. H_2O_2, urea, were purchased from Wako Pure Chemical Industries, Ltd. HCl was purchased from nacalai tesque, INC. $FeSO_4 \cdot 7H_2O$ was purchased from KANTO CHEMICAL CO.,INC. All the chemicals were used directly without further purification.

Characterization instrumentation and experimentation. Freeze-dried of GO was performed by ADVANTEC DRZ350WC. XPS was measured by JPS-9030 with a pass energy of 20 eV. The crystalline structure of samples was characterized by X-ray diffraction (XRD) using a PANalytical Co. X' part PRO using Cu Kα radiation (l= 1,541 Å) in the 2θ range of 5–75°. The operating tube current and voltage were 30 mA and 40 kV, respectively. The data was collected at the step size of 0.017° and the type of scan was continuous. The morphology was measured by transmission electron microscopy (TEM) JEOL JEM-2100F and atomic force microscopy (AFM) SHIMADZU SPM-9700HT. Heating treatment was conducted using a tube furnace KTF055N1 from KOYO THERMO SYSTEMS.

Graphene oxide (GO) synthesis. GO was synthesized using our modified Hummers' method.[8] Natural flake graphite (3.0 g) was stirred in 95% H_2SO_4 (75 mL). $KMnO_4$ (9.0 g) was gradually added to the solution keeping the temperature <10 °C. The mixture was then stirred at 35 °C for 2 h. The resulting mixture was diluted by water (75 mL) under vigorous stirring and cooling so that temperature does not exceed 50 °C. The suspension was further treated by 30% aq. H_2O_2 (7.5 mL). The resulting suspension was purified by centrifugation with water until neutralization, and freeze-dried.

3D graphene (G) synthesis. In the first step, iron hydroxide was formed on the surface of the GO layer. In a 0.5 wt% GO aqueous dispersion, $FeSO_4 \cdot 7H_2O$ (0.5 to 2.5 weight equivalent of GO) and urea (1.1 weight equivalent of $Fe_2SO_4 \cdot 7H_2O$) were consecutively added and dispersed by sonication for 30 minutes. As prepared mixture was continuously stirred and heated at 90 °C for 2 hours. The composite was collected by filtration or centrifugation, then freeze-dried. In the second step, the thermal treatment (90 to 600 °C) was conducted under N_2 atmosphere. The temperature was increase form R.T to 200 in 1 hour, from 200 to target temperature with 19 °C min^{-1}, kept at the target temperature for 30 minutes. In the last step, 3D graphene was obtained by washing out FeO_x particles with concentrated hydrochloric acid with the aid of sonication for 2 hours.

LIB preparation and evaluation. The CR2032 coin cells were assembled in an Ar-filled glove box to evaluate the electrochemical performance of G_x samples as anode materials for lithium-ion batteries. The slurry was prepared by mixing G_x (90%) and of poly(vinylidene fluoride) binder (10%) in an N-methylpyrrolidone (NMP) as a solvent. The anode was produced by coating the slurry onto copper foil as flat film with a thickness of 0.1 mm by doctor blade. Thin Lithium foil (0.6 mm thick) was employed as the counter electrode and a glass microfiber was used as the separator. The electrolyte was 1 M lithium hexafluorophosphate ($LiPF_6$), dissolved in 1/1 (V/V) ethylene carbonate (EC)/diethyl carbonate (DEC). The coin cells were tested in galvanostatic mode at various currents within a voltage range of 0.01 V to 3.0 V using a 580 Battery Test System (Toyo corporation).

SIB preparation and evaluation. The CR2032 coin cells were assembled in an Ar-filled glove box to evaluate the electrochemical performance of G_x samples as anode materials for sodium-ion batteries. The slurry was prepared by mixing G_x (90%) and of poly(vinylidene fluoride) binder (10%) in an N-methylpyrrolidone (NMP) as a solvent. The anode was produced by coating the slurry onto copper foil as flat film with a thickness of 0.1 mm by doctor blade. Thin sodium foil (0.6 mm thick) was employed as the counter electrode and a glass microfiber was used as the separator. The electrolyte was 1 M sodium hexafluorophosphate ($NaPF_6$), dissolved in 1/1 (V/V) ethylene carbonate (EC)/diethyl carbonate (DEC). The coin cells were tested in galvanostatic mode at various currents within a voltage range of 0.01 V to 3.0 V using a 580 Battery Test System (Toyo corporation).

REFERENCES

1. Ji, K. *et al.* Lithium intercalation into bilayer graphene. *Nat. Commun.* **10**, 1–10 (2019).
2. Yoshino, A. The Birth of the Lithium-Ion Battery. *Angew Chem Int Ed* **51**, 5798– 5800 (2012).
3. Whittingham, M. S. Batterie à Base de Chalcogénures. *Belg. Pat. No* 819672 (1975).
4. Li, H. *et al.* An advanced high-energy sodium ion full battery based on nanostructured Na2Ti3O7/VOPO4 layered materials. *Energy Environ. Sci.* **9**, 3399–3405 (2016).
5. David, L., Bhandavat, R. & Singh, G. MoS2/Graphene Composite Paper for Sodium-Ion Battery Electrodes. *ACS Nano* **8**, 1759–1770 (2014).
6. Mizushima, K., Jones, P. C., Wiseman, P. J. & Goodenough, J. B. LixCoO2 (0. *Mater. Res. Bull.* **15**, 783–789 (1980).
7. Kubota, K. *et al.* Structural Analysis of Sucrose-Derived Hard Carbon and Correlation with the Electrochemical Properties for Lithium, Sodium, and Potassium Insertion. *Chem. Mater.* (2020) doi:10.1021/acs.chemmater.9b05235.
8. Morimoto, N., Kubo, T. & Nishina, Y. Tailoring the Oxygen Content of Graphite and Reduced Graphene Oxide for Specific Applications. *Sci. Rep.* **6**, 21715 (2016).
9. Morimoto, N. *et al.* Real-Time, in Situ Monitoring of the Oxidation of Graphite: Lessons Learned. *Chem. Mater.* **29**, 2150–2156 (2017).
10. Zhu, X., Zhu, Y., Murali, S., Stoller, M. D. & Ruoff, R. S. Nanostructured Reduced Graphene Oxide/Fe2O3 Composite As a High-Performance Anode Material for Lithium Ion Batteries. *ACS Nano* **5**, 3333–3338 (2011).
11. Downs, R. T., Bartelmehs, K. L., Gibbs, G. V. & Boisen, M. B. Interactive software for calculating and displaying X-ray or neutron powder diffractometer patterns of crystalline materials. *Am. Mineral.* **78**, 1104–1107 (1993).
12. Yang, D. *et al.* Chemical analysis of graphene oxide films after heat and chemical treatments by X-ray photoelectron and Micro-Raman spectroscopy. *Carbon* **47**, 145–152 (2009).
13. Campéon, B. D. L. *et al.* Non-destructive, uniform, and scalable electrochemical functionalization and exfoliation of graphite. *Carbon* **158**, 356–363 (2020).
14. Pei, S. & Cheng, H.-M. The reduction of graphene oxide. *Carbon* **50**, 3210–3228 (2012).
15. Gadipelli, S. & Guo, Z. X. Graphene-based materials: Synthesis and gas sorption, storage and separation. *Prog. Mater. Sci.* **69**, 1–60 (2015).

16. Diby Ossonon, B. & Bélanger, D. Synthesis and characterization of sulfophenyl-functionalized reduced graphene oxide sheets. *RSC Adv.* **7**, 27224–27234 (2017).

CHAPTER 5

CONCLUSION

In conclusion, this manuscript report the research conducted during my doctor course at Okayama University. This research has been guided with the intention to develop original methods for the synthesis and functionalization of carbon material for electrical application.

In order to design original research projects, previous scientific literature concerning graphene synthesis and application toward LIBs were investigated and a brief summary has been given in the introduction chapter of this manuscript. Several problems were found hindering the commercialization of graphene-based LIBs, which were related to graphene synthesis:

- Cost
- Scalability
- Toxicity
- Quality uncertainty leading to hazardous LIBs results

In the following chapters, several research projects were reported aiming to move toward the resolution of those issues:

- Non-destructive, uniform, and scalable electrochemical functionalization and exfoliation of graphite

- Sophisticated rGO synthesis and pre-lithiation unlocking full-cell lithium-ion battery high-rate performances

- Iron nanoparticle templates for constructing 3D graphene frame-work with enhanced performance in sodium-ion batteries

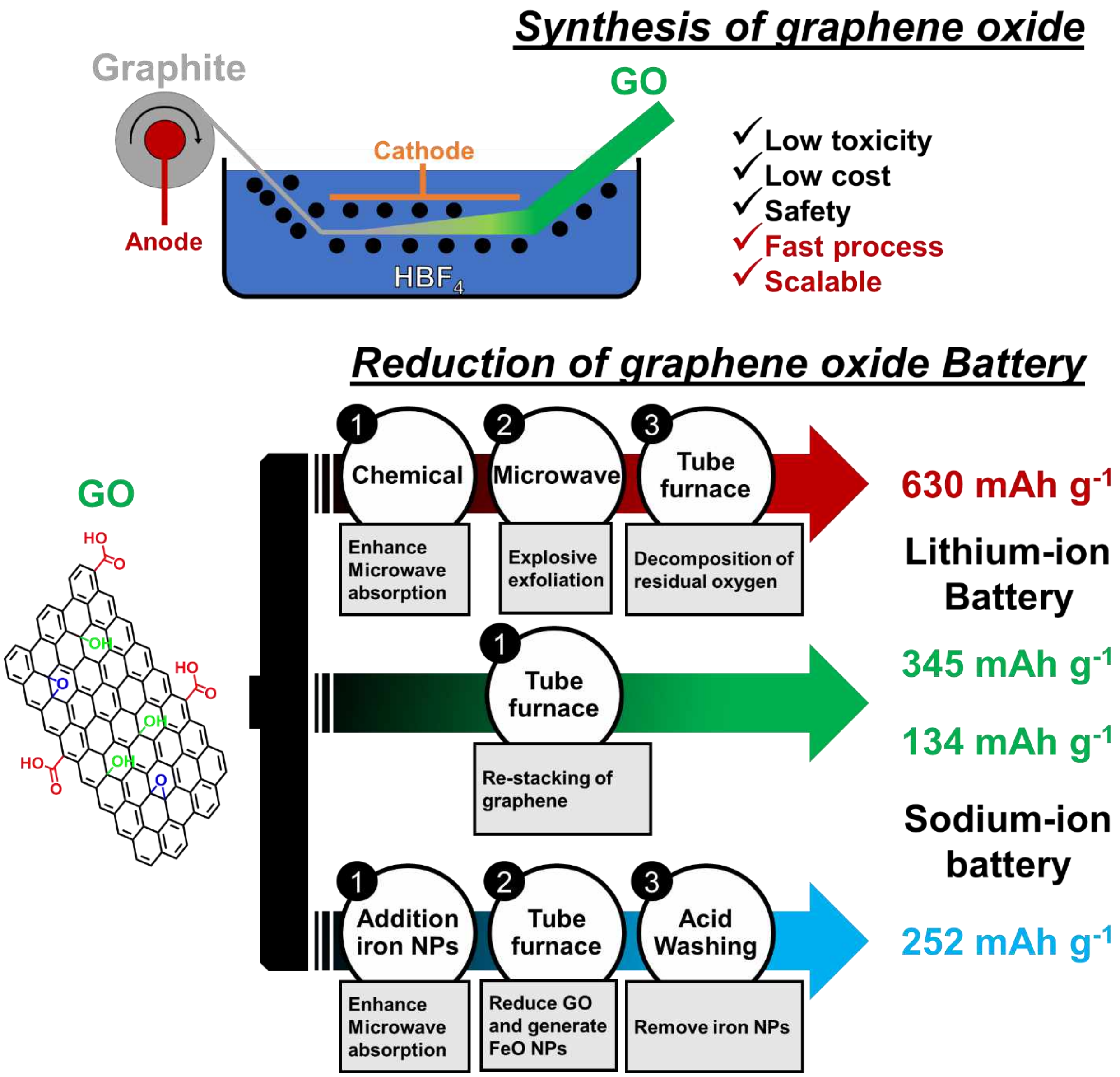

Figure 1: Illustration of progressed realized for the synthesis of GO and its reduction in rGO for Battery technologies.

The first project presented in chapter 2 shows a crucial innovation for the commercial democratization of graphene oxide synthesis. Usually graphene oxide is synthesized via chemical oxidation via the application of strong acid (H_2SO_4) and oxidant ($KMnO_4$) which rise safety and scalability issues. In our research, we design an electrochemical method using HBF_4 diluted in water (MeOH as well) allowing the safe, easy, and scalable synthesis of graphene oxide. The investigation of this electrochemical graphene oxide shows similar to superior properties and performances (LIBs and water purification) compared with our chemical graphene oxide guaranteeing this synthesis efficiency.

The second project presented in chapter 3 shows an important comparative study of reduced graphene oxide synthesis for its application toward full-cell LIBs. At this moment a myriad of synthesis methods for the production of reduced graphene oxide have been done but most comparative investigation of reduce graphene oxide synthesis focused on its anode half-cell performance only. In our research, reduced graphene oxide analogs were synthesized via a safe, fast, and scalable combined synthesis method. Their characterization and evaluation for anode half-cell and full-cell LIBs indicates that the best synthesis method for LIBs application is obtained via strong chemical reduction followed by tube oven annealing at 1000 °C. Other investigated synthesis methods results in lower cyclability and require superior N/P ratio decreasing the overall LIBs energy density. The full-cell compose of $LiCoO_2$@$BaTiO_3$ cathode and optimized reduced graphene oxide anode shows high energy density and extremely high power density, 604 Wh kg^{-1} at 432 W kg^{-1} and maintained 293 Wh kg^{-1} at 8,658 W kg^{-1} and 20 Wh kg^{-1} at 43,333 W kg^{-1}.

The third project presented in chapter 4 shows a simple and scalable method for the preparation of reduced graphene oxide for SIBs. The motivation for graphene application toward SIBs stands on its ability to absorb ion on both its sides, whereas graphite rigid and compact crystal structure is unable to accommodate and store large sodium ions. However, the synthesis of reduced graphene oxide often results in the partial restacking of its layers hindering sodium ions diffusion and absorption. In this research, we design a scalable method for the synthesis of un-stacked reduced graphene oxide via the consecutive in situ formation and etching of iron nano-particle template. The results demonstrate that graphene prepared via this method show superior SIBs behavior and performances.

In my current research, I am engaged in several projects:

- Synthesis of EGO in organic solvent. My first competed project show that water and methanol could be used to dilute HBF_4 and that it results in GO with different functionalities. I am now investigating other organic solvent for EGO electrolyte to extend the functionalities and process ability of EGO.
- Synthesis of graphene carbon nano tubes network. Based on my third completed work, I am now using in situ formed iron nano particles to grow carbon nano tubes between

graphene layers. Such 3 dimensional network will present tunable interlayer distance and structure and superior strength allowing its application for thick electrode coating.

For my future research, I will focus on applying graphene as an additive for high energy density cathode materials. In the recent years, lithium excess cathode materials have arisen as a promising solution for higher energy density LIBs. However, this class of materials suffers from low conductivity and poor cyclability. I will embed lithium excess nano-particles with graphene to improve their conductivity, stability, and overall LIBs performances.

LIST OF PUBLICATIONS

(1) Non-destructive, uniform, and scalable electrochemical functionalization and exfoliation of graphite

Benoît D. L. Campéon, Mitsuo Akada, Muhammed S. Ahmad, Yasushi Nishikawa, Kazuma Gotoh, Yuta Nishina

Carbon, 2020, 158, 356-363

(2) Iron nanoparticle templates for constructing 3D graphene frame-work with enhanced performance in sodium-ion batteries

Benoît D. L. Campéon, Chen Wang, Yuta Nishina

Nanoscale, 2020, *Accepted*

ACKNOWLEDGEMENT

Je dédie cette thèse à mes parents.

This doctor thesis was conducted in Nishina Laboratory at Okayama University.

I would like to pay my special regards to my sensei Prof. Yuta Nishina who did me the honor of supervising and supporting this thesis and who assured with patience and understanding the good progress of this work.

I wish to show my gratitude to Dr. Bernard Chenevier and A. Prof. Takashi Teranishi for inviting me at Okayama University during my Master thesis and creating this thesis opportunity.

I wish to express my deepest gratitude to my dear friend Aurélien Castellini for being such a friend and having introduced me Dr. Bernard Chenevier.

I would like to thank all the members of the jury for the time they have spent to evaluate my work and any interesting remarks they may have made during the defense.

I would like to express my gratitude to Okayama University for waving my admission and tuition fees.

I wish to thank all the people whose assistance was a milestone in the completion of this project: Prof. Yuta Nishina, A. Prof. Takashi Teranishi, Dr. Cheng Wang, Dr. Mitsuo Akada, M. Muhammad Sohail Ahmad. It is whole-heartedly appreciated that your great advices for my study proved monumental towards the success of this study.

I owe a very important debt to my laboratory members for making our laboratory a place where I felt home: M. Sohail, M. Rizwan, M. Zhou, Dr. Cheng, Dr. Nizami, Nusrat, M. Takata, M. Hori, Tamagawa, Tomita, Dr. Akada, Dr. Matsumura, Dr. Obata, Dr. Nakano, Dr. Azuma, Dr. Komoda, Nakagawa, Fujii, Takeda, Yamagiwa, Dr. Yonehara.

Je voudrais aussi remercier mes parents Thierry et Dominique, mon frère Guillaume et ma soeur Camille, son fiancé Etienne, et leurs enfants Marcel et Léopold pour m'avoir encouragé et aidé à accomplir mon rêve. Je vous aime très fort!

Je voudrais aussi remercier mon oncle André et ma sœur Camille pour avoir montré qu’il n’y avait rien d’impossible.

私の日本の家族、かたやまやすおさん、かずえさん、テン　ロマ、エルザ、リカ、リョウ　へたくさんの家の思い出を与えて下さった私の日本の家族に心から感謝しています。

I would like to thank all my friends who helped me making unforgettable memories during those 4 years at Okayama.

Finally, I would like to thank my best friend and my love Haruka who brings into my life infinite joy and happiness. I cannot wait to see the next chapter of our life.